

N7714745 3083

DECLASSIFICATION STATEMENT A  
Approved for public release  
Distribution Unlimited

DTIC QUALITY INSPECTED 3

A Service of:

19970814 063



National Aeronautics and  
Space Administration

Scientific and Technical  
Information Program Office  
Center for AeroSpace Information

PID (PROPORTIONAL INTEGRAL DERIVATIVE) MODELING TECHNIQUES APPLIED TO  
STUDIES OF MOTION AND PERIPHERAL DISPLAY EFFECTS ON  
HUMAN OPERATOR PERFORMANCE\*

By Daniel W. Repperger and Andrew M. Junker

Aerospace Medical Research Laboratory  
Wright-Patterson Air Force Base, Ohio 45433

SUMMARY

A preliminary approach to system identification is introduced in which a man in a closed loop tracking task is modeled in a Proportional Integral Derivative (PID) manner. In order to obtain a PID type model for man's transfer function, a choice of state variables had to be selected in a proper manner. The PID type model presented here is an approximation and is accurate within the linear representation of man's transfer function. Closed loop remnant signals may also influence PID parameters. Therefore, an investigation of human remnant (remnant reflected at the human's observation point) was also studied. This type of modeling approach yields interesting results on the manner in which man uses the displayed error signal to generate his stick response. The data base for this study includes motion cues of a roll axis tracking task and also a peripheral display experiment, both of which studied effects on tracking performance.

INTRODUCTION

The term PID (Proportional Integral Derivative) controller is well known from process control and other applications as indicated by Athans, reference (1). Recently in the area of manual control, PID type optimal control models have been considered by Phatak and Kessler, reference (2). The approach presented here is not an optimal control technique but is a method to identify particular structures of man when he is involved in a closed loop tracking task. The optimal control models can be considered as methods to predict performance in the future (~~this~~ may be termed "A Priori" modeling). The approach presented in this paper is to investigate what happened in the past from an experiment when all the data has been collected (~~this~~ may be termed "A Posteriori" modeling.) The modeling technique presented here can be used only after the data has been collected; this technique cannot be used to pre-

\*The research reported in this paper was sponsored by Aerospace Medical Research Laboratory, Aerospace Medical Division, Air Force Systems Command, Wright-Patterson Air Force Base, Ohio 45433. Further reproduction is authorized to satisfy needs of the U.S. Government.

dict performance ahead of time as compared to the optimal (A Priori) control type models. The approach presented here combines modern control theory techniques (a least squares identification algorithm) with describing function techniques. A study of human remnant effects must be considered and a rudimentary statistical analysis is done. It is emphasized here that the results obtained are only preliminary because of some approximations which must be made in the sequel of this paper. It will take a more complete study to consider this problem without the approximations.

#### Description of the Data Base Used

The study of motion effects on man and peripheral displays is extensive as indicated in the work of Shirley, reference (3), Young, reference (4), Stapleford, reference (5), Ringland, reference (6), and others. The data base from the roll axis tracking study used here differs from the data used in the above references by the following:

(1) The roll motion in the Aerospace Medical Research Laboratory (AMRL) study was strictly in the roll axis with no washout circuits built in to align the g-vector with the spine of the subject.

(2) In the AMRL motion study, the input was purely a command signal; i.e. the plant was driven only by the subject's control inputs. In the earlier studies, the input disturbance was applied in such a manner that both the visual display and the motion simulation were driven by the input (i.e. the input was applied essentially in parallel with the pilot's control).

(3) The plant dynamics in the AMRL study were higher order than those in the previous studies.

Reasons (2) and (3) were pointed out by W. Levison, reference (7) and in the report by Levison and Baron, reference (8). In the report, reference (8), phase droop was identified as one of the important factors which is a consequence of motion effects and also they were able to predict (in an A Priori manner) when motion would help performance for simpler plant dynamics as a function of attention allocation. The data base discussed in this paper has been discussed by Junker and Price, reference (9), Moriarty, reference (10), and Price, reference (11), and details of the particular experiment can be found in any of these references. It is noted that some of the analytic results presented here for this motion study may not be in complete agreement with the analytic results of previous studies, references (3,4,5,6). The primary reason for this fact is that different simulators were used. Since the study of motion effects is a very deep and complex area, the analytic results from different simulators should be considered separately. Perhaps if the analytic techniques presented here were applied to the earlier data, the same conclusions would have been obtained.

#### The Tracking Problem of Interest

With reference to Figure (1a), the typical man-in-the-loop problem is illustrated. The input forcing function is a sum of sine waves with

randomized initial phase angles.  $e(t)$  denotes the displayed error signal and  $st(t)$  denotes the stick output signal of man (rate command). The machine denotes all non-human elements appearing in the closed loop which includes the effects of the display and other non-human factors. For the data presented here, the plant had dynamics characterized by:

$$H(s) = \frac{14.0}{s^2(1+s/.5)(1+s/6.)} \quad (1)$$

Although this plant appears very difficult to control, the input forcing function to the closed loop had a  $1/2$  power point at 0.5 radians; hence this plant is actually between second and third order (with respect to the input forcing function).

Three modes of operation were considered in this study, they were

- (1) Static
- (2) Motion
- (3) Peripheral

where the motion mode of operation was in the roll axis and the peripheral mode consisted of TV monitors mounted on the side of the simulator in a fixed base situation. Details of different aspects of this experiment can be found in references (8,9,10,11).

It is interesting to observe how performance in the closed loop changed during the three possible modes of operation. Of the five subjects involved in this experiment, Table 1 illustrates the performance results averaged over the subjects after a sufficient training period for the same plant and input.

From Table 1, it is observed that the peripheral (fixed base) mode of operation was apparently as helpful in improving performance (using the static case as a reference point) as compared to the motion case (which is a moving base simulation). These results made the data base very attractive to study and also to apply some new analysis techniques.

#### The PID Modeling Approach

With reference to Figure (1b), an internal loop approach will be considered. This can only be done if the measured time series  $e(t)$  and  $st(t)$  are available to do the modeling. For this study,  $e(t)$  and  $st(t)$  were stored on magnetic tape and represent the input (displayed error) and output (force stick response) of the man. By taking this internal loop approach, certain advantages exist for purposes of modeling. With reference to Figure (1b),  $\hat{st}(t)$  denotes the estimate of  $st(t)$  from the computer model. The output modeling error in Figure (1b) represented the difference between the true data  $st(t)$  and the estimate  $\hat{st}(t)$  from the computer model. Ideally we would like to have the output modeling error identically zero; in this manner the model and the man would agree exactly. In the true application, however, the output



modeling error is never zero due to many sources of uncertainty (including human remnant). There are two reasons why this internal loop approach has advantages for modeling. First, when remnant is modeled in a closed loop, it is best represented by a point injected (vector) noise source at the point  $e(t)$ . This has been discussed by Jex, Allen, and Magdaleno, reference (12). The variance of the remnant injected noise source when normalized with respect to the magnitude of the closed loop error signal is down to almost -20db as a colored noise source for most practical plants. Using the number .01 $\pi$  as a magnitude relationship, one can expect by going internal to the loop that a 3% input to a linear system will only affect the output by 3% when normalized. Thus remnant will not distort the modeling answers by that much of a factor. It is true for this particular plant that the remnant spectrum was higher on a db scale (a high lead case) when normalized but the above argument still holds. A second advantage in this internal loop approach is that modeling is a correlation between the input and the output time series. A white injected noise at the point  $e(t)$  does not influence correlation because the noise source is white. Hence the remnant will only bias the variance of the output modeling error and not directly affect the linear model obtained.

#### Motivation (For Physiological Studies) For a PID Structure

With reference to Figure (2), it is desired to replace the man in the closed loop by a PID type structure. This approach to modeling is not limited to just man-in-the-loop problems but can be applied to any two measured time series (for this case  $e(t)$  and  $s(t)$ ) which may result from any biological process. The representation transfer function of the man-in-the-loop is specified by:

$$\text{Man} = G(s) = a_0 + a_1 s + a_2 s^2 + \frac{a_3}{s} + \frac{a_4}{s^2} \quad (2)$$

where  $s$  indicates the Laplace transform operator. The advantages of this simple type structure to investigate how the input-output time series are related can be seen by rewriting equation (2) as follows:

$$\text{Man} = a_0 \left[ 1 + c_1 s + c_2 s^2 + \frac{c_3}{s} + \frac{c_4}{s^2} \right] \quad (3)$$

where the terms  $c_1$  and  $c_2$  indicate the ability of the man to differentiate and  $c_3$ ,  $c_4$  indicate how memory (or integration) is being used. The term  $a_0$  depends on the display gain, stick gain, scaling and other factors. With reference to equation (3), and recalling the classical definition of pilot lead (displayed in Figure (3)), one can relate pilot lead to the bracketed terms of equation (3). The terms  $c_1$  and  $c_2$  may be dominant with respect to 1 if they are non zero. Also, the memory terms  $c_3$  and  $c_4$  may or may not be zero. The question of the existence of the coefficients (being non zero) can only be answered in a statistical manner. The choice of the form of equation (3) including the terms  $c_3$  and  $c_4$  was chosen for tracking tasks which may not be compensatory. In the well known book of Sheridan and Ferrell, reference (13), it is mentioned that the three hierarchies of tasks (precognitive, pursuit,

and compensatory) are of interest in the study of man-machine systems. The choice of the structure given in equation (3) was motivated by the need to have a modeling approach applicable for all types of tasks (precognitive, pursuit, and compensatory).

It is now necessary to consider two basic problems that arise. First, we must determine  $a_i$  ( $i = 0, \dots, 4$ ) given in equation (2) and secondly it is necessary to implement this modeling approach.

#### The Technical Approach to Determine the PID Coefficients

Laplace transforming equation (2) yields:

$$\frac{ST(s)}{E(s)} = \frac{a_2 s^4 + a_1 s^3 + a_0 s^2 + a_3 s + a_4}{s^2} \quad (4)$$

in order to apply state variables to such an expression as equation (4), certain difficulties arise. Taking the reciprocal of both sides of equation (4) yields:

$$\frac{E(s)}{ST(s)} = \frac{s^2}{a_2 s^4 + a_1 s^3 + a_0 s^2 + a_3 s + a_4} \quad (5)$$

In the time domain, this can be written

$$a_2 \ddot{\ddot{e}} + a_1 \dot{\ddot{e}} + a_0 \ddot{e} + a_3 \dot{e} + a_4 e = \ddot{st} \quad (6)$$

For simplicity, equation (6) will be written:

$$\ddot{\ddot{e}} + b_1 \dot{\ddot{e}} + b_2 \ddot{e} + b_3 \dot{e} + b_4 e = b_5 \ddot{st} \quad (7)$$

It is necessary to now discuss what physically occurred in the transition from equation (4) to equation (5). In order to determine the coefficients  $b_1, \dots, b_5$ , an input error identification procedure must be used. This is a consequence of going from equation (4) to (5).

With reference to Figure (4), a comparison between output error identification and input error identification is illustrated. For input error identification,  $st(t)$  is the input into the computer model and  $\hat{e}(t)$  is the best estimate of  $e(t)$  generated by the computer model. Input error identification has been used by Shinnars (14), and is used commonly in Europe as discussed by Astrom, reference (15). In order to implement this type of identification, the input-output data channels have to be switched in order and the time lag (approximately .2 seconds) is accounted for in the input-output data by a shift of an integral multiple of the sampling rate (25 hz). The time lag is actually positive with this type of shift on the data channels. It is noted that input error identification has advantages over output error identifi-

cation if  $e(t)$  is known with more certainty (i.e., less noise) than  $st(t)$ . The choice of the modeling approach may depend on the type of data available.

#### Implementation of the PID Model

In order to implement equation (7), the following state variables are chosen:

$$x_1(t) = e(t) \quad (8a)$$

$$\dot{x}_1(t) = x_2 \quad (8b)$$

$$\dot{x}_2(t) = x_3 + b_5 st(t) \quad (8c)$$

$$\dot{x}_3(t) = x_4 + (-b_1 b_5) st(t) \quad (8d)$$

and  $\dot{x}_4$  satisfies equation (7).

Differentiating the state vector yields the following state equations:

$$\dot{\bar{x}} = \mathbf{A} \bar{x} + \mathbf{B} st(t) \quad (9a)$$

$$y(t) = \mathbf{H} \bar{x} = [1, 0, 0, 0] \bar{x} = e(t) \quad (9b)$$

Where:

$$\mathbf{A} = \begin{bmatrix} 0, 1, 0, 0 \\ 0, 0, 1, 0 \\ 0, 0, 0, 1 \\ -b_4, -b_3, -b_2, -b_1 \end{bmatrix}, \quad \mathbf{B} = \begin{bmatrix} 0 \\ b_5 \\ -b_1 b_5 \\ (b_1^2 - b_2) b_5 \end{bmatrix} \quad (10)$$

It is noted that the  $[\mathbf{A}, \mathbf{H}]$  matrix is observable but  $\mathbf{A}$  may not be stable (for  $b_1 > 0$ ). The  $[\mathbf{A}, \mathbf{B}]$  matrix is in a form in which it cannot be determined if it is controllable due to the non-linear relationships which appear in the third and fourth elements of  $\mathbf{B}$ . It would be necessary to now implement a constrained (with these non-linear constraints) least squares algorithm on the unknowns  $b_1, \dots, b_5$ . For reasons to be mentioned in the sequel, the following approach is chosen to implement this method. Choose:

$$\mathbf{B} = \begin{bmatrix} 0 \\ b_5 \\ b_6 \\ b_7 \end{bmatrix} \quad (11)$$

where  $b_6$  and  $b_7$  are free. There are three practical engineering reasons for doing this: (1) After allowing  $b_6$  and  $b_7$  to be identified, the average values of  $b_1, \dots, b_7$  are checked by the following non-linear constraint relationship:

$$b_6 = -b_1 b_5 \quad (12a)$$

$$b_7 = (b_1^2 - b_2) b_5 \quad (12b)$$

since  $b_6$  and  $b_7$  are identified independently of  $b_1, \dots, b_5$ , the non-linear constraint relationship seems to check within the same order of magnitude. Hence, even with the constrained least squares algorithm, the results are probably not different. (2) Let us now examine the third and fourth state variable of equation (9a):

$$\dot{x}_3 = x_4 + (-b_1 b_5) st(t) \quad (13a)$$

$$\dot{x}_4 = -b_4 x_1 - b_3 x_2 - b_2 x_3 - b_1 x_4 + (b_1^2 b_5 - b_2 b_5) st(t) \quad (13b)$$

with reference to Table 1, and recalling that  $b_1, \dots, b_5$  were identified independently of the remaining parameters, the terms  $\ddot{e}$  and  $\ddot{e}^*$  were compared to the non-linear terms multiplying  $st(t)$ . In all cases the non-linear product terms were significantly below 1% of  $\ddot{e}$  and  $\ddot{e}^*$ . In other words, the non-linearities were well below the noise level in the time series measurement  $e(t)$ . This technique is typical of control theory problems such as in the area of digital filtering. State variables which are two derivatives below the measured time series are generally only approximated. (3) If we were to omit the memory terms ( $c_3$  and  $c_4$ ) of equation (3), the non-linear constraints disappear. Since this experiment was a compensatory tracking task, we would expect  $c_3$  and  $c_4$  to not exist but the method is presented here for completeness in hope of its possible application in a precognitive or pursuit type tracking task.

#### Statistical Analysis of the PID Coefficients

The statistical analysis section of this paper will answer two important questions concerning the coefficients  $c_1, c_2, c_3$  and  $c_4$  of equation (3):

- (1) The question of existence (non-difference from zero).
- (2) The question of change (from the static mode, the motion mode, and the peripheral mode of operation).

One method to study the question of existence of the coefficients  $c_1, c_2, c_3$  and  $c_4$  is to test whether they are statistically non-different from zero (using their means and variances). A two-tailed t-test versus zero was performed using a pooled variance. Three subjects were chosen based on the plots of their respective time series (although Pouldon, reference (16), recommends a minimum of six subjects for any intra or between subject variability) and

six replications were used (averaged over subjects) with the results presented in Table 2. It is noted that these averages contained outlying points (outliers) and in some cases points were rejected using outlier tests in the same manner as is done in FFT studies. In FFT studies, a frequency measurement will be rejected if it differs significantly from adjacent measurements.

In all cases (static, motion, and peripheral), the coefficients  $c_3$  and  $c_4$  were not statistically non-different from zero. Hence they did not exist in a statistical sense. This is to be expected since this was a compensatory tracking task and  $c_3$  and  $c_4$  were representative of memory terms. The following interesting statistical relationships arise from Table 2:

$$c_{3_{p,m,s}} = 0 \quad (14a)$$

$$c_{4_{p,m,s}} = 0 \quad (14b)$$

The subscripts  $p$ ,  $m$ , and  $s$ , of course, correspond to the peripheral, motion, and static modes of operation.

From the results of Table 2, we can conclude that the transfer function of man can be written in the following manner:

$$M_{an} = a_0 [1 + c_1 s + c_2 s^2] \quad (15)$$

In other words, his transfer function was of a second order nature.

The second question the statistical analysis must answer is the question of changes between coefficients. To answer this question, a two-tailed t-test of the means of the coefficients (with a pooled variance) was computed. The results are presented in Table 3.

The three permutations of static-motion, static-peripheral, and motion-peripheral are displayed. At a .05  $\alpha$  level the following statistical results can be determined:

$$c_{1_m} \approx c_{1_p}, c_{2_m} \approx c_{2_p}, c_{2_m} > c_{2_s}$$

At a .1  $\alpha$  level it can be said that:

$$c_{2_p} > c_{2_s}$$

But it cannot be said that:

$$c_{1_m} > c_{1_s}, \text{ or } c_{1_p} > c_{1_s}$$

even though the means of these variables indicate this fact. Also it is interesting to note that in the motion mode of operation the  $\alpha$  level distin-

guishing  $c_{2m} > c_{2s}$  is much sharper than the  $\alpha$  level distinguishing  $c_{2p} > c_{2s}$ . This indicates that in the motion mode of operation the double lead term  $c_2$  is the most important factor. In the peripheral case, however, the double lead term  $c_2$  may not be that important. The results on the motion study agree (for this simulator) with those results presented by Junker, Repperger, and Neff, reference (17). What is perhaps most interesting about this analysis is that if we were to look at Table 1 for the error scores, it would be concluded the motion and peripheral modes of operation had similar effects on the closed loop error and one mode of operation could not be distinguished from another based on the error scores. Looking at Table 3, however, it is easily seen that there exists changes in the means of these coefficients (although statistically they cannot be distinguished) and in addition, sharper changes in the  $\alpha$  levels for  $c_{2m}$  versus  $c_{2s}$  compared to  $c_{2p}$  versus  $c_{2s}$ . Hence the statistical test gives us some insight into some model parameter changes which cannot be seen by looking directly at the error scores.

#### CONCLUSIONS

An A Posteriori approach to modeling a man involved in a static, motion, peripheral experiment was considered. The PID coefficients were identified (based on an engineering approximation) and a statistical analysis was performed. For the data base of the simulation used here, the man was found to be of a second order nature, and he used second order lead information in the motion mode, less second order lead information in the peripheral mode, and the smallest second lead information in the static mode of operation.

#### REFERENCES

1. Athans, M., "On the Design of PID Controllers Using Optimal Linear Regular Theory", Automatica, Vol. 7, 1971, pp 643-647.
2. Phatak, A.V., and Kessler, K.M., "Evaluation of Optimal Control Type Models for the Human Gunner in an Antiaircraft Artillery (AAA) System", The Eleventh Annual Conference on Manual Control, Ames Research Center, Moffett Field, California, NASA TM X-62,464.
3. Shirley, R.S., "Motion Cues in Man-Vehicle Control", M.I.T., Cambridge, Mass., Sc.D. Thesis, January, 1968.
4. Young, L.R., "The Current Status of Vestibular System Models", Automatica, Vol. 5, pp 369-383, 1969.
5. Stapleford, R.L., Peters, R.A., and Alex, F., "Experiments and a Model for Pilot Dynamics with Visual and Motion Inputs", NASA CR-1325, May, 1969.
6. Ringland, R.F. and Stapleford, R.L., "Experimental Measurements of Motion Cue Effects on STOL Approach Tasks", NASA CR-114458, April, 1972.

7. Levison, W.H., "A Model for the Pilots Use of Motion Cues", The Twelfth Annual Conference on Manual Control, University of Illinois at Urbana-Champaign, May 25-27, 1976.
8. Levison, W.H. and Baron, S., "Modeling the Effects of Environmental Factors on Human Control and Information Processing", Bolt, Beranek and Newman, Report No. 3258, March, 1976.
9. Junker, A.M. and Price, D., "Comparison Between a Peripheral Display and Motion Information on Human Tracking About the Roll Axis", AIAA Visual and Motion Simulation Conference, Dayton, Ohio, April, 1976.
10. Moriarty, T.E., Junker, A.M., and Price, D.R., "Roll Axis Tracking Improvement Resulting from Peripheral Vision Motion Cues", The Twelfth Annual Conference on Manual Control, University of Illinois at Urbana-Champaign, May 25-27, 1976.
11. Price, D.R., "A Study of the Effect of Peripheral Vision Motion Cues on Roll Axis Tracking", Master of Science Thesis, Air Force Institute of Technology, December, 1975.
12. Jex, H.R., Allen, R.W., and Magdaleno, R.E., "Display Format Effects on Precision Tracking Performance, Describing Functions, and Remnant", AMRL-TR-71-63, Systems Technology, Inc., August, 1971.
13. Sheridan, T.B. and Ferrell, W.R., "Man-Machine Systems: Information, Control, and Decision Models of Human Performance", The M.I.T. Press, 1974.
14. Shinnars, S., "Modeling of Human Operator Performance Utilizing Time Series Analysis", IEEE Transactions on Systems, Man, and Cybernetics, September, 1974, pp 446-458.
15. Astrom, K.J. and Eykhoff, P., "System Identification - A Survey", Automatica, Vol. 7, pp 123-162.
16. Poulton, E.C., "Tracking Skill and Manual Control", Academic Press, 1974.
17. Junker, A.M., Repperger, D.W., Neff, J.A., "A Multiloop Approach to Modeling Motion Sensor Responses", Eleventh Annual Conference on Manual Control, NASA TM X-62, 464, May, 1975.

TABLE 1

<sup>e</sup> RMS ERROR	<sup>e</sup> RMS SCORES IN DEGREES		
	STATIC	MOTION	PERIPHERAL
	33.714	18.73	19.21
RATE VARIANCE FOR ERROR	22206.	1031.2	1211.3

TABLE 2

RESULTS OF THE T-TEST VERSUS ZERO (EXISTENCE OF COEFFICIENTS):

S T A T I C	COEFFICIENTS			MEAN	VARIANCE	N <sub>1</sub>	MOTION			MEAN	VAR.	N <sub>1</sub>	t STATISTIC	α
	C <sub>1</sub>	.3912	.2343	6	0	0	6	4.0898	.0022					
	C <sub>2</sub>	.5571	.3559	6	0	0	6	3.8343	.0033					
	C <sub>3</sub>	.8479	1.5913	6	0	0	6	1.3052	.2211					
	C <sub>4</sub>	1.49	2.5952	6	0	0	6	1.4063	.1899					
	C <sub>1</sub>	.426	.297	6	0	0	6	3.5134	.0056					
	C <sub>2</sub>	1.327	.58	6	0	0	6	5.6043	.0002					
	C <sub>3</sub>	.4187	1.3905	6	0	0	6	.7376	.4777					
	C <sub>4</sub>	1.1294	1.6201	6	0	0	6	1.7076	.1185					
	C <sub>1</sub>	.4401	.2851	6	0	0	6	3.7812	.0036					
	C <sub>2</sub>	1.132	.6721	6	0	0	6	4.1256	.0021					
	C <sub>3</sub>	1.0813	1.7482	6	0	0	6	1.5151	.1607					
	C <sub>4</sub>	1.1893	1.8751	6	0	0	6	1.5536	.1513					



TABLE 3

T-TESTS VERSUS MEANS (CHANGES IN COEFFICIENTS):

	COEFFICIENT	MEAN	VAR	N <sub>1</sub>	MEAN	VAR	N <sub>2</sub>	t STATISTIC	α
STATIC VERSUS MOTION	C <sub>1</sub>	Static			Motion			-.2253	.8263
		.3912	.2343	6	.426	.297	6		
	C <sub>2</sub>	Static			Motion			-2.7713	.0197
		.5571	.3559	6	1.327	.58	6		
STATIC VERSUS PERIPHERAL	C <sub>1</sub>	Static			Peripheral			-.3246	0.7522
		.3912	.2343	6	.4401	.2851	6		
	C <sub>2</sub>	Static			Peripheral			-1.8517	.0938
		.5571	.3559	6	1.132	.6721	6		
MOTION VERSUS PERIPHERAL	C <sub>1</sub>	Motion			Peripheral			-.0839	.9348
		.426	.297	6	.4401	.2851	6		
	C <sub>2</sub>	Motion			Peripheral			.538	.6023
		1.327	.58	6	1.132	.6721	6		

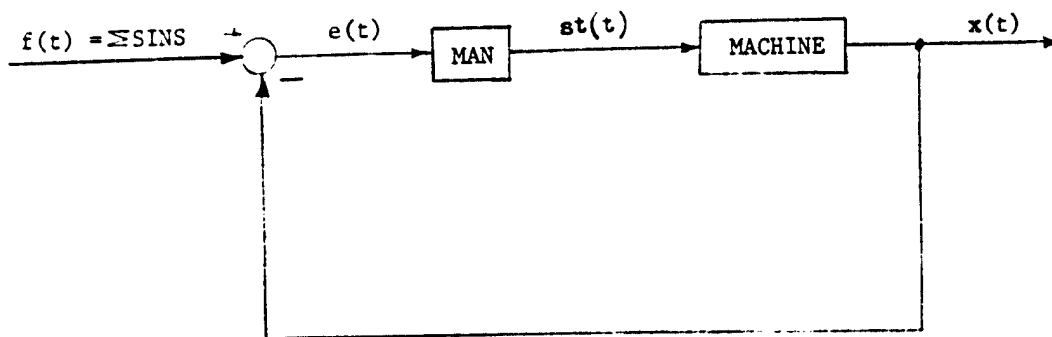


Figure (1a) - The Closed Loop Tracking Task

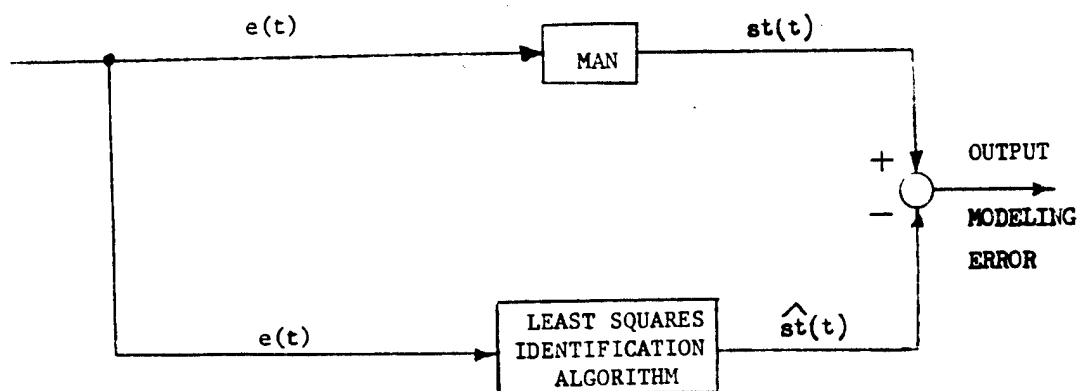


Figure (1b) - The Internal Loop Approach

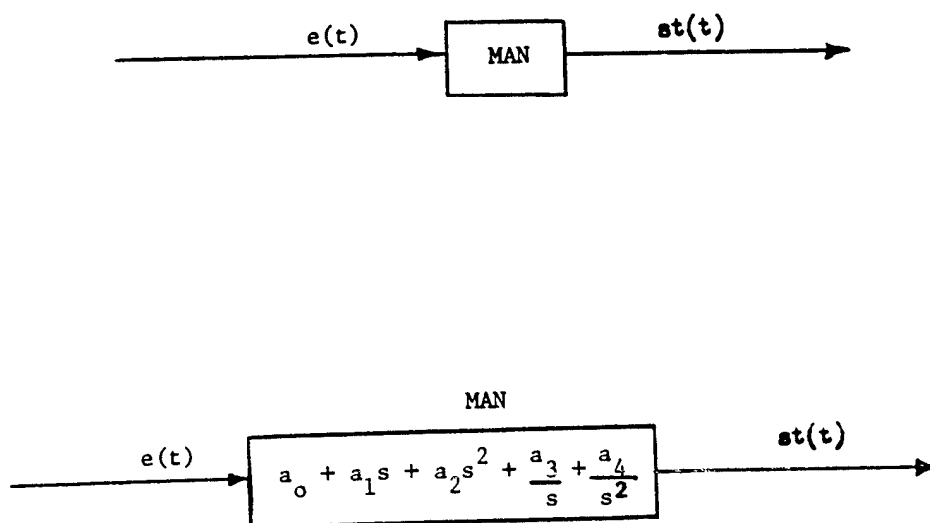


Figure (2) - Replacing Man By His PID Parameters

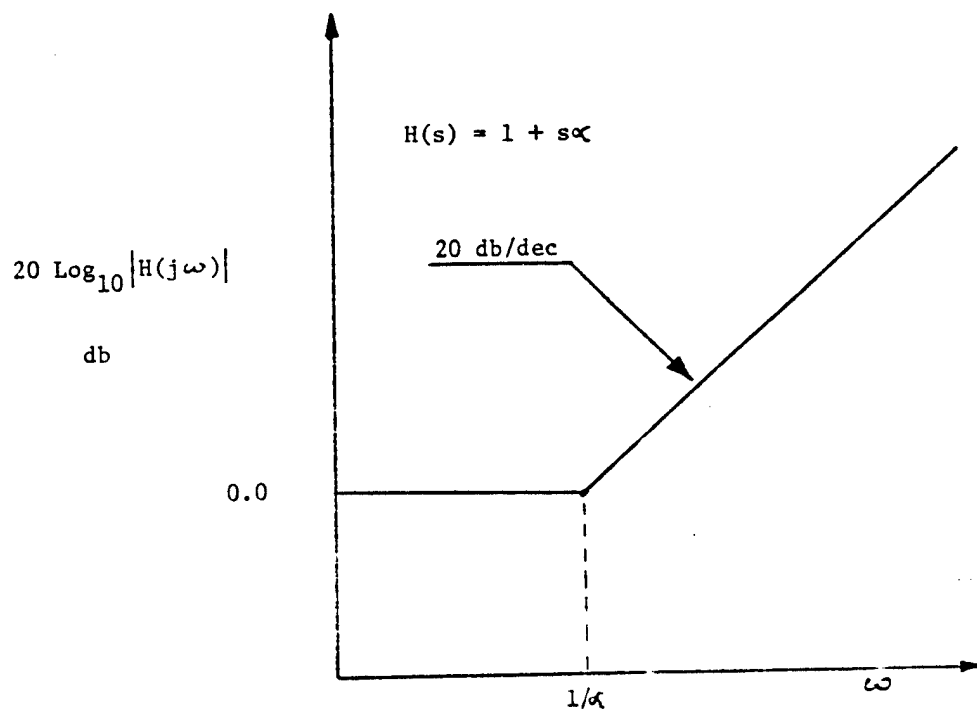


Figure (3) - The Definition of Pilot Lead

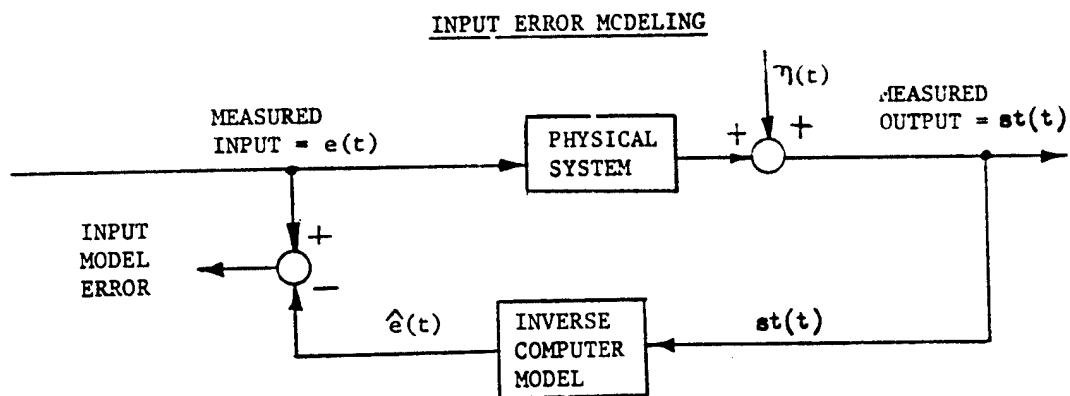
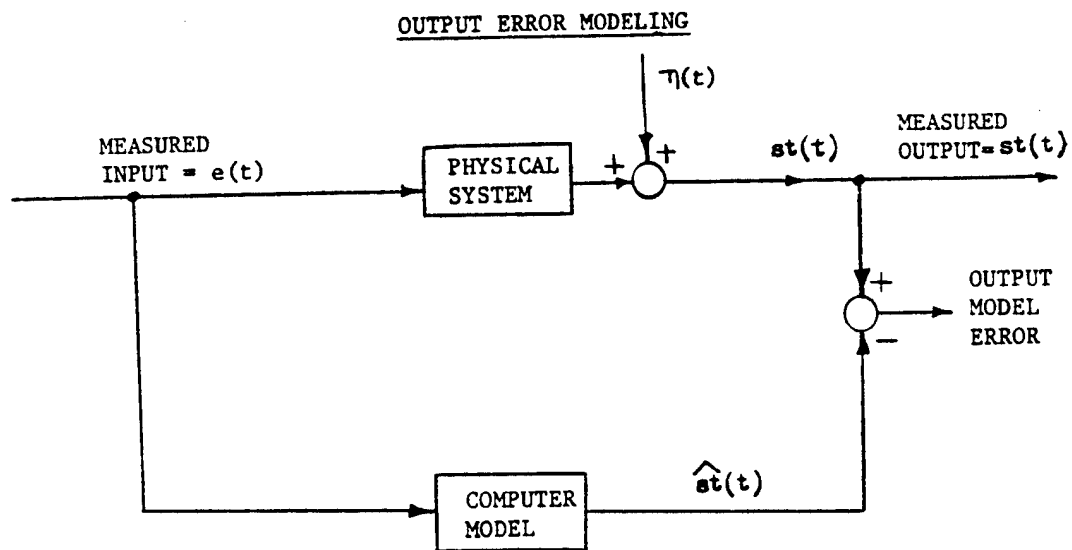


Figure (4) - Output Error Modeling Compared To Input Error Modeling

# SENSITIVITY ANALYSIS OF MOTION AND PERIPHERAL DISPLAY

## EFFECTS ON TRACKING PERFORMANCE\*

By Daniel W. Reppeger and Andrew M. Junker

Aerospace Medical Research Laboratory  
Wright-Patterson Air Force Base, Ohio 45433

### SUMMARY

A study of sensitivity was initiated in an effort to determine what variables effect the decision making processes of a human as he performs a tracking task. If the sensitivity of the closed loop tracking error can be determined with respect to data variables such as displayed error and its respective derivatives, then some knowledge can be obtained about the decision making aspects of the human. In addition, if some other data is useful for the human in his tracking, sensitivity analysis will indicate this pertinent data. A Proportional Integral Derivative (PID) type modeling approach was used with a sum of sins input tracking task to enable sensitivity coefficients to be calculated. Coefficients of sensitivity were computed at each frequency and comparisons of these coefficients were determined over a wide frequency range for different experimental conditions. Data from a motion experiment and a peripheral display experiment were used in this study.

### INTRODUCTION

The study of sensitivity in control theory has its origin from the classical paper of Cruz and Perkins reference(1). More recently Boniveto reference(2) has defined the term sensitivity in a manner which is related to identifiability. What is meant by this statement is that in a modeling approach in which data has already been collected (A Posteriori modeling), it is important to ascertain which parameters are important or sensitive and thus determine the proper model structure. If a parameter in a modeling approach is a sensitive parameter, then this parameter is important in the chosen model structure. Conversely, if a parameter is not sensitive in the modeling approach, then it should probably not be considered for the model

\*The research reported in this paper was sponsored by Aerospace Medical Research Laboratory, Aerospace Medical Division, Air Force Systems Command, Wright-Patterson Air Force Base, Ohio 45433. Further reproduction is authorized to satisfy needs of the U.S. Government.

structure. From the sensitivity analysis, it is possible to determine the influential parameters and thus to concentrate our effort and attention on these parameters.

In this paper a conjecture is made on how to guess cost function weightings on optimal control models based on calculated sensitivities. Since most optimal control models require weighting of the closed loop error (and its derivatives), a method will be explored to choose these weightings based on the sensitivity (or gradients) of the closed loop error with respect to parameters.

Since error in the closed loop is a measure of performance for the closed loop tracking task, it is of interest to observe how this error changes or how its sensitivity varies as a function of the parameters in the closed loop system. In this manner it is possible to see how performance in the closed loop is influenced by certain relevant or sensitive parameters.

Using the (A Posteriori) PID model presented in reference (3), the sensitivity of the closed loop error was calculated with respect to the PID parameters already obtained. The data base and experiments used here are the same as in reference (3).

#### Closed Loop Error Sensitivity

With reference to Figure 1, the transfer function of man (using the PID model) is denoted as:

$$\text{Man} = G(s) = a_0 + a_1 s + a_2 s^2 \quad (1)$$

using the fact that

$$\frac{X(s)}{F(s)} = \frac{GH}{1+GH} \quad (2)$$

and

$$\frac{X(s)}{E(s)} = GH \quad (3)$$

yields

$$\frac{E(s)}{F(s)} = \frac{X(s)}{F(s)} \cdot \frac{1}{\left(\frac{X(s)}{E(s)}\right)} = \frac{1}{1+GH} \quad (4)$$

or

$$E(s) = \frac{F(s)}{1+G(s)H(s)} \quad (5)$$

therefore

$$E(s) = \frac{F(s)}{1+(a_0 + a_1 s + a_2 s^2)H(s)} \quad (6)$$

Equation (6) is in an ideal form. On the right hand side of the equation is all the loop variables which influence the closed loop error. This includes the external forcing function, the plant, and the man represented by PID parameters. On the left hand side of equation (6) is the isolated expression for the closed loop error as a Laplace transform. The simplicity of equation (6) is that the performance in the loop is isolated on the left hand side of the equation and all the possible variables that effect this performance are isolated on the right hand of this expression.

Since a sum of sines input was used in these experiments, it is possible to set  $s = j\omega_i$  ( $i = 1, 2, \dots, 12$  frequencies used) and for each value of  $\omega_i$ , the error and (as it will be shown in the sequel) the partial derivatives of  $E(s)$  with respect to the parameters  $a_0$ ,  $a_1$ , and  $a_2$  can also be obtained.

In order to obtain the partial derivatives of the closed loop error with respect to the PID parameters, it is noted that at each fixed value of frequency  $\omega_i$ , the partial derivatives of the closed loop error with respect to the parameters  $a_0$ ,  $a_1$ , and  $a_2$  can be obtained quite easily. Simple differentiation (for a fixed  $\omega_i$ ) of equation (6) with respect to  $a_0$ ,  $a_1$ , and  $a_2$  yields:

$$\frac{\partial E}{\partial a_0} = \frac{-F(s)H(s)}{[1+(a_0+a_1s+a_2s^2)H(s)]^2} = \frac{A_1 e^{j\theta_1}}{A_2 e^{j\theta_2}} \quad (7a)$$

$$\frac{\partial E}{\partial a_1} = \frac{-sF(s)H(s)}{[1+(a_0+a_1s+a_2s^2)H(s)]^2} = \frac{A_3 e^{j\theta_3}}{A_2 e^{j\theta_2}} \quad (7b)$$

$$\frac{\partial E}{\partial a_2} = \frac{-s^2F(s)H(s)}{[1+(a_0+a_1s+a_2s^2)H(s)]^2} = \frac{A_4 e^{j\theta_4}}{A_2 e^{j\theta_2}} \quad (7c)$$

Equations (7a-c) are written in phasor notation since both the numerator and denominator have different magnitude and phase angle shifts respectively at each value of frequency. The following relationship can easily be shown:

$$\frac{\partial E}{\partial a_2} = s \frac{\partial E}{\partial a_1} = s^2 \frac{\partial E}{\partial a_0} \quad (8)$$

Using equations (7a-c), the gradients (or sensitivities) of  $E$  with respect to  $a_0$ ,  $a_1$ , and  $a_2$  were calculated. The results were given in Table 1.

The plots of the (averaged) sensitivities are displayed in Figure (2) for the static case. In this plot it is noted that the sensitivity functions peak near the crossover frequency which was approximately 1.35 radians for the static mode of operation. The frequency at which peaks of all three curves occurred did not differ by more than 1 radian.

In Figure (3) the sensitivity functions are plotted for the motion case. In Figure (3) the curves of  $\partial E/\partial a_0$  and  $\partial E/\partial a_1$  were not radically different. The curve for  $\partial E/\partial a_2$ , however, had an unusually different peak three times as large as the other two peaks and shifted to the right (beyond the crossover frequency) by almost 2 radians. Since these results are averaged over subjects and replications, it appears that in the motion mode of operation, the closed loop error has its greatest sensitivity to the double lead parameter  $a_2$ . This is in concurrence with reference (3) where the statistical analysis was performed and also with some previous work done in reference (4).



In Figure (4), the sensitivity curves are plotted for the peripheral case (ensemble averaged) and they appear similar to the static case. The peaks are only 0.5 radians apart and are located near the crossover frequency.

When comparing the peripheral case to the static case, however, the peripheral peaks are much higher than the static case. Comparing the  $\partial E/\partial a_2$  curves (the second lead term), for the peripheral mode of operation versus the motion mode, the motion case has the greatest shift to the right (and beyond the crossover frequency) but not as great a magnitude as in the peripheral case. Hence it appears that the second lead term  $a_2$  is more dominant in the motion case, less dominant in the peripheral case, and much less dominant in the static case. These results agree with the statistical analysis obtained in reference (3). A method of choosing cost function weightings based on the inverse variances of the sensitivity functions will now be conjectured.

#### Conjecture: How To Pick Cost Function Weightings in An A Posteriori Sense

Figure (5) illustrates a close up view of the static mode of operation of Figure (2) near the crossover frequency. Also illustrated on this plot is one standard deviation (at the frequency 1.572 radians) of the averages obtained for the three curves. Since a greater variance in the estimate of this sensitivity indicates less effect of this parameter on the closed loop error, the following conjecture arises:

Conjecture: Given a cost function of the form

$$J = \frac{1}{T} \int_0^T \left[ K_1 |e(t)|^2 + K_2 |\dot{e}(t)|^2 + K_3 |\ddot{e}(t)|^2 \right] dt \quad (9)$$

where T may become infinite. One may attempt to pick the unknown cost functions  $K_1$ ,  $K_2$ , and  $K_3$  in the following manner:

$$K_1 = \alpha [\text{VAR } \partial E/\partial a_0]^{-1} \quad (10a)$$

$$K_2 = \alpha [\text{VAR } \partial E/\partial a_1]^{-1} \quad (10b)$$

$$K_3 = \alpha [\text{VAR } \partial E/\partial a_2]^{-1} \quad (10c)$$

where  $\alpha$  = A constant of proportionality. If cost function weightings are chosen in this manner, then for parameters with a large variance in the sensitivity values the corresponding weighting matrices should have the smallest values in the cost function. In other words if the closed loop error is not sensitive to a particular parameter (which is indicated by a large variance), then the weighting for this parameter should be small. Conversely if the closed loop error has a large sensitivity with respect to a given parameter

(as indicated by a small variance in the estimate of the sensitivity function), then the cost function should be weighted more. In Figure (5), we would weight  $K_1$  and  $K_2$  (corresponding to  $e(t)$  and  $\dot{e}(t)$ ) more than we would weight  $K_3$  (corresponding to  $\ddot{e}(t)$ ). This approach is consistent with the inverse of the standard deviations shown in Figure (5) and also has agreement with the statistical analysis demonstrated in reference (3). It is hoped that with additional work, this conjecture can be more carefully quantified and perhaps more rigorously shown.

#### CONCLUSIONS

A study of closed loop error sensitivity is introduced for a PID type model structure. The closed loop error sensitivity is computed for the three PID parameters across three tasks denoted as the Static, Motion, and Peripheral mode of operation. The peak sensitivities show quite a bit of difference between the three modes of operation. For this simulator the second lead term seems to have the greatest sensitivity of the closed loop error in the motion (roll axis) task. A method of guessing at cost function weightings based on the inverses of the variances of the sensitivities is hypothesized. Further work needs to be done on this topic.

#### REFERENCES

1. Cruz, J.B. and Perkins, W.R., "A New Approach to the Sensitivity Problem in Multivariable Feedback System Design", IEEE Transactions on Automatic Control, Vol. AC-9, No. 3, 1964, pp 216-223.
2. Boniveto, C., "Structural Insensitivity Versus Identifiability", IEEE Transactions on Automatic Control, April, 1973, pp 190-192.
3. Repperger, D.W. and Junker, A.M., "PID Modeling Techniques Applied to Studies of Motion and Peripheral Display Effects on Human Operator Performance", The Twelfth Annual Conference on Manual Control, May, 1976.
4. Junker, A.M., Repperger, D.W., Neff, J.A., "A Multiloop Approach to Modeling Motion Sensor Responses", Eleventh Annual Conference on Manual Control, NASA TM X-62, 464, May, 1975.

TABLE 1

TABLE OF CALCULATED GRADIENTS

FREQUENCY	STATIC			MOTION			PERIPHERAL		
	$\frac{\partial E}{\partial a_0}$	$\frac{\partial E}{\partial a_1}$	$\frac{\partial E}{\partial a_2}$	$\frac{\partial E}{\partial a_0}$	$\frac{\partial E}{\partial a_1}$	$\frac{\partial E}{\partial a_2}$	$\frac{\partial E}{\partial a_0}$	$\frac{\partial E}{\partial a_1}$	$\frac{\partial E}{\partial a_2}$
.077	.0313	.00241	$1.855 \times 10^{-4}$	$3.155 \times 10^{-2}$	$2.43 \times 10^{-3}$	$1.87 \times 10^{-4}$	$3.15 \times 10^{-2}$	$2.43 \times 10^{-3}$	$1.86 \times 10^{-4}$
.192	.3825	.0394	$7.565 \times 10^{-3}$	$2.175 \times 10^{-1}$	$4.17 \times 10^{-2}$	$8.005 \times 10^{-3}$	.214	$4.11 \times 10^{-2}$	$7.89 \times 10^{-3}$
.307	.68	.1175	$3.61 \times 10^{-2}$	.4465	.137	$4.21 \times 10^{-2}$	.4295	.132	$4.045 \times 10^{-2}$
.460	1.339	.313	.144	1.008	.463	.213	.9215	.423	.1945
.690	1.339	.9205	.6365	2.79	1.925	1.328	2.39	1.649	1.1345
1.035	5.26	5.445	5.635	39.76	41.13	42.6	4.655	4.815	4.9805
1.572	4.795	7.565	11.855	1.3592	2.1365	3.3585	12.185	19.1335	30.11
2.378	1.2505	2.9665	7.05	.2988	.6635	1.5845	.67	1.593	3.788
3.567	.1825	.651	2.32	$7.68 \times 10^{-2}$	.2744	.9765	.1179	.4196	1.497
5.369	.04845	.260	1.398	.002101	.1127	.6065	$3.325 \times 10^{-2}$	.1783	.958
8.053	.0115	.0429	.748	.000704	.05685	.4575	$.85 \times 10^{-2}$	.0685	.5525
12.08	$5.09 \times 10^{-4}$	$6.125 \times 10^{-3}$	$7.425 \times 10^{-2}$	.0007	.003965	.	$6.87 \times 10^{-4}$	$8.28 \times 10^{-3}$	$1.003 \times 10^{-2}$

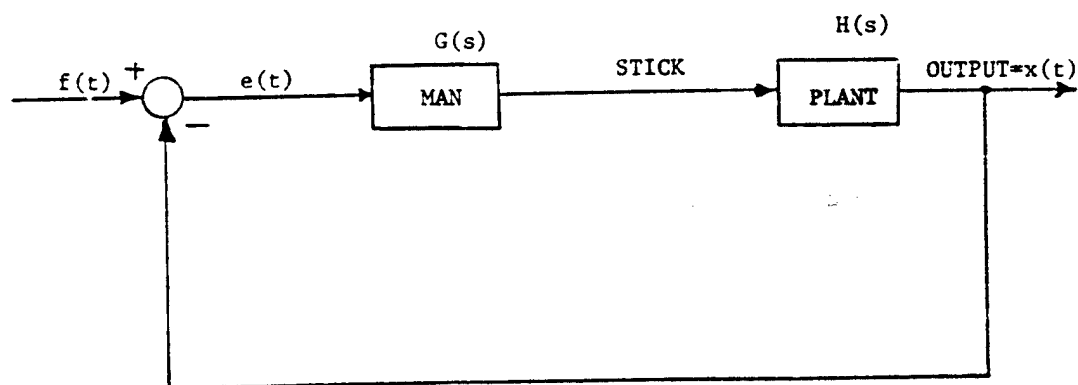
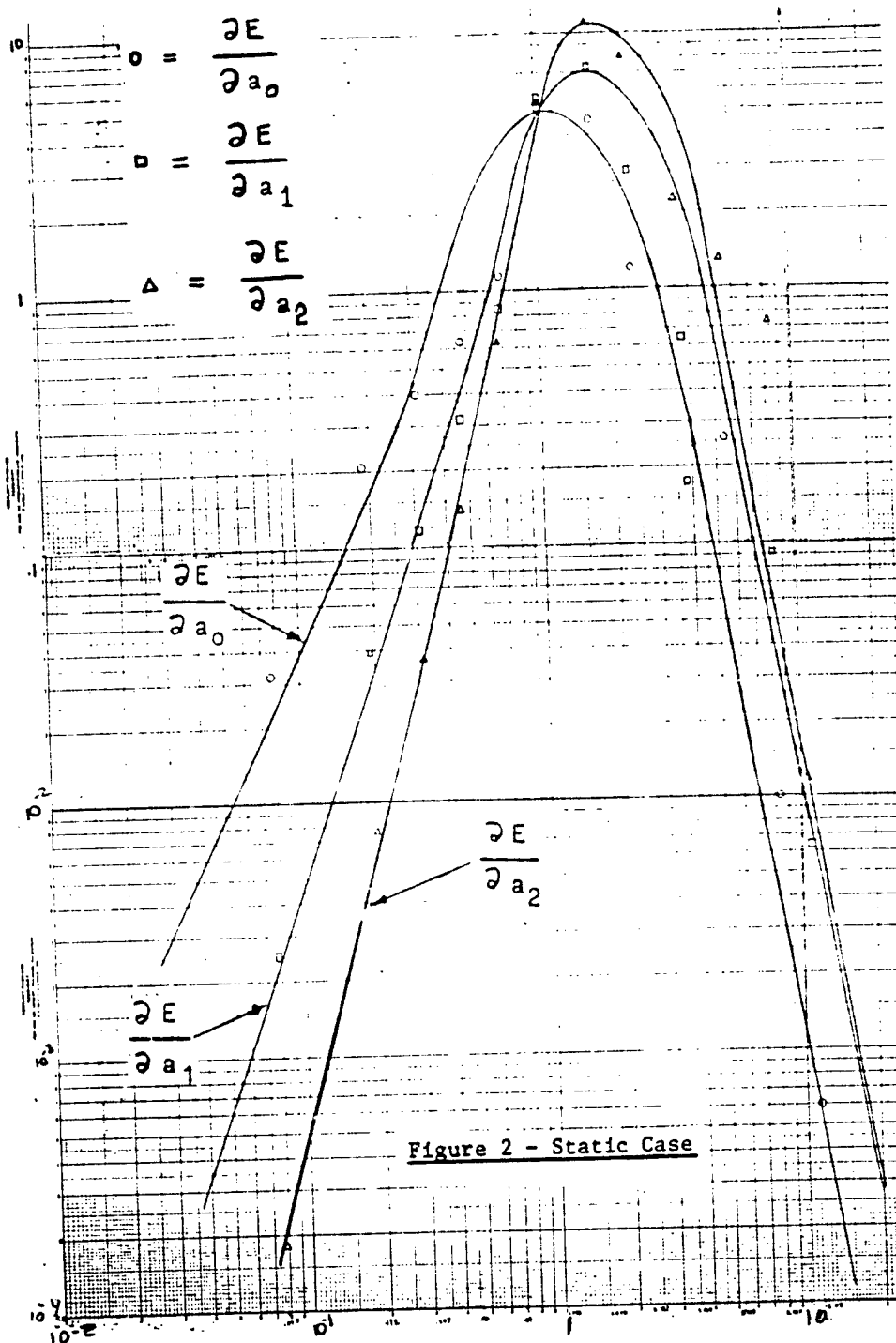
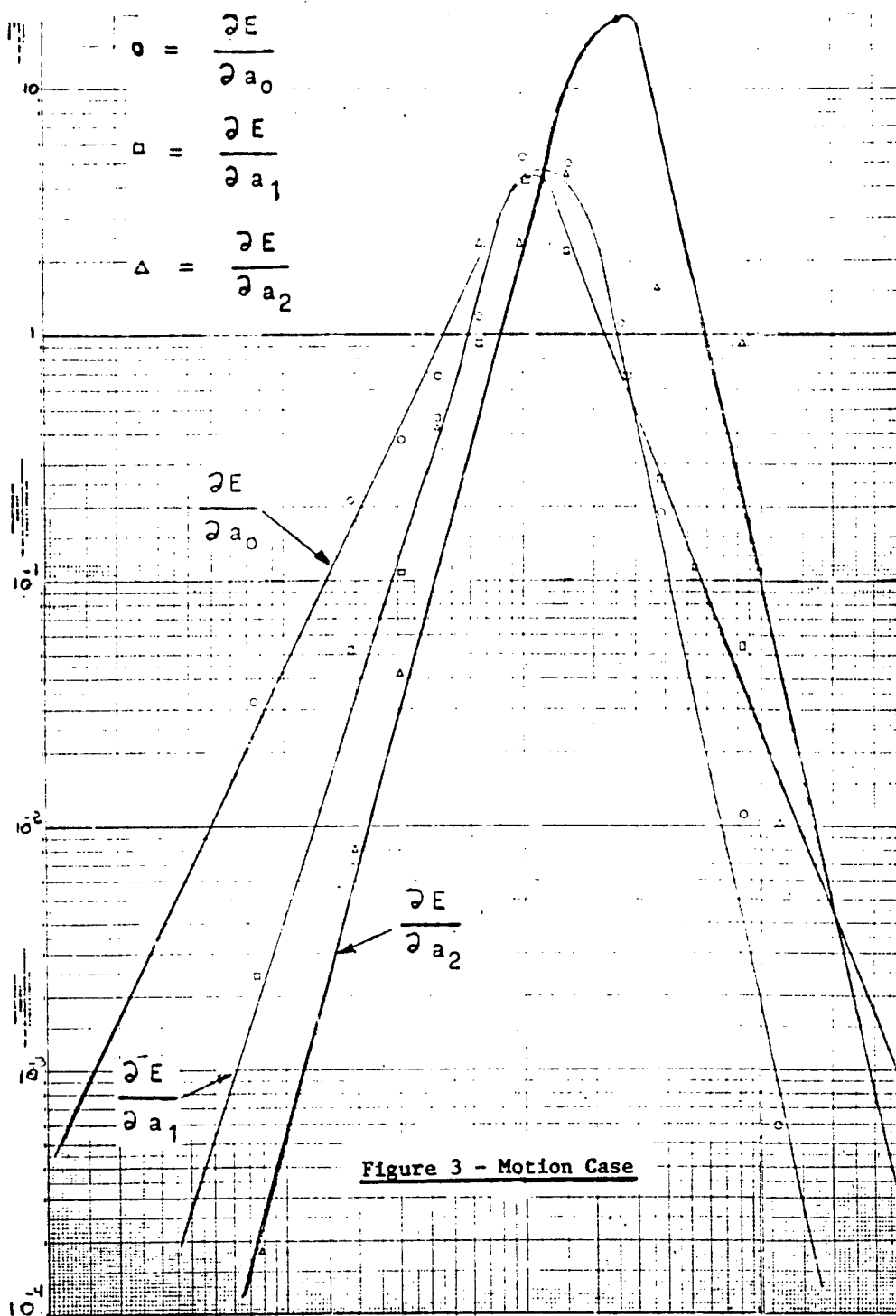
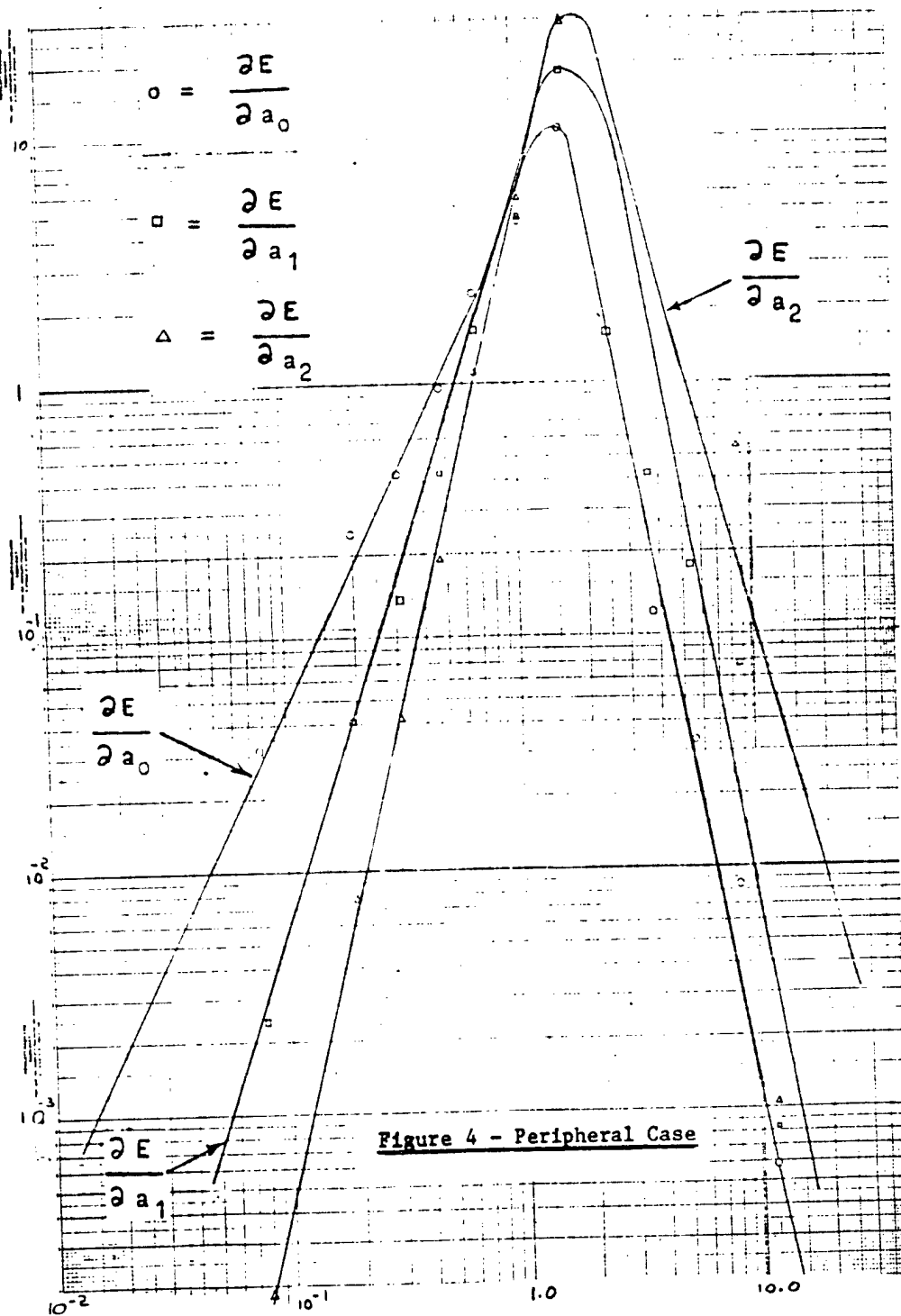
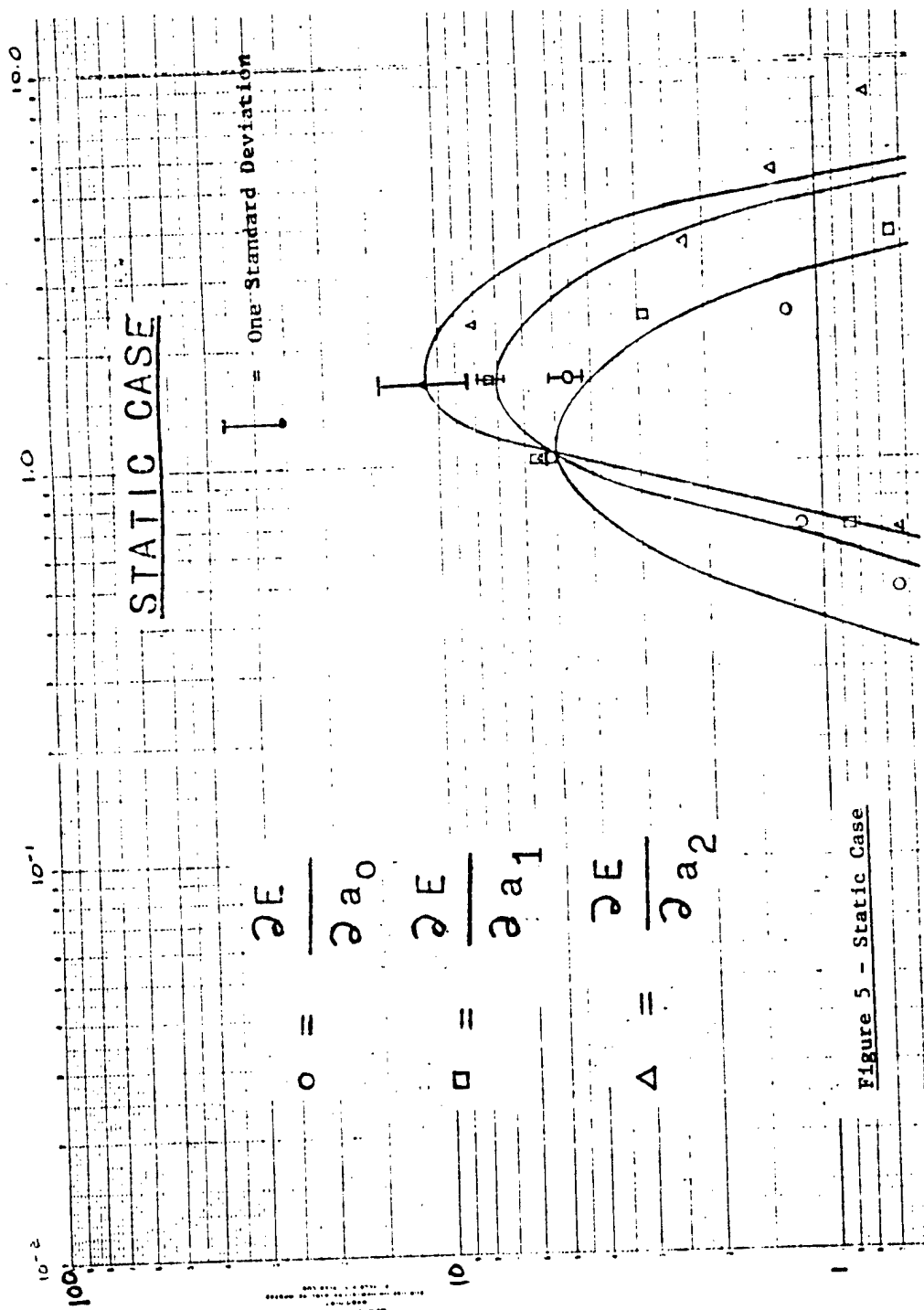


FIGURE 1 - CLOSED LOOP ERROR SENSITIVITY











SESSION X  
CONTROL MODELS

Chairman: S. Baron

PRECEDING PAGE BLANK: NOT FILMED

## LOW VISIBILITY LANDING SIMULATION EXPERIMENTS

Capt R.V. Gressang, Capt J.J. Pollard and Mr. D.L. Kugel  
Air Force Flight Dynamics Laboratory

### SUMMARY

The paper describes two experiments which simulated a transport aircraft landing in reduced visibility. The experiments were conducted as part of a low visibility landing simulation program sponsored at the Air Force Flight Dynamics Laboratory by the Federal Aviation Administration. Data during the experiments were collected in a form suitable for use in an optimal control pilot model.

For the experiments, a C-135B was simulated using six degree of freedom nonlinear equations on a hybrid simulator. Visual, motion, and sound cues and a gust disturbance were provided. The effects of reduced visibility were simulated by driving a sky plate in the TV lense system focal plane.

The first experiment used two subjects, and considered four visibility conditions. The second experiment used one subject, and considered three visibility conditions. The experiment results included statistics on glide slope and localizer tracking and on touchdown conditions. Pilot comments were recorded, and limited data are available from the second experiment on pilot eye scanning.

### I. INTRODUCTION

This paper describes two experiments conducted to collect data suitable for developing a pilot model of low visibility landing. A sampling of the results is presented in this paper, and the complete results can be found in References 1 and 2.

These experiments were conducted as part of a low visibility landing simulation program conducted for the Federal Aviation Administration (FAA) by the Air Force Flight Dynamics Laboratory (AFFDL). The program was to investigate low visibility landing operations while minimizing new equipment costs by making maximum use of AFFDL flight simulators. The overall program aims were as follows: to develop a capability to evaluate and validate pilot workload and performance in Category II and III weather conditions; to determine the utility of visual cues in Category II and III landing operations; and to identify simulator improvements required for adequate and realistic engineering simulation of low visibility landing operations.

As part of the low visibility landing program, the Flight Dynamics Laboratory undertook to develop a pilot model. The rationale for developing a low visibility landing pilot model was that a pilot model would permit analytical studies of low visibility landing to be made for a relatively large number of aircraft configurations, visibilities, and disturbances.

These analytical studies would then be used in planning to effectively allocate use of the engineering flight simulator.

The pilot model being developed (and described in another paper given at this conference) is of the optimal control type, and is adapted to tasks which are time varying. A model capable of treating time varying tasks was chosen because of the variations in task dynamics as a function of range and due to the flare maneuver. To develop this model, ensemble statistics of the landing task state variables are required as a function of range. Thus the data base for the pilot model must be established using experiments containing sufficient replications for ensemble statistics to be meaningful.

The data base for the pilot model was established through two experiments using the multicrew cab simulator. The first experiment was conducted and the data from it analyzed, which revealed some limitations of the simulation. Efforts were made to reduce these limitations, and the second experiment was then conducted.

## II. DESCRIPTION OF THE SIMULATION

The aircraft used for this manned simulation was the military C-135B transport, which is similar to the commercial Boeing 707. The aircraft configuration had a weight of 160,000 pounds, the center of gravity located at 28.2 percent of the mean aerodynamic chord, a flap setting of 50 degrees, and the landing gear down. The aircraft mathematical model used was a six degree of freedom nonlinear model, and was programmed on a hybrid computer. Each experimental run began from trimmed flight conditions at 956 feet altitude on a three degree glide slope.

A conventional C-135B flight control system was used in the simulation. The controls included wheel (aileron), column (elevator), and rudder pedals. Thumb buttons for pitch and roll trim were located on the wheel; a crank for rudder trim was on the center console. Throttle, flap, gear, and speed brake handles were fully operational.

The cockpit instruments were those typical of the C-135B. The instruments driven during the simulation were the attitude director indicator (ADI), horizontal situation indicator (HSI), airspeed indicator, rate of climb indicator, barometric altimeter, radar altimeter, angle of attack indicator, G meter, Mach meter, clock, compass indicator (RMI), engine pressure ratio gauges, tachometers, exhaust gas temperature gauges, fuel flow meters, and oil pressure gauges. Annunciators for the outer, middle, and inner markers were driven. Flight director pitch and roll steering command bars were driven in accordance with the glide slope tracking mode of the Collins FD-109 flight director.

The aircraft simulated during the first experiment did not have a yaw damper. Between the two experiments, a yaw damper was added to the aircraft model. This yaw damper was used throughout the second experiment.

The cockpit used was an actual C-135 cockpit modified for use as a research and development simulator. It was mounted upon a three degree of freedom motion base, and capable of limited pitch, roll, and heave motion. Sound cues duplicating the sound of four turbojet engines were produced. These cues were proportional to throttle position and airspeed.

Visual cues simulating real world changes in size and perspective with respect to aircraft movements were produced using an illuminated three dimensional terrain model and television camera-screen projection system. The field of view of the screen was 60 degrees diagonally with appropriate cockpit cutoff angles for the C-135. The view was large enough to present a realistic scene through the front windows, but there were no peripheral cues. The pilot saw a daylight rural terrain with an airport complex including strobe, approach, and VASI lights. The visual display was automatically controlled by computer to simulate homogeneous fog with the following initial visual contact altitude/runway visual range conditions:

- a. Unlimited/unlimited
- b. 400 feet/1600 feet
- c. 300 feet/1200 feet
- d. 100 feet/1200 feet

The reduced visibility conditions were generated by driving a knife edge in the focal plane of the TV camera. The visibility conditions were settled upon in consultation with the first experiment's subject pilots so as to appear realistic.

During the simulation runs, light turbulence was added as a disturbance to the aircraft. This turbulence had the Dryden spectra of MIL-F-8785B corresponding to an average altitude of 500 feet<sup>[3]</sup>.

During the simulation, the pilot's task was to conduct an instrument flight rules (IFR) landing. The pilots had no auxiliary tasks, such as communication, to perform. The pilot was assisted by a copilot, but this assistance was limited to the copilot calling the initial appearance of cues in the visual scene and the copilot monitoring such quantities as airspeed and altitude.

During the course of the experiments, certain limitations of the simulation became apparent. The most serious limitations were difficulty in obtaining a satisfactory representation of the lateral directional dynamics of the C-135 on the simulator, too high sink rates at touchdown in the simulator, and an overly sensitive flight director command bar. Between the two experiments, the simulation was modified to improve the lateral dynamics data match, the flight director gains were modified, a yaw damper was added, a landing gear simulation was added, the ground effects model was modified, the instrument drive signals were refined, and new plumbicon tubes were installed to improve the visual display. The simulation fidelity was improved in the second experiment. The main limitation remaining in

the second experiment was a mean touchdown sink rate which was still higher than that obtained in actual aircraft.

The subject pilots used in the experiments were USAF Rated Officers with C-135 experience. The pilots in the first experiment had 2930 and 2686 total flying hours. The pilot in the second experiment had 970 total flying hours.

Further information about the simulation can be obtained in References 1 and 4.

### III. DESCRIPTION OF THE EXPERIMENTS

The main objective of the experiments was to obtain ensemble statistics for developing the pilot model. Subsidiary objectives were to determine the effect of reduced visibility upon the pilot's landing performance, and in the second experiment to measure the pilot's inside/outside cockpit scan behavior.

The first experiment used a complete factorial experiment plan, with the factors being pilot (two levels) and visibility (four levels). The experiment was replicated 10 times, resulting in a total of 80 simulation runs. The order of presentation of the visibility conditions to the pilots was random. Each pilot had a training session of about one hour duration before data were collected.

The second experiment used a randomized block plan, with three different visibilities ( $\infty/\infty$ , 400/1600, 100/1200). The order of presentation of the visibility conditions to the pilot was random, and he had had about four hours of experience on the simulator before the experiment was conducted.

Each simulation run was initiated with the aircraft trimmed, on the glide slope and localizer, at a range of 15,000 feet from the glide path intercept point (GPIP). The pilot did not know in advance what the visibility conditions would be, and he was instructed to fly the simulator as if it were a real aircraft. He was also instructed not to execute a missed approach, but to land regardless of circumstances, and comment later if he thought he should have gone around. He was briefed that there would be light to moderate turbulence, but no crosswinds.

The simulation run was ended after touchdown, and pilot comments were then collected via a questionnaire. During the simulation runs, the variables listed in Table 1 were recorded at a rate of 10 samples per second. During the second experiment, whether the pilot was looking inside or outside the cockpit was determined using electro-oculography. The electro-oculographic method used is described in Reference 2, where are also presented the results of a pre-experiment which established that wearing the electrode assembly did not affect the pilot's performance.

TABLE 1. VARIABLES RECORDED DURING THE EXPERIMENTS

1. R - Range, ft.
2. Y - Cross track error, ft.
3.  $h_{cg}$  - c.g. height, ft.
4.  $h_{eye}$  - Eye height, ft.
5.  $\dot{x}, \dot{y}, \dot{h}$  - Earth referenced velocities, ft/sec.
6. u, v, w - Body axis referenced velocities, ft/sec.
7.  $a_x$  - Longitudinal acceleration, ft/sec<sup>2</sup>.
8.  $n_z$  - Normal acceleration, g.
9.  $\psi, \theta, \phi$  - Euler angles, degrees
10.  $\gamma$  - Flight path angle, degrees.
11. p, q, r - Body axis angular velocities, deg/sec.
12.  $\dot{\psi}$  - Yaw rate, deg/sec.
13.  $\dot{h}_{ind}$  - Indicated sink rate, ft/min.
14.  $V_e$  - East velocity, knots.
15. PSB - Pitch steering bar.
16. RSB - Roll steering bar
17. G/S Error<sub>ind</sub> - Indicated glide slope error.
18. Loc error<sub>ind</sub> - Indicated localizer error.
19. RPM 1, 2, 3, 4 - Engine RPM, for 4 engines, percent.
20.  $\delta_{e_c}$  - Elevator deflection, degrees.
21.  $\delta_{a_c}$  - Aileron deflection, degrees.
22.  $\delta_{r_c}$  - Rudder deflection, degrees.
23.  $T_{\delta_1}, T_{\delta_2}, T_{\delta_3}, T_{\delta_4}$  - Throttle positions, for 4 engines, degrees.
24.  $V_{wind}$  - Wind velocity.

25. Event
26.  $u_g, v_g, w_g, p_g, q_g, r_g$  - Gust disturbances.
27. SVR - Slant visual range, ft.
28.  $\Delta X, \Delta Y$  - Aim point coordinates, ft.
29. Run number
30. Time, sec.

#### IV. RESULTS OF THE EXPERIMENTS

Ensemble statistics were computed for each combination of pilot and visibility existing in both experiments. Using the data from the ten simulation runs for each combination of pilot and fog condition, a mean value and a standard deviation were calculated as a function of range (equivalent to time) for localizer error, glide slope error, roll, pitch, aileron deflection, and elevator deflection. In addition, for experiment two calculations were also made for displayed glide slope error, displayed localizer error,  $x, u, y, v, h, w, p, q, \psi, r$ , and  $\delta_r$ . These quantities were then plotted as a function of range, in the form of a mean trajectory and plus or minus one standard deviation about the mean. The glide slope error and localizer error plots for the  $\infty/\infty$ , 400/1600, and 100/1200 cases of experiment two are given as Figures 1 through 6. References 1 and 2 present the complete set of plots.

Overall, the ensemble statistics indicate that all three pilots improved their tracking of the glide slope as out of the cockpit visibility deteriorated. Based upon pilot comments and the in/out scanning data, this improvement in glide slope tracking was caused by increased attention being paid to the flight instruments. Localizer tracking also tended to improve as visibility decreased. In the first experiment, difficulties with the flight director mechanization resulted both pilots exhibiting an "s" curve phenomena in tracking the localizer.

In the first experiment the pilots were unable to execute a proper flare and touchdown. Pilot comments indicated that this was due to difficulty in judging height and sink rate from the visual display, due to lack of peripheral vision cues. Therefore statistics were not computed for touchdown position and sink rate for experiment one. In the second experiment, however, the pilot was able to execute a flare and the touchdown sink rates, while high, were not unrealistic. The touchdown statistics for experiment two are given in Table 2. The only statistically significant effects due to visibility in the touchdown data were the mean and standard deviation of the longitudinal touchdown point were larger for the 100/1200 visibility case.

In addition to the ensemble statistics, means and standard deviations of  $h, y, \psi, \dot{\psi}, \phi, p, q, r, \delta_e, \delta_a$ , and  $\delta_r$  were computed for all of the data

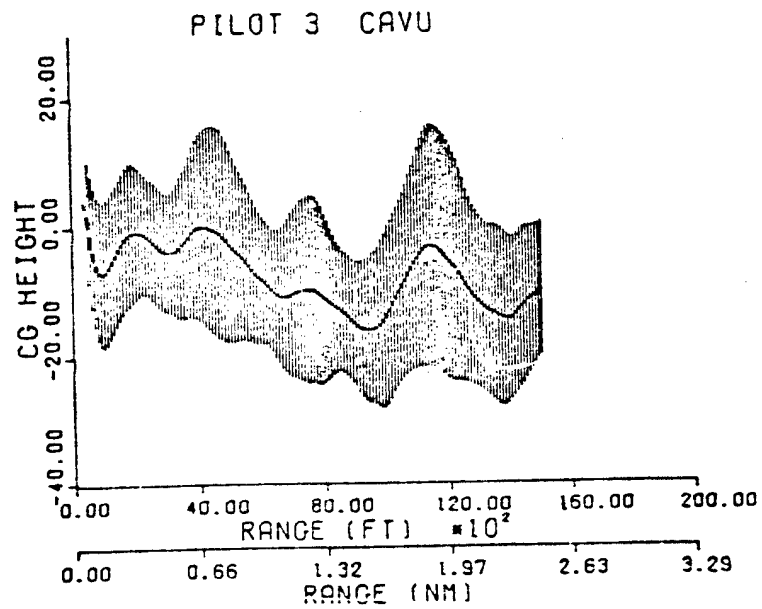


FIGURE 1. GLIDE SLOPE ERROR ENSEMBLE STATISTICS,  $\infty/\infty$

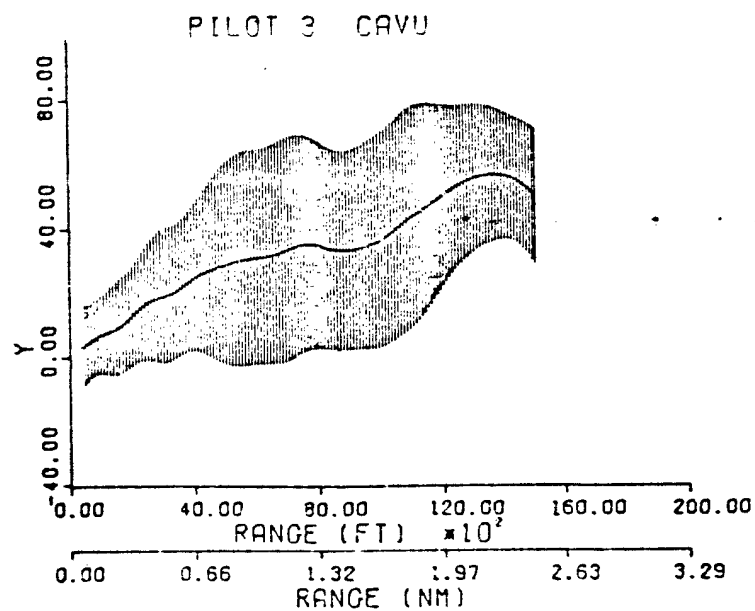


FIGURE 2. LOCALIZER ERROR ENSEMBLE STATISTICS,  $\infty/\infty$



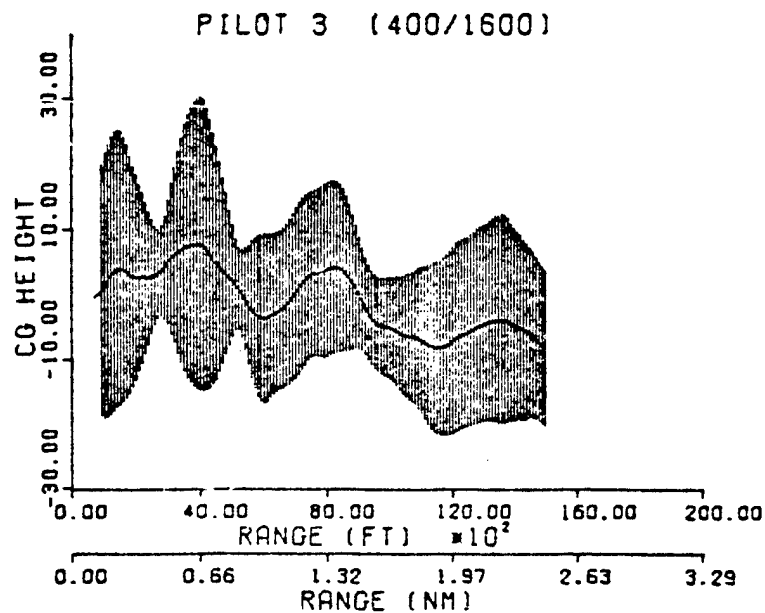


FIGURE 3. GLIDE SLOPE ERROR ENSEMBLE STATISTICS, 400/1600

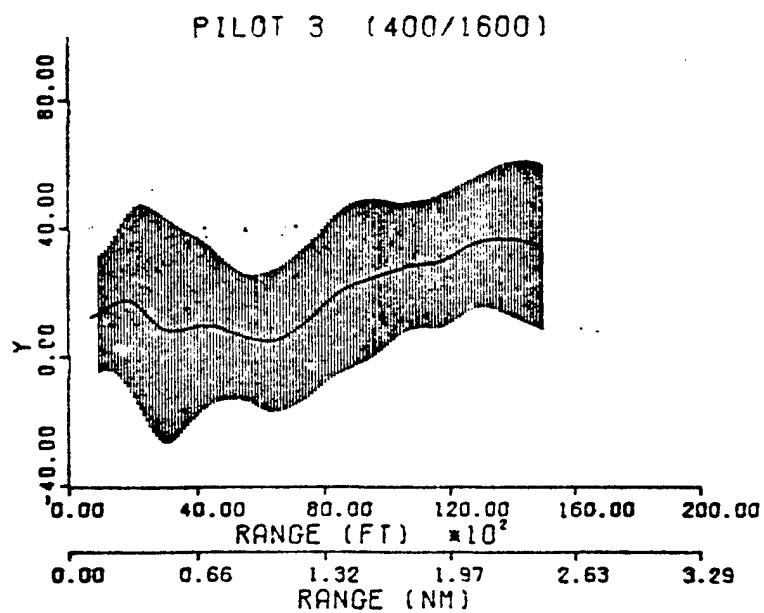


FIGURE 4. LOCALIZER ERROR ENSEMBLE STATISTICS, 400/1600

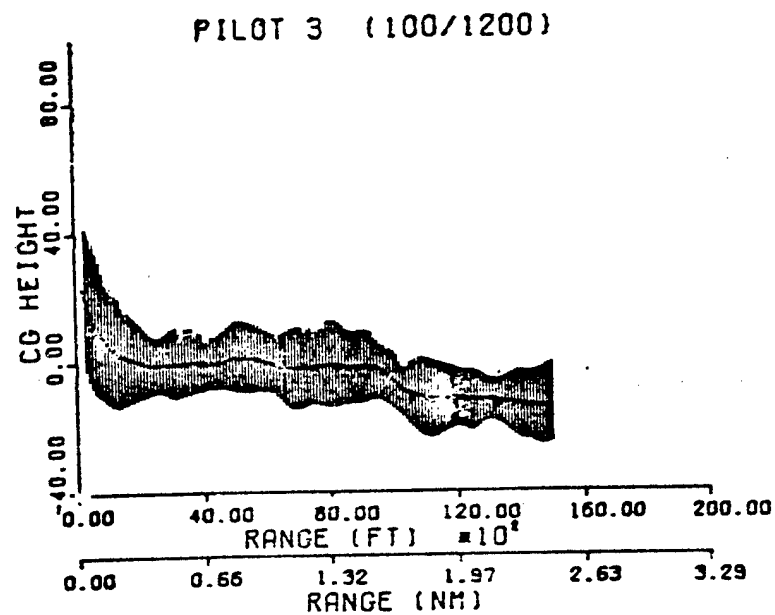


FIGURE 5. GLIDE SLOPE ERROR ENSEMBLE STATISTICS, 100/1200

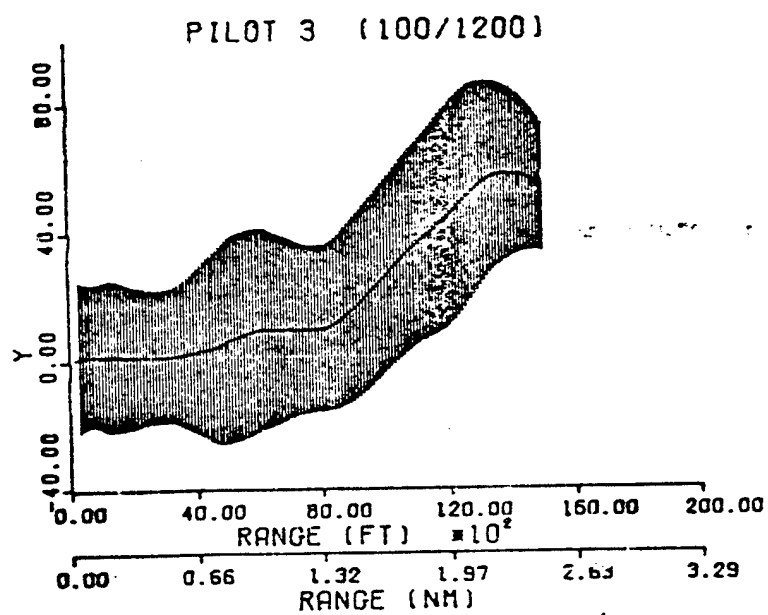


FIGURE 6. LOCALIZER ERROR ENSEMBLE STATISTICS, 100/1200

collected on each run for ranges to the GPIIP of from 5000 ft to 1500 ft. The standard deviations of all the runs that each pilot made in each visibility condition were then averaged, and used as a measure of the pilot's glide slope and localizer tracking performance. These average standard deviations are presented in Table 3 for all three pilots. The third pilot seemed to use more control in the longitudinal axis, which resulted in somewhat larger standard deviations when compared with the first two pilots. He used smaller control inputs in the lateral axes than the first two pilots, and achieved better performance there. This might be due to the yaw damper improving the handling qualities of the aircraft. Visibility did not seem to strongly influence the pilot's performance for any of the three pilots. Most differences in the data between pilots and visibilities can be related to differences in the control inputs  $\delta_e$ ,  $\delta_a$ , and  $\delta_r$ , and the probable cause of these differences is the difference between pilots.

TABLE 2: TOUCHDOWN STATISTICS, EXPERIMENT TWO

STATISTIC	VISIBILITY	
	$\infty/\infty$ AND 400/1600	100/1200
x mean	125 ft	743 ft
x standard deviation	474 ft	1031 ft
y mean	6.3 ft	.9 ft
y standard deviation	19 ft	31 ft
correlation coefficient	-.14	-.015
$\dot{h}$ mean	-6.5 ft/sec	
$\dot{h}$ standard deviation	2.4 ft/sec	
probability ellipse parameters		
semi major axis	559 ft	1214 ft
semi minor axis	22 ft	37 ft
eccentricity	.999	1.000

TABLE 3: AVERAGE STANDARD DEVIATIONS

PILOT	VISIBILITY		
	$\infty/\infty$	400/1600	100/1200
Glide Slope Error - h - ft			
1	6.78	5.40	5.77
2	6.17	7.64	3.65
3	5.26	11.63	8.95
Localizer Error - y - ft			
1	13.66	16.44	27.18
2	12.10	21.40	18.90
3	11.79	11.93	11.33
Yaw - $\psi$ - degrees			
1	1.24	1.19	.91
2	.73	1.00	1.05
3	.95	.73	.81
Pitch - $\theta$ - degrees			
1	.56	.51	.70
2	.66	.64	.54
3	.72	.95	.80
Roll - $\phi$ - degrees			
1	1.56	1.45	1.57
2	1.73	2.17	1.20
3	2.08	2.59	1.28
Yaw Rate - p - deg/sec			
1	.79	.87	.80
2	.96	1.24	.97
3	.58	.90	.75
Pitch Rate - q - deg/sec			
1	.51	.49	.57
2	.59	.55	.55
3	.67	.73	.70

TABLE 3: CONTINUED

PILOT	VISIBILITY		
	$\infty/\infty$	400/1600	100/1200
Roll Rate - $r$ - deg/sec			
1	.64	.52	.67
2	.53	.77	.57
3	.84	.78	.55
Elevator Deflection - $\delta_e$ - degrees			
1	.84	.78	.87
2	1.04	.95	.95
3	1.07	1.72	1.47
Aileron Deflection - $\delta_a$ - degrees			
1	3.54	3.67	2.57
2	4.20	5.60	3.82
3	4.07	4.27	4.11
Rudder Deflection - $\delta_r$ - degrees			
1	.14	.04	.00
2	.12	.84	.00
3	.84	.78	.55

During the second experiment, data were collected on whether the pilot was looking inside or outside the cockpit during the approach. These data were collected using an electro-ocularographic technique, which is fully described in Reference 2. The data as to whether the pilot was looking inside the cockpit at the instruments or outside the cockpit at the visual display were used to determine the number of in/out/in scans made on each run, the duration of each scan, the time intervals between scans, the duration of the interval immediately before touchdown during which the pilot was completely visual, and the wheel height at which the pilot went completely visual. For each visibility condition, medians and ranges of the quantities were determined, and are presented in Table 4. Medians and ranges were used instead of means and standard deviations because the data were obviously distributed in a nongaussian manner.

The pilot was always flying visually at touchdown, and never referred to the instruments below a wheel height of 40 feet. Since the copilot called initial visual contact, the pilot never scanned outside the cockpit before initial visual contact.

For 100 feet initial visual contact, the pilot did not scan on the majority of runs, and commented that there was not enough time. He stated

that any references back to the instruments were for the purpose of checking aircraft attitude.

On those runs where the pilot always had visual ground contact, he scanned back and forth between the instruments and the visual display throughout the run, finally transitioning to only the visual display around 150 feet altitude. While scanning between the instruments and visual display, the pilot apportioned his time so that an average of 61 percent was spent on the instruments. Kolmogorov-Smirnov tests accepted the hypothesis that the duration of the intervals of time spent inside the cockpit and outside the cockpit had exponential distributions. This implies that the probability that the pilot will scan outside the cockpit is not affected by the time since his last scan[5].

TABLE 4: PILOT SCANNING STATISTICS

VARIABLE	STATISTICS	VISIBILITY		
		$\infty/\infty$	400/1600	100/1200
Duration of Final	Median	18.5 sec	16.25 sec	14.3 sec
Fully Visual Period	Range	23.2 sec	14.4 sec	22.8 sec
Wheel Height at	Median	147.5 ft	105 ft	60 ft
start of final fully	Range	285 ft	115 ft	40 ft
visual period				
Number of scans outside	Median	7	1.5	0
cockpit during approach	Range	5	3	1
Duration of outside	Median	1.8 sec	.9 sec	1.2 sec
cockpit scans	Range	29.6 sec	.9 sec	8.6 sec
Duration of intervals	Median	4.0 sec	4.5 sec	.6 sec
between outside cockpit	Range	22.2 sec	20.9 sec	.4 sec
scans				

When the initial visual contact altitude was 400 feet, the pilot's scanning behavior was intermediate between the 100 foot case and the  $\infty$  case. Scanning from the instruments to the visual scene and back was present on the majority of these runs, only now the pilot apportioned 83% of his time to the instruments, and transitioned to the visual display at about 100 feet altitude. The histogram of the scan times outside the cockpit indicated that this time was almost constant at .6 to .8 seconds, while the times between scans were nearly uniformly distributed over the interval of 1 to 8 seconds.

These results indicated that the pilot's scanning behavior changed radically as the visibility conditions changed. The approach and touchdown statistics for the aircraft trajectory are not strongly affected by changes in visibility, indicating that the pilot increases his reliance on the instruments as visibility degrades, and thus successfully maintains a consistent landing performance.

Pilot comments were obtained during the course of both experiments as to what instruments the pilot referred to after he considered that he had transitioned to visual flight, what if any special conditions occurred when he transitioned to visual flight, and he was asked to give a rating of the difficulty of the landing task in that visibility. The rating scale used was a modification of the Cooper Harper scale used for handling qualities. Further development is required to adapt it to rating low visibility approaches, as all three pilots tended to rate the aircraft rather than the task, thus the rating differences were very small. The modification of the rating scale used in the second experiment did exhibit constant sensitivity, a characteristic of the psychological continuum<sup>[6]</sup>.

The instruments most often referred to after transitioning to visual flight were the ADI (for aircraft attitude), the airspeed indicator, and the vertical velocity indicator. All three pilots were unable to correctly estimate what the visibility conditions were, usually giving the initial visual contact altitude as being lower than it actually was, and thinking that the runway visual range was greater than it was. For the 100 foot initial visual contact runs, all three pilots stated that there was insufficient time to refer back to the instruments after transitioning out of the cockpit. The special circumstances surrounding transition all occurred in the 100/1200 visibility condition. They involved either initially interpreting the aircraft as being in a severe nose down attitude, or the aircraft appeared to be lower than it was, or the pilot could not detect cross runway drifts early enough.

## V. CONCLUSIONS

The three pilots involved in these two experiments were able to compensate for reduced visibility and achieve performance comparable to their clear air performance in the situations considered in these simulations. The main factor involved in the compensation appears to be increasing the amount of attention devoted to the instruments and modifying the pilot's

inside/outside scan pattern as visibility is degraded. The variation in performance between pilots was as great as any variation in a single pilot's performance due to visibility changes. The data collected has been usable for developing an optimal control type pilot model for glide slope and localizer tracking.

#### REFERENCES

1. Gressang, Stone, Kugel, and Pollard. Low Visibility Landing Pilot Modeling Experiment and Data. AFFDL TR 75-41, December 1975.
2. Gressang. Low Visibility Landing Pilot Modeling Experiment and Data, Phase II. AFFDL TR 75-57, August 1975.
3. Chalk, Neal, Harris, Pritchard, and Woodcock. Background Information and User Guide for MIL-F-8785B(ASG), "Military Specification -- Flying Qualities of Piloted Airplanes." AFFDL TR 69-72, August 1969.
4. Bunnell and Eicher. C-135B Low Visibility Landing Simulation. AFFDL TM 75-60 FGD, June 1975.
5. Parzen. Modern Probability Theory and Its Applications. John Wiley, New York, 1960.
6. McDonnell. Pilot Rating Techniques for the Estimation and Evaluation of Handling Qualities. AFFDL TR 68-76, December 1968.



# THE APPLICATION OF PILOT MODELING TO THE STUDY OF LOW VISIBILITY LANDING

By Captain Walter W. Harrington

AFFDL/FGD  
Wright-Patterson AFB

## SUMMARY

The optimal pilot model is developed for the analysis of simulation experiments conducted by AFFDL/FGD for the FAA to investigate the effects of low visibility conditions on approach and landing. To adequately model the experiments, the complete aircraft system is considered. Thus, the aircraft system model contains both longitudinal and lateral dynamics in the form of linearized equations for the control feel system, aerodynamics, gusts, and instruments, including Collins FD-109 flight director dynamics for this application. To provide effective analysis of the experiments, developments are made to the optimal human response model. Areas of development include the control law, i.e., state penalties, control rate and amplitude penalties, and control bandwidth, and the information processing model, i.e., observed quantities, indifference thresholds, and degradation of performance due to work load. The resulting model is designed for confident analysis of the low visibility experiments and easy extension to other aircraft systems and tasks.

## INTRODUCTION

Low visibility conditions create a hazardous environment for aircraft approach and landing. The Air Force Flight Dynamics Laboratory (AFFDL) conducted a simulation program, in support of the FAA/USAF Inter-Agency Agreement DOT-FA70WAI-173, Modification No. 12, to investigate pilot interaction with this environment. Specific objectives included the evaluation and validation of visual clues, pilot work load, and flight performance in Category II and III landing operations. As one possible method of approaching the objectives, an effort was undertaken to develop a mathematical model of the pilot's control activity. Experiments were conducted under two phases of simulation to collect data for pilot modeling [1, 2]. This paper presents the pilot model developed from this data base and the analysis of the Phase II experiments.

## SYMBOLS

$a_1, a_2$       Control feel system coefficients

A	Open loop dynamics matrix ( $n_s \times n_s$ )
$A_{cl}$	Closed loop dynamics matrix ( $n_s \times n_s$ )
$A_p$	Open loop dynamics matrix containing neuromuscular filter ( $n_s \times n_s$ )
$A_0, A_1$	Second order system response coefficients
B	Control distribution matrix ( $n_s \times n_c$ )
C	Measurement distribution matrix ( $n_m \times n_s$ )
$C_m$	Motor noise coefficient
$C_y$	Measurement noise coefficient
D	Vertical deviation
E	Expected value
E	Disturbance distribution matrix ( $n_s \times n_d$ )
F	Feedback matrix ( $n_c \times n_s$ )
G	Control amplitude penalty matrix ( $n_c \times n_c$ )
i	Index
I	Moment of inertia
j	Complex coefficient, $\sqrt{-1}$
J	Control cost
$\underline{m}$	Pilot's commanded control ( $\underline{u}$ ) a vector of dimension $n_c$
$n_c$	Number of controls
$n_d$	Number of disturbances
$n_m$	Number of measurements
$n_s$	Number of states
P	Riccati control gain matrix ( $n_s \times n_s$ )
$P_m$	Motor noise to signal ratio
$P_y$	Measurement noise to signal ratio
Q	Measurement penalty matrix ( $n_m \times n_m$ )

$R$	Control rate penalty matrix ( $n_c \times n_c$ )
$t$	Time
$T$	Gaussian input describing function for measurement indifference threshold
$\underline{u}$	Pilot's control input, a vector of dimension $n_c$
$\underline{v}_m$	Autocovariance of motor noise, a vector of dimension $n_c$
$\underline{v}_y$	Autocovariance of measurement noise, a vector of dimension $n_m$
$\underline{w}$	A disturbance vector of Gaussian white noise of dimension $n_d$
$\underline{x}$	State of the system, a vector of dimension $n_s$
$X$	State covariance matrix
$\underline{y}$	A vector of observations, or measurements, available to the pilot, of dimension $n_m$
$Y$	Lateral tracking deviation
$\delta_c$	Controller deviation, a vector of dimension $n_c$
$\zeta$	Damping ratio
$\pi$	Pi
$\sigma$	Root-mean-square of subscripted parameter
$\underline{P}$	Riccati filter covariance matrix ( $m_j \times n_j$ )
$\tau$	Pure time delay
$\phi$	Phase angle
$\omega_c$	Control cutoff frequency
$\omega_d$	Damped natural frequency
$\omega_n$	Natural frequency
$\omega_N$	Neuromuscular frequency
Subscript:	
$a$	Augmented
$p$	Perceived

Superscripts:

T           Transpose  
\*           Optimal  
^           Estimated parameter

Abbreviations:

BH           Breakout Height  
CAVU          Ceiling and Visibility Unlimited  
RVR           Runway Visual Range

SYSTEM TO BE MODELED

This modeling effort is directed to the synthesis and analysis of low visibility piloted approach as simulated by AFFDL. The Phase II pilot modeling simulation visual test matrix contained Category I through Category III linear for structures.

<u>FOG STRUCTURE SPECIFICATION (BH/RVR)</u>	<u>PHASE II SIMULATION (PILOT 3)</u>
CAVU	10 Runs
122m/488m (400 ft/1600 ft)	10 Runs
30.5m/366m (100 ft/1200 ft)	10 Runs

Figure 1: Phase II Pilot Modeling Test Matrix

The particular aircraft used in the simulation is the Boeing C-135B. The C-135B (a military version of the Boeing 707) is a large swept wing four engine jet transport. It has fan jet engines, and conventional arrangement of control surfaces. It falls within Category III of MIL-F-8785B, and is representative of its class.

The AFFDL multicrew cab (C-135 cockpit) was used for the simulation. Cockpit support systems include a three degree-of-freedom motion base system (pitch, roll, and heave), instrument, visual display, control force loading, communication, and sound effect systems. Instrumentation for the simulation included a Collins FD-109 flight director system.

The approach task required tracking of a .05 radian (3. degree) glide slope from a range of 4,572 meters (15,000 feet) to flare. The pilot was instructed to follow the flight director and use raw data and visual cues as required.

## OPTIMAL PILOT MODEL

The optimal pilot model concept, developed by Kleinman, Baron, and Levison [3 - 20], was selected for this application due to its apparent success in modeling similar [12] and complex, time varying [13] control tasks. The optimal pilot model is a mathematical construct designed to synthesize pilot control performance and behavior. The model is based on the assumption that the human operator will control a dynamic, stochastic system optimally subject to his inherent limitations. These limitations are considered to be

1. A time delay, representing cognitive, visual central processing, and neuromotor delays.
2. "Remnant" signals, divided into an observation noise to represent signal degradation due to work load, scanning effects, and signal thresholds, and a motor noise to represent random errors in executing the intended control.
3. A "neuromuscular lag" to represent neuromuscular dynamics.

The control commands are synthesized by a continuous linear equalization network which contains a full state optimal filter (Kalman filter), a full state optimal predictor, and a full state optimal feedback control law. The control law is derived for an augmented state system which results from introducing the neuromuscular lag by means of a control rate penalty. The structure of the model results from a suboptimal solution to a control problem involving a time delay and observation noise. The model is shown in Figure 2.

The mathematical algorithm of the optimal pilot model is developed from the following control problem:

Given the quadratic cost functional of the form

$$J = 1/2 \int_0^{\infty} E \{ \underline{y}^T(t) Q \underline{y}(t) + \underline{u}_a^T(t) R \underline{u}_a(t) \} dt$$

Subject to the constraints

$$\dot{\underline{x}}_a(t) = A_a \underline{x}_a(t) + B_a \underline{u}_a(t) + E_a w_a(t)$$

$$\underline{y}(t) = C_a \underline{x}_a(t - \tau) + \underline{v}_y(t - \tau),$$

determine the non-anticipation feedback control  $\underline{u}_a^*(t)$  which minimizes the cost functional.

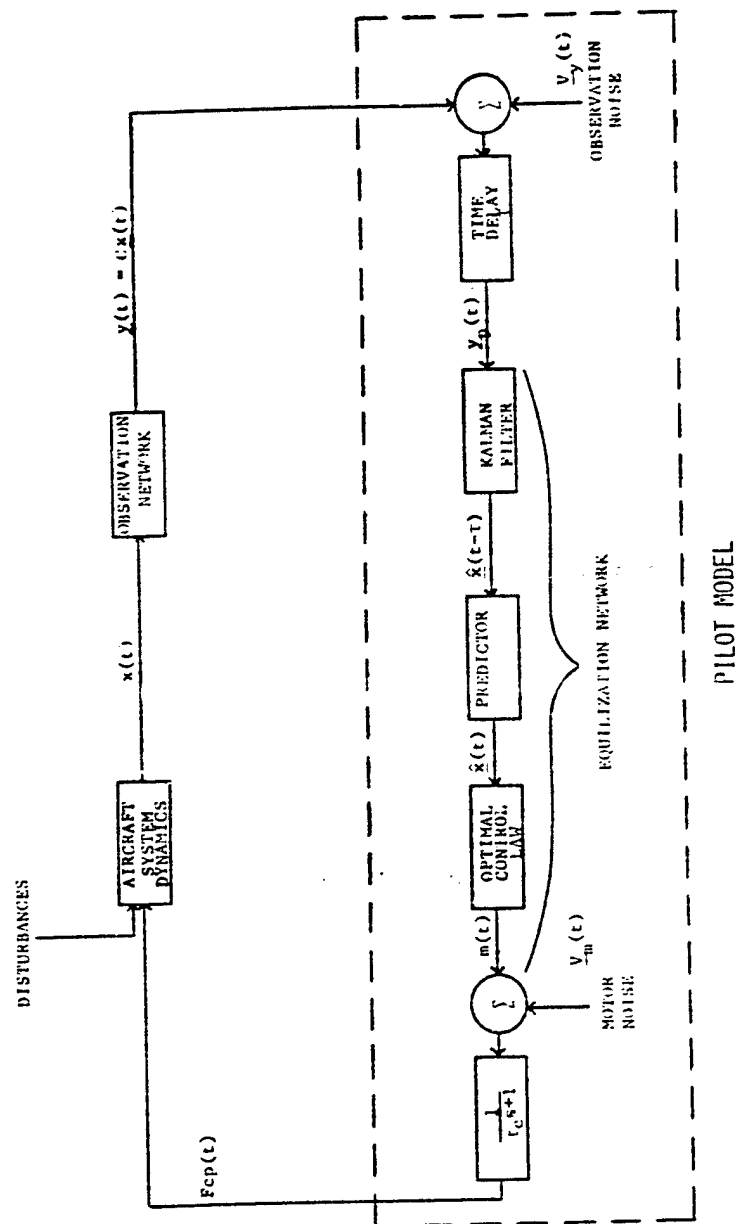


Figure 2 Structure of Optimal Pilot Model

The mathematical algorithm, including developments, of the optimal pilot model is presented in the following sections.

#### Optimal Pilot Model Computer Program

The optimal pilot model algorithm is executed by the digital computer program FGD PILOT. FGD PILOT is a "batch run" Fortran computer program designed for the Cyber 74 computer. The program uses subroutines from a version of Kleinman's pilot model program [16] except for the solution of the steady state Riccati equations and the filter estimate covariance equation. The program originally used a Newton Raphson method of solving steady state Riccati equations developed by Kleinman [17, 18]. However, the subroutines proved to be unsuitable for the C-135B lateral equations [21]. The program now uses a diagonalization of the canonical equations method [22, 18] from the program OPTSYS, which was furnished to AFFDL by Dr. Earl Hall of Systems Control, Inc.

The program FGD PILOT is designed for easy, confident analysis. Developments to the programming algorithm are presented in the following sections.

#### Application of the Optimal Pilot Model to the AFFDL Low Visibility Simulation

The flight simulation which is to be modeled contained a nonlinear, time varying, six degree-of-freedom, hybrid aircraft system model. Some considerations and assumptions allow the hybrid simulation to be modeled within the constraints of the optimal pilot model structure.

The optimal pilot model provides steady state optimal control and state estimation. The flight simulation dynamics were time varying. But, they can be considered slowly time varying for the approach task. It is then assumed that the steady state solution of control and filter gains at each point in time represents the adaptive abilities of the pilot in a physically realizable manner. The model is thus applied to a slowly time-varying system with the calculations repeated with updated parameters as the system varies.

The optimal pilot model requires a linear representation of the aircraft system dynamics. It is therefore required that the components of the simulated aircraft system be represented by sets of first order, linear, piecewise constant coefficient, differential equations. The development of a system model of this form is discussed below.

The mathematical model of the aircraft system is augmented to allow the introduction of a first order, closed loop, pilot lag. This lag is first order and linear by definition. But, since it results from the solution of the nonlinear control Riccati equation, iteration is required to obtain the desired filter coefficient.

The filtered  $\delta c(t)$  signal is the force the pilot applies to the aircraft controller. The C-135B contains a conventional wheel and rudder controller configuration. These devices can be modeled as nonlinear, second order systems. Controller deflection is given by

$$\delta \ddot{c}(t) = \frac{1}{I} F_{cp}(t) - a_1 (\sigma_{\dot{c}}) \delta \dot{c}(t) - a_0 (\sigma_{cc}) \delta c(t)$$

$$\delta \dot{c}(t) = \int \delta \ddot{c}(t) dt$$

where  $a_0$  and  $a_1$  are nonlinear coefficients. Statistical linearization techniques [9] can be applied to linearize these coefficients. Iteration is required, then, to adapt the coefficients to the resulting system performance.

The controller deflection to surface deflection transfer functions can be modeled by pure gains for the C-135B dynamics. These are easily incorporated into the linearized dynamics.

The surface deflections provide inputs to the airframe dynamics. Airframe equations are derived by linearizing the nonlinear six degree-of-freedom equations for rigid body motion about a trim condition. The trim condition used corresponds to the aircraft being in the nominal landing configuration with .93 radian (50 degree) flaps and a flight path angle of -.05 radians (-3. degrees). The differential equations are written in the stability axis coordinate system [23]. Aerodynamic forces and moments are represented by dimensional, primed stability derivatives obtained from a link data package used for C-135B simulators [24]. The stability derivatives need not be varied with state or time since they vary only slightly throughout the range of conditions corresponding to approach. Instead, they are maintained constant at the values of a typical trim condition, thus resulting in a linear constant coefficient system.

The Phase II simulation C-135B lateral airframe dynamics were augmented by a first order, linear yaw damper. The yaw damper equation satisfies the model constraints without modification.

In addition to stability dynamics, positional dynamics were generated in the flight simulation. Glide slope and localizer error are considered important for modeling the instrumented approach task. Both can be synthesized by linear, piecewise constant coefficient, differential equations.

Turbulence disturbances to the aircraft were provided in the simulation by implementation of the state variable model derived by Healey [25] of the Dryden spectrum of wind gusts described in MIL SPEC 8785B. Constant model scales were used corresponding to an altitude of 152 meters (500 feet) as specified by MIL SPEC 8785B for powered approach. The intensity of the turbulence was nominally to be 1/4 of the 152 meter (500 feet) moderate turbulence level. The state variable model is a linear system driven by white noise. For a constant turbulence level, the result is a linear constant coefficient system.



Control command cues were presented to the pilot by a Collins FD-109 flight director. The flight director contains dynamic, nonlinear, and time varying elements. Statistical linearization techniques [9] can be applied to the nonlinear elements. Iteration is then required to adapt the linearized coefficients to the current flight director performance. The time varying elements can be considered slowly time varying. Thus, the flight director is modeled as a linearized, piecewise constant coefficient system.

Raw aircraft data were presented to the pilot through instrument, visual, and motion cues. The dynamics of instruments providing raw data are neglected for this model. Then raw data instrument cues and visual cues can be modeled by the same information channels. Discrimination between instrument cues and visual cues is thus left to the human operator model. Motion cues are assumed negligible considering the C-135B dynamics, the low turbulence levels, and the limited response of the C-135 cockpit motion drive system.

The aircraft system model presented above satisfies the constraints of the optimal pilot model. In addition, the model is separable into two single control input, linearized, piecewise constant coefficient systems.

#### Optimal Pilot Model Control Law

The optimal pilot model equalization network contains a full state optimal feedback control law. The pilot model determines the feedback control  $\underline{u}_a^*(t)$  which minimizes the cost functional

$$J = 1/2 \int_0^{\infty} E \{ \underline{y}^T(t) Q \underline{y}(t) + \underline{u}_a^T(t) R \underline{u}_a(t) \} dt$$

subject to the constraints

$$\dot{\underline{x}}_a(t) = A_a \underline{x}_a(t) + B_a \underline{u}_a(t)$$

$$\underline{y}(t) = C_a \underline{x}_a(t)$$

by the solution of the steady state Riccati control matrix equation

$$A_a^T P_a + P_a A_a + C_a^T Q C_a - P_a B_a R^{-1} B_a^T P_a = 0$$

where

$$\underline{u}_a^*(t) = R^{-1} B_a^T P_a \underline{x}_a(t).$$

The control law therefore requires the specification of the measurement penalty matrix  $Q$  and the control rate penalty matrix  $R$ .

If the pilot does not intentionally couple the longitudinal and lateral axis systems, i.e.,  $Q$  and  $R$  are block diagonal in a manner similar to the decoupling of the system equations, the control problem formed by seeking the

feedback control  $u^*(t)$  which minimizes  $J$  decouples into two separate control problems. Each control problem can be addressed separately, reducing the dimension of the system, and subsequently the time and core requirements for computer implementation of the pilot model. Also, only a single control input pilot model is required for this application. Thus the matrix  $R$  reduces to a scalar.

The measurement penalty matrix  $Q$  is then specified to provide rms minimization of measured quantities in each axis system. The matrix  $Q$  is normally specified as a diagonal matrix. Therefore, to simplify and clarify the specification of this matrix, the vector  $TASK$  is defined such that:

$$TASK = \text{Diagonal } (Q).$$

The vector, of dimension  $n \times 1$ , provides one-to-one correspondence of measurement penalties to the measurements given by the vector  $y(t)$ . The vector is named  $TASK$  so that it will be thought of as a numerical presentation of the flight task.

For the low visibility approach task, the pilot was instructed to follow the flight director and use raw data and visual cues as required. The flight director task required the minimization of pitch steering bar and roll steering bar deviations. Due to the flight director task, the C-135B dynamics, and the low turbulence levels, it is assumed that the measured raw data quantities were not controlled in an rms sense. Instead, the information was used to evaluate the safety of the aircraft and the performance of the flight director, i.e., to detect adverse flight conditions or flight director failures. The measurement of raw data and visual cues is therefore considered a side task. The primary flight task is simply the minimization of pitch steering bar and roll steering bar amplitude deviations.

The minimization of flight director steering bar deviations is a simple, well defined task. The  $TASK$  vector is specified as a numerical representation of this task by:

$$TASK(i:y(i) = \text{steering bar amplitude}) > 0$$

otherwise

$$TASK(i) = 0.$$

The amplitude of the  $TASK$  vector is related to the control rate penalty  $R$  in the following section. For complex tasks, the elements of the  $TASK$  vector can be estimated based upon expected maximum errors [11] or upon the weightings of similar tasks.

#### Control Frequency Response

Pilot control frequency response is regulated in the optimal pilot

model by a first order filter which processes the commanded control signal. The filter cutoff frequency,  $\omega_c$ , is an output of the control solution and is determined by the relative amplitude of control penalties to measurement penalties (TASK vector). It is required by the closed loop dynamics matrix,

$$A_{cl} = A_a - B_a R^{-1} B_a^T P_a,$$

that, for a single control input system,

$$\omega_c = \frac{P_c}{R}$$

where  $P_c$  is the Riccati gain matrix element associated with the control filter.<sup>c</sup> The control law therefore requires iteration to adjust  $R$  or  $P_c$  until the control frequency  $\omega_c$  attains a desired value.

Consider the more general cost functional for a single control input system:

$$J = \frac{1}{2} \int_0^{\infty} E\{y^T(t) Q y(t) + R u_a^2(t) + G u^2(t)\} dt$$

where  $u(t)$  is the control amplitude and  $G$  is a control amplitude penalty. Then, for a given TASK vector,  $G$  and  $R$  can be adjusted to regulate  $P_c/R$  to attain the desired control frequency. It is then required to specify  $\omega_c$ ,  $R$ , and  $G$  uniquely for a given control problem.

The model has assumed that the pilot is highly motivated and controls the system to his neuromuscular frequency limit. Neurological data [23, 26, 27] indicate that the neuromuscular time constant is given by

$$\tau_N \approx .1 \text{ seconds.}$$

Thus, the model has assumed that

$$\omega_c = \omega_N = \frac{1}{\tau_N} \approx 10 \text{ radians/second.}$$

It has also been assumed that  $G = 0$ , thus requiring adjustment of only the control rate penalty  $R$ . This, incidentally, results in a unique solution to the control law for a given task specification. The control rate penalty  $R$  adapts to the TASK vector to attain the desired frequency response. This results in a unique control solution which is independent of the actual numerical value of the TASK vector. However, this algorithm has been found to predict "optimistic" performance for the control of real aircraft systems.

To account for the degradation of pilot control performance encountered in real aircraft systems, the estimation of control rate and amplitude penalties based upon expected maximum control performance [11] has been considered. Thus,

$$R \propto \frac{1}{(u_a^2(t))_{\max}}$$

and

$$G \propto \frac{1}{(u^2(t))_{\max}}$$

But, the maximum values of control rate and amplitude can be difficult to predict, i.e., control force rate and amplitude to a controlled.

It is therefore desired to create a control law algorithm which can be used predictively yet account for the controller configuration, the aircraft dynamics, and the pilot's workload. Consider the following approach. We make the following assumption:

Assumption: A pilot's control activity is limited to that required by the system dynamics under the condition of a normal aircraft workload. Thus, the pilot can control the aircraft system with a bandwidth less than that of the neuromuscular system. The control frequency,  $\omega_c$ , is then a "commanded control frequency." Furthermore,  $\omega_c$  is limited by the pilot's neuromuscular response for the particular controller configuration, i.e.,:

$$\omega_c \leq 10 \text{ radians/sec for a side stick controller}$$

$$\omega_c \leq 3.3 \text{ radians/sec for a center stick or wheel controller.}$$

The 3.3 radians/sec figure for the center stick and wheel controllers is a first order estimate of the frequency response of the extended arm system these controllers require and is consistent with the force gradients allowed for these controllers. [28].

The control law is handled as follows. The control rate penalty  $R$  appears to determine the control  $u^*(t)$ . The control amplitude penalty  $G$  merely allows the increase of  $\omega_c$  by the reduction of the augmented control  $u^*(t)$ . The control law is apparently overspecified by the introduction of the control amplitude penalty  $G$ . We, therefore, let  $G = 0$  so that  $\omega_c$  directly reflects the control activity of the pilot. Note that the control solution is then unique if  $\omega_c$  is specified.

The control frequency  $\omega_c$  must reflect the system dynamics as well as the pilot's workload. Consider "normal" aircraft dynamics, i.e., damped

short period, phugoid, and Dutch roll modes, a stable roll mode, and a stable or slightly divergent spiral mode. System oscillations occur at damped natural frequencies,  $\omega_d$ , and decay or diverge at a rate determined by the product of the damping ratio,  $\zeta$ , and the natural frequency,  $\omega_n$ . Given the aircraft dynamics described above and a normal aircraft work load, let

$$\omega_c = (\omega_d)_{\max}, \text{ the maximum damped natural frequency of the closed loop system}$$

where

$$\omega_c \leq \omega_N \text{ (controller).}$$

The closed loop damped natural frequencies can be determined by an eigenvalue analysis of the closed loop dynamics. We thus require that the control solution outputs  $\omega_c$  and  $(\omega_d)_{\max}$  be equal. This can be accomplished by adjusting the control rate penalty  $R$  in a manner similar to previous control law algorithms until  $\omega_c$  is satisfactorily close to  $(\omega_d)_{\max}$ . This iteration is done automatically in the computer program FGD PILOT with the algorithm

$$R(k+1) = \frac{P_c(k)}{(\omega_d)_{\max}(k)}$$

with the convergence criteria

$$|| \omega_c(k) - (\omega_d)_{\max}(k) || \leq \epsilon$$

where

$$\omega_c(k) = \frac{P_c(k)}{R(k)}.$$

The control law is therefore uniquely determined, based on the controller configuration, the aircraft dynamics, and the pilot's work load. The only entries required by the computer program for the control law are the non-zero elements of the vector TASK and the pilot's neuromuscular frequency limit for the particular controller configuration.

The control law entries required for this application are therefore

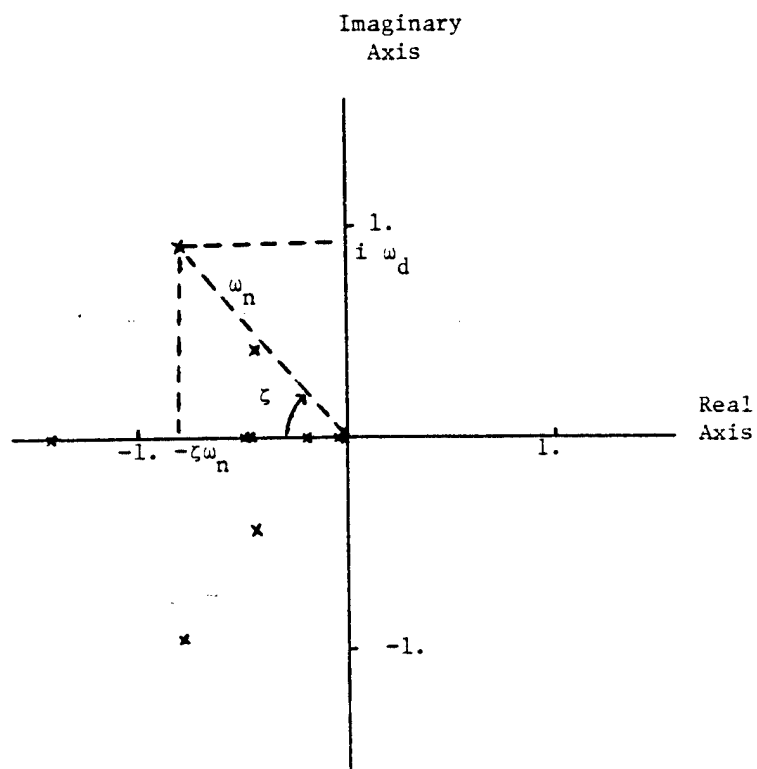
$$\text{TASK } (i:\underline{y}(i) = \text{steering bar amplitude}) > 0$$

and

$$\omega_N = 3.3 \text{ radians/second.}$$

As an example, consider the longitudinal dynamics of the C-135B. The pole plot is shown in Figure 3. The system dynamics require that

$$\omega_c = .94 \text{ radians/second}$$



Real Pole Response:

$$C(t) = A_0 + A_1 e^{st}$$

Complex Pair Response:

$$C(t) = A_0 + A_1 e^{-\zeta \omega_n t} \sin (\omega_d + \phi)$$

Figure 3 Closed Loop Poles of C-135B Longitudinal Dynamics

which is considerably less than the neuromuscular frequency response of 3.3 radians/second for a control wheel. The predicted  $\omega_c$  corresponds reasonably well with the measured half power point of the power spectral density of elevator deflection obtained from simulation data reduction, as shown in Figure 4. Furthermore, the resulting performance predictions are very good, as shown for vertical tracking error in Figure 6. The predicted control frequency is further supported by control frequency sensitivity curves, which are presented in Figure 5 for selected turbulence conditions. A similar analysis applies to the C-135B lateral dynamics.

#### Full State Estimation

The optimal pilot model equalization network generates a full state estimate of the aircraft system based on noisy, delayed observations of the system. This estimate is the output of a Kalman filter. The Kalman filter gains are determined from the covariance matrix  $\Sigma$  which is the solution to the steady state Riccati filter equation

$$A_p \Sigma + \Sigma A_p^T + W - \Sigma C_a^T V_y^{-1} C_a \Sigma = 0$$

where  $A_p$  is a modified open loop dynamics matrix containing the pilot control filter generated by the control law,

$$W = E V_d E^T$$

where  $E$  is the state disturbance distribution matrix and  $V_d$  is the variance matrix of state disturbances of which the autocovariance  $V_m$  of the motor noise  $\underline{v}_m$  is an element, and

$$\underline{V}_y = \text{Diagonal} (V_y)$$

where  $\underline{V}_y$  is the autocovariance of the measurement noise. The filter therefore requires specification of the autocovariance of the measurement noise  $\underline{V}_y$  associated with the measurements  $\underline{y}(t)$  and the autocovariance of the motor noise  $\underline{V}_m$  associated with the control  $u(t)$ . A prerequisite to this is the specification of the pilot model measurements  $\underline{y}(t)$ .

#### Pilot Model Measurements

The optimal pilot model is well suited for realistic synthesis of human operator information processing. The pilot model can observe those instruments or quantities which the pilot would observe to perform the flight task. Furthermore, the pilot model can contain algorithms for amplitude and rate information processing, instrument scanning, and signal perception. These concepts are discussed below.

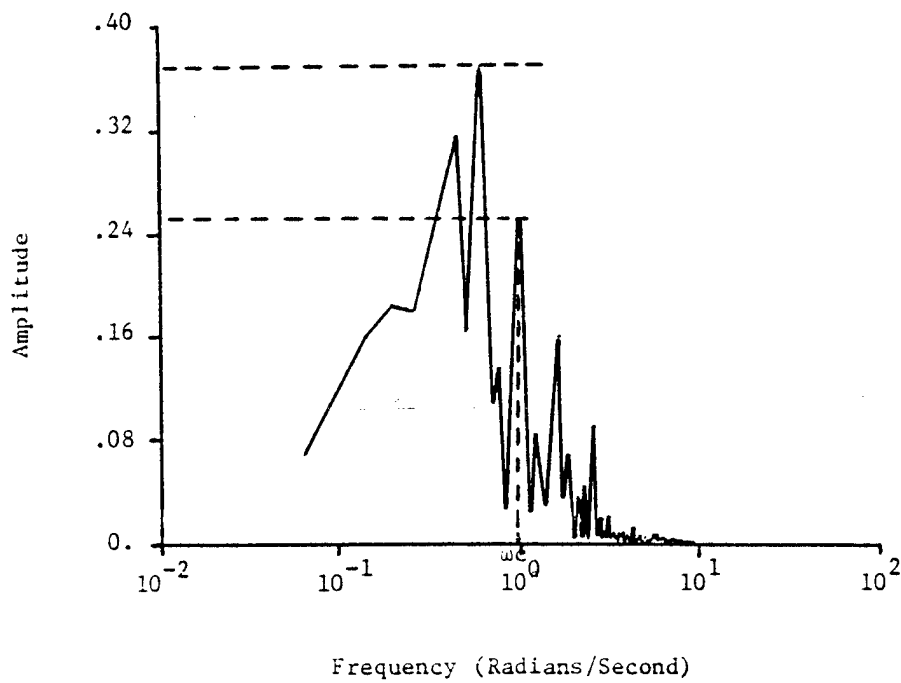


Figure 4 Power Spectral Density of C-135B Elevator Deflection From Simulated Power Approach



Turbulence Amplitude  
meters/second (feet/second)

Curve	$\sigma_{u \text{ gust}}$	$\sigma_{w \text{ gust}}$
A	1.5 (5.)	1. (3.3)
B	.76 (2.5)	.5 (1.65)
C	.38 (1.25)	.25 (.825)
D	.19 (.625)	.125 (.4125)

NOTE: perceptual threshold = .008 radians

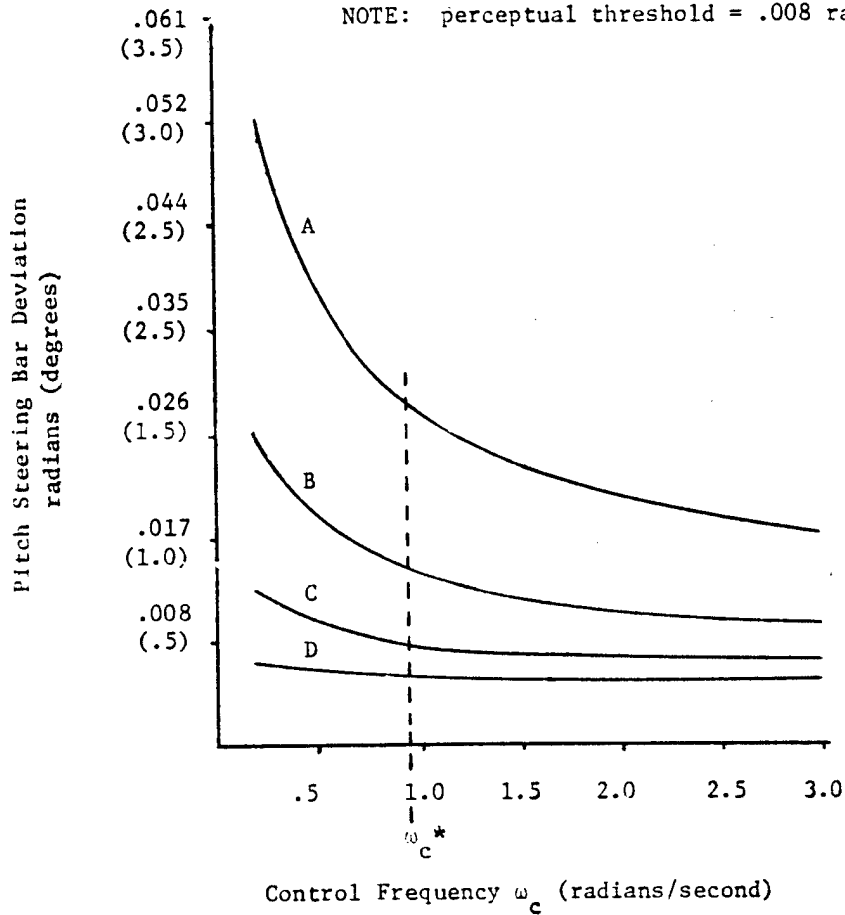


Figure 5 Pitch Steering Bar Sensitivity Curves  
for Selected Turbulence Conditions

The observations available to the pilot are given by the vector  $\underline{y}(t)$ . To specify those instruments or quantities selected by the pilot to perform the flight task, the vector SCAN, of dimension  $n_m$ , is defined such that

SCAN(i: $\underline{y}(i)$  is observed) = 1.

SCAN(i: $\underline{y}(i)$  is not observed) = 0.

This vector is used to activate observation of the specified instruments or quantities in the computer program FGD PILOT. For this application, the only observation required to perform the primary flight task is of the flight director. The required entry is then

SCAN(i: $\underline{y}(i)$  = steering ear amplitude) = 1.

The model has assumed that both the amplitude and first derivative of an observed quantity are available to the pilot. But, the pilot must estimate the rate of an explicitly displayed quantity by observing its time rate of change. This rate estimation process is a function of the Kalman filter in the pilot model. Therefore, let the pilot model observe only those quantities explicitly displayed to the pilot; and, let the rate estimation process be a part of the state estimation process performed by the Kalman filter.

Although only one observation is required in each axis system for the main flight task, a scanning algorithm is required to synthesize the degradation of information quality due to the multi-axis control task and the side task. Scanning can be described by the qualities of pattern, frequency, and dwell time. These qualities have two basic effects on information processing:

1. The effective perceptual threshold of an observed quantity is increased as the frequency at which it is observed is decreased.
2. The quality of the perceived information is decreased as the dwell time for which the quantity is observed is decreased.

Scanning algorithms [29] have addressed information degradation as a function of total attention to an observed quantity. However, this approach does not account for the dynamics of an observed quantity, nor the frequency or dwell time with which it is scanned. Thus, it is desired to create a scanning algorithm which realistically accounts for the effects of scanning.

Consider the following approach. Three types of thresholds are defined:

1. Perceptual threshold: The minimum deviation of an observed quantity which the pilot can detect.
2. Scanning threshold: The effective perceptual threshold which results from the superposition of scanning on the dynamics of an observed quantity.
3. Indifference threshold: The deviation of an observed quantity below which the pilot will not take control action.

The perceptual threshold can be calculated [12] from the pilot's minimum arc of resolution (typically .00087 radians (.05 degrees)), the distance to the display, and the display scale. The scanning threshold arises from the dynamics of an observed quantity and the pattern and frequency with which it is observed. The following assumption is made:

Assumption: For a well designed scanning pattern of displays in a real aircraft system and normal pilot work load, the scanning threshold of an observed quantity will be approximately half the standard deviation of that quantity.

This assumption allows the pilot model to adapt to the dynamics of the displayed quantities as well as a changing aircraft environment. The indifference threshold is subjective and represents the deviations of an observed quantity which the pilot will tolerate. The observation threshold used in the pilot model is defined to be the maximum of the three thresholds discussed above:

$$\text{Threshold} = \text{Maximum} (\text{perceptual threshold, scanning threshold, indifference threshold})$$

Due to the hazardous flight conditions of low visibility approach, it is assumed that the indifference threshold will not exceed the scanning threshold. The observation thresholds are then given by

$$\text{Threshold } (y(i)) = \text{Maximum} (\text{perceptual threshold } (y(i)), 1/2 \sigma_{y(i)})$$

The quality of information perceived by the pilot when observing a quantity will depend upon the dwell time, the scanning frequency, and also upon the correlation of the quantity with other observed quantities. In the optimal pilot model, information quality is given by the noise to signal ratio of the observation noise. For the scanning of displays for a two axis control task, across which information is uncorrelated, it has been found that the noise to signal ratio of observations should be increased by 3 dB or a factor of two. Correlated observations should not require as much signal degradation. Thus, the following measurement noise coefficient is proposed:

$$C_y = 2 \times \text{number of observations.}$$

This form results in a 3 dB increase in noise to signal ratio of the observation noise for the two axis control task, and proportionately smaller increases for additional observations in the same axis system.

This scanning algorithm is incorporated into the observation noise algorithm of the optimal pilot model. The observation noise algorithm is presented in the following section.

### Pilot Model Observation Noise

The optimal pilot model contains observation noise to represent signal degradation due to work load, scanning effects, and signal thresholds. The autocovariance of the observation noise  $\underline{V}_y$  is given by

$$\underline{V}_y(i) = \frac{C_y \pi P_y}{T(\underline{y}(i))} E \{ \underline{y}^2(i) \}$$

where  $P_y$  is the noise to signal ratio given by

$$P_y = .01,$$

$C_y$  is the measurement noise coefficient given by

$$C_y = 2 \times \text{number of observations},$$

and  $T(\underline{y}(i))$  is a Gaussian input describing function for the threshold non-linearity [9]

$$T(\underline{y}(i)) = \text{cerf} \frac{\text{threshold}(\underline{y}(i))}{\sqrt{2} (E \{ \underline{y}^2(i) \})^{1/2}}$$

Iteration of the covariance calculations is required since the threshold gain is a function of system performance. This iteration is done automatically in the computer program FGD PILOT.

### Pilot Model Motor Noise

The optimal pilot model contains motor noise to represent random errors in the execution of the intended control. The autocovariance of the motor noise  $\underline{V}_m$  is given by

$$\underline{V}_m = C_m \pi P_m E \{ u^2(t) \}$$

where  $P_m$  is the noise to signal ratio given by

$$P_m = .003$$

and  $C_m$  is a motor noise coefficient to give a 3 dB increase for the two axis control task, given by

$$C_m = 2.$$

The autocovariance of the motor noise completes the specification of quantities required by the Kalman filter.

### Full State Prediction

The optimal pilot model equalization network contains an optimal, full state predictor which updates the delayed full state estimate generated by the Kalman filter. It is required by the predictor to specify the pure time delay  $\tau$  by which the observations  $y(t)$  are delayed. The typical value of .2 seconds [3 - 12] is selected for the pilot model algorithm.

### Pilot Model Performance Prediction

The optimal pilot model synthesizes pilot control performance by the generation of piecewise constant aircraft system statistics. The state covariance matrix  $X$  arises from the sum of the covariance of the filter estimate, the covariance of the estimation error, and the covariance of the predictor error [10]. Thus,

$$\begin{aligned} X &= E \{ \underline{x}_a(t) \underline{x}_a^T(t) \} \\ &= \int_0^\infty e^{A_c \sigma} e^{A_p \tau} [C_a^T V_y^{-1} C_a] e^{A_p \tau} e^{A_c \sigma} d\sigma \\ &\quad + e^{A_p \tau} e^{A_p \tau} + \int_0^\tau e^{A_p \sigma} W e^{A_p \tau - \sigma} d\sigma. \end{aligned}$$

The standard deviation of the aircraft states is then given by

$$E \{ \underline{x}_i(t) \} = \sqrt{(X)_{ii}}.$$

Pilot model analysis can then be performed by the evaluation of the performance statistics. Evaluation is typically based on the subjective criterion of whether or not the pilot model predictions exhibit sufficient correlation with the experimental results. The additional criterion that the pilot model performance be within the 95% confidence interval [30] of the experimental results is imposed. This gives a firm, but realistic, measure of the correlation between the pilot model performance and experimental results.

### Analysis of Phase II Simulation

Both ensemble statistics and stationary statistics were calculated for the three visibility conditions from the recorded simulation data. The stationary statistics were found to be consistently smaller than the ensemble statistics, indicating insufficient run length to obtain a stationary system. Therefore, pilot model analysis can be applied only to the ensemble statistics. Furthermore, only ten data runs were made for each visibility condition, resulting in a relatively low confidence data set. Therefore,

statistically significant trends are evaluated relative to the 95% confidence intervals.

The mean and standard deviation of the ensemble statistics were plotted as a function of range from the glide slope intercept point. The plots for the vertical and lateral tracking error for the three visibility conditions are presented in Figures 6 through 8. The lateral tracking error is initially displaced to the right, in all three cases, indicating an erroneous initial trim condition. The time varying means are indicative of the non-stationarity of the system. The deviations of the mean error from the nominal were found to be reasonably correlated with the nonstationary gust statistics. Therefore, the gust model in the pilot model program is scaled to piecewise constant gust statistics measured from the simulation.

#### ANALYSIS OF PHASE II PROGRAM OBJECTIVES

Pilot model performance predictions were made at 30.5 meter (100 feet) altitude increments. To provide comparison by visual inspection, the pilot model standard deviation predictions are plotted about the experimental mean in Figures 5 through 10. By visual inspection, the pilot model predictions and simulation performance appears to be well correlated, with the exception of the performance at 30.5 meters (100 feet) altitude. Analysis of the pilot model indicates that due to large gust statistics at that altitude, limiters in the flight director had become saturated. Therefore, insufficient control information is provided to the pilot with just the flight director. In the flight simulation, the pilot must have changed his control strategy, based on raw data scanning, to compensate for the poor flight director performance. Motion cues may also have assisted the pilot in performing the tracking task.

To evaluate the effect of the visibility conditions on the pilots performance, scatter diagrams of the predicted versus measured performance were plotted. The 95% confidence intervals for the measured data were included for the evaluation. The scatter diagrams for the vertical and lateral tracking error are presented in Figures 9 and 10. Except for a few data points, particularly those from the 30.5 meter (100 feet) altitude cases, all the predicted data points are within the 95% confidence intervals of the measured data. Therefore, no statistically significant trends occur between visibility conditions.

#### SUMMARY OF OPTIMAL PILOT MODEL

An optimal pilot model algorithm has been developed for the analysis of the complete aircraft system. The aircraft system model contains both longitudinal and lateral dynamics in the form of linearized, piecewise constant coefficient equations for the control feel system, aerodynamics, stability augmentation, gusts, and instruments. Statistical linearization is applied as required. Developments to the human response model include (1) an optimal

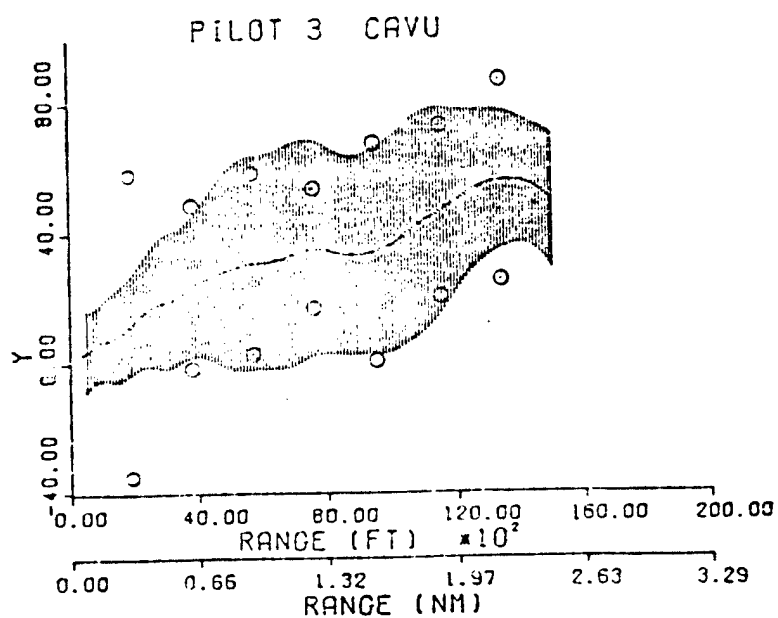
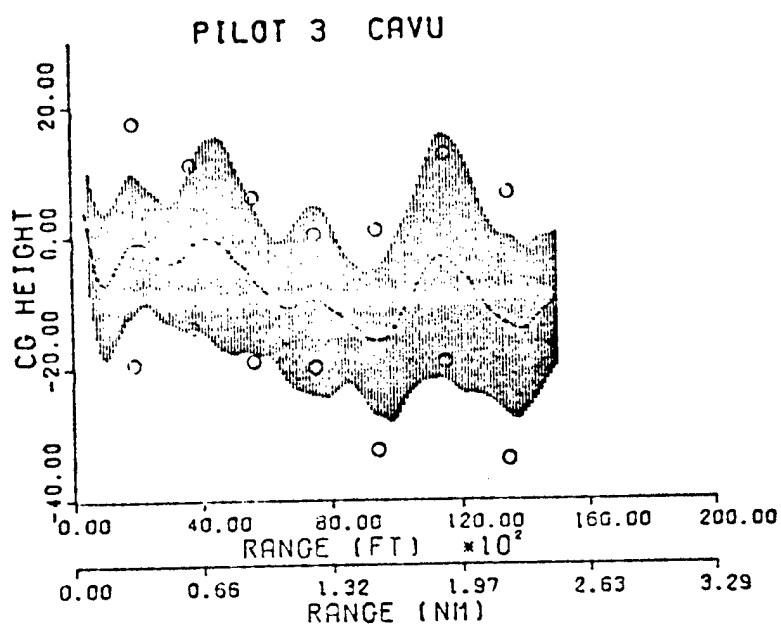


Figure 6 Ensemble Tracking Statistics, Phase II  
Simulation, CAVU Weather Conditions

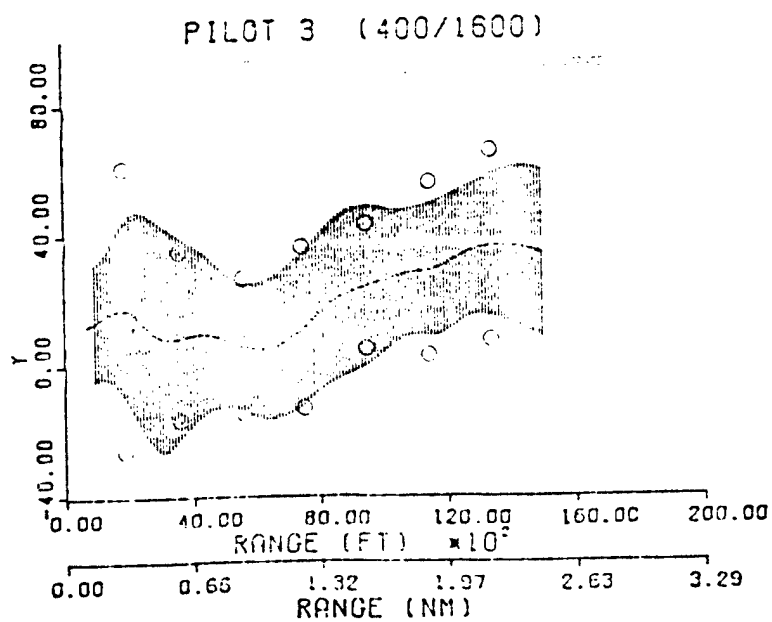
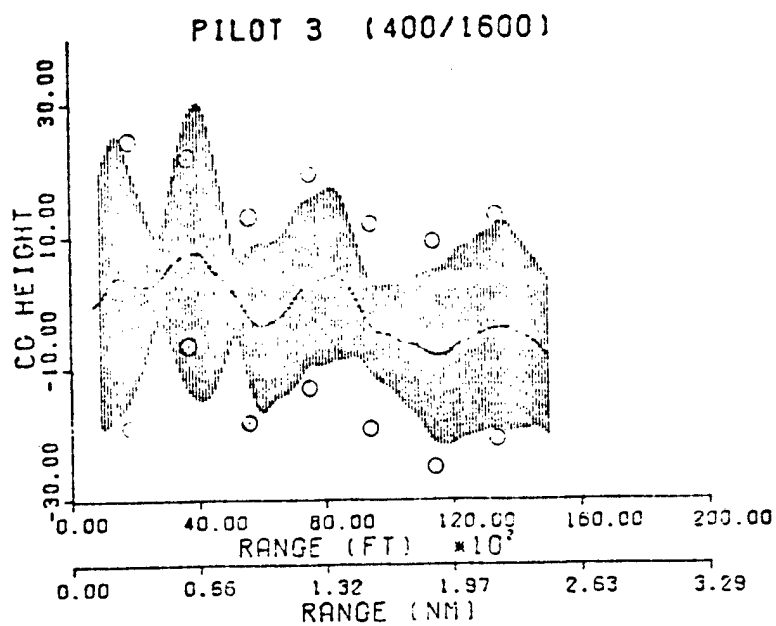


Figure 7 Ensemble Tracking Statistics, Phase II  
Simulation, 400/1600 Weather Conditions



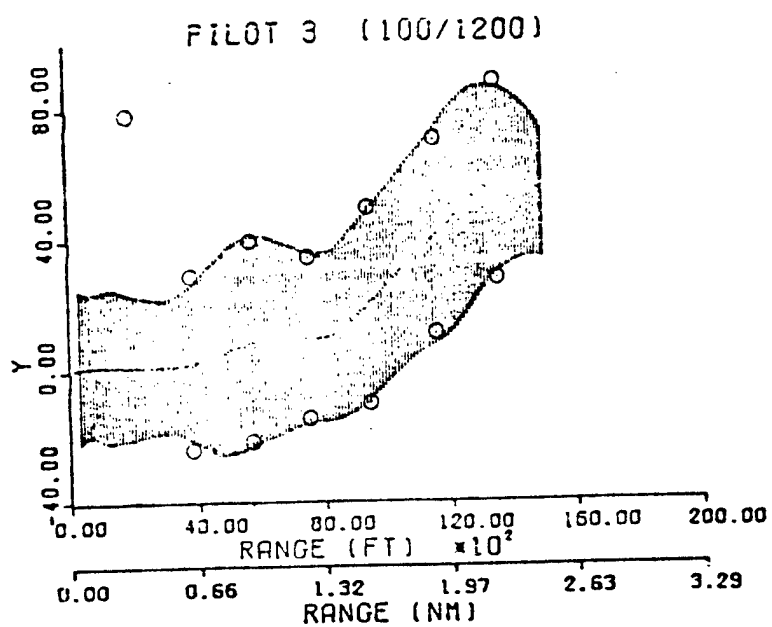
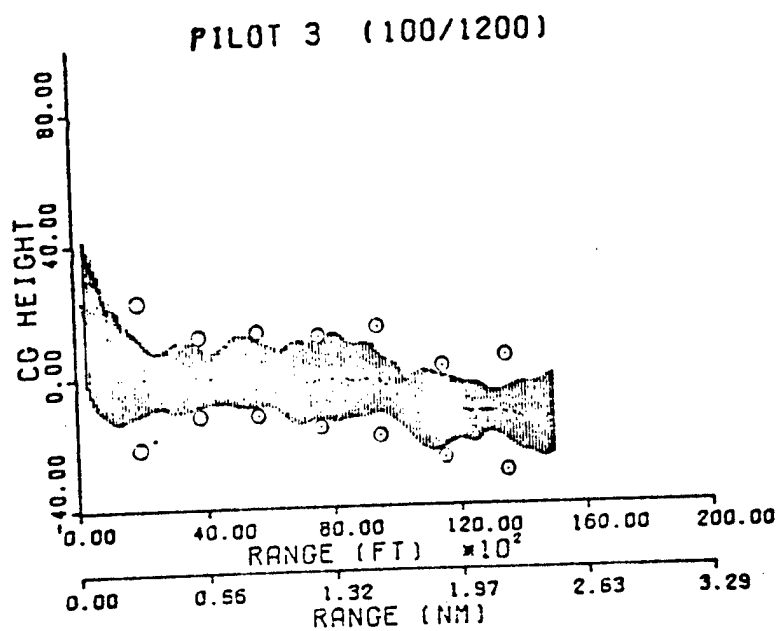


Figure 8 Ensemble Tracking Statistics, Phase II  
Simulation, 100/1200 Weather Conditions

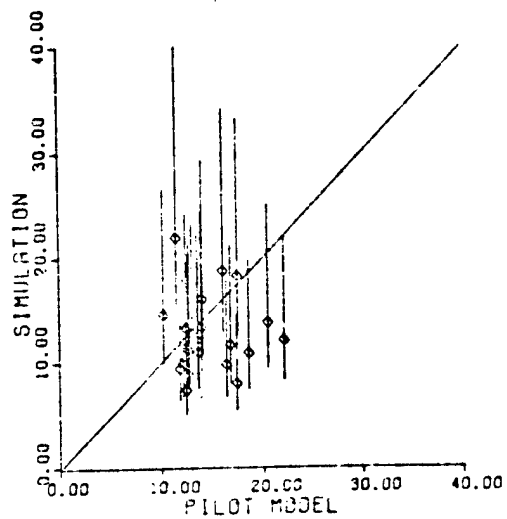


Figure 9 Scatter Diagram for Vertical Tracking Error, Phase II Simulation

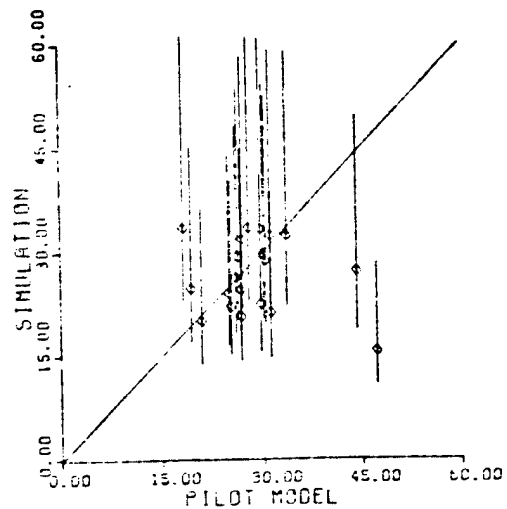


Figure 10 Scatter Diagram for Lateral Tracking Error, Phase II Simulation

control law which represents the task, is related to the closed loop system frequency response, and is unique, (2) a full state estimator which observes those instruments or quantities available to perform the flight task, and (3) a scanning algorithm which accounts for the scanning pattern, frequency, and dwell time, as well as the dynamics of the observed quantities.

The optimal pilot model is executed by the digital computer program FGD PILOT. The program requires specification of the aircraft configuration, the appropriate stability derivatives and aircraft model gains, and the gust parameters. The program requires minimal inputs for the pilot model to perform the control task: (1) the TASK vector to define the flight task, (2) the neuromuscular frequency limit for the controller configuration, (3) the SCAN vector to define the instruments or quantities available to perform the flight task, and (4) the perceptual thresholds of those instruments or quantities. Otherwise, the program is self-contained and executes the control frequency analysis, the scanning algorithm, and all iterations required to satisfy the control law and statistical approximations made in the aircraft model. Thus, the program is designed for easy use and extension to other aircraft systems and tasks.

#### SUMMARY OF THE ANALYSIS OF THE PHASE II LOW VISIBILITY SIMULATION

The following conclusions are drawn about the data base:

1. The data base from the simulation is nonstationary, precluding optimal pilot analysis of the stationary statistics.
2. Initial trim condition problems resulted in non-zero mean lateral tracking error.

The following conclusions are drawn from or supported by the pilot model analysis:

1. The glide slope and localizer tracking errors depend significantly upon the current gust statistics.
2. Under the conditions of approach with a flight director through linear fogs in a gusty environment with no cross wind, glide slope and localizer tracking performance does not depend upon the fog structure.
3. The Collins FD-109 flight director can saturate at low altitude, requiring the pilot to change his control strategy. Although the saturation property can aid in aircraft safety by reducing control activity at low altitude, the resulting degradation of information quality can produce a dangerous control situation during a critical phase of low visibility approach.

## CONCLUDING REMARKS

The optimal pilot model has demonstrated effective synthesis of a complete piloted aircraft system. The pilot model algorithm should be extended and verified for aircraft systems with other stability characteristics, controller configurations, displays, and for other control tasks. This development process will result in a pilot model which can be used confidently for performance prediction and analysis of aircraft systems.

## REFERENCES

1. Gressang, Stone, Pollard, and Kugel: Low Visibility Landing Pilot Modeling Experiment and Data, Phase I. AFFDL TR 75-41, April 1976.
2. Gressang: Low Visibility Landing Pilot Modeling Experiments and Data, Phase II. AFFDL TR 75-57, August 1975.
3. McRuer and Krendel: Mathematical Models of Human Pilot Behavior. AGARDograph No. 188, January 1974.
4. Baron and Kleinman: The Human As An Optimal Controller and Information Processor. IEEE Trans. Man-Machine Systems, Vol. MMS-10, March 1969, pp 9 - 17.
5. Baron et al: Application of Optimal Control Theory to the Prediction of Human Performance In A Complex Task. AFFDL TR 69-31, March 1970.
6. Kleinman, Baron, and Levison: A Control Theoretic Approach to Manned-Vehicle Systems Analysis. IEEE Trans. Auto. Control, Vol. AC-16, December 1971, pp 824 - 832.
7. Kleinman, Baron, and Levison: An Optimal-Control Model of Human Response, Part I: Theory and Validation. Automatica, Vol. 6, 1970, pp 357 - 369.
8. Kleinman: Optimal Control of Linear Systems With Time-Delay and Observation Noise. IEEE Trans. Auto. Control, Vol. AC-14, October 1969, pp 524 - 527.
9. Graham and McRuer: Analysis of Nonlinear Control Systems. Dover Publications, New York, 1971, Chapter 6.
10. Baron and Levison: An Optimal Control Methodology for Analyzing the Effects of Display Parameters On Performance and Work Load in Manual Flight Control. IEEE Trans. on Systems, Man, and Cybernetics, Vol. SMC-5, July 1975, pp 423 - 430.

11. Bryson and Ho: Applied Optimal Control. Ginn and Co., Waltham, Mass., 1969, Chapter 5.
12. Kleinman and Baron: Analytic Evaluation of Display Requirements for Approach to Landing. NASA CR-1952, October 1971.
13. Kleinman and Perkins: Modeling Human Performance in a Time-Varying Anti-Aircraft Tracking Loop. IEEE Trans. Auto. Control, Vol. AC-19, August 1974, pp 297 - 306.
14. Harvey: Application of An Optimal Control Pilot Model to Air-to-Air Combat. AFIT Thesis GA/MA/74M-1, March 1974.
15. Dillow, Picha and Anderson: Slushy Weightings for the Optimal Pilot Model. 11th Annual Conference on Manual Control, May 1975.
16. Kleinman: Computer Programs Useful in Linear Systems Studies. Systems Control, Inc., Technical Memorandum, December 1971.
17. Kleinman: On An Iterative Technique for Riccati Equation Computation. IEEE Trans. Auto. Control, Vol. AC-13, February 1968, pp 114 - 115.
18. Kwakernaak and Sivan: Linear Optimal Control Systems. John Wiley, New York, 1972, Chapter 3.
19. McRuer, Ashkenas, and Graham: Aircraft Dynamics and Automatic Control. Princeton University Press, 1973, Chapters 5 and 6.
20. Kleinman and Killingsworth: A Predictive Pilot Model for STOL Aircraft Landing. NASA CR-2374, March 1974.
21. Gressang: A Note on Solving Riccati Equations Associated with Optimal Pilot Models. AFIT/AIAA Mini Symposium on Recent Advances in Aeronautical Research Development, and Systems, WPAFB, 26 March 1975.
22. Bryson and Hall: Optimal Control and Filter Synthesis by Eio-envector Decomposition. Report, Dept. of Aero. and Astr., Stanford University, December 1971.
23. McRuer and Graham: Human Pilot Dynamics in Compensatory Systems. AFFDL TR 69-72, July 1965.
24. C-135B Aerodynamic, Flight, Ground, and Engine Equations. Report ER-459, Link Division, General Precision, Inc., Binghamton, NY, 11 January 1963.
25. Heath: State Variable Model of Wind Gusts. AFFDL/FGC TM-72-12, July 1972.
26. Stark: Neurological Control Systems, Studies in Bioengineering. Plenum Press, New York, 1968.

27. Milsum: Biological Control Systems Analysis. McGraw-Hill Book Company, New York, 1966.
28. Chalk, Neal, Harris, Pritchard, and Woodcock: Background Information and User Guide for MIL-F-8785B(ASG), "Military Specification -- Flying Qualities of Piloted Airplanes". AFFDL TR 69-72, August 1969.
29. Curry, Young, Hoffman, and Kugel: A Pilot Model with Visual and Motion Cues. AIAA Visual and Motion Simulation Conference, Dayton, Ohio, April 1976.
30. Crow, Davis, and Maxwell: Statistics Manual, Dover Publications, New York, 1947.

STABILITY OF THE PILOT-AIRCRAFT SYSTEM  
IN MANEUVERING FLIGHT\*

by

John R. Broussard and Robert F. Stengel  
The Analytic Sciences Corporation  
Six Jacob Way  
Reading, Massachusetts 01867

ABSTRACT

A control-theoretic pilot model is incorporated in the analysis of pilot-aircraft motions during maneuvers. The pilot model is found to be of value for the definition of maneuvering flight stability boundaries, and it simulates pilot control actions during a representative task with reasonable fidelity. It is concluded that the pilot model developed here, which is synthesized rapidly using new algorithms for solution of matrix Riccati equations, provides important capabilities for evaluation of flying qualities and for identifying proper piloting procedures during difficult maneuvers.

INTRODUCTION

High-performance aircraft are susceptible to degraded flying qualities during maneuvering flight, and the effects of piloting actions play a significant role in determining overall system stability. The pilot's task is made difficult by the need to adapt control strategies to varying aircraft dynamics, by potentially high work load, and by the physical and mental stresses associated with maintaining safe flight. Under such circumstances, improper piloting procedures can lead to inadvertent loss of control. This paper presents results from a study of pilot-aircraft interactions during high angle-of-attack flight. A multi-input/multi-output, control-theoretic human operator model is developed

---

\*Contract No. N00014-75-C-0432 for the Office of Naval Research, Department of the Navy.

Presented at the 12<sup>th</sup> Annual Conference on Manual Control, Urbana, Illinois, May 25-27, 1976.

and applied to the stability problem. Effects of control mechanisms (e.g., conventional stick-surface linkages and aileron-rudder interconnect), and pilot adaptation to flight condition are described. Proper (i.e., stabilizing) control actions for maneuvering flight are illustrated, and an example of pilot-induced oscillation (PIO) due to pilot non-adaptivity is demonstrated.

### CONTROL THEORETIC PILOT MODEL

The optimal control pilot model (Fig. 1) used for this analysis contains the following elements: an estimator, which processes the pilot's observations to provide an estimate of the aircraft state; a controller, which mechanizes the pilot's regulating functions and transmits the results to the neuromuscular dynamics; and a neuromuscular model, which represents

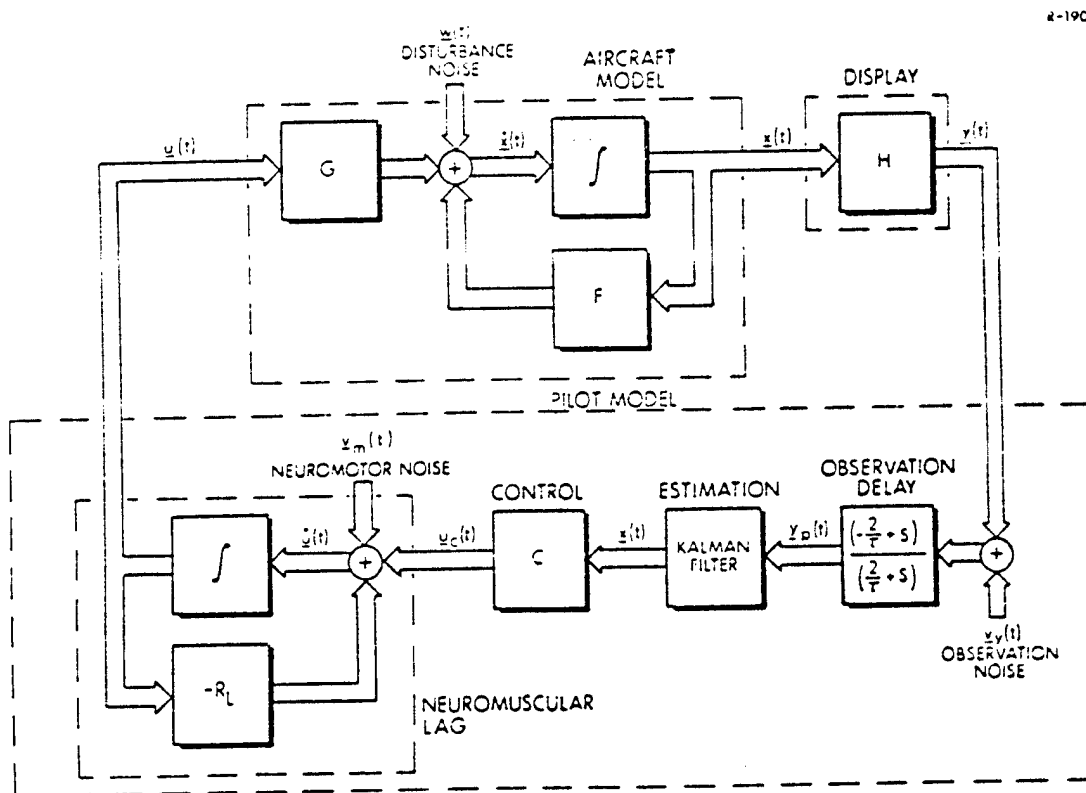


Figure 1. Block Diagram of the Pilot Model Containing the Pade approximation to Pure Time Delay



the dynamics of the pilot's limbs. A block diagram of the model depicting the three elements is shown in Fig. 1. The model replaces the pure time delay that is commonly modeled in human observations (Ref. 1) by a first-order Padé approximation, a substitution frequently made in analysis of human response using quasi-linear human models (Ref. 2). The substitution is useful, because it allows the predictor equations in the pure-time-delay optimal-control model to be eliminated. The aircraft and pilot model then can be combined in a single linear, time-invariant equation, shown by Eq. 6 in the appendix. This form is easier to simulate, and its stability and response characteristics are readily defined by eigenvalues and eigenvectors. From the separation principle for linear-optimal stochastic regulators (Ref. 3), the stability of the pilot model's estimation and control dynamics can be defined independently, i.e., the eigenvalues (or poles) of the pilot estimator are uncoupled from the closed-loop poles of the pilot controller-aircraft system. Similarities between the pure-time-delay model and the model in Fig. 1 include identical numerical values for the pilot control strategy matrix,  $C$ , the observation covariance matrix associated with  $\Delta y_v(t)$ , and the neuromotor noise covariance matrix associated with  $\Delta y_u(t)$ .

Two new algorithms have been derived for generating the coefficients of the pilot model. One solves the regulator Riccati equation and the other solves the estimator Riccati equation. These algorithms, are self starting and completely automated for computer implementation. The regulator algorithm is shown in the appendix, and the estimator algorithm can be found in Ref. 4. A unique feature of these algorithms is that any number of controls can be used, and current results have been obtained with up to three concurrent pilot outputs (longitudinal stick, lateral stick, and rudder pedals). The pilot model for this analysis is supported by a fully coupled, linear, six degree-of-freedom, aircraft simulation, (Ref. 5). The pilot model longitudinal/lateral-directional modes are coupled or uncoupled depending on the coupling in the aircraft model.

Investigations of pilot-aircraft instability using the control-theoretic pilot model fall into two categories: those in which the pilot fails to stabilize an unstable aircraft, and those in which the pilot destabilizes a stable aircraft. In the first case, the pilot's time delay, observation noise, neuromuscular time constants, and scanning factors are important parameters. Assuming that the aircraft's linearized dynamics have one or more unstable eigenvalues, the analysis determines pilot parameters for which the optimal control model fails to exist. The optimal control model fails to exist when one of the model algorithms diverges, i.e., when it is not possible to obtain a steady-state solution to one of the Riccati equations.

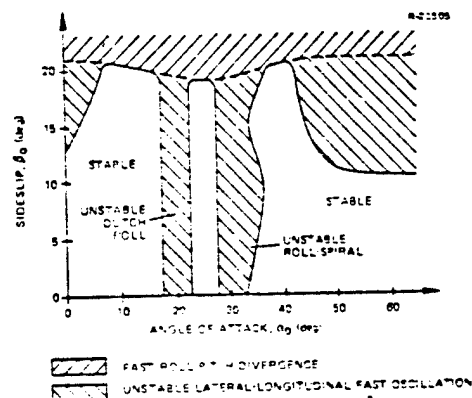
The second category is related to the pilot's ability to adapt to changing flight conditions. Straight-and-level flight at low angles of attack is a typical operating condition. In

many situations, such as air combat and tracking, the pilot must maneuver the aircraft through widely varying flight conditions at high angles of attack, resulting in rapidly changing aircraft dynamics. These include such changes as the onset of adverse yaw due to ailerons, the migration of roll and spiral roots to unstable positions, and large variations in the natural frequency and damping of short period and Dutch roll modes. With the mean angle of attack,  $\alpha_0$ , changing in some instances faster than a degree per second, the pilot may not have the time to update his control strategy fast enough, and local instabilities can result. For example, pilot-induced oscillations (PIO) and departures can occur because a control strategy which is appropriate to one flight condition is destabilizing in another.

The control-theoretic pilot model can be used to analyze nonadapting pilot behavior in a straightforward manner. In the examples considered here, the pilot model's control strategy matrix,  $C$ , is first determined at a low- $\alpha_0$  flight condition. This gain matrix is frozen and the aircraft's dynamics are allowed to change. The stability of the pilot-aircraft system is determined by its eigenvalues. The Kalman filter dynamics are always assumed to be adapted and stable; thus, the Kalman filter only affects the simulation transient of the non-adapted pilot model and does not affect its stability.

#### EFFECTS OF FLIGHT CONDITIONS ON PILOT-AIRCRAFT STABILITY

The open-loop stability limits of the reference aircraft are shown in Fig. 2. The primary instabilities are an unstable Dutch roll mode in a band centered near  $\alpha_0 = 20$  deg and an unstable roll/spiral combination in a band near  $\alpha_0 = 30$  deg.

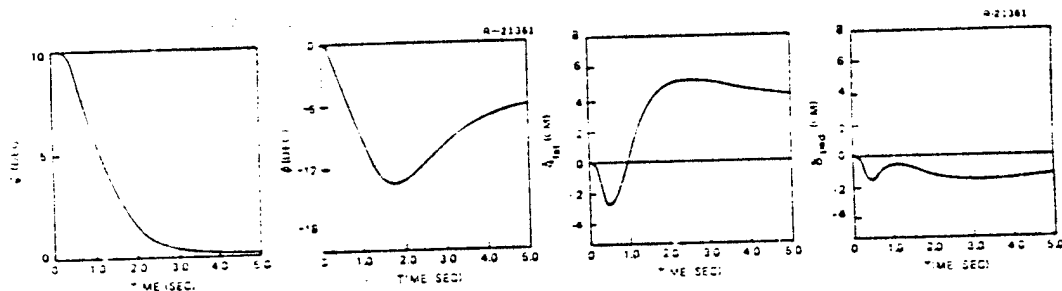


ORIGINAL PAGE IS  
OF POOR QUALITY

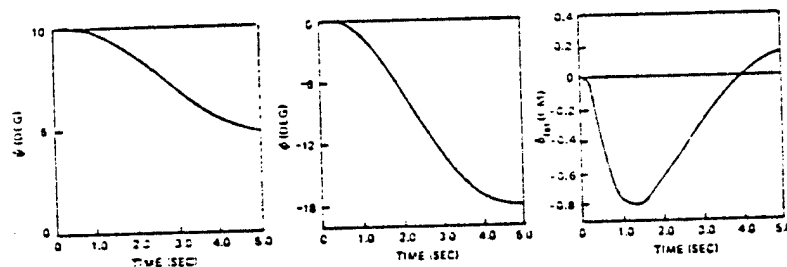
Figure 2. Open-Loop Stability Limits of the Reference Aircraft

The pilot's control outputs can include lateral stick for roll control, longitudinal stick for pitch control, and pedals for yaw control. When the aileron-rudder interconnect system (ARI) is engaged, the lateral stick commands to aileron are phased out as  $\alpha_0$  increases beyond 10 deg, and lateral stick-to-rudder commands are phased in. Above  $\alpha_0 = 30$  deg, the lateral stick controls rudder only. The purpose of the ARI is to reduce adverse yaw effects due to aileron at high  $\alpha_0$ , allowing the pilot to use low- $\alpha_0$  strategies at high angle of attack. This will be verified with the nonadapted pilot model.

The next three figures show simulations of the adapted linear-time-invariant control-theoretic model. In all cases, the noise terms are set to zero, and the model starts with a 10-deg heading error, which is to be nulled by the pilot model. Figure 3 shows piloting procedure at low- $\alpha_0$  flight conditions using lateral stick alone and lateral stick plus rudder pedal. The figures illustrate that the modeled control patterns are very similar to the normal operating procedures of a human pilot. Initially, negative lateral stick movement rolls the aircraft and starts the heading change; this is followed by positive stick deflection to null roll rate and to zero roll angle at the new heading. The figure also demonstrates how the pilot can quicken lateral response by coordinated control of stick and pedals.



a) Lateral Stick Plus Rudder Pedal



b) Lateral Stick Alone

Figure 3. Adapted Piloting Procedures at  $\alpha_0 = 10$  deg

At higher angles of attack, adapted pilot model behavior with and without the ARI can be determined. Figure 4 shows such behavior at  $\alpha_0 = 30$  deg,  $\beta_0 = 0$  deg for control with lateral stick alone. When the ARI is off, as in Fig. 4b, the pilot model must use a stick deflection which is opposite to the normal movement to null the yaw angle. When the ARI is on, as in Fig. 4a, the pilot model uses normal low- $\alpha_0$  procedure to null the yaw angle, i.e., negative lateral stick to roll negatively. From Fig. 4, it can be seen that the ARI achieves its purpose, in terms of maintaining the same piloting procedure at high and low- $\alpha_0$  for lateral stick control.

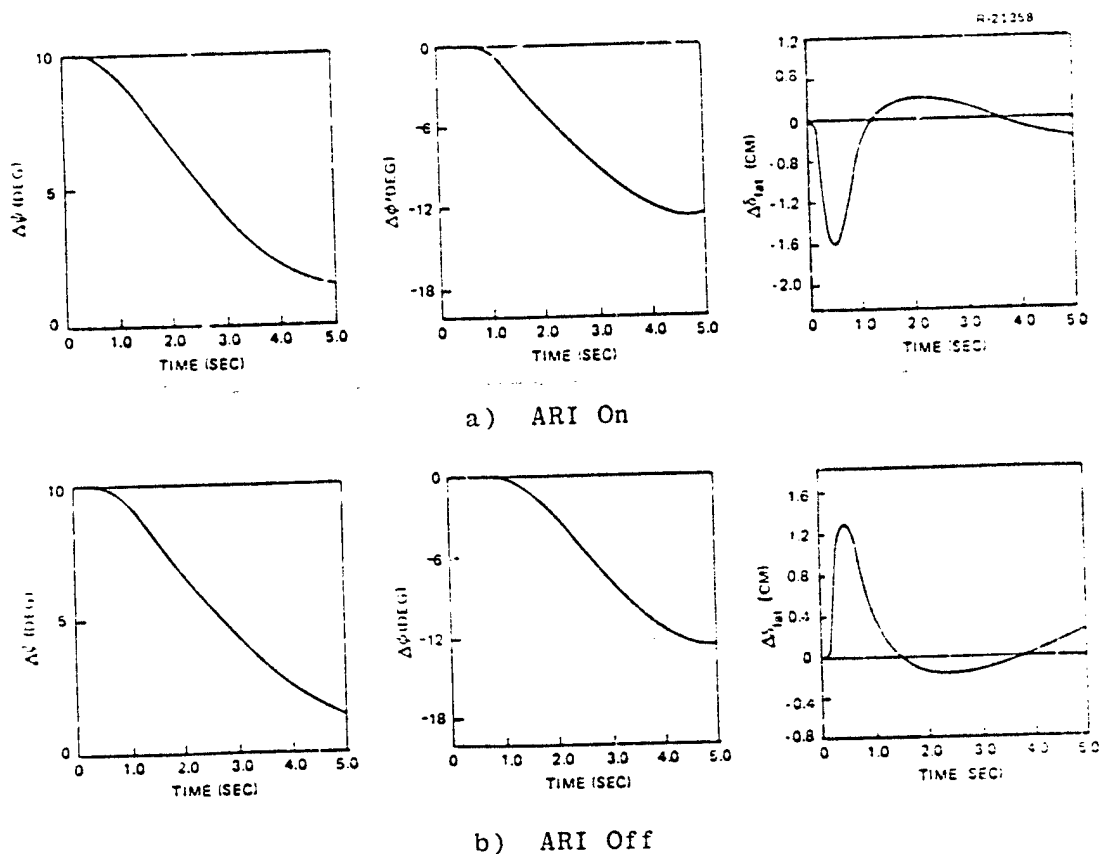


Figure 4. Adapted Lateral Stick Alone  
Piloting Procedure at  $\alpha_0 = 30$  deg

Figure 5 shows adapted pilot model behavior at high- $\alpha_0$  for combined control with lateral stick and pedals. A comparison of Fig. 5b with Fig. 3a shows that the lateral stick movements are similar, as are the initial pedal movements; however, the final pedal positions are opposite in sign. The positive pedal position in Fig. 5b is counteracting the adverse yaw caused by

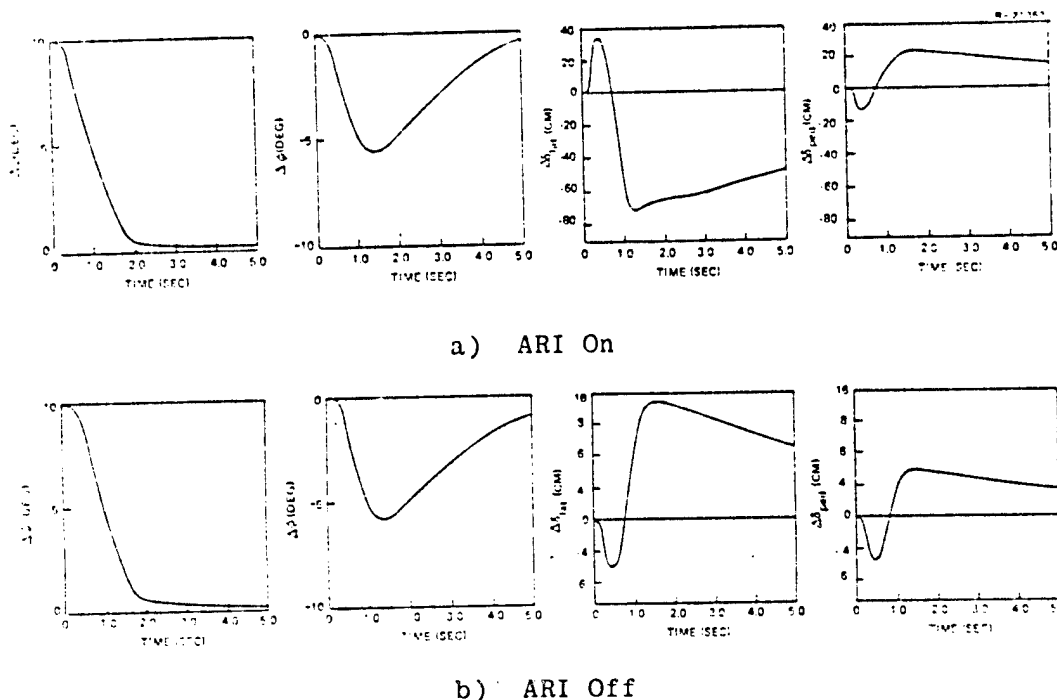


Figure 5. Adapted Lateral Stick and Pedal  
Piloting Procedure at  $\alpha_0 = 30$  deg

positive lateral stick at high  $\alpha_0$ . Figure 5a shows stick/pedal control procedure at high  $\alpha_0$  with the ARI on. The large control movements are not unexpected. At  $\alpha_0 = 30$  deg, lateral stick and pedal both control only rudder and their movements conflict. It would be possible to incorporate this known conflict by increasing the appropriate penalty weights in the design equation. In the present examples, the weighting matrices are held constant to illustrate the effects of the pilot maintaining constant trade-offs between allowed state errors and control usage.

Nonadapted piloting effects on pilot-aircraft stability regions can be presented in the aircraft's  $\alpha_0$ - $\beta_0$  plane. The regions of instability are determined, as previously mentioned, by fixing pilot control strategy, C, and determining eigenvalues of the closed-loop system (Eq. 6). Figure 6 shows the stability regions for three-control piloting procedures, and Fig. 7 shows stability regions under the assumption that the pilot does not use pedal control. In all cases the pilot model is adapted to  $\alpha_0 = 10$  deg and  $\beta_0 = 0$  deg (denoted by  $\odot$  in the figures). The instabilities of the longitudinal modes (phugoid and short period) are the same in both cases, since the ARI does not affect longitudinal control. From Fig. 3a and 4b, it is evident that if the pilot model does not adapt, at some point low- $\alpha_0$  piloting

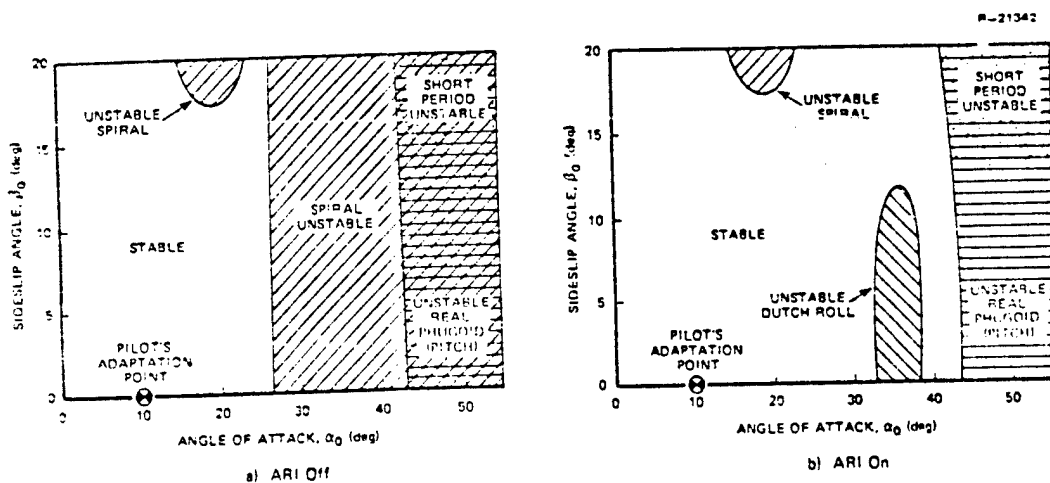


Figure 6. Stability Boundaries for 3-Control Piloting Procedures

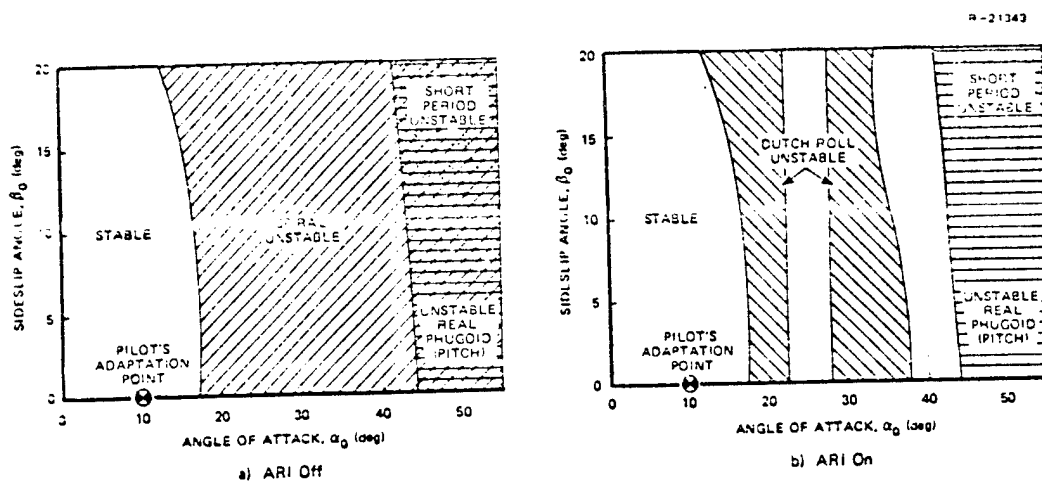


Figure 7. Stability Boundaries for 2-Control Piloting Procedures

procedure will cause an instability because of adverse yaw. In Fig. 7a this occurs at  $\alpha_0 \approx 17$  deg, and the incorrect procedure is characterized by an unstable (closed-loop) spiral mode. When three controls are used with the ARI off, the instability due to incorrect procedure does not occur until  $\alpha_0 \approx 26$  deg, as shown in Fig. 6a. Figures 6b and 7b indicate that the ARI eliminates the spiral instability seen in Figs. 6a and 7a, but it introduces an unstable Dutch roll mode. In the stick-alone case, the instability occurs in bands centered on 20 deg and 32 deg angle of attack.

Simulations of nonadapted procedure are readily obtained using the control-theoretic model, and these are shown in Figs. 8 and 9. Figure 8b shows the unstable spiral mode response with ARI off where negative lateral stick yaws the aircraft positively. Figure 8a shows the unstable Dutch roll mode with ARI engaged, of which only one cycle is evident. Note that negative lateral stick deflection causes the correct initial yaw response, but the pilot model's stick movement does not compensate fast enough. Figure 9b shows the unstable spiral mode for three controls with the ARI off. The initial direction in yaw angle is correct, but sluggishness in control movement, particularly in pedal, causes the instability. The simulation in Fig. 9a is stable for three controls with the ARI on. A comparison of Fig. 9a with Fig. 3a shows that the pilot model successfully uses the same strategy in both cases, but the 10-deg strategy provides too little damping at  $\alpha_0 = 30$  deg.

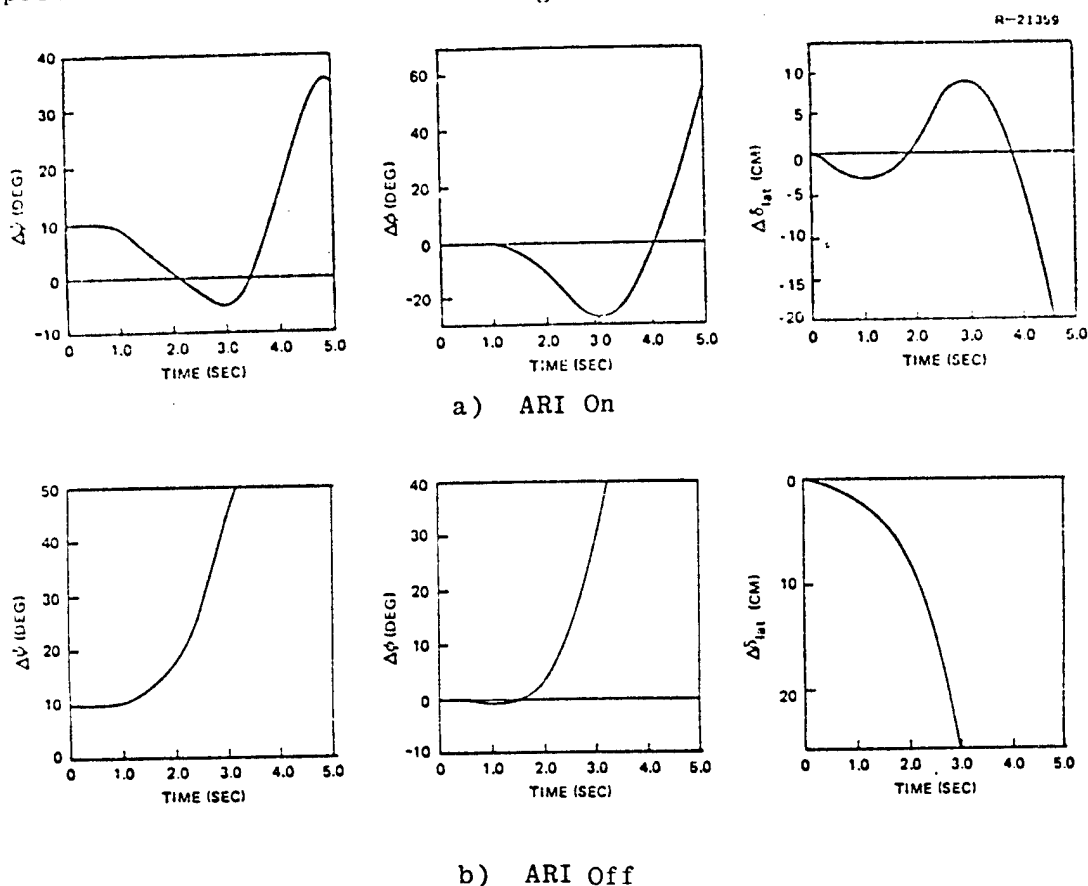


Figure 8. Use of Low- $\alpha_0$  Piloting Procedure in High- $\alpha_0$  Flight With Lateral Stick Alone. Pilot is Adapted to  $\alpha_0 = 10$  deg; aircraft is at  $\alpha_0 = 30$  deg.

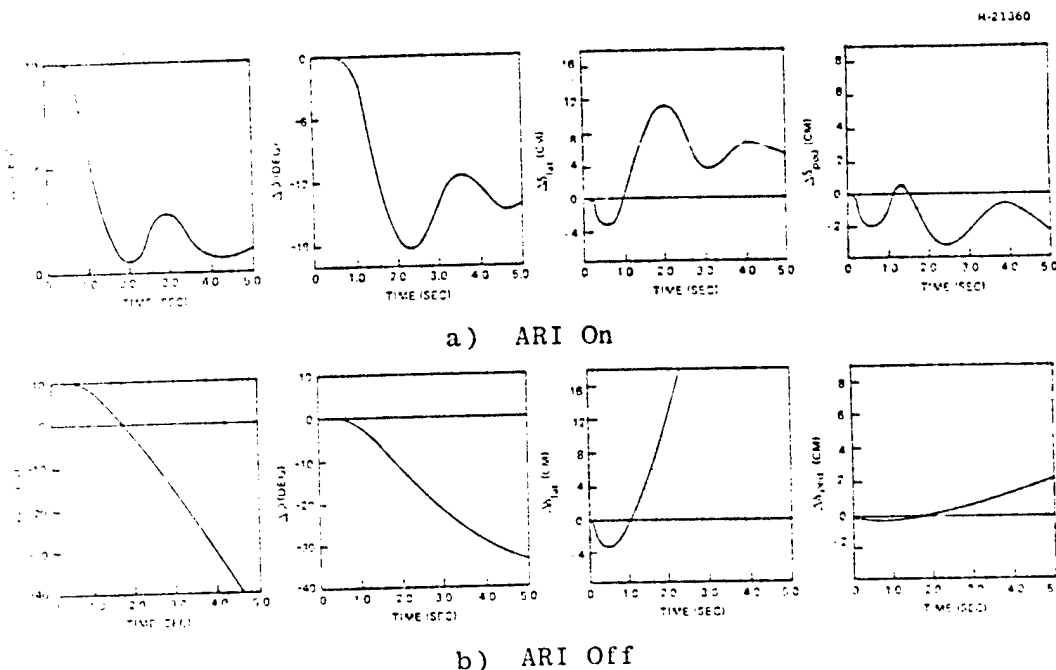


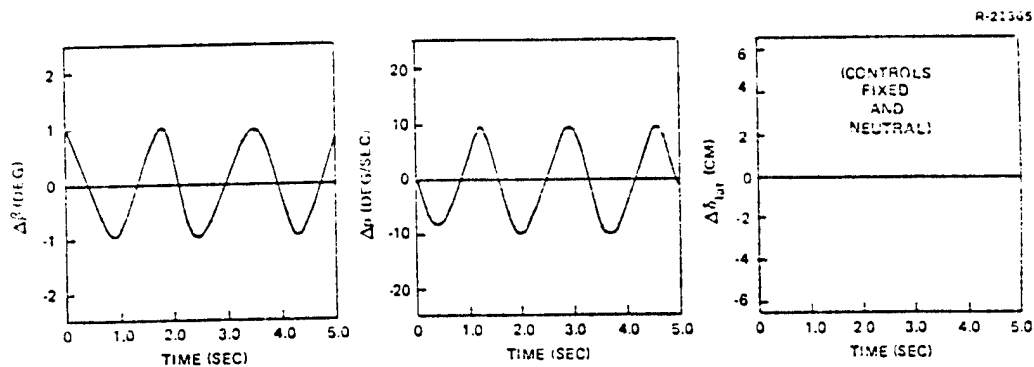
Figure 9. Use of Low- $\alpha_0$  Piloting Procedure in High- $\alpha_0$  Flight with Lateral Stick Plus Rudder Pedals

A direct indication of the destabilizing influence which a nonadapted pilot could have and which could lead to pilot induced oscillations is illustrated in Fig. 10. Figure 10a shows the natural rolling motion of this aircraft at  $\alpha_0 = 20$  deg, which is a consequence of a slightly unstable Dutch roll mode. In Fig. 10b, the ARI is on, the pilot model is adapted to  $\alpha_0 = 10$  deg flight, and there is an initial sideslip perturbation ( $\Delta\beta$ ) of one deg. If the pilot uses the low- $\alpha_0$  learned response to attempt to null  $\Delta\beta$  and  $\Delta p$ , he may inadvertently "pump" energy into the growing  $\Delta\beta$  oscillation through the aileron's adverse yaw. The result is a pilot-induced diverging oscillation whose characteristics would normally be associated with wing rock. The highly oscillatory nature of the control actions presumably is the result of limitations on the control rates which the pilot model is able to use.

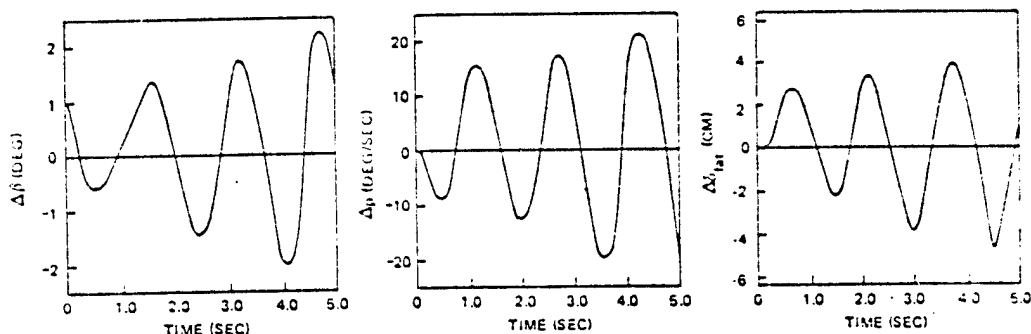
### LIMITS OF CONTROLLABILITY

For the reference aircraft and flight conditions, no pilot model algorithm instabilities are encountered in this





a) Open Loop Response



b) Piloted Response

Figure 10. Sideslip Response at  $\alpha_0 = 20$  deg with Lateral Stick Alone, ARI On, and the Pilot Model Adapted to  $\alpha_0 = 10$  deg

analysis, even when parameters of the pilot model are varied within accepted limits of neurophysiological capability. In other words, the model indicates that the pilot is capable of adapting his control strategy to stabilize the aircraft throughout the flight regime investigated here. Nevertheless, for other aircraft or flight conditions, the model could fail to exist, and this would be a direct indication that a human pilot could not provide effective control in a similar situation.

The lack of an optimal control pilot model for certain conditions has been shown indirectly in Refs. 6 and 7, and examples of the nonexistence of optimal control pilot models are shown explicitly in Ref. 4 for a scalar system with time constant,  $\tau_s$ . Reference 4 indicates that the pilot model regulator Riccati equation does not have a solution if  $2\tau_n \leq -\tau_s$ , where  $\tau_n$  is the neuromotor time constant. A comparison of this result with actual experimental results contained in Ref. 8 can be made. In Ref. 8,

values of  $\tau_s$  which first resulted in unstable conditions are determined. Values of  $\tau_n$  can be predicted as  $\tau_n = -\tau_s/2$ , since this is the stability boundary for the control-theoretic pilot model. Table 1 summarizes the results of the comparison. There is good agreement between values of  $\tau_n$  shown in Table 1 and known values of  $\tau_n$  (0.08 to 0.12 sec). The control-theoretic model has existence difficulties for the regulator if the system's unstable eigenvalues are greater than 5.0 ( $\tau_n \geq .10$ ). Experience with the pilot model estimator algorithm in Ref. 4 has shown that estimator existence difficulties can be encountered with system open-loop eigenvalues as low as 1.0. In this case, the pilot's attention allocation becomes the deciding factor for instability.

Table 1  
Experimental Stability Boundaries

Subject	Value of $\tau_s$ at Stability Boundary in Ref. 8, sec	Corresponding Optimal Control Model Predicted $\tau_n$ , where $\tau_n = -\tau_s/2$ , sec
ETP	-0.152	0.076
EWV	-0.169	0.085
MHS	-0.182	0.091
KED	-0.222	0.111

## CONCLUSION

This paper has illustrated several ways in which a control-theoretic pilot model can be useful for examining the stability of the pilot-aircraft system. It is shown that this system can be unstable for one of two reasons: either the aircraft itself is unstable and the pilot is incapable of providing stabilizing control actions or the pilot can destabilize an otherwise stable aircraft by inappropriate control actions. The latter case can result when the pilot does not adapt to changing flight conditions, applying control strategies which are suitable for one flight condition in a dynamically dissimilar situation. Although not detailed in this paper, the stability boundaries and simulated time histories established with the nonadapted pilot model are compatible with experimental results obtained from manned simulation and flight test.

An inverse interpretation of the results obtained with the adapted pilot model is that they specify what the pilot must do in a given dynamic condition to achieve well-behaved, stable aircraft response. Given the accepted physiological parameters contained in the design equations, the model illustrates what the well-motivated pilot can do to null flight path errors with available control effectors; hence, it identifies logical cues for compensatory control, and it graphically depicts control deflection histories which can be learned as adjuncts to precognitive control. It is concluded that the control-theoretic pilot model is a valuable tool for further analysis of aircraft handling qualities and for understanding the piloting skills which are necessary for maneuvering flight.

#### REFERENCES

1. Kleinman, D.L., Baron, S., and Levison, W.H., "A Control Theoretic Approach to Manned-Vehicle Systems Analysis," IEEE Trans. on Automatic Control, Vol. AC-16, No. 6, December 1971.
2. Kugel, D.L., "Determination of In-Flight Pilot Parameters Using a Newton-Raphson Minimization Technique," Proceedings of the Tenth Annual Conference on Manual Control, April 9-11, 1974.
3. Tse, E., "On the Optimal Control of Stochastic Linear Systems," IEEE Trans. on Automatic Control, Vol. AC-16, No. 6, December 1971.
4. Taylor, J.H., Broussard, J.R., Berry, P.W., and Stengel, R.F., "Analytical Techniques for High Angle-of-Attack Stability and Control," The Analytic Sciences Corp., TR-612-1 (to appear as an ONR Contractor Report).
5. Stengel, R.F. and Berry, P.W., "Stability and Control of Maneuvering High Performance Aircraft," The Analytic Sciences Corp., TR-587-1 (to appear as a NASA Contractor Report), January 1976.
6. Curry, R.E., Kleinman, D.L., and Hoffman, W.C., "A Model for Simultaneous Monitoring and Control," Proceedings of the Eleventh Annual Conference on Manual Control, May 21-23, 1975.
7. Kleinman, D.L., "Optimal Stationary Control of Linear Systems with Control Dependent Noise," IEEE Trans. Automatic Control, Vol. AC-14, No. 6, December 1969.

8. Pitkin, E.T. and Vinje, E.W., "Evaluation of Human Operator Aural and Visual Delays with the Critical Tracking Task," Proceedings of the Eighth Annual Conference on Manual Control, May 17-19, 1972.
9. Kleinman, D.L., "On an Iterative Technique for Riccati Equation Computations," IEEE Trans. Automatic Control (Correspondence), Vol. AC-13, February 1968.
10. Kleinman, D.L., "Numerical Solution of the State Dependent Noise Problem," IEEE Trans. Automatic Control (Correspondence), Vol. AC-21, June 1976.

## APPENDIX

### Mathematical Equations

Small perturbations in aircraft motion are approximated by the linear-time-invariant system

$$\Delta \dot{\underline{x}}(t) = F \Delta \underline{x}(t) + G \Delta \underline{u}(t) + \Delta \underline{w}(t) \quad (1)$$

where  $\Delta \underline{x}(t)$  represents the perturbation motion,  $\Delta \underline{w}(t)$  represents disturbance noise, and  $\Delta \underline{u}(t)$  is the pilot's compensatory control. The observations of the pilot are assumed to be

$$\Delta \underline{y}(t) = H \Delta \underline{x}(t-\tau) + D \Delta \underline{u}(t-\tau) + \Delta \underline{v}_y(t-\tau) \quad (2)$$

where  $\tau$  is the pilot time delay and  $\Delta \underline{v}_y(t)$  represents pilot observation noise. The pilot is assumed to choose  $\Delta \underline{u}(t)$ , when behaving optimally, by minimizing an infinite-time quadratic cost functional. This produces the control law

$$\Delta \dot{\underline{u}}(t) = -R_L \Delta \underline{u}(t) + C \Delta \hat{\underline{x}}(t) + \Delta \underline{v}_u(t) \quad (3)$$

where  $\Delta \underline{v}_u(t)$  represents pilot neuromotor noise. The matrix,  $C$ , is the pilot's feedback control strategy and the matrix,  $R_L$ , has the form

$$R_L = \begin{bmatrix} \frac{1}{\tau_{n1}} & 0 & 0 \\ 0 & \frac{1}{\tau_{n2}} & 0 \\ 0 & 0 & \frac{1}{\tau_{n3}} \end{bmatrix} \quad (4)$$

where the scalars,  $\tau_{ni}$ , are neuromotor time constants of human limbs. The vector,  $\Delta\hat{x}(t)$ , represents the pilot's estimate of the aircraft states based on observing  $\Delta y(t)$ . The pilot model observations can be restructured by using the Padé approximation to  $e^{-\tau s}$  in Eq. (2) as follows:

$$\Delta y(s) = \frac{2-\tau s}{2+\tau s} (H\Delta x(s) + D\Delta u(s) + \Delta v_y(s)) \quad (5)$$

Using Eq. (1), (3), and (5), the closed-loop pilot aircraft system can be shown to be

$$\begin{bmatrix} \Delta\dot{x}(t) \\ \Delta\dot{u}(t) \\ \Delta\dot{z}(t) \\ \Delta\dot{\hat{x}}(t) \\ \Delta\dot{\hat{u}}(t) \\ \Delta\dot{\hat{z}}(t) \end{bmatrix} = \begin{bmatrix} F & G & 0 & 0 & 0 & 0 \\ C & -R_L & 0 & C & 0 & 0 \\ H & D & \left[ \frac{2}{\tau} I \right] & 0 & 0 & 0 \\ \hline 0 & 0 & 0 & F_f & 0 & 0 \end{bmatrix} \begin{bmatrix} \Delta x(t) \\ \Delta u(t) \\ \Delta z(t) \\ \Delta\hat{x}(t) \\ \Delta\hat{u}(t) \\ \Delta\hat{z}(t) \end{bmatrix} + \begin{bmatrix} I & 0 \\ \hline -I & K \end{bmatrix} \begin{bmatrix} \Delta w(t) \\ \Delta v_u(t) \\ \Delta v_y(t) \\ -\Delta v_y(t) \end{bmatrix} \quad (6)$$

In Eq. (6),  $F_f$  is the closed-loop filter matrix and  $K$  is the Kalman filter gain. The states  $\Delta\hat{x}(t)$ ,  $\Delta\hat{u}(t)$ , and  $\Delta\hat{z}(t)$  are the estimation errors. The states  $\Delta z(t)$  are used to represent the delay after the Padé approximation. The matrix  $C$  does not change.

#### Assumptions

The pilot model outputs drive the aircraft through the matrix,  $G$ , which is adjusted to account for the ARI being on or off. The pilot is assumed to observe only the perturbation angles and angular rates of the aircraft. The pilot's observation noise-to-signal ratio is set at  $0.025\pi$  to account for scanning. The neuromotor noise-to-signal ratio is set at  $0.003\pi$ . The pilot is assumed to have a time delay of 0.2 sec and a neuromuscular time constant of 0.1 sec for each limb.

The state and control weighting matrix,  $Q$ , is adjusted until a reasonable set of mean-square covariance values of the aircraft states are obtained (Ref. 4). Present results indicate that closed-loop eigenvalues of the pilot model regulator may be relatively insensitive to  $Q$ . The adjustment of the control-rate weighting to maintain  $R_L$  in the optimal control pilot model appears to have a strong effect on relative weightings of states and controls. The control-rate weighting matrix,  $R$ , is found using the following new algorithm.

### Pilot Model Regulator Algorithm

The pilot model regulator Riccati equation is given by

$$0 = SF' + F'^T S + Q - SG'R^{-1}G'^T S \quad (7)$$

where R weights the control rate and Q weights the states and controls in a quadratic cost functional. The following substitutions are made:

$$F' = \left[ \begin{array}{c|c} F & G \\ \hline 0 & 0 \end{array} \right] \quad (8)$$

$$G' = \left[ \begin{array}{c} 0 \\ -I \end{array} \right] \quad (9)$$

$$S' = \left[ \begin{array}{c|c} S_{11} & S_{12} \\ \hline S_{21} & S_{22} \end{array} \right] \quad (10)$$

$$R_L = R^{-1}S_{22} \quad (11)$$

Solving for R in Eq. (11) and using Eq. (9), Eq. (7) can be restated as follows:

$$0 = SF' + F'^T S + Q - SG'(G'^T SG'R_L^{-1})^{-1} G'^T S \quad (12)$$

Using a procedure similar to that of Ref. 9, if an initial  $S_0$  can be found in the contraction mapping convergence sphere of Eq. (12), repeated substitution converges to the solution of Eq. (12). The following iterative scheme strives to achieve the solution:

- (1) Choose a positive definite  $R_0$  and solve for  $S_0$   
in

$$0 = S_0 F' + F' S_0 + Q - S_0 G' R_0^{-1} G'^T S_0$$

- (2) Continue with the following until some convergence criterion is satisfied (unless  $R_1$  does not become greater than  $R_2$ ):

$$R_K = G'^T S_{K-1} G' R_L^{-1}$$

$$C_K = R_K^{-1} G'^T S_{K-1} \quad K = 1, 2, \dots$$

$$F'_K = F' - G' C_K$$

$$0 = S_K F'_K + F'_K S_K + Q + C_K^T R_K C_K$$

(3) If  $R_1$  does not become greater than  $R_2$ , increase  $R_0$  and go back to (1).

(4) If  $R_0$  exceeds a maximum acceptable value, either  $R_0$  is larger than the stopping value or no solution exists.

The philosophy is to choose a stabilizing  $S_0$  that is greater than the solution  $S$ . Reference 10 provides a similar algorithm in which  $R_L = \sigma I$ , where  $\sigma$  is a scalar;  $R$  is therefore symmetric (Eq. (11)). The algorithm developed here requires only that  $R_L$  be an appropriate positive definite matrix; hence,  $R$  may be asymmetric.

ANALYSIS OF A MANNED ANTI-AIRCRAFT ARTILLERY (AAA)  
SYSTEM USING A PROPORTIONAL-INTEGRAL-DERIVATIVE (P-I-D)  
STRUCTURE OPTIMAL CONTROL GUNNER MODEL\*

By Anil V. Phatak and Kenneth M. Kessler

Systems Control, Inc. (Vt)  
Palo Alto, California

INTRODUCTION

An important problem in threat analysis is the evaluation and prediction of system performance of a manned anti-aircraft artillery (AAA) system. A systematic approach to manned threat quantification requires the development and integration of models for the weapon system, the target trajectory and the human gunner into a composite analysis algorithm that can be used for analytical and predictive purposes. The accuracy and, hence, the confidence in the analysis algorithm is clearly dependent on the fidelity of the models used to describe the individual subcomponents of the weapon system and most importantly the human gunner.\*\* There exist several computer simulation programs [1] for predicting aircraft attrition when exposed to various air defense systems. However, a serious weakness of existing anti-aircraft artillery attrition algorithms is in the submodels they utilize to describe human target tracking performance. Typically, fixed empirical models for the human gunner are used without adequate theoretical justification or systematic validation.

This paper describes the formulation and validation of a human gunner model suitable for inclusion into a general anti-aircraft artillery attrition algorithm. An optimal control theoretic model with a proportional-integral-derivative (P-I-D) controller structure is shown to describe the human gunner's input-output characteristics in the most effective manner. Experimental data from manned AAA simulations is used in formulating and validating the P-I-D optimal control gunner model. The gunner model includes target trajectory dependent parameters to account for the adaptive characteristics of the human controller, and allows for lower order internal (to the human) representations of the system dynamics (weapon system and target trajectory) to reflect realistic human psychophysical limitations. The model formulation is in terms of the tracking error and a sufficient number of its higher order derivatives. This output vector model formulation represents a significant

---

\* This work was supported by the 6570th Aerospace Medical Research Laboratory, Wright-Patterson Air Force Base, Ohio, under Contract No. F33615-76-C-5001.

\*\* In practice, as in the case described in this paper, there may be two gunners involved in the AAA task. However, the singular form is used here to indicate one or more gunners.



departure from the standard optimal control model [2] which requires explicit state vector representation of the plant/noise (weapon system/target trajectory in this case) dynamics. The P-I-D formulation in terms of the display output (tracking error) in the AAA task has improved mathematical properties over the standard representation (e.g., complete controllability with respect to the control input) and, in addition, has the advantage of being intuitively appealing and easily reconcilable with classical control theory methodology.

The human gunner response data used for developing and validating the gunner model was obtained from experiments conducted at the Aerospace Medical Research Laboratory (AMRL/EMT), WPAFB, Ohio. A brief description of the anti-aircraft artillery (AAA) simulation is given below to provide the reader with the necessary background to interpret the results presented in this paper.

#### THE ANTI-AIRCRAFT ARTILLERY TASK

The general configuration of the manned AAA simulation is shown in Figure 1. Two gunners, one each for the azimuth and elevation axes, observe the target aircraft through a gunsight with approximately a  $5^\circ$  field of view. The size of the displayed aircraft subtends approximately a constant  $0.5^\circ$  visual angle with respect to the gunner. Consequently, no range information can be obtained from the visual display. The gunsight dynamics were selected to be representative of an actual AAA weapon system. Rate-aided sight dynamics given by

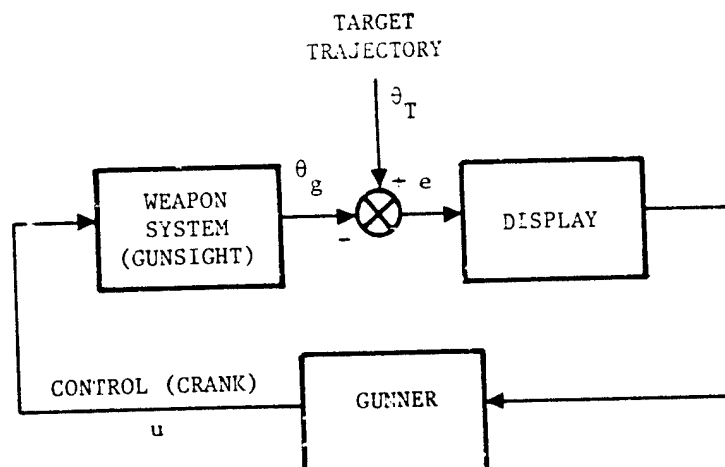


Figure 1. Configuration of the Manned AAA Simulation Experiments (Conducted at the AMRL, WPAFB, Ohio)

$$G(s) = \frac{\theta_g(s)}{u(s)} = \frac{64(s+1)}{s(s^2 + 12s + 64)} \quad (1)$$

were used for both the azimuth and elevation axes. The two axes are uncoupled and have two independent hand cranks for use by the human gunners. Target aircraft fly-bys of 45 s duration corresponding to various levels of difficulty were selected in a randomized fashion from a set of 4 trajectories as shown in Figure 2. The operators were sufficiently trained before tracking data was collected. Specifically, 15 runs per target trajectory were conducted. Time histories corresponding to the azimuth and elevation axes were recorded for target trajectory, gunsight position, gunsight rate and crank position and digitized at 25 Hz. These data were ensemble averaged across the 15 runs per team to yield the ensemble statistics of the recorded variables. Any representation for the human gunner must be capable of duplicating these response patterns according to some consistent functional model. The following paragraphs describe the development and validation of a human gunner model that is consistent with the AMRL experimental data and known human psychophysical characteristics and limitations.

#### HUMAN GUNNER MODEL DEVELOPMENT

Several different approaches toward human operator modeling have been proposed over the past thirty years. The human has been characterized as a digital controller, a finite-state machine, a describing function, and an optimal feedback controller. However, since its formulation about seven years ago, the standard optimal control model [2] has emerged as one of the most promising models for the study of complex man-in-the-loop control systems. The primary reason for the success of the optimal control theoretic model lies in the flexibility of the modeling technique in handling multivariable, multi-axes, multi-cue, nonlinear and nonstationary stochastic control situations within a well developed and general state variable optimal control (Linear-Quadratic-Gaussian) framework. The details of the standard optimal control model are documented extensively in the literature and, therefore, are not discussed in this paper. However, recent efforts have shown the utility of using a simplified version of the standard optimal control model [3-5].

The modified optimal control model [4] retains the basic hypothesis that a trained human operator in a precision control task behaves like an optimal estimator and controller in achieving the task objectives subject to his inherent psychophysical limitations or constraints. Specifically, the model assumes that: (1) the trained human operator has an internal state variable model relating the displayed variables to his controls, (2) the operator has a noisy perceptual channel and perceives the displayed variables (not rates) contaminated by observation noise, (3) the operator is a full state (internal model state) estimator and controller, and (4) the operator chooses a control law that minimizes a quadratic cost functional in terms

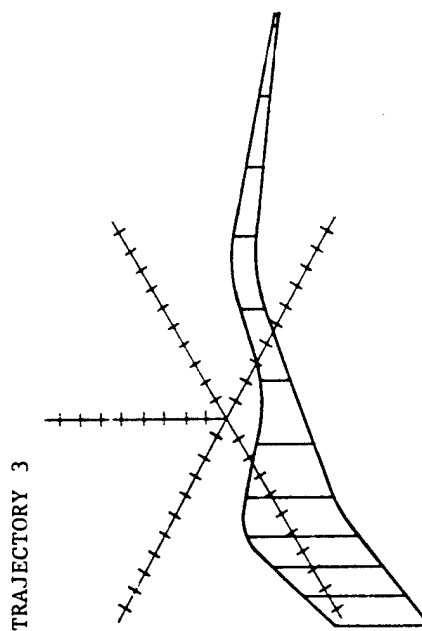
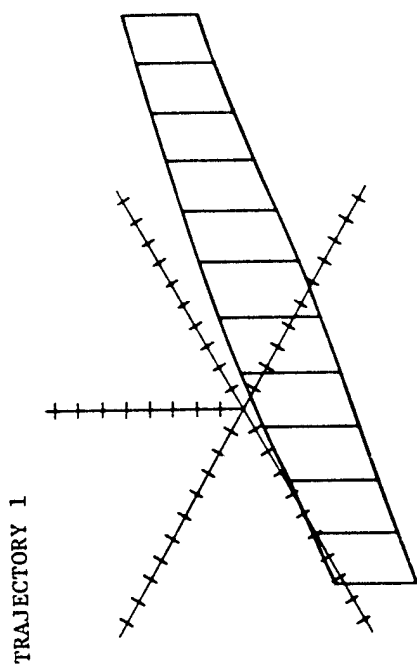
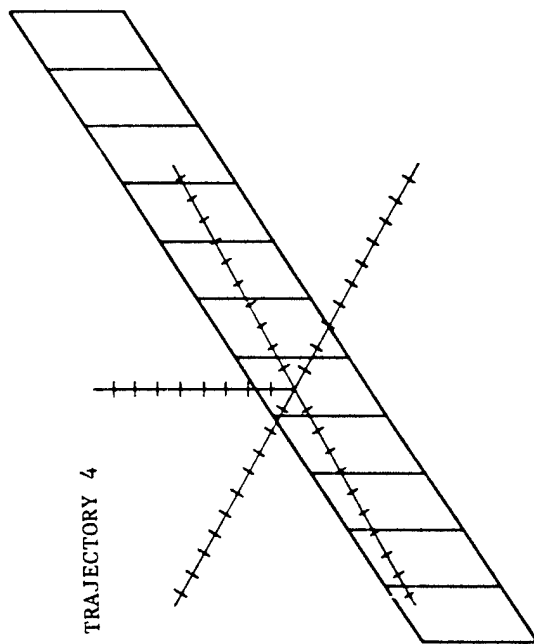
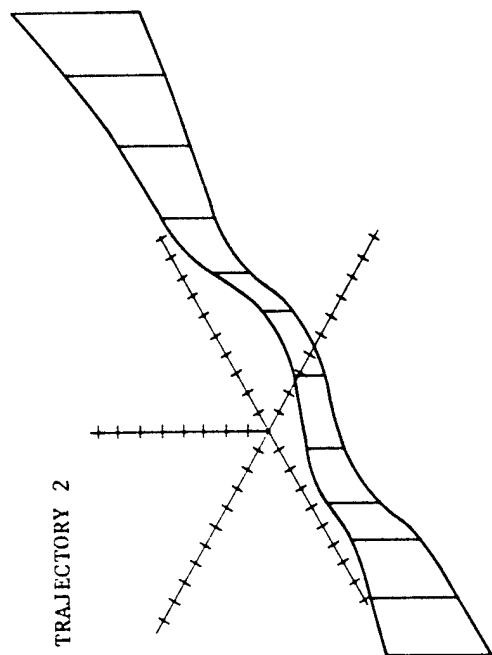


Figure 2. Perspective View of Four Target Trajectories

of the internal state vector, the control vector, and in some cases, higher order control derivatives ( $k^{\text{th}}$  derivative formulation). The resulting modified optimal control model [4] is as shown in Figure 3. The displayed state  $y(t)$  is corrupted by observation noise  $v_y(t)$  and the operator is assumed to perceive their sum. The Kalman filter utilizes the internal state variable model adopted by the human operator in estimating the internal states. The controller subsequently operates on this state estimate according to an optimal control law to yield the operator's control actions (inputs to the controlled system).

Inherent to this approach is the central assumption that the human has learned or developed an internal state variable model for the system from knowledge of his control (efferent) and perceived (afferent) variables. The standard approach is to assume that the human has explicit internal state variable models for the controlled system dynamics (gunsight), noise disturbances and command inputs (target trajectories). An alternative formulation is to assume that the human learns an input-output type of internal model relating the human's control variables to the displayed variables alone, requiring no explicit representation of the actual system dynamics or disturbance/command inputs. Such a model is feasible and preferable from an analytic as well as intuitive viewpoint for describing human gunner behavior in an AAA tracking task [5]. Under these assumptions, the resultant modified optimal control model (shown in Figure 3) has the familiar proportional-integral-derivative (P-I-D) controller structure which has improved mathematical properties over the standard representation and is easily reconcilable with classical control theory methods.

The objective of this paper is to show the applicability and utility of the P-I-D controller modified optimal control model [5] in describing and predicting human gunner response in AAA tracking tasks. The next few paragraphs give the details of the model structure formulation for the AAA task.

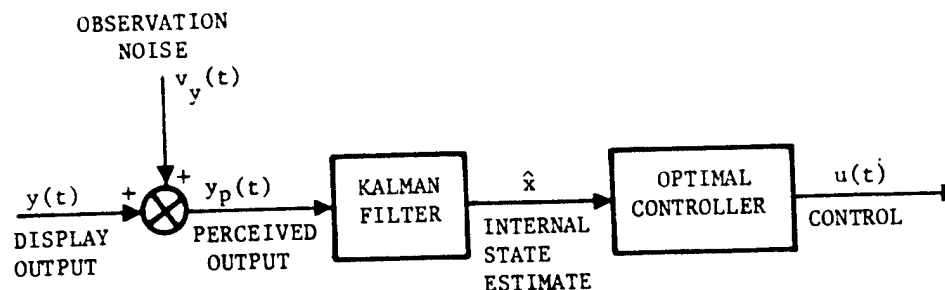


Figure 3. Modified Optimal Control Model for the Human Operator

### P-I-D Controller Formulation

The P-I-D controller formulation assumes that the human operator has an internal model for the AAA task in terms of the tracking error and its higher derivatives. However, before such a model can be formulated it is first necessary to have reasonable representations of the internal models for the target trajectories and gunsight dynamics implicitly assumed by the human operator. The following development assumes decoupled azimuth and elevation axes and is consistent with the AMRL experimental design. Extension to coupled multivariable situations should be feasible, although, with increased difficulty and complexity.

Internal model for target trajectory.- The actual target trajectories in azimuth and elevation coordinates are characterized by deterministic functions of time that are not finite polynomial representations. However, a reasonable internal model for the target motion that may be assumed by the human gunner is

$$\theta_T^{(k)}(t) = w(t); \quad W(t) = \text{Var}[w(t)] \quad (2)$$

where  $w(t)$  is colored noise with variance  $W(t)$  representing internal model uncertainty. For  $k=2$ , this model represents a constant velocity target assumption; for  $k=3$  a constant acceleration assumption, and so on. A piecewise constant velocity ( $k=2$ ) internal model for the target motion is shown to be adequate for this application.

Internal model for gunsight dynamics.- The actual sight dynamics as given by Eq. (1) have a zero at  $s=-1$ , a real pole at  $s=0$  and a pair of complex poles with a damping coefficient of 0.75 and a natural frequency of 8 rad/s. An appropriate internal model of the sight dynamics is

$$\frac{\theta_g}{u} = \frac{s+1}{s}$$

or

$$\dot{\theta}_g = u + \dot{u} \quad (3)$$

The complex poles can be neglected in the internal model in view of their high natural frequency (8 rad/s) and near critical damping ( $\zeta = 0.75$ ).

Internal model in terms of tracking error.- The tracking error is given by

$$e(t) = \theta_T(t) - \theta_g(t) \quad (4)$$

Then

$$\begin{aligned}\ddot{e} &= \ddot{\theta}_T - \ddot{\theta}_g \\ &= w - \ddot{u} - \dot{u}\end{aligned}$$

or

$$\ddot{e} = -\ddot{u} + w \quad \text{where} \quad \ddot{u} = \dot{u} + \ddot{u} \quad (5)$$

In state vector form

$$\dot{x} = Fx + G\ddot{u} + \Gamma w \quad (6)$$

$$y = Hx$$

where

$$x' = [e \quad \dot{e}]$$

$$F = \begin{bmatrix} 0 & 1 \\ 0 & 0 \end{bmatrix}; \quad G' = [0, -1]$$

$$\Gamma' = [0 \quad 1]; \quad H = [1 \quad 0] \quad (7)$$

represents the internal model used by the human operator for estimation and control.

Task cost functional.— The human gunner is assumed to behave as an optimal controller with respect to the cost functional

$$J(u) = E \left\{ \frac{1}{T_f} \int_0^{T_f} (e^2 + g\ddot{u}^2) dt \right\} \quad (8)$$

Optimal controller and Kalman filter.— The optimal control law is given by

$$\ddot{u}(t) = \ddot{u}(t) + \dot{u}(t) = -\lambda' \hat{x}(t) \quad (9)$$

where  $\hat{x}(t)$  is the output of a Kalman filter

$$\dot{\hat{x}} = (F - G\lambda' - KH)\hat{x} + Ky_p = F^+ \hat{x} + Ky_p \quad (10)$$

where

$$y_p = Hx + v_y = e + v_y ; \quad v_y(t) = \text{var}[v_y(t)] \quad (11)$$

$\lambda$  and  $K$  are obtained by solving the appropriate control and filter Riccati equations [6].

Human gunner transfer function.- For stationary assumptions, Eqs. (9)-(11) give the transfer function for the gunner model as

$$\frac{u(s)}{y_p(s)} = \frac{u}{\tilde{u}}(s) \frac{\tilde{u}}{y_p}(s) \quad (12)$$

$$= \frac{1}{s(s+1)} [-\lambda^*(sI - F^T)^{-1}K]$$

$$= \frac{1}{s(s+1)} \frac{2 \frac{\psi^2}{\omega_n^2} \left( \frac{\omega_n}{\psi} s + 1 \right)}{\left\{ \frac{s^2}{\omega_n^2} + \frac{2(.707)s}{\omega_n} + 1 \right\}} \quad (13)$$

where

$$\psi = \frac{1}{\sqrt{2}} \left( \frac{\gamma}{g} \right)^{1/4}$$

$$\omega_n = \gamma^{1/4} + \frac{1}{g^{1/4}}$$

$$\gamma = \frac{W}{V_y} \quad (14)$$

The block diagram for the stationary closed-loop manned AAA system is given in Figure 4.

The overall time-varying closed-loop manned AAA system can be simulated digitally by solving the vector-matrix differential equation

$$\dot{z} = \Lambda_1 z + \Lambda_2 (\theta_T + v_y) \quad (15)$$

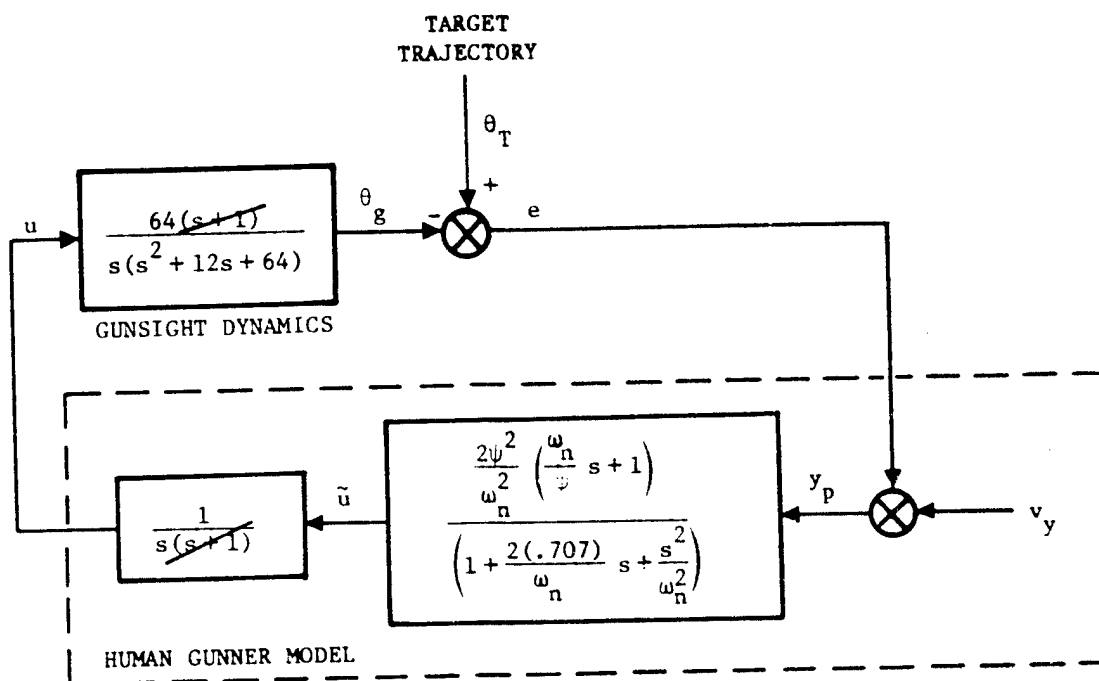


Figure 4. Stationary Closed-Loop Manned AAA System Block Diagram (Azimuth and Elevation)

where

$$z' = [\hat{x}, x_g, x_u]$$

where  $\hat{x}$  is obtained from Eqs. (10) and (11).

$$\dot{x}_g = F_g x_g + G_g x_{1u} \quad (16)$$

$$x'_g = [\theta_g, \dot{\theta}_g]$$

corresponds to the transfer function

$$\frac{\theta_g}{x_{1u}} = \frac{64}{s^2 + 12s + 64}$$

and

$$\dot{x}_u = F_u x_u + G_u \tilde{u} \quad (17)$$

$$x'_u = [x_{1u}, x_{2u}]$$



corresponds to the transfer function

$$\frac{x_{1u}}{\ddot{u}} = \frac{1}{s^2}$$

Thus, Eqs. (16) and (17) represent the equivalent transfer function between  $\theta_g$  and  $\ddot{u}$ , namely

$$\frac{\theta_g}{\ddot{u}} = \frac{\theta_g}{x_{1u}} \frac{x_{1u}}{\ddot{u}} = \frac{64}{s^2 + 12s + 64} \frac{1}{s^2} \quad (18)$$

The matrices  $\Lambda_1$  and  $\Lambda_2$  in Eq. (15) can be derived by appropriate augmentation of Eqs. (4), (10), (11), (16) and (17).

The human gunner model  $\left(\frac{u}{y_p}\right)$  has some interesting structural properties. The transfer function has a zero and four poles (two real poles at  $s=0$  and  $-1$  and a pair of complex poles with a damping coefficient of 0.707 and a natural frequency of  $\omega_n$ ). Note that the invariant pole at  $-1$  exactly cancels the zero in the gunsight dynamics. The values of  $\psi$  and  $\omega_n$  depend only upon the ratio  $W/V_y$ . Since the noise variances  $W$  and  $V_y$  are in general time dependent, the low frequency gain  $2\psi^2/\omega_n^2$ , the zero  $\psi/\omega_n$  and the complex pole natural frequency  $\omega_n$  are not expected to remain constant throughout the course of the tracking engagement. The migration of these varying parameters as well as their operating range is considered in greater detail in the next section. The most important property in this transfer function is the existence of a pole at  $s=0$  which guarantees zero steady state tracking error if the target trajectory maintains constant velocity. The open-loop man/gunsight dynamics have a type 2 structure for a constant velocity model for the target motion. Similarly, a type "k" open-loop man/gunsight transfer function is obtained for a constant (k-1)th derivative assumption on the target motion. Such a model structure implies integral feedback compensation--hence, the name proportional-integral-derivative (P-I-D) controller. The P-I-D controller structure, by definition, gives zero steady state tracking error for exact model assumptions on target dynamics. However, the tracking error deviates from zero whenever the internal target model assumptions do not match actual data.

While the transfer function representation is convenient from a structural point of view, Eq. (15) must be used to compute the (time-varying) mean, covariance, and perhaps a sample solution for the augmented state,  $z$ . This formulation of the P-I-D structure was used in a computer program called HOGUM (Human Operator Gunner Model) to match input-output human gunner tracking data in response to four target trajectories for both azimuth and elevation axes. Results of this validation process are discussed next.

## MODEL VALIDATION RESULTS

The key parameters of the P-I-D modified optimal control gunner model are: (1)  $k$  - the order of the human gunner's internal model of the target motion, (2)  $W(t)$  - the variance of the human gunner's uncertainty in the internal model for the target motion, (3)  $V_y(t)$  - the observation noise variance corresponding to the displayed tracking errors, and (4)  $g(t)$  - the control weighting in the human's cost functional. The values of these parameters over the tracking period are determined using HOGUM in an iterative fashion until model predictions of the ensemble means and standard deviations of the tracking errors match actual human gunner tracking error ensemble statistics obtained from data. The resulting functional model for the parameters that consistently describes the data for the four target trajectories (azimuth and elevation) is as follows:

$$k = 2$$

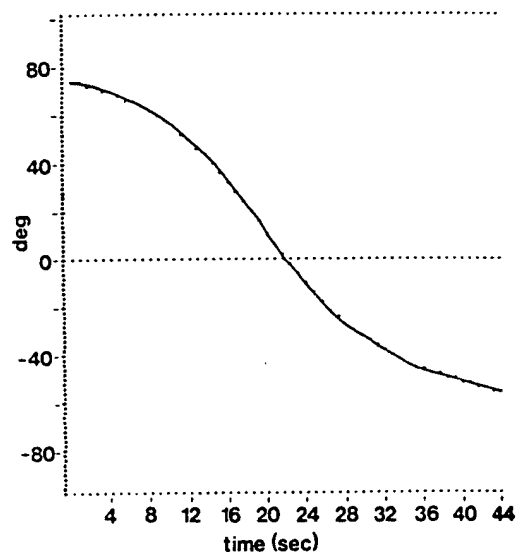
$$W = \left[ \frac{1}{T_f} \int_0^{T_f} \{\ddot{\theta}_T(t)\}^2 dt \right]^{1/2}$$

$$V_y(t) = .000375 (10) |\ddot{\theta}_T(t)| \quad (19)$$

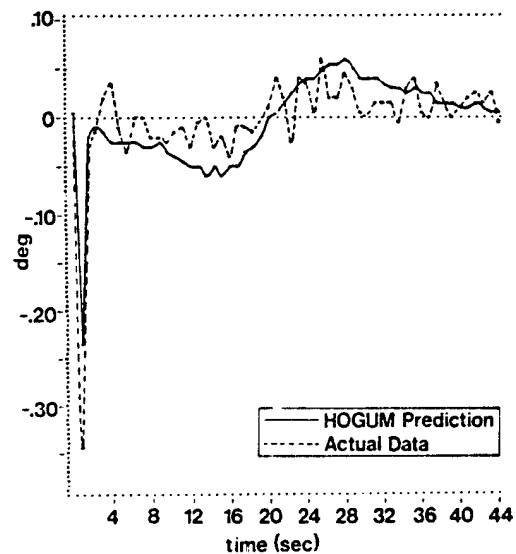
$$g \leq 10^{-4}$$

The parameter functional model is extremely simple and is easily reconcilable with known human psychophysical limitations and constraints. Moreover, the "tuning" process is only a function of the target trajectory. This mechanization allows for predicting tracking performance while performing a sensitivity analysis on various target trajectories and weapon systems parameters. Model predictions of the tracking errors and control inputs in azimuth and elevation coordinates are compared with data in Figures 5-8. Both the tracking error and control crank predictions using HOGUM compare very favorably with actual gunner response data. (The crank predictions match almost identically. Only trajectories 2 and 3 in elevation show any discernible deviation.)

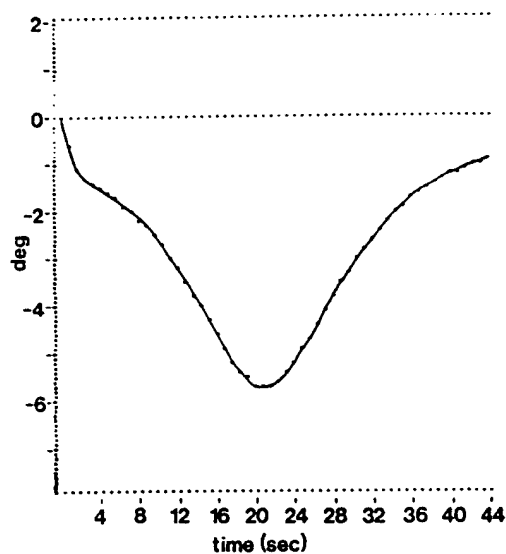
Trajectory 3 (elevation) indicates a sharp spike in tracking error near 28.5 seconds. This is a direct result of a sudden slope change in the trajectory caused inadvertently in the mechanization of the AAA simulation. It is interesting, however, that HOGUM predicts the same type of discontinuity in the error. This is because the actual target motion is directly utilized as input to HOGUM instead of a numerical approximation of this function.



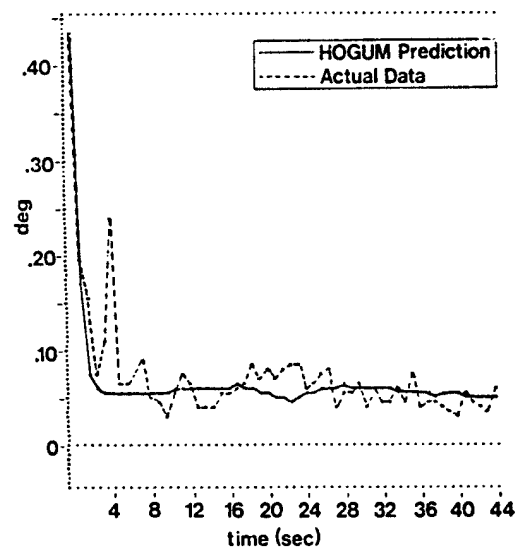
(a) Target Trajectory



(c) Mean Tracking Error

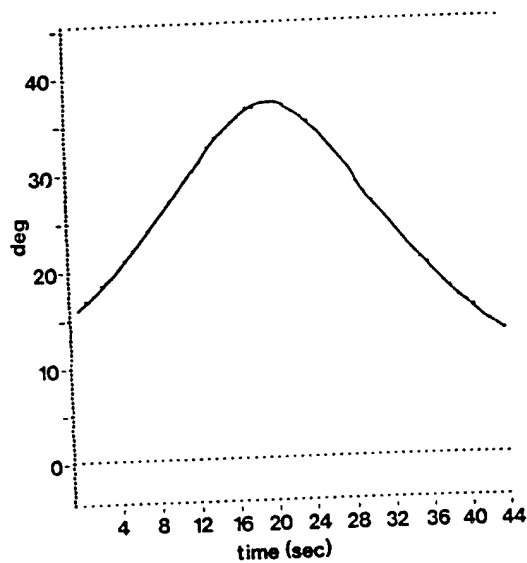


(b) Crank Position

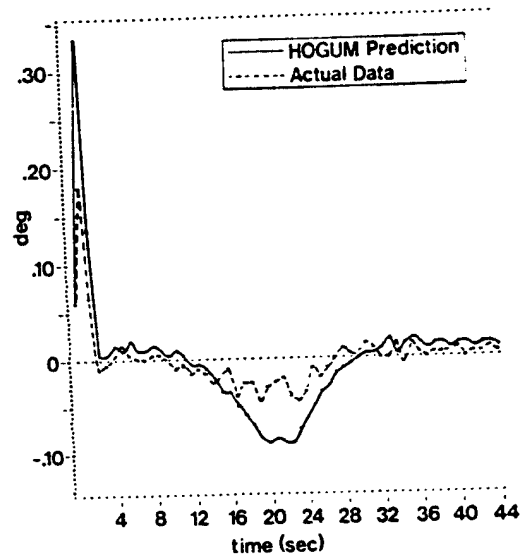


(d) Standard Deviation of Error

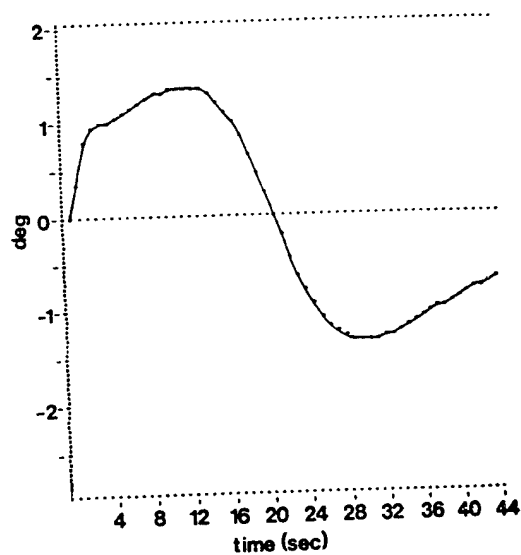
Figure 5a. Trajectory 1 - Azimuth (HOGUM Predictions and Data)



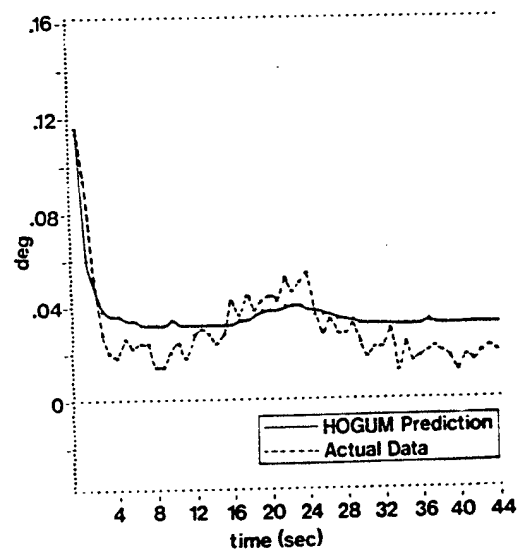
(a) Target Trajectory



(c) Mean Tracking Error

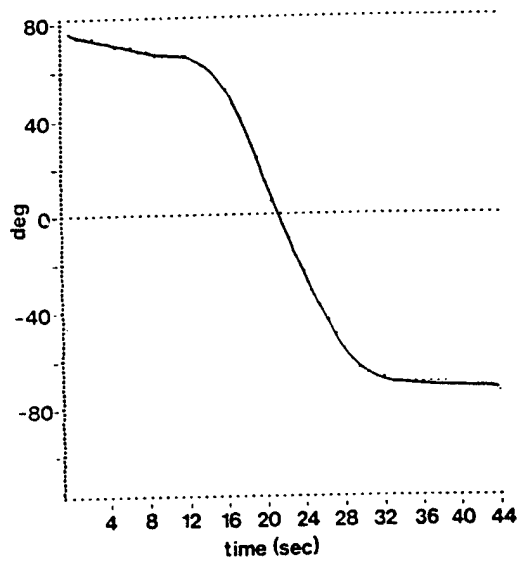


(b) Crank Position

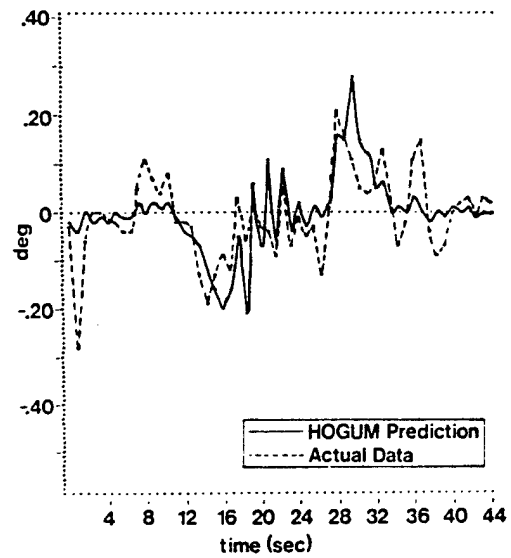


(d) Standard Deviation of Error

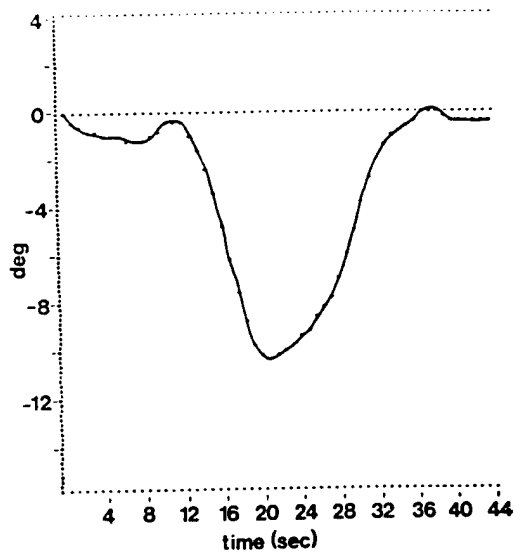
Figure 5b. Trajectory 1 - Elevation (HOGUM Predictions and Data)



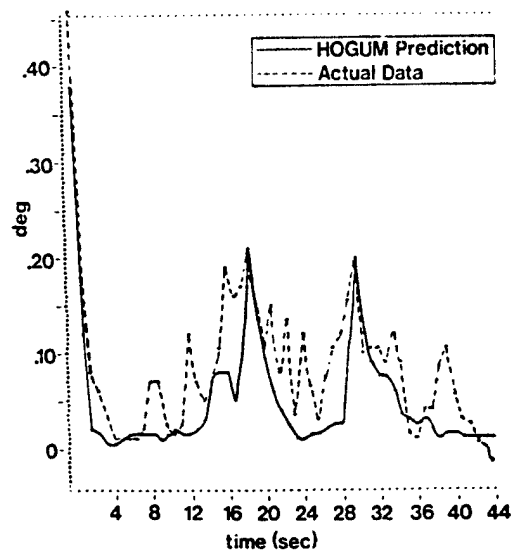
(a) Target Trajectory



(c) Mean Tracking Error

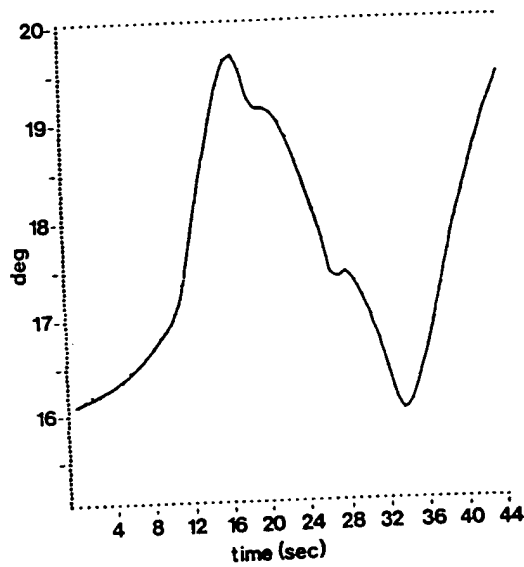


(b) Crank Position

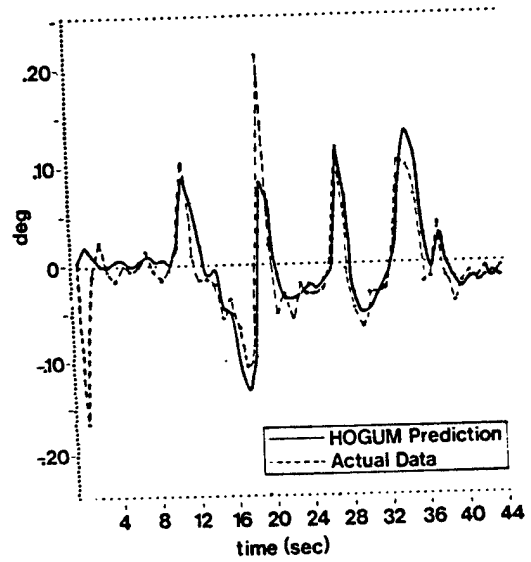


(d) Standard Deviation of Error

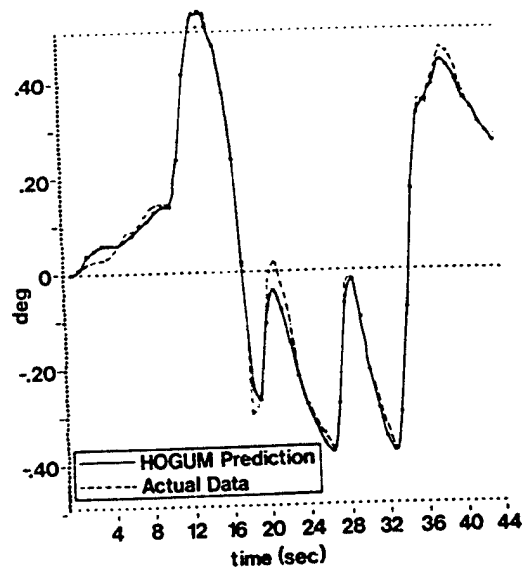
Figure 6a. Trajectory 2 - Azimuth (HOGUM Predictions and Data)



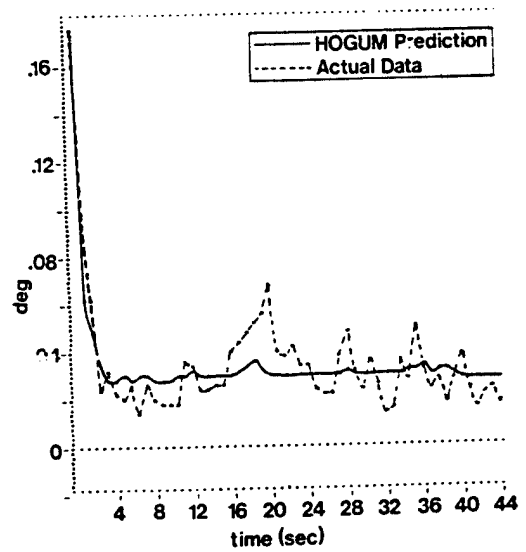
(a) Target Trajectory



(c) Mean Tracking Error

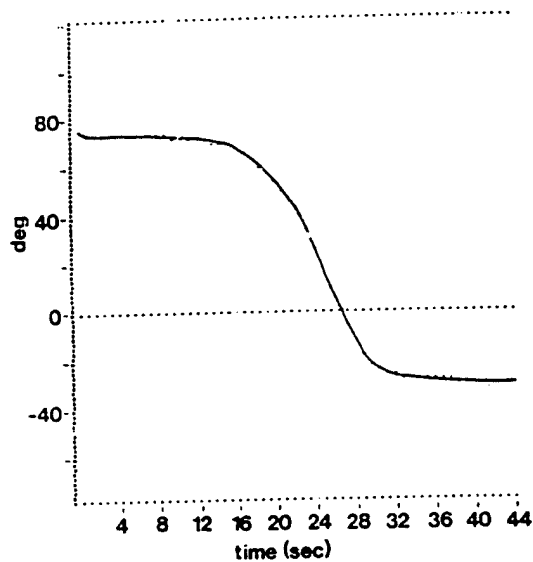


(b) Crank Position

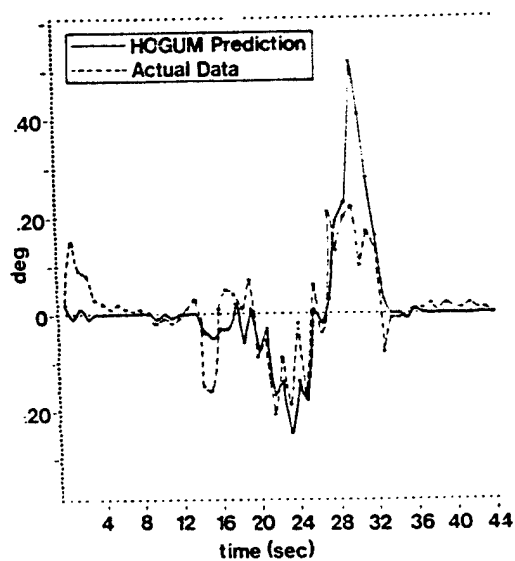


(d) Standard Deviation of Error

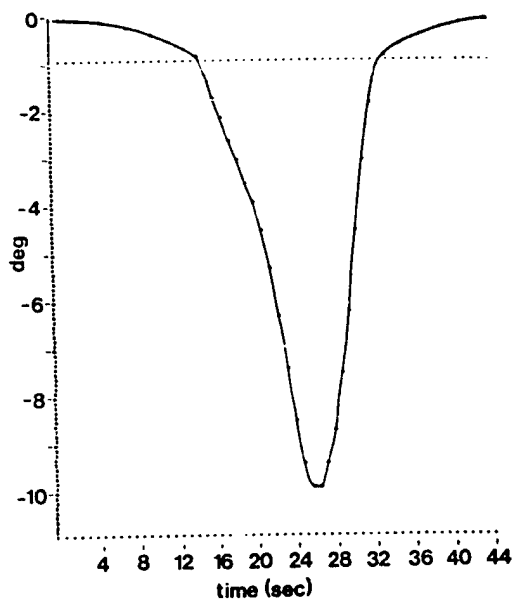
Figure 6b. Trajectory 2 - Elevation (HOGUM Predictions and Data).



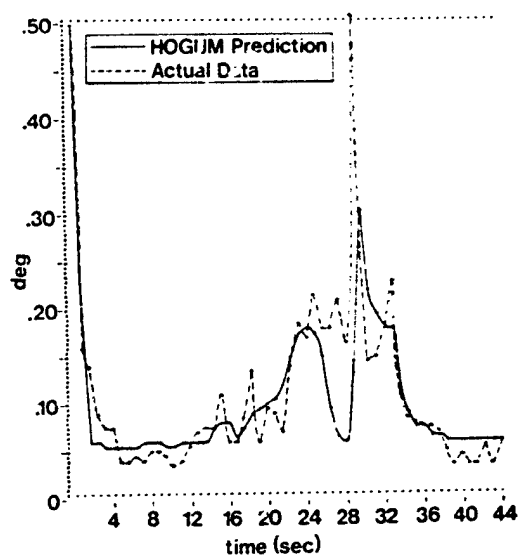
(a) Target Trajectory



(c) Mean Tracking Error

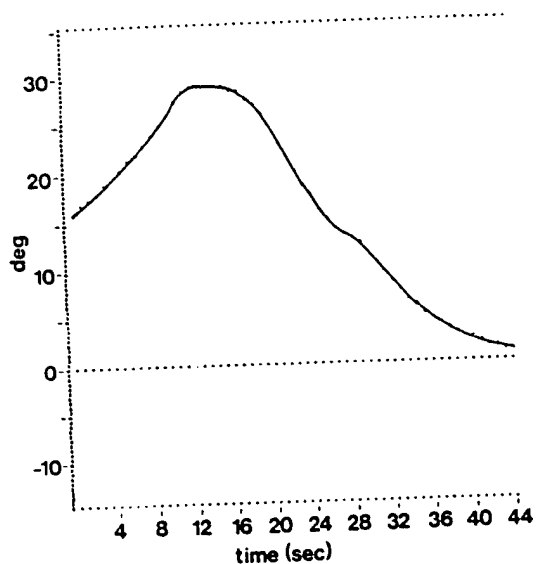


(b) Crank Position

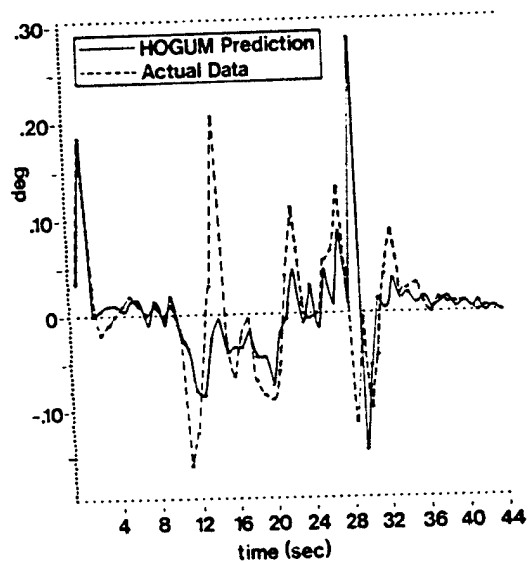


(d) Standard Deviation of Error

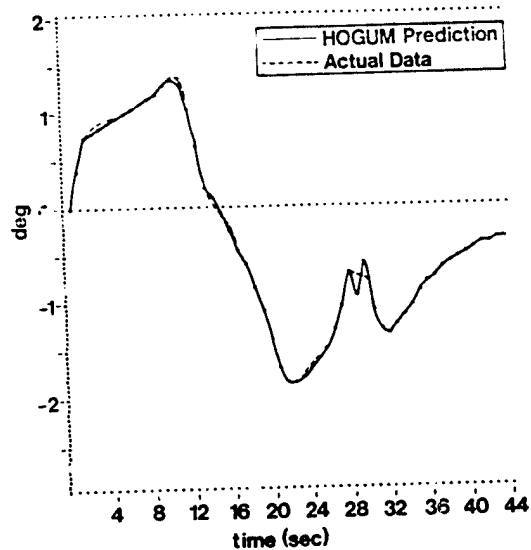
Figure 7a Trajectory 3 - Azimuth (HOGUM Predictions and Data)



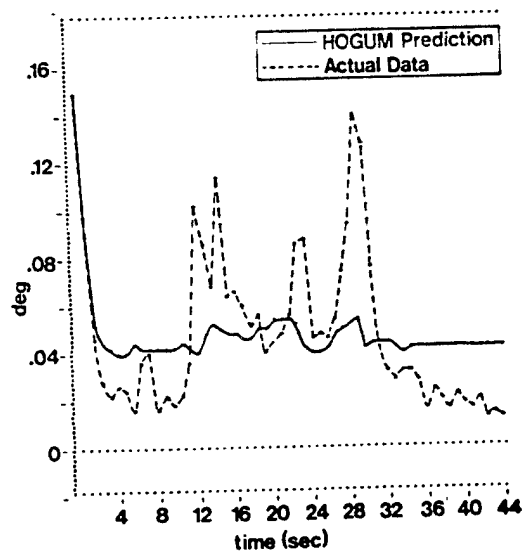
(a) Target Trajectory



(c) Mean Tracking Error



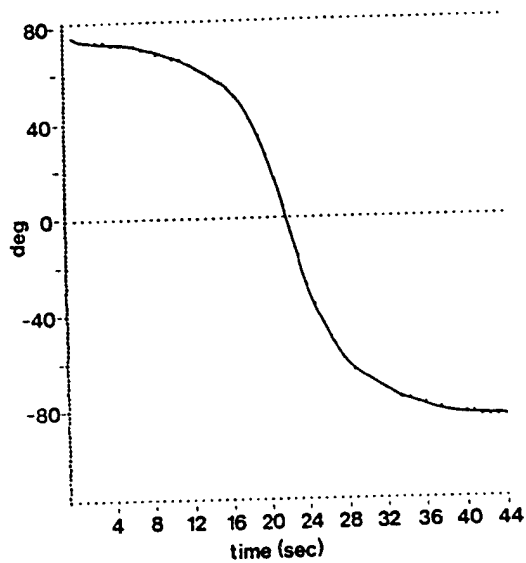
(b) Crank Position



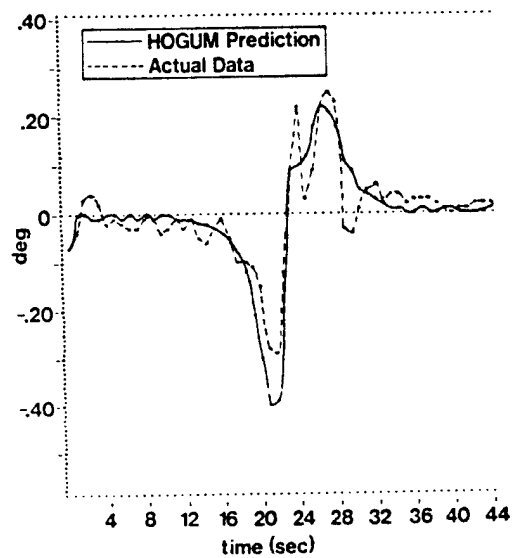
(d) Standard Deviation of Error

Figure 7b. Trajectory 3 - Elevation (HOGUM Predictions and Data)

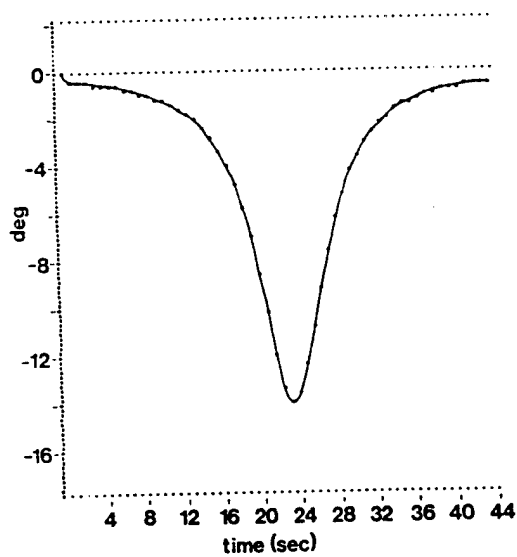




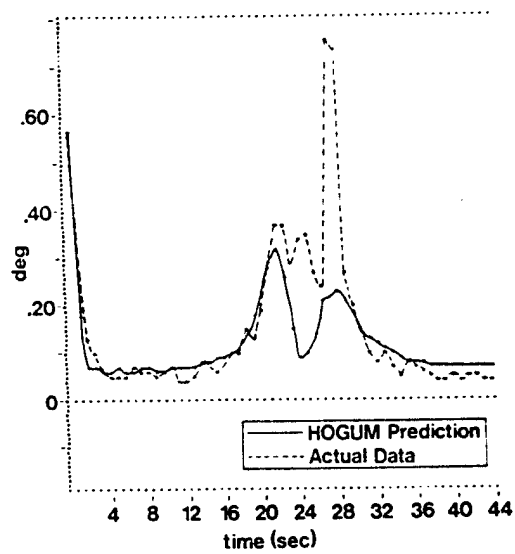
(a) Target Trajectory



(c) Mean Tracking Error

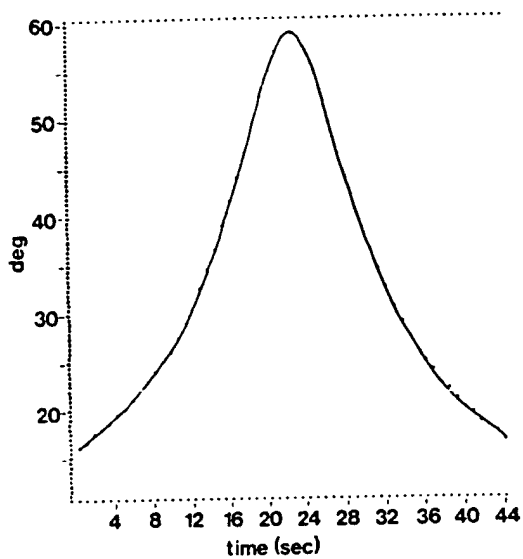


(b) Crank Position

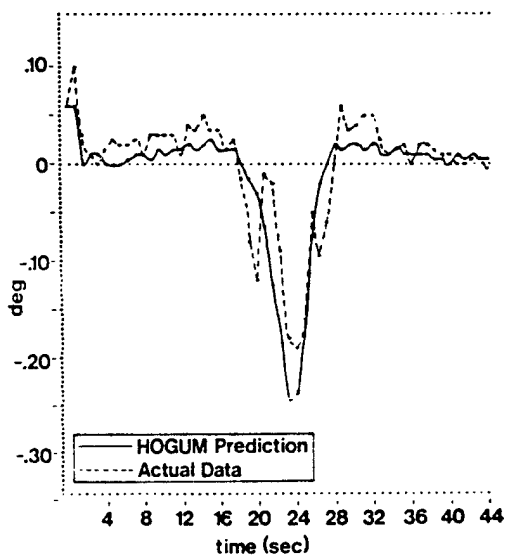


(d) Standard Deviation of Error

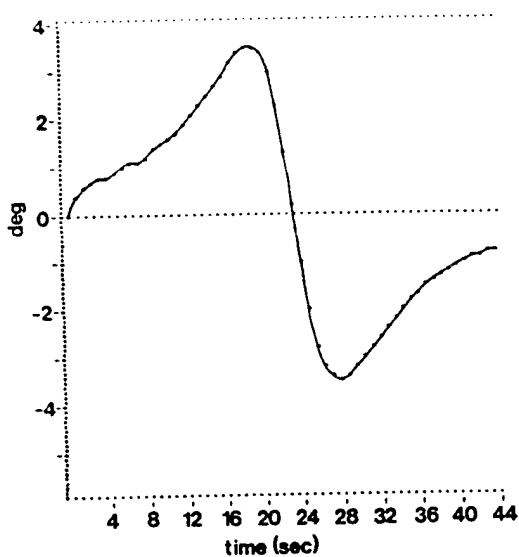
Figure 8a. Trajectory 4 - Azimuth (HOGUM Predictions and Data)



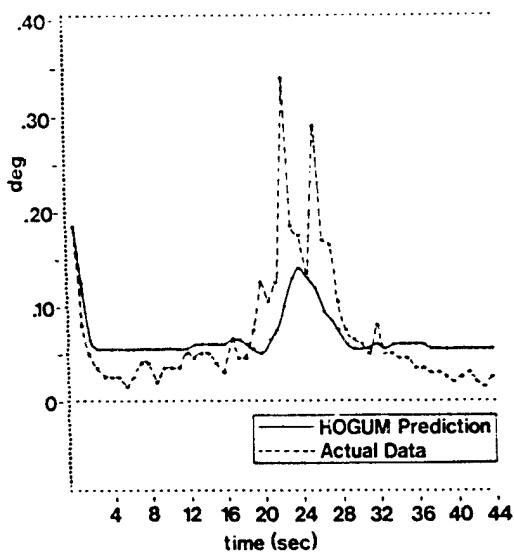
(a) Target Trajectory



(c) Mean Tracking Error



(b) Crank Position



(d) Standard Deviation of Error

Figure 8b. Trajectory 4 - Elevation (HOGUM Predictions and Data)

The general methodology used in this model tuning process is presented in the following paragraphs. It results in the identification of a functional model for the selection of HOGUM parameters for the four different target trajectories. Note that the analysis here is limited to independent or uncoupled azimuth and elevation axes. Extension to coupled gunsight dynamics should follow, although, with greater complexity.

Selection of k: The value of  $k$  assigns a structure to the internal model of the target motion adopted by the human gunner. For example,  $k=2$  implies a constant velocity target motion,  $k=3$  a constant acceleration assumption and so on. Under steady-state conditions, the value of  $k$  also defines the "type" of the gunner transfer function model given by Eq. (12). A value of  $k=2$  gives a type 1 gunner transfer function (i.e., one pole at  $s=0$ ) as given by Eq. (13);  $k=3$  gives a type 2 gunner model, and in general for a rate-aided gun,  $k=m$  implies a type  $(m-1)$  gunner transfer function. A human operator in a closed-loop tracking task is able to track a constant velocity (within reasonable limits) target motion with zero steady-state mean error (reasonably short setting time). On the other hand, it is not always possible for a human to track an accelerating target with zero mean tracking error. These observations indicate a value of  $k=2$  as being consistent with known human psychophysical limitations and, therefore, is used as the standard value in the gunner model.

Selection of  $W(t)$ :  $W(t)$  reflects the uncertainty in the human gunner's mind about the accuracy of his internal model for the assumed target motion. Target trajectories in an AAA task do not satisfy the constant velocity assumption at all times. Thus  $W(t)$  should be approximately proportional to  $\{\ddot{\theta}_T(t)\}^2$ , the square of the target acceleration. However, it seems unreasonable to assume that the human gunner learns a time-varying internal representation for the target model uncertainty  $W(t)$ . A sensitivity analysis of  $W(t)$  using the HOGUM program indicates that a constant value of  $W(t) = W$  throughout the tracking period is reasonable in describing gunner response data. A value of

$$W = \left[ \frac{1}{T_f} \int_0^{T_f} \ddot{\theta}_T^2(t) dt \right]^{1/2}$$

is chosen (RMS value of  $\ddot{\theta}_T(t)$ ).

Selection of  $V_y(t)$  and  $g(t)$ : Given  $k=2$  and fixed  $W$  as above, there remain only two free parameters with which to tune the HOGUM program outputs-- $g(t)$  and  $V_y(t)$ . The gunner model transfer function in Eq. (13) indicates that the model parameters--namely the low frequency gain, the zero and the pair of complex poles--depend only upon  $g$  and  $(W/V_y)$ . Note that it is not mathematically proper to entertain the concept of transfer functions for time-varying systems. However, it is still possible to get considerable

insight into the gunner model characteristics using quasi-stationary or frozen-point analysis arguments. Figure 9 shows the migration of the low frequency gain, zero and the natural frequency  $\omega_n$  of the complex poles with respect to  $g$  and the ratio  $(W/V_y)$ . As previously mentioned, the pair of complex poles with a damping coefficient of 0.707 and a natural frequency  $\omega_n$  could be considered to be analogous to the "so-called" neuromotor time constant  $[1/(T_N s + 1)]$  referred to in human modeling literature [2]. A value of  $\omega_n \geq 10$  rad/s would be adequate from the neuromuscular system viewpoint. Figure 9 shows that  $\omega_n$  is quite insensitive to variations in  $(W/V_y)$  and depends primarily on the value of  $g$ . A value of  $g \leq 0.0001$  results in  $\omega_n \geq 10$  rad/s. Hence  $g = 0.0001$  is adopted as the constant control term weighting in the cost functional given by Eq. (8).

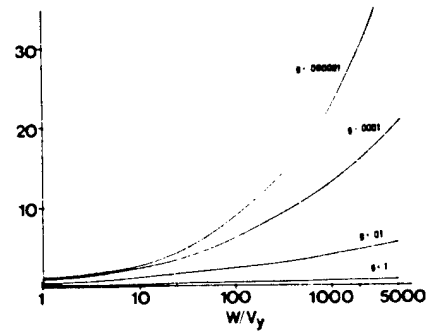
The only remaining parameter to be tuned is  $V_y(t)$  - the observation noise covariance. Tracking error data in Figures 5-8 reveals some interesting characteristics. The mean error is nearly zero and the standard deviation constant for segments of the target trajectories which agree with the human's internal model assumption of constant velocity motion. This is equivalent to constant  $g$ ,  $W$  and  $V_y$ . However, both the mean and the standard deviation of the error deviate from their nominal values between target trajectory segments satisfying the constant velocity assumptions. Data in Figures 5-8 show that both the mean and the standard deviation of the tracking error  $e(t)$  relate monotonically with  $|\ddot{\theta}_T|$ . A similar relationship holds with respect to  $V_y$  in steady state. Thus  $V_y(t)$  should vary monotonically with  $|\ddot{\theta}_T(t)|$ . The functional model

$$V_y(t) = .000375 (10)^{|\ddot{\theta}_T(t)|}$$

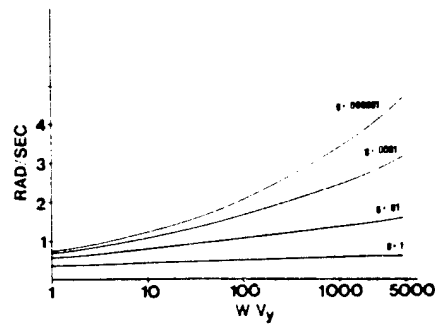
gives the best fit of the model predictions to ensemble data as seen in Figures 5-8. The functional model for  $V_y(t)$  takes on an intuitive meaning if one observes that

$$10 \log V_y(t) \left( = V_y(t) \Big|_{\text{dB}} \right)$$

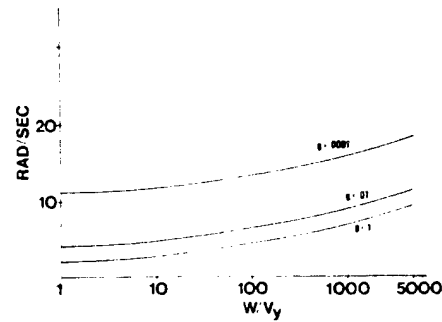
is proportional to  $|\ddot{\theta}_T(t)|$ , which indicates that the observation noise in decibels is proportional to  $|\ddot{\theta}_T|$ . The changing value of  $V_y(t)$  in conjunction with the actual target trajectory (input to HOGUM) deviating from constant velocity motion, causes error transients in both the mean and standard deviation.



(a) Low Frequency Gain,  $\frac{2\psi^2}{\omega_n^2}$



(b) Zero Location,  $\frac{\omega_n}{\psi}$



(c) Natural Frequency,  $\omega_n$

Figure 9. Characteristics of  $\left(\frac{\tilde{u}}{y_p}\right)$ ; Human Gunner Model Transfer Function  
(Stationary Assumptions)

Table 1 indicates the range of  $\gamma$  values  $\left(\gamma = \frac{W}{V_y}\right)$  corresponding to each of the four trajectories for both azimuth and elevation. Typically, the smaller values of  $\gamma$  occur near crossover (when  $\ddot{\theta}_T(t)$  obtains maximum values). From Figure 9, it is possible to determine the corresponding range of values for the low frequency gain, the zero location and the natural frequency of the transfer function representing the human operator.

The functional model discussed above is not claimed to be unique. However, it does reflect reasonable assumptions on the known psychophysical characteristics of the human operator.

Table 1  
Range of  $\gamma$  Values  $\left(\frac{W}{V_y}\right)$

TRAJECTORY	AZIMUTH	ELEVATION
1	250-50	27-15
2	2700-175	13-8
3	2100-350	160-100
4	4000-200	960-275

#### CONCLUDING REMARKS

The P-I-D controller model has been shown to accurately predict human tracking behavior. This model can be used as a baseline to determine the effects on human performance due to differing environmental conditions, target motions, countermeasure tactics as well as sight system parameters. In addition, various system configurations can be incorporated into this model with only minimal modification. The computer program, HOGUM, is fast, efficient and modular, and, as such, can be effectively used to determine performance sensitivity to various system parameters.

It is to be noted that these functional relationships have been validated using four target trajectories. Due to the highly adaptive nature of the human operator, these relationships might require modification for extreme values of  $\ddot{\theta}_T(t)$ . Additional trajectories would be required to validate the model in such cases.

The P-I-D gunner model as represented by HOGUM can be used to describe human gunner performance in general purpose air defense evaluation programs such as the AFATL P001 [1]. Extensions of this model to include coupled gun-sight dynamics, two-axis control cross coupling and task interference effects, and on-carriage tracking (using some form of fire control system) is recommended to generalize the capability of HOGUM for evaluating different AAA weapon systems.

#### ACKNOWLEDGEMENTS

The authors wish to thank Dr. C.N. Day, Capt. J. Hull, Dr. D. Reppeger and Mr. W. Summer of the 6570th Aerospace Medical Research Laboratory, WPAFB, Ohio, for their continued support throughout the entire project effort. The assistance of Mr. R. Ducot of SCI (Vt) was invaluable in developing and implementing HOGUM, and is gratefully acknowledged.

#### REFERENCES

1. J. Severson and T. McMurchie, "Antiaircraft Artillery Simulation Computer Program - AFATL Program P001 - Vol. I, User Manual," Developed by Air Force Armament Laboratory, Eglin AFB, Florida; Published under the Auspices of the Joint Aircraft Attrition Program, Advanced Planning Group.
2. D. Kleinman, S. Baron, and W.H. Levison, "A Control Theoretic Approach to Manned-Vehicle Systems Analysis," IEEE Trans. Automatic Control, AC-16, pp. 824-832, 1971.
3. S. Baron and W.H. Levison, "A Manual Control Theory Analysis of Vertical Situation Displays for STOL Aircraft," NASA CR-114620, April 1973.
4. A. Phatak, H. Weinert, I. Segall and C. Day, "Identification of a Modified Optimal Control Model for the Human Operator," Automatica, Vol. 12, pp. 31-41, 1976.
5. A.V. Phatak and K.M. Kessler, "Evaluation of Optimal Control Type Models for the Human Gunner in an Anti-Aircraft Artillery (AAA) System," Eleventh Annual NASA Conf. on Manual Control, NASA/Ames Research Center, Moffett Field, CA 94035, May 1975.
6. A.E. Bryson, Jr., and Y.C. Ho, Applied Optimal Control, John Wiley and Sons, 1975.

Analysis of Controls and Displays for a  
Terminal Controlled Vehicle

by

William H. Levison and Sheldon Baron  
Bolt Beranek and Newman Inc.  
Cambridge, Massachusetts

The optimal-control pilot/vehicle model was applied to the analysis of a Terminal Controlled Vehicle in approach and landing. Approach tracking errors and landing statistics were predicted for two control configurations (attitude control wheel steering and velocity control wheel steering) and for two display conditions (with and without electronic presentation of a perspective runway). Steady-state analysis was performed to explore performance-workload tradeoffs for these control/display combinations, and time-varying analysis was performed to obtain approach and landing statistics in the presence of zero-mean turbulence. The results of this analysis were compared with experimental data obtained in fixed-base simulations performed at NASA Langley Research Center.



A MODEL OF THE EMG-  
TORQUE-MOVEMENT RELATIONSHIPS FOR  
KNEE EXTENSION\*\*

By

Etienne Dombre  
Laboratoire d'Automatique de Montpellier  
U.S.T.L., Place E. Bataillon,  
34060 MONTPELLIER CEDEX, France\*

George A. Bekey, Ph.D.  
Department of Biomedical Engineering  
University of Southern California\*

Jacquelin Perry, M.D.  
Chief, Pathokinesiology Service  
Rancho Los Amigos Hospital, Downey, California

ABSTRACT

This paper describes work currently in process at Rancho Los Amigos Hospital on further clarification of the quantitative relationship between the electrical activity of a muscle and the movement it produces. The usefulness of such a relationship is obvious for rehabilitation purposes.

This research is based on the use of intramuscular wire electrodes to provide specific signals from each muscle at a given joint. The output of the system is the angular position of the moving limb. This input-output relationship is represented by a dynamic mathematical model which includes the length-tension and velocity-tension relationships of the actuating muscles as well as a mechanical model of the knee joint. Methods for quantifying and validating the model are described.

Our objective is to build a model which is valid even near the limits of the range of motion when various conditions of external constraints are applied and when different modes of contraction are considered.

\*\*This work was supported in part by the Rehabilitation Services Administration, DHEW, under Grant #RD-23-P-55442.

\*Currently at Rancho Los Amigos Hospital, Downey, California

## INTRODUCTION

Since the work of LIPPOLD (1952), (reference #9) it is known that the EMG - tension relationship in isometric situations is linear (although, some disagreement exists concerning the precise value of the constant of proportionality, as shown by LINDSTROM et al., 1974) (reference #8). But, problems arise when the same relationship has to be described in the presence of movement. Generally, these studies are performed with constraints of constant velocity or of constant loading as in past studies at the kinesiology laboratory at Rancho Los Amigos Hospital (PERRY et al., 1974) (reference #11). Such limitations lessen the clinical usefulness of the results since no one knows exactly how to handle the information content of the EMG signal produced by the muscle during free motion.

Among the large number of muscle models which have been proposed since HILL's classical work (1938) (reference #6) only a few attempts have been made to build mathematical models of the EMG-muscle force relationship in the presence of movement.

GOTTLIEB and AGARWAL (1971), (reference #5) published a model which relates EMG and force for the anterior tibialis muscle during isometric effort. Basically, the model consists of series and parallel elastic elements, a parallel dissipative element and an active contractile element. The contractile element was represented by a first order filter acting on the raw EMG signal picked up by the surface electrodes. The model responses match measured forces very well during repeated isometric plantar flexions. A similar model was used to simulate the EMG-force relation in the human triceps brachii by COGGSHALL (1968), (reference #4) and in the human gastrocnemius and soleus muscles by AGARWAL et al., (1971), (reference #1). Apparently, these models have not yet been applied successfully to non-isometric situations.

An alternative approach to relating EMG and force has been based on summing the electrical activity and twitch produced by single motor units using an appropriate recruitment hypothesis. OSTROY et al., (1970) (reference #10) then BRODY et al., (1974) (reference #3) synthesized such a model from an isometric study of the cat flexor hallucis longus muscle and of the human biceps brachii respectively. More recently, WANI and GUHA (1975), (reference #14) obtained EMG-motion characteristics for elbow flexion by a similar approach. As far as we know, this is the only dynamic model which is not limited to isometric cases. However, models based on motor-unit recruitment incorporate so many assumptions that their validity is questionable.

This paper deals with a model of the EMG-tension-position relationships in the knee joint without restriction to isometric or isokinetic movements. Eccentric and concentric contractions are modeled as well. The validity of the model will be shown by a

tridimensional representation of the length-velocity-tension relationships. The performance of the process will be described with a simple example. Finally, methods for quantifying and validating the model will be outlined.

In what follows, we call EMG the electrical activity of the muscle after it has been rectified and integrated. The raw EMG is picked up by dual intramuscular wire electrodes to provide specific signals from each muscle at the knee joint. The recording and processing techniques have been described by PERRY et al., (1974) (reference #11).

#### MODEL OF THE EMG-FORCE-POSITION RELATIONSHIP IN PRESENCE OF MOVEMENT

The fundamental assumption of this model is that the EMG is proportional to the neural input of the muscle. In other words, the actual representation of the process by a single input and two parallel outputs can be described using a series representation as shown in figure 1.

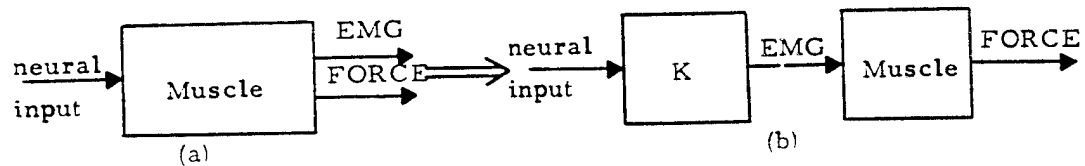


Figure 1: Neural input- EMG- muscular force relationships  
(a) actual parallel representation, (b) assumed model using  
two series elements.

The EMG signal is then considered as an input of the process rather than as a parallel output. Furthermore, it is assumed that the EMG-neural input relationship is static and time invariant so that the EMG signal is representative of the actual muscle input whatever the movement.

In isometric contractions, the EMG-tension relationship is linear. Taking into account the foregoing hypotheses, a simple EMG-tension relationship in presence of movement should also exist. If this is not so, the variables which do not appear in the static mode must be more carefully described. It is then necessary to concentrate on the muscle dynamics and on the joint dynamics.

## Muscle Model

Let us consider for instance the input-output model of GOTTLIB and AGARWAL (1971)(reference 5), (figure 2a). It relates the raw EMG to the isometric tension produced by the muscle for a fixed muscle length. If changes in length occur, the model is no longer valid unless its parameters are fitted again. The proposed model, (figure 2b) allows one to get rid of this constraint.

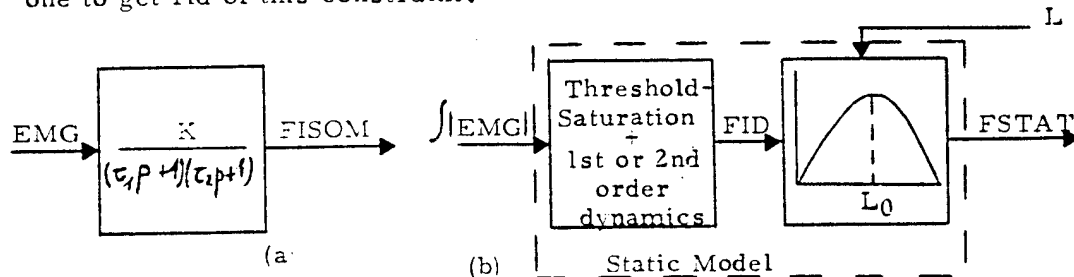


Figure 2: (a) GOTTLIB and AGARWAL (1971)(reference#5) model  
(b) Static model for the muscle

The changes in the muscle length  $L$  are automatically accounted for, using the length-tension characteristic as a filter on the output of an "ideal" black box. This black box would be sufficient to model the muscle if its force output were not dependent on length. Actually, the first block yields an ideal force  $FID$  which is the isometric force at rest length ( $L_0$ ) whatever the muscle state. The static force  $FSTAT$  is the filtered ideal-force which represents the muscle behavior in isometric mode at any length. Therefore,  $FSTAT$  is equal to  $FID$  when the muscle is at rest length.

The first box of figure 2b is similar<sup>\*\*</sup> to GOTTLIB's model. A threshold-saturation type of non-linearity, followed by a first or second order filter will be used.

In order to generalize the static model to non-isometric situations, the muscle velocity has to be included. The tension-velocity characteristic is used for this purpose and used similarly to the length-tension filter: the static force  $FSTAT$  is filtered by it to yield the actual dynamic force  $FDYN$  produced by the muscle during movement (figure 3). In isometric situations, this filter behaves as a gain whose value is one.

\*\* It might be identical if the experimental conditions (type of electrode, electrode location...) and the signal processing techniques used were the same.

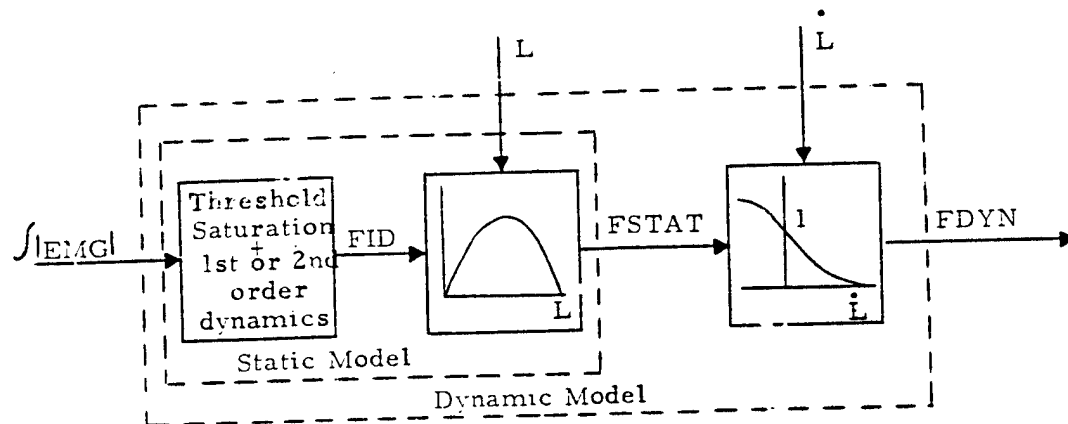


Figure 3: Overall muscle model

The muscle is then represented by the overlapping of a static and a dynamic model. The first one can represent isometric contraction by itself. Since the dynamic force is not observable, a model of the joint is necessary in order to relate  $FDYN$  to the limb position  $\hat{e}$ .

#### Model of the Knee Joint

Let us consider the joint shown in figure 4. In what follows, the study is restricted to the knee joint and the **extensor muscle group** of the leg (quadriceps). For sake of simplicity, it will be assumed that the five muscles in the quadriceps group may be represented by a single muscle whose dynamic properties are equivalent to the whole extensor muscle group dynamics. The thigh is assumed to be firmly secured in a horizontal position and at right angles with the trunk.

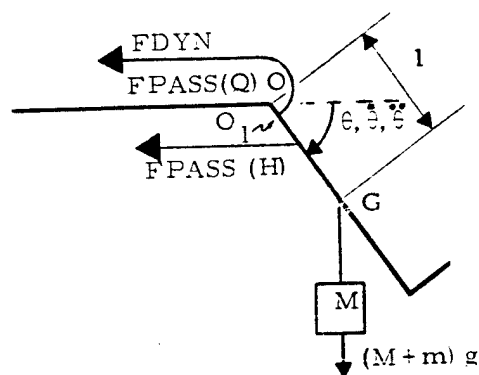


Figure 4: Forces applied to the leg.

The meaning of the parameters and variables of figure 4 is as follows:

- $g$  is the mass acceleration due to gravity.
- $m$  is the mass of leg.
- $M$  is an external load assumed to be hung at the center of gravity  $G$  of the lower leg.
- $l$  is the distance from the center of gravity of the leg to the center of rotation  $O$  of the knee. The foot is assumed to keep a constant angle with respect to the tibia. Furthermore, it is assumed that the changes in the center of rotation  $O$  of the knee are not significant with respect to  $l$ .
- $FDYN$  is the dynamic force produced by the quadriceps and is equal to the output of the muscle model.
- $FPASS(H)$  is the passive force developed by the antagonist muscle group when it is lengthened beyond its rest length.
- $FPASS(Q)$  is the passive force developed by the quadriceps under the same conditions as  $FPASS(H)$ .

The directions of  $FDYN$ ,  $FPASS(H)$  &  $FPASS(Q)$  are assumed to be parallel to the femur.

Note that  $FPASS(Q)$  corresponds to the passive force of the length-tension diagram. It is necessary to represent it in this part of the model since the length-tension filter of the muscle model deals only with the active force (figure 5):

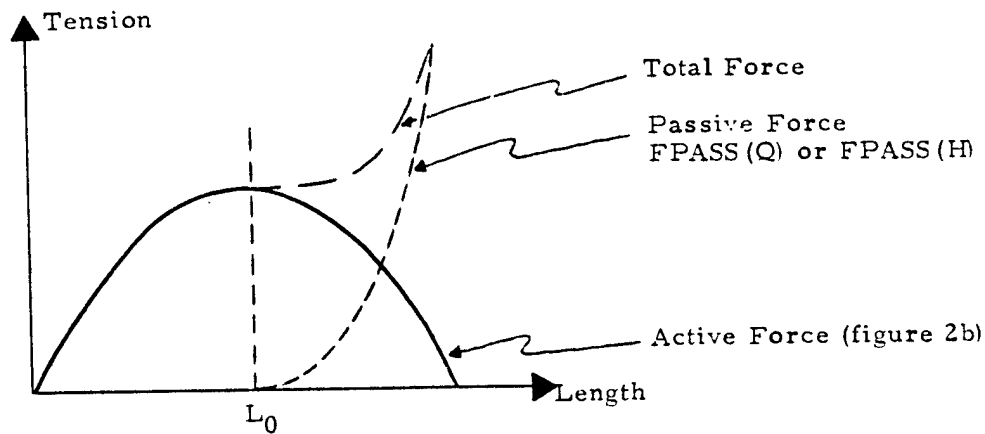


Figure 5: Length-Tension diagram

The dynamic equation of motion for the system shown in figure 4 is given by:

$$J_{\dot{\theta}}^{\ddot{\theta}} = \text{TDYN} + \text{TPASS}(\dot{Q}) - \text{TPASS}(\dot{H}) - C\dot{\theta} - g l(M + m) \cos \theta$$

- J is the moment of inertia of the lower leg.
- C is the damping coefficient in the knee joint and its surrounding soft tissue.
- $\theta, \dot{\theta}, \ddot{\theta}$  are the position, velocity and acceleration of the leg respectively.
- TDYN is the torque corresponding to FDYN.
- TPASS(H) and TPASS(Q) are the torques corresponding to FPASS(H) and FPASS(Q). They include stretching of tendon and ligaments and are significant beyond the rest position  $\theta$ .

[illegible]

826

In this diagram:

- $s$  is the Laplace transform variable.
- $L$  and  $\dot{L}$  are the muscle length and velocity respectively, corresponding to  $\theta$  and  $\dot{\theta}$ . The functions  $g$  and  $g'$  realize these transformations. Since the  $L - \theta$  relationship is non linear, it may be written:

$$L = g(\theta)$$

yielding:

$$\dot{L} \frac{\partial g}{\partial \theta} \dot{\theta} = g'(\theta, \dot{\theta})$$

$g'$  is then a function of the position and velocity of the joint.

- The joint dynamics box transforms FDYN into TDYN accounting for the changes in the center of rotation of the knee which imply a non linear variation of the moment arm  $OO_1$  of figure 4 with respect to the knee position  $\theta$ .

## INTERPRETATION OF THE MUSCLE MODEL

The effects of the L.T. and V.T. filters may be explained by a tridimensional diagram where the axes are length ( $L$ ), velocity ( $V$ ) and tension ( $T$ ). SONNENBLICK (1965) (reference #12) and BAHLER (1968) (reference #2) used this representation to study the interconnections between L., T. and V. . .

Let us follow what happens to the ideal force FID when the muscle contraction is anisotonic at non-constant velocity (figure 7a). The ideal force FID is first transformed into a static force FSTAT in the L.T. plane. FSTAT belongs to a surface which would contain the dynamic force if the muscle behavior were not dependent on velocity. If this hypothesis is true, the so-called FDYN-IDEAL would be the anisotonic muscle force. Actually, the dynamic force FDYN belongs to a surface which is elicited from the previous theoretical one by the V.T. filter.

Different modes of contraction may be described with this representation, (as shown by curves b and c in figure 7) as well as the dependence of the V.T. relationship on the initial muscle length.





Let us show now the behavior of the L.T. and V.T. filters when submaximal forces are developed during eccentric or concentric contractions.

A linearized form is chosen for the L.T. characteristic as shown in figure 8. Each point of the solid lines represents the maximal force produced at a given muscle length within the range [ LMIN - LMAX ]. LMIN and LMAX represent the minimum and maximum lengths the muscular group can have during a functional movement.

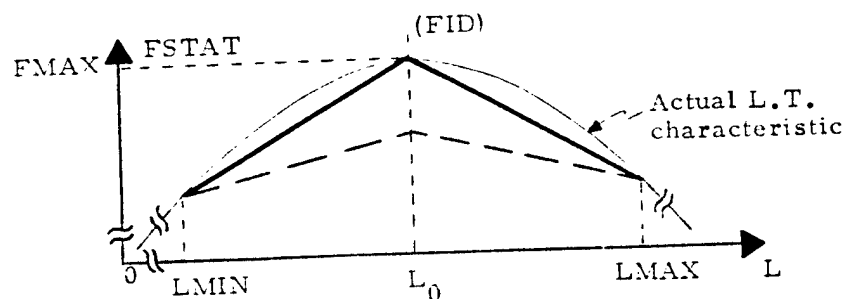


Figure 8: Structure of the L.T. filter

We shall assume that the level of activation of a muscle is directly related to its cross section rather than its length: when a muscle is fully activated, it develops its maximum force and the whole cross-section is involved. If its activation is half the maximum, the maximal force is halved at any length and the slopes of the lines in figure 8 are halved.

The ideal force FID represents the level of activation of the muscle but is independent of its length. Therefore, a variation of FID(t) is equivalent on the figure 8 to a variation on the FSTAT (L = L0) axis, whatever the changes in length. The actual value of the static force, taking into account the changes in length at a given time, is the ordinate of a point belonging to the straight line:

$$FSTAT(L) = \begin{cases} \frac{L - LMIN}{L_0 - LMIN} \times FID & \text{If } L \leq L_0 \\ \frac{L - LMAX}{L_0 - LMAX} \times FID & \text{If } L \geq L_0 \end{cases}$$

The slope of the line is determined by the instantaneous ideal-force. When FID is equal to FMAX, FSTAT(L) is given by the solid lines of figure 8. If FID(t) is equal to FMAX/k, the slope is divided by k (broken lines). The L.T. filter process is illustrated by an example in figure 9.

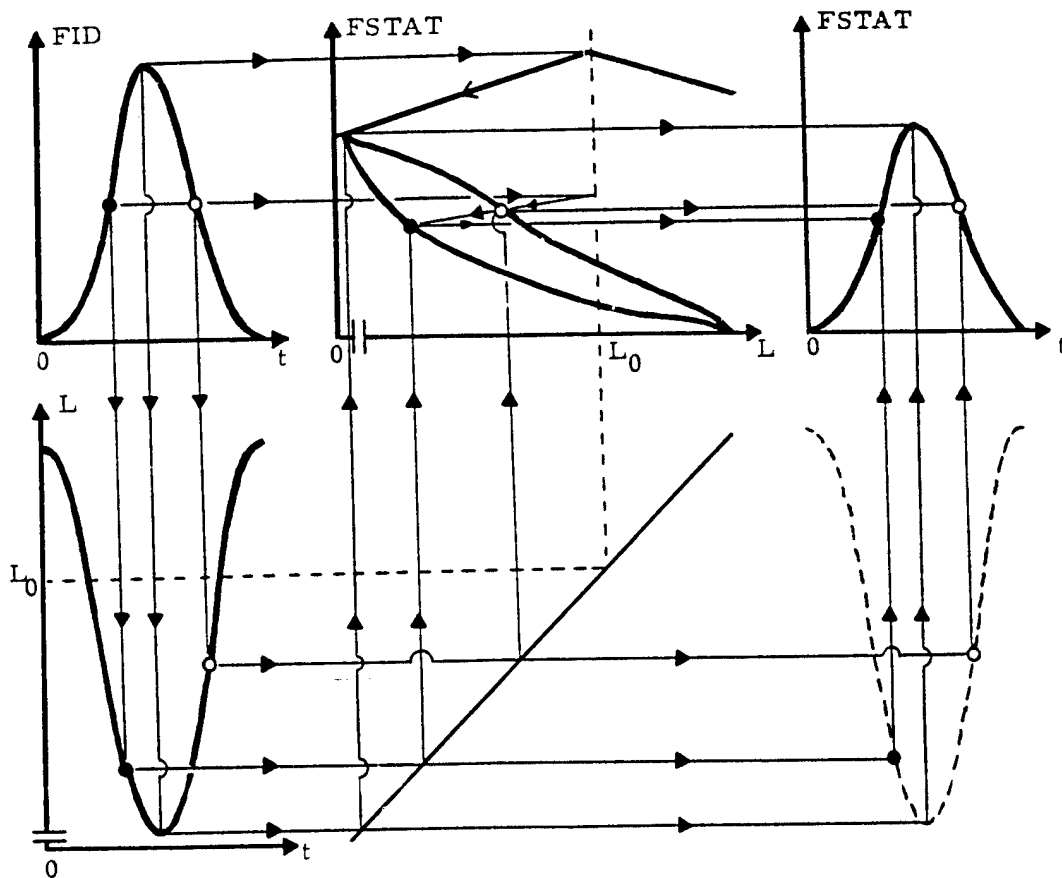
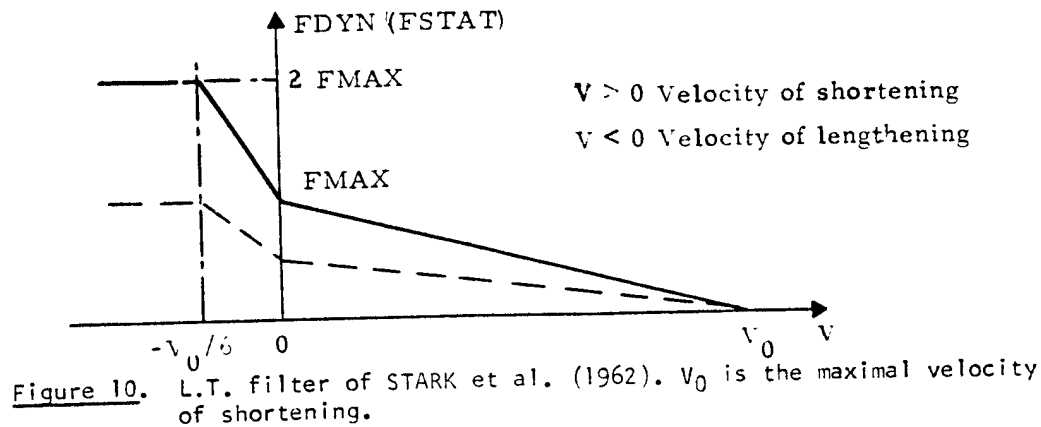


Figure 9 Effect of the L.T. filter on the ideal force FID. FID (t) (top left) is arbitrary for free movement. The muscle length L is assumed to be time varying in a sinusoidal manner (bottom left). The contraction of the quadriceps is concentric when L decreases and eccentric when L increases. The antagonist muscular group is passive during the movement. The FSTAT (L) curve (top center) is elicited by construction from FID (t) and L (t) as shown with dots ● and ○. These two dots belong to the same L.T. characteristic but are related to different muscle lengths. The FSTAT (t) curve (top right) represents the L.T. filter output.

The representation of STARK et al., (1962)(reference #13) has been adopted to characterize the V.T. filter. It is a linearized model of HILL's curve (1938) which has been generalized by KATZ (1939)(reference #7) for eccentric contractions (figure 10). STARK used this diagram for simulation of the agonist-antagonist muscle system behavior during hand motion.



As mentioned above, the muscle force depends on its cross-section. Furthermore, its maximal velocity  $V_0$  is a function of the muscular fiber length and hence, is a constant of the process. Then, as for the L.T. characteristic, when the muscular force is reduced, the slope of the relation is lessened proportionally (broken lines of figure 10).

The static force FSTAT appears on the FDYN ( $V=0$ ) axis (figure 10). Each value of FSTAT corresponds, then, to a value of FDYN resulting in the association of the instantaneous muscle velocity and the force FSTAT produced at the same time. FDYN can be written as:

$$FDYN(V) = \begin{cases} 2 \times FSTAT & \text{If } V \leq -V_0/6 \\ \frac{|V| + V_0/6}{V_0/6} \times FSTAT & \text{If } -\frac{V_0}{6} \leq V \leq 0 \\ \frac{V_0 - V}{V_0} \times FSTAT & \text{If } V \geq 0 \end{cases}$$

The V.T. filter works as the L.T. filter does. Its effect is shown in figure 11 with the same example used in figure 9.

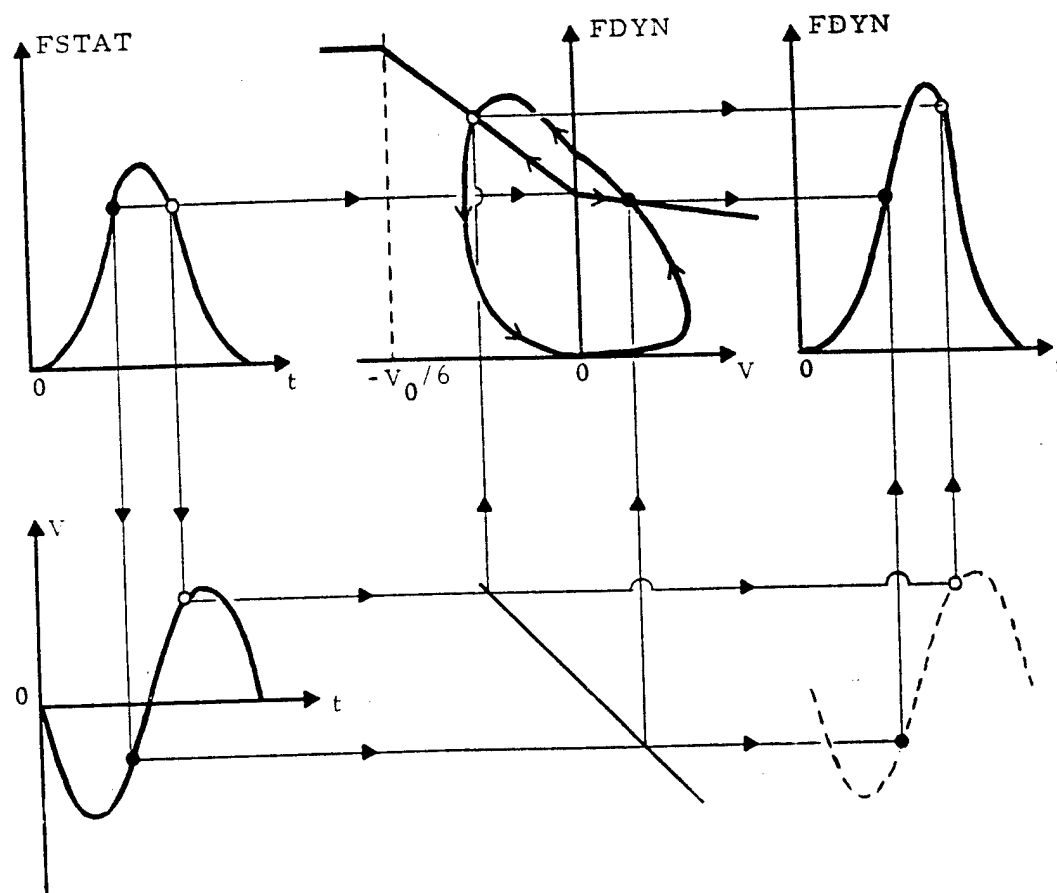


Figure 11 Effect of the V.T. filter on the static force  $F_{STAT}$ . The  $F_{STAT}(t)$  curve (top left) is the L.T. filter output of figure 9. The  $V(t)$  curve (bottom left) is the first derivative with respect to time of the previous  $L(t)$  curve. For this example, concentric contraction occurs when  $V < 0$ . The sign of  $V$  must then be reversed (bottom center) in order to keep the same V.T. diagram as figure 10. The  $FDYN$  curve (top center) is elicited by construction from  $F_{STAT}(t)$  and  $V(t)$  as shown with the dots  $\bullet$  and  $\circ$ . These two dots belong to the same V.T. characteristic: the first is related to a velocity of shortening, the second is related to a velocity of lengthening. The  $FDYN(t)$  curve (top right) represents the overall muscle model output.

## DATA ANALYSIS

Quantification and validation of the model will be performed in the following sequence of steps:

- a. First, the basic parameters of the model will be obtained by experiments. These parameters include the mass of the leg segments, the damping of the knee, the inertia of the lower leg, the passive tensions of the agonist and antagonist muscular group, the maximum isometric force with respect to limb position, etc.
- b. The second step is the calculation of the ideal force produced by the muscle from the knee position data, by simulation. While in figure 6, the force appears as the input and the position as the output, the recorded knee position will be used as the input to a computer simulation and FID will be calculated.
- c. Then, a parameter identification procedure will be performed to determine the parameters of the relationship between the integrated EMG and the ideal force. It is expected that a non-linearity which includes threshold and saturation and a first or second order model would be adequate to represent the process.
- d. Finally, the aggregate model of both muscle and joint will be verified. For a given integrated EMG and taking into account the experimental conditions, the model must give the same knee position as the corresponding recorded actual position.

## CONCLUSION

The model of the EMG-force-position relationships we propose includes:

- a muscle model using the length-tension and velocity-tension relationships as basic elements. The series filter representation makes it possible to relate EMG to force during isometric contractions as well as during more general movements without constraints on velocity, length or force.
- a model of the knee joint accounting for its mechanical characteristics (damping, changes in the center of rotation...) and the passive torques produced by muscles.

The tridimensional representation shows the validity of the model for various types of contraction. The velocity-tension diagram used

enables concentric and eccentric movements to be modeled. Submaximal forces may be described as well, as pointed out by the example.

Therefore, the proposed model is a general model of the joint and its actuators, relating the electrical activity of the muscles to the angular displacement of the moving limb and providing a prediction of internal muscle force.

#### REFERENCES

1. Agarwal, C.C.; Cecchini, L.R.; and Gottlieb, G.L.: Further Observations on the Relationship of EMG and Muscle Force. Proc. of the 7th Annual Conference on Manual Control, pp.115-118, 1971.
2. Bahler, A.S.: Modeling of Mammalian Skeletal Muscle. IEEE Trans. Biomed. Engng., BME-15: 249-257, 1968.
3. Brody, G.; Scott, R.N.; and Balasubramanian, R.: A Model for Myoelectric Signal Generation. Med. and Biomed. Engng., 12: 29-41, 1974.
4. Coggs, J.C.: Mathematical Models of Muscle. Ph.D. Thesis, Technical Report, USCEE Report 303, U.S.C., 1968.
5. Gottlieb, G.L.; and Agarwal, G.C.: Dynamic Relationship Between Isometric Muscle Tension and the Electromyogram in Man. J. App. Physiol., 30: 345-351, 1971.
6. Hill, A.V.: The Heat of Shortening and the Dynamic Constants of Muscle. Proc. Roy. Soc. (London), B126: 136-195, 1938.
7. Katz, B.: The Relation Between Force and Speed in Muscular Contraction. J. Physiol., 96: 45-64, 1939.
8. Lindström, L.; Magnusson, R.; and Petersén, I.: Muscle Load Influence on Myo-Electric Signal Characteristics. Scand.J. Rehab. Med., Suppl.3: 127-148, 1974.
9. Lippold, O.C.J.: The Relation Between Integrated Action Potentials in Human Muscle and its Isometric Tension. J. Physiol. 117: 492-499, 1952.
10. Ostroff, L.; Phatak, A.V.; and Bekey, G.A.: On the Grading of Tension during Voluntary Contraction of Skeletal Muscle. Proc. of the 6th Annual Conf. on Manual Control, 1970.

11. Perry, J.; Antonelli, D.; and House, K.: *Électromyography as a Force Measurement*. N.I.H. Grant AM-13466, Dec., 1974.
12. Sonnenblick, E.H.: *Determinants of Active State in Heart Muscle: Force, Velocity, Instantaneous Muscle Length, Time*. *Fed. Proc.*, 26: 1396-1409, 1965.
13. Stark, L.; Houk, J.C.; Willis, P.A.; and Elkind, J.L.: *The Dynamic Characteristics of a Muscle Model Used in Digital Computer Simulation of an Agonist-Antagonist Muscle System in Man*. *Quart. Prog. Rept.*, Research Lab. of Electronics, M.I.T., 64: 309-315, 1962.
14. Wani, A.M.; and Guha, S.K.: *Summation of Fibre Potentials and the EMG-Force Relationship during the Voluntary Movement of a Forearm*. *Med. and Biol. Engng.*, 12: 174-181, 1974.



A MODEL OF THE REFLEX ARC AND ANALYSIS OF THE BEHAVIOR  
OF THE PERIPHERAL RECEPTORS DURING CLONUS

Joseph E. Dollman  
The University of Toledo  
Toledo, Ohio 43606

Anthony M. Iannone  
Medical College of Ohio  
Toledo, Ohio 43614

Lee T. Andrews  
Medical College of Ohio  
Toledo, Ohio 43614

INTRODUCTION

At the present time, our knowledge of the physiology of peripheral receptors, the reflex arc and skeletal muscle has progressed to the point, where reasonable models of each of these individual elements is now described. It was the purpose of this project to combine these elements into a model of the entire skeletal muscle system. The system model was then thoroughly tested to insure its accuracy. Upon verification, the model provided a facility which allowed a prediction of the behavior of each element of the system, during rapid and reflex movement, to be made and compared with physiological observations. Of primary interest were the changes in system specifically related to rhythmic oscillation of skeletal muscle referred to as clonus.

The ability of the model to portray rapid and reflex movement was of primary importance, as the mechanisms of these movements were believed to be directly involved in the tremorous instabilities, which were of interest in this study. Each peripheral receptor was, therefore, thoroughly analyzed to determine its role in the regulation of reflex contraction. The complexity of the model was minimized by assuming a simple monosynaptic reflex. This assumption allowed us to omit those elements which are primarily involved in higher level controls of posture and deliberate movement. Thus, the joint receptor, the renshaw cell and secondary spindle endings do not appear in our model. The elements included in the model appear in Figure 1.

FORMULATION OF THE MODEL

Selection Criteria

In the process of reviewing publications, to select information necessary for the formulation of any of the elements of this model, certain selection criteria must be established. A comparison to these criteria will provide a method, by which information may be evaluated and the most feasible representation of the individual elements selected. Primary consideration, of course, should be given to the accuracy with which a given model portrays the characteristics of the system. In formulating such an accurate model care must be taken not to lose track of the physiological meaning of the parameters in the

model. That is to say, it is possible to very accurately fit the response curve of a particular organ with a high order equation. What is lost, though, is the physiological explanation for the coefficients of that equation. This makes implementation of changes, representing physiological phenomenon, very difficult. Thus, the task of relating the behavior of such a model to that of the physiological system becomes unduly complicated.

Another desirable trait of the model is simplicity. This will allow for efficient use of the facilities plus greatly enhance the ease with which the model can be operated. It was also deemed to be more representative, if when programmed, each model would have a single input and single output as this not only facilitated response studies of individual organs but also was considered more realistic. Therefore, the criteria for choosing a particular model were finalized as:

- 1) the accurate portrayal of the characteristics of the organ,
- 2) the physiological realizability of the model,
- 3) the minimum of complexity.

#### Muscle Fiber

The section of the model representing muscle tissue was the first subsystem concentrated on. The literature presently contains a very large number of applicable models. The complexity of these models vary from the simple viscoelastic representation to models based on the nonlinear Hill force velocity equation.

The final representation, shown in Figure 2, was chosen to be a contractile force generator in parallel with the passive tissue representation used by Houk [4] in his Golgi Tendon Organ experiments.

The parallel elements  $K_m$  and  $K_c$  represent the elasticity of the muscle tissue and the connective tissue, respectively. Using this representation also allows the Golgi Tendon Organ to be positioned in such a way that the entire tension developed by the contractile force generator is transmitted through the tendon organ. Tension developed by passive loading, however, is distributed between the tendon organ and the connective tissue which will enhance the representation of the Golgi Tendon Organ.

The parameters suggested by Houk for this model were

$$\begin{aligned}K_1 &= K_c + K_m = 346 \text{ g/mm} \\K_2 &= 420 \text{ g/mm} \\K_c &= 233 \text{ g/mm} \\K_m &= 113 \text{ g/mm} \\B &= 18 \text{ g/mm/sec}\end{aligned}$$

When tested the parameters proved very satisfactory.

The step response of the fiber with an appropriate mass attached is shown in Figure 3. Increasing the damping caused increased oscillation involving the  $K_2$  term, the elasticity of the tendon, as it effectively stiffened the contractile unit. Decreasing the damping was seen to increase oscillation related to the series combination of the springs  $K_1$  and  $K_2$ . It was decided, therefore, to use these parameters as they provided what appeared to be an adequate response.

The limb dynamics involved in motion play an important part in causing inertial effects in the muscle response. Without these inertial effects the overshoot seen in the figure would not be present. Therefore the limb dynamics were assumed to be the movement of a mass,  $M$ , representing the mass of the limb and the mass of the muscle. Limb motion was assumed to be directly proportional to the muscle length for the magnitude of movements to be involved in the study.

The transfer function for the model can then be derived in terms of the input force. If we let  $G$  represent the total force, that is the acceleration due to gravity plus the disturbance,  $F_1$ , then the displacement,  $E_p$ , is given by

$$E_p(s) = \frac{M(K_m + K_c + K_2 + BS)}{MB(s^3 + \frac{K_m + K_c + K_2}{B}s^2 + \frac{K_2}{m}s + K_2 \frac{(K_m + K_c)}{MB})} G(s)$$

#### Golgi Tendon Organ

The Golgi Tendon Organ is the source of inhibitory signals in the reflex arc. These signals serve as a load detector and overload protection mechanism in the muscle control system. A great deal of work has been published by J. C. Houk [4,5,6] and his associate on the function and modelling of these organs. The tendon, in these works, is modelled with a linear equation. The nonlinearities known to be present in the system were defined as adaptation and threshold functions preceding and following the linear dynamics, respectively. The saturation curve precedes the linear dynamics so as not to decrease the overshoot in response to rapid movements. Conversely, the threshold was seen to follow the linear dynamics, as it was Houk's conviction that this phenomenon was the product of conversion of receptor potentials to  $I_b$  potentials.

By fitting recorded data to exponential responses Houk originally derived a second order transfer function,  $h(s)$ .

$$h(s) = K \frac{(s + .95)(s + 13.65)}{(s + 1.8)(s + 25.0)}$$

Further work indicated that a third order term representing the low frequency "mechanical filtering" of the muscle tissue was needed. However, Houk stated his transfer function as a response to a force input at the end of the tendon. The input to the tendon organ in the proposed model has been chosen to be the tension,  $T_{IN}$ , at the point previously indicated, Figure 2, between

the contractile element and the tendon. In calculating the tension at this point from displacement, load and contractile force information, the low frequency "mechanical" filtering required by Houk has already taken place. Thus, the second order system will accurately model the dynamics of system in question.

The nonlinearity related to threshold proved to have a very significant effect when studying instabilities in the motor system. The inhibitory effects of the tendon signals, which exceeded the threshold, were responsible for limiting otherwise growing oscillations. Increased sensitivity to these signals and/or lowered thresholds could also be seen to have a significant effect on the damping of what would otherwise be sustained oscillation. The adaptation function, however, did not appear to have extraordinary effects on the system. The movements being studied were caused by forces of a magnitude such that they fell below levels which would be thought to cause significant adaptation. Leaving this term out would also help compensate for the different response to active force by not saturating during the high tension conditions which those forces cause.

Another control must be considered before accepting this model for the system. The degree to which the  $\alpha$  motor neuron responds to the inhibitory signals, propagated along the  $I_b$  neuron, is in some way controlled by the central nervous system. A suggestion for this is that the nervous system controls the excitability of the interstitial neurons forming the polysynaptic connection between the  $I_b$  and the  $\alpha$  motor neuron. This can be represented as gain, ranging from 0 to 1, which is controlled by a central nervous system input. The final form of the model is described in Figure 4, where  $h(s)$  is the second order representation stated above.

#### Muscle Spindle

The muscle spindle provides excitatory feedback to the contractile force generator. These signals are essential in the proprioceptive network, necessary for rapid movement and reflex activity. The secondary endings located in the nuclear chain fibers of the spindle are slow responding and more adapted to postural control. Therefore, only a model of the rapidly responding nuclear bag fiber of the spindle was deemed necessary for this model.

The works of Rudjord [10] and of Andrews [1,2] both strongly suggest that a second order model would be accurate for this case. A number of second order Bode plots were given to demonstrate how well these models would fit the actual data.

The Bode plots suggest a pole near 100 which caused the decrease in phase and the leveling off of the gain as it approached that frequency. A zero,  $z_1$ , is seen to be in the neighborhood of 1 Hz. The second pole was chosen to be around 200 Hz, so as to represent the great attenuation in response which is seen at frequencies near 500-1000 Hz. The second zero,  $z_2$ , was chosen so as to cancel the phase lag effects the pole at 200 has on high frequency response. The value was also chosen high enough so as to eliminate any effects it would have on the low frequency response. Thus  $z_2$  was set to 600. The

asymptotic approximation of the Bode plot is shown in Figure 5. The transfer function is then:

$$h(s) = K_Y \frac{(s + z_1)(s + z_2)}{(s + 100)(s + 200)}$$

where  $z_2$  has been chosen to have a value of 600. The choice of an exact value for  $z_1$  requires that consideration be given to the effects of  $\gamma$  innervation on the low frequency response of the system. If the elastic stiffness in the bag fiber were to increase with innervation, the position of  $z_1$  would change, moving farther into the left half plane. Green [11] has suggested neural control of stiffness and damping was responsible for control of the contractile element of muscle so why not the same effect for the control of the contractile sections of the spindle fibers. Rudjord, however, had indicated doubt that this change in stiffness was an accurate portrayal of the effects of innervation on the spindle and suggested the effects were similar to those of a force generator in parallel with elements of fixed value. The idea of a force generator seemed a more logical representation of gamma control of muscle length. However, it did not seem sufficient to explain the ease with which the system could be driven unstable under conditions of high  $\gamma$  innervation. An examination of a typical plot of extension versus tension for muscle fiber shows a significant increase in stiffness as tension increases. Thus, even if  $\gamma$  does not directly control the stiffness of the fiber, increased activation of the contractile force generator will increase tension in the fiber thereby increasing the stiffness.

It was decided, therefore, to make the position of  $z_1$  a function of  $\gamma$  while also including a  $\gamma$  controlled force generator. The force generator was to be represented in a manner similar to Dijkstra's [3]. That is, the stretch sensed by the spindle is measured with respect to some reference length,  $E_{p\_reference}$ . The force generator is, therefore, a control of that reference length and can be represented merely as a level to be added or subtracted from the actual displacement. The input to the system,  $E_{p_{in}}$ , becomes then:

$$E_{p_{in}} = E_p + E_p(\gamma)_{reference}$$

with the transfer function of the spindle being:

$$H(s) = \frac{(s + z_1(\gamma))(s + 600)}{(s + 100)(s + 200)}$$

Similar to the  $I_b$  activity, the signals transmitted along the  $I_a$  neuron do not have a constant effect on the  $\alpha$  motor neuron. Even in the case of a monosynaptic connection with the  $\alpha$  motor neuron, sensitivity to excitation is controlled by the central nervous system. The physiological explanation for this is that inhibitory signals from the central nervous system can reduce the sensitivity of the anterior horn cell to  $I_a$  inputs. To account for this a sensitivity term, having a value between 0 and 1, is multiplied by the  $I_a$  at its input to the contractile force generator. The only other addition to the model is a diode in the feedback path which limits the excitation to the di-

rection of contraction only.

#### Contractile Force Generator

The contractile forces generated by muscle fibers are known to be functions of spindle, tendon organ and central nervous system activity. Effects from renshaw cells and from the linkage with antagonist muscles were neglected due to their absence from the model. The contractile force was then defined as  $f_c$  where:

$$f_c = K(CNS + k_1 I_a - k_2 I_b)$$

The gain,  $K$ , represents the conversion from frequency of firing in the  $\alpha$  motor neuron to actual contractile force. The gains,  $k_1$  and  $k_2$ , represent the sensitivity term of the anterior horn cell and the interstitial neurons discussed in the spindle and tendon organ models.

The inhibitory effect of the  $I_b$ , modeled by subtracting it from the summation of excitatory inputs, could, in an extreme case, cause a sign change in the contractile force. Since this would be analogous to the muscle pushing the limb, a physiological impossibility, a diode was used to rectify the generated contractile force thus assuring that it always maintains a positive value.

#### Initial Analysis

The above elements were assembled in the proper order. A root locus analysis was carried out under two conditions:

- 1) the Golgi Tendon Organ sensitivity set to zero, and
- 2) the Golgi Tendon Organ inputs predominant.

The characteristics predicted by the model were very closely related to those which would be expected of a skeletal muscle system. That is:

- 1) The open loop response shows less than critical damping,  $\zeta=1$ , for physical parameters of the system.
- 2) Feedback from the spindle, at moderate levels, increases damping in the systems step response.
- 3) Excessive sensitivity to spindle output can cause oscillation.
- 4) Significant changes in the position of the gamma controlled zero,  $z_1(\gamma)$ , will induce oscillation.
- 5) Feedback from the Golgi Tendon Organ is the limiting factor in the magnitude of the oscillation and affects the sensitivity to  $I_a$  needed to sustain oscillation.

#### Verification of the Model

The initial analysis of the system showed the model to be very promising. Therefore, the model was wired on the analog computer. Before attempting to model clonus, however, more tests were made to verify the model.

To check the reflex loop, steps in stretch were applied under open loop, normal and high tendon organ activity situations. A step response run during high tension conditions was run to check the function of the diodes in the feedback paths.

Satisfied that the reflex loop was operating properly, simulations of activated movements were made to insure that the model adhered to currently accepted theory of  $\alpha$ ,  $\gamma$  and  $\alpha$ - $\gamma$  linked innervation of movement. The model performed very well in these tests adding support to the assumption that spindle innervation includes a control of a  $\gamma$  dependent zero in the bag fiber.

The satisfactory completion of these tests indicated that the model was very representative of a skeletal muscle control system. A study of clonus using this model, therefore, could be expected to produce accurate results.

#### CLONUS

##### Explanation and Analysis

Mountcastle [9] defines clonus as "the tendency to oscillate at approximately 8 to 12 hz., a behavior that is believed to be caused by excessive feedback from spindle receptors". Generating a 10 hz. sinusoid, however, is not the major point behind the model. The model should not only display the sinusoidal movement but also the proper phase relationship between the excitatory signals and movement. To determine what the relationship should be data, recorded by Iannone, Angle et. al. [8], on ankle clonus was examined. A plate taken from Iannone's notes is shown in Figure 6. In the photograph down is the direction of stretch with the spindle output being the upper trace, the EMG activity the center and displacement the lower trace. It can be seen in the recording that spindle activity begins increasing significantly with movement in the direction of stretch. The EMG activity is seen to reach its maximum approximately 20 msec before the muscle reaches maximum stretch. The frequency of the oscillation, being approximately 10 hz., means the excitatory signal leads the displacement by approximately 72°. In his notes Iannone mentions the results of recording the afferent activity of Golgi Tendon Organs. It is his finding that the activity of the Golgi Tendon Organ occurs just after the EMG has ended. It is his contention that the purpose of the Golgi Tendon Organ during clonus is more one of inhibiting excitation during the returning phase of the oscillation than one of ending the excitation itself.

The implications of this statement about the function of the Golgi Tendon Organ are that the  $I_b$  response should be almost in phase with the displacement itself. If one assumes the spindle output to be primarily proportional to the rate of stretch, the time delay involved in the 100 m/sec. propagation rate of the  $I_a$  fiber will shift the phase of the excitatory signal to a neighborhood of 72° of lead, quite easily. Likewise, the small velocity component of the tendon organ transfer function can cause the tendon output to lead the displacement by only a small amount. The time delay involved in propagating these signals along the  $I_b$  fiber, whose propagation rate is similar to that

of the  $I_a$ , could then easily compensate for this, putting the inhibitory effects in phase with the displacement. Another comment made by Iannone was that large Golgi Tendon Organ events took place occasionally during clonus. This would seem to indicate that clonus generates tensions which only occasionally exceed the threshold necessary to generate effective inhibitory signals from the tendon organ. Thus, the  $I_b$  threshold of the model can be set at a level just above that which would inhibit small magnitude oscillations and still be representative of the actual circumstances.

This assumption, about the threshold of the  $I_b$ , was tested on the model by simulating a condition with very large position sensitivity in the feedback loop. Such a condition will, unless inhibited, cause an oscillation which will grow in magnitude continuously until reaching the limits of the simulation. With the Golgi Tendon Organ threshold set at a specific level the oscillations were noted to grow until the tension required to excite them exceeded the tendon organ threshold. The magnitude of the oscillation ceased to grow at this point with the  $I_b$  activity taking place at peak tension and inhibiting the excitation. Similarly, the level of such an oscillation could be lowered by further lowering the  $I_b$  threshold. For marginally stable systems, the excitatory signals were seen to produce subthreshold tensions only large enough to sustain the oscillation. Lowering the  $I_b$  threshold in such a case was seen to damp out these oscillations. Since Mountcastle had commented on the small magnitude of clonic oscillation and a marginally stable system would allow the largest amount of phase lead in the excitatory signal, it was justifiable to set the  $I_b$  threshold high enough that inhibitory signals would not effect the oscillation of the system under marginally stable conditions. In doing this it is felt that the model of clonus would be able to give the maximum phase lead possible and still represent the tendon organ effects seen by Iannone.

#### Model Results

The phase relationship, established above, was readily duplicated by the model. The phenomenon of clonus was initiated by allowing the system to reach steady state, then adjusting the position of the zero for marginal stability. After the zero had been adjusted a disturbance was added to the load to initiate a movement.

Figures 7 and 8 display the phase relationships produced by the model. The spindle activity was seen to lead the displacement by 19 to 20 msec., that is  $68^\circ$  to  $72^\circ$  of lead. The Golgi Tendon Organ activity leads displacement by less than .01 seconds. This timing of the tendon organ activity reinforces the suggestion by Iannone that they are primarily responsible for suppression of ill-timed signals. Since the properly timed excitatory signals are already rapidly decaying when the tendon organ activity is building, the role of tendon organ in terminating these excitations is not shown to be significant.

#### Conclusions

The proposed model has been tested with respect to step response,  $\alpha$ ,  $\gamma$  and  $\alpha$ - $\gamma$  linked activations. The results being outputs which can be explained



by current theory and compare adequately with published data. This being the case, the changes made in the model in order to cause clonus can be assumed to be analogous to those which take place in the physiological system itself. Those changes being primarily excess  $\gamma$  activity represented in two forms. This activity causes increased tension, analogous to reference length changes in the contractile regions of the spindle. Due to this change in tension, changes in the elasticity of the fiber also take place, which when represented in the model greatly enhance the ability of the model to portray clonus.

#### Comments

To understand motor behavior it is imperative to have a thorough understanding of each of the peripheral elements. We feel that knowledge of the individual elements is extensive and there is a need to integrate this knowledge into model of the motor system. Thus, allowing a study of the interaction of these elements in generating control commands from the feedback loops of the motor system. We believe the model presented here has accomplished a first step in this direction and can now be extended to include the higher level influences of the central nervous system.

#### REFERENCES

1. Andrews, L. T., Ewing, D. J., and Iannone, A. M., "An Anatomically Based Mathematical Model of Mammalian Muscle Spindle," Modeling and Simulation, Vol. 4, Proc. of the 4th Annual Pittsburgh Conference, April 1973, pp. 386-390.
2. Andrews, L. T., Iannone, A. M., and Ewing, D. J., "The Muscle Spindle as a Feedback Element in Muscle Control," 9th Annual Conference on Manual Control, May 1973.
3. Dijkstra, S. J., and Denier VanderGon, J. J., "An Analog Computer Study of Fast, Isolated Movements," Kybernetik 12, 102-110, 1973.
4. Houk, James, "A Viscoelastic Interaction Which Produces One Component of Adaptation in Responses of Golgi Tendon Organs," J. Neurophysiol., 1967, Vol. 30, pp. 1482-1493.
5. Houk, James and Henneman, Elwood, "Response of Golgi Tendon Organs to Active Contraction of the Soleus Muscle of the Cat," J. of Neurophysiology, Vol. 30, 1967, pp. 466-481.
6. Houk, James and Simon, William, "Responses of Golgi Tendon Organs to Forces Applied to Muscle Tendon," J. of Neurophysiology, Vol. 30, 1967, pp. 1466-1481.
7. Houk, J. C., Singer, J. J., and Goldman, M. R., "An Evaluation of Length and Force Feedback to Soleus Muscles of Decerebrate Cats," J. of Neurophysiology, Vol. 33, 1970, pp. 784-811.

8. Iannone, A. M., Angel, R., and Zajac, F. E., "Laboratory Notebook, Subject: Clonus," Stanford University, 1967.
9. Mountcastle, Vernon, Medical Physiology, 12th Ed., C. V. Mosby Co., St. Louis, 1968.
10. Rudjord, T., "A Second Order Mechanical Model of Muscle Spindle Primary Endings," Kybernetik, February 1970, Vol. 6, pp. 205-213.
11. Green, D. G., "A Note on Modeling Muscle in Physiological Regulators," Med. Biol. Eng., Vol. 7, 1969, pp. 41-48.

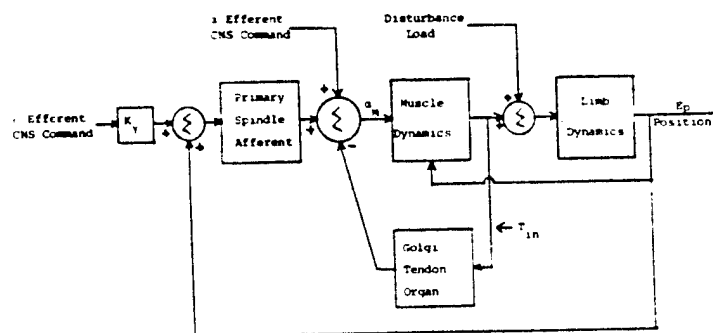


Figure 1

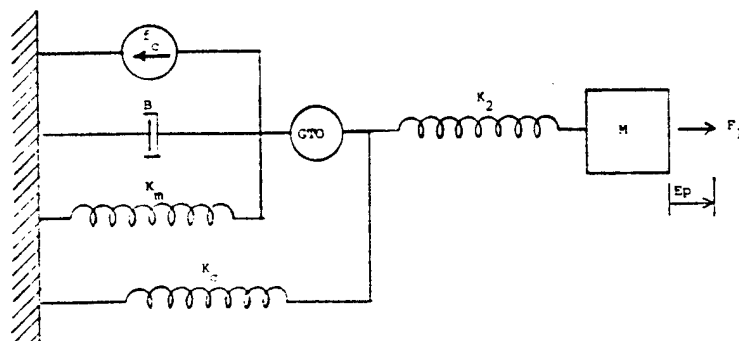


Figure 2

Figure 3

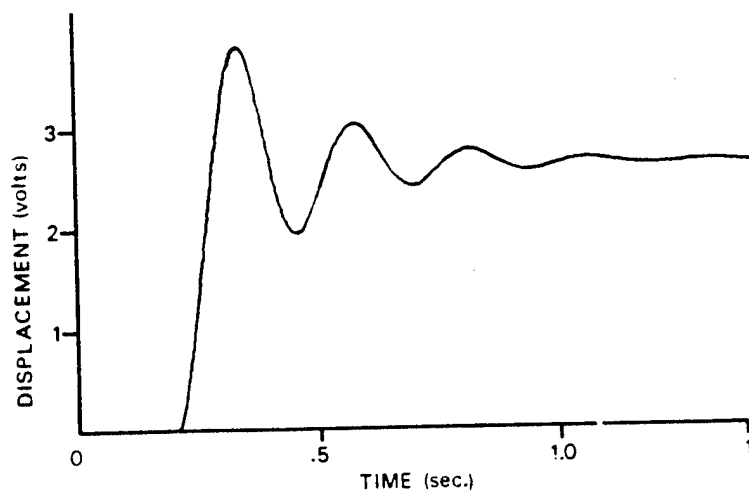


Figure 4

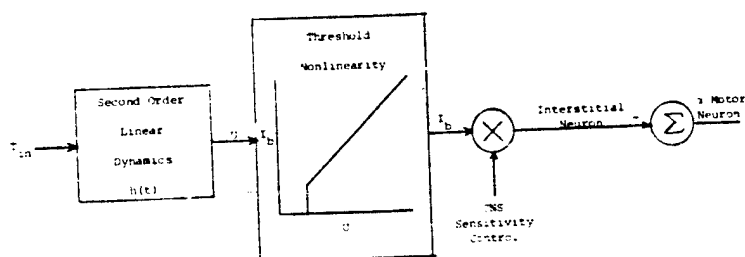


Figure 5

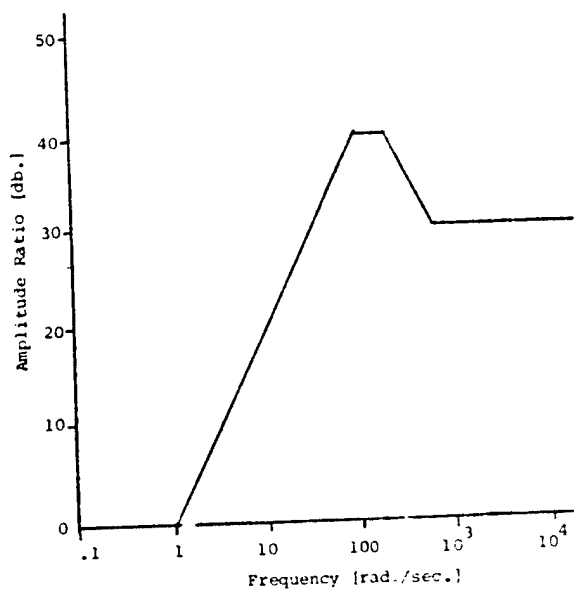


Figure 6

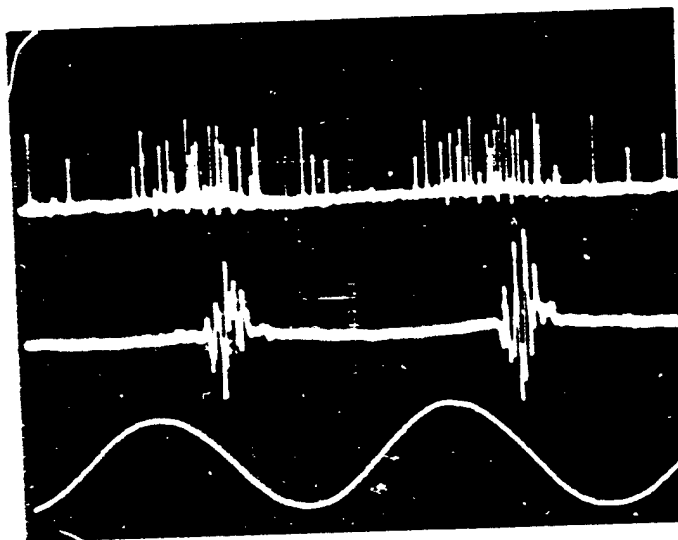


Figure 7

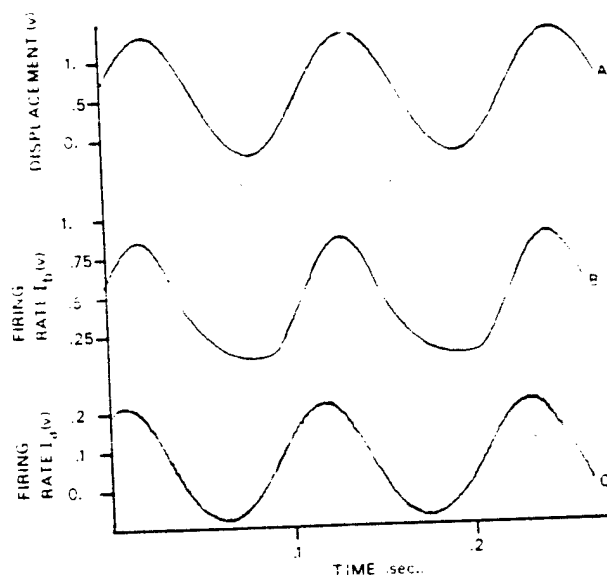
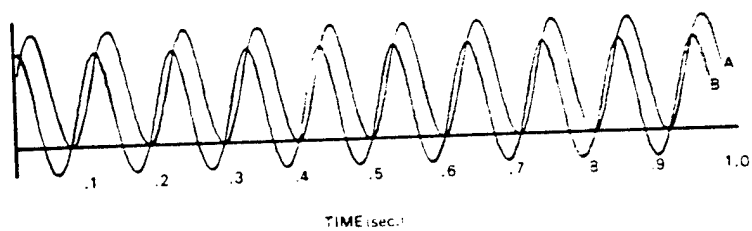


Figure 8



SESSION XI  
MOTION AND VISUAL CUES

Chairman: R. C. Williges

PRECEDING PAGE BLANK NOT FILMED

# A PILOT MODEL WITH VISUAL AND MOTION CUES\*

Renwick E. Curry  
Massachusetts Institute of Technology  
Cambridge, Massachusetts

Lawrence R. Young  
Massachusetts Institute of Technology  
Cambridge, Massachusetts

William C. Hoffman  
Aerospace Systems, Inc.  
Burlington, Massachusetts

Daniel L. Kugel  
Flight Dynamics Lab  
Wright Patterson AFB, Ohio

## Abstract

A model of pilot control performance is developed to account for the effects of motion cues and external visual (VMC) cues. The starting point for the model is the optimal control model of the human operator, which has been well validated in fixed-base IMC (e.g., instrument cues) situations. The first goal was to incorporate motion cues by augmenting the controlled-state vector with the dynamic description of the vestibular sensory organs (semi-circular canal and otolith). Comparison of the model predictions with experimental results of motion-only tracking indicates that the noise signal ratio for the vestibular measurements can be modeled as approximately -18 dB. This new model was applied to a VTOL hovering task and did an excellent job of describing the control performance with and without motion cues, both on an absolute and relative basis. The difference between IMC and VMC visual cues was accounted for in the model by decreasing the quadratic penalty on roll rate (i.e., higher roll rates are allowed). The model provides a good description of control performance with and without motion and VMC cues, and predicts the change in scanning behavior observed under these conditions.

tion information, whereas the equalization and improvement in tracking ability comes primarily through the semi-circular canal contribution. Reference 4 used the data of Reference 5 to provide some interesting ideas concerning the weighting of perceived variables rather than absolute variables.

The objective in this effort is to provide a model which describes the important aspects of motion and VMC cues with the eventual intent of determining simulator requirements. Specifically, the goals are to show the differences in control performance between moving-base and fixed-base conditions as well as IMC and VMC conditions. The approach has been to modify the optimal control model of the human operator from those conditions in which it has already been validated (i.e., fixed-base IMC cues). To this end, the model was first applied to the roll tracking data of Reference 5 to determine those components in the model which describe the data. This portion of the model was next validated with the VTOL hovering task reported in Reference 6. The effects of VMC cues on the model parameters were evaluated using the data of Reference 7, and were then compared with both VMC and motion cues in other data reported in Reference 7.

## I. Introduction

Many successful attempts have been made to model the rms performance and equalization strategies of the human operator in the control loop. The two basic approaches are the frequency domain approach (Reference 1) and the optimal control formulation (Reference 2). These two approaches have stressed the fixed-base condition with visual cues being derived from instrument displays. The extensions of these models to include motion cues and VMC cues has been based on experimental data generated before the advent of the modeling effort. Reference 3 has compiled experimental data for a roll tracking task covering a wide range of controlled elements for three experimental conditions: motion only, visual only (IMC), and visual and motion combined. Reference 6 compared the pilot performance in the fixed-base configuration and moving-base with angular-only motion cues and linear and angular cues. Reference 7 reports roll control data taken in fixed-base IMC conditions, fixed-base VMC (large contact-analog display), in-flight IMC, and in-flight VMC.

Two attempts at combining these and other data into a model are described in References 3 and 4. Reference 3 concludes that the otolith provides low frequency orienta-

## II. Modeling Motion Cues

A block diagram of the optimal control model of the pilot is presented in Figure 1, which shows the information flow and the interaction of the pilot with the controlled element. The displayed information,  $y(t)$ , passes through the threshold element (either a psychophysical threshold or an indifference threshold). Perceptual observation noise,  $V_y(t)$ , is added to this quantity, which then passes through the perceptual time delay,  $\tau$ . The perceived displays,  $\hat{y}_p(t)$ , are the inputs to the core of the model, which consists of a Kalman filter and predictor to compensate for the observation noise and time delay. The current state estimate,  $\hat{x}$ , is combined linearly to provide a commanded control signal, to which is added motor noise,  $v_u$ , with the result passing through a neuromuscular/manipulator first order lag. The covariance of each observation noise depends on several important parameters and has the form

$$V_{y_i} = \frac{p_i}{f_i} \left[ \frac{\sigma_{y_i}}{N(\sigma_{y_i}, \alpha_i)} \right]^2 \quad (1)$$

where in the above expression  $V_{y_i}$  is the covariance of the

\* Research sponsored by USAF Flight Dynamics Laboratory, under Contract No. F33615-75-C-3069.

Paper also presented at the AIAA Visual Motion and Simulation Conference, 1976.

white observation noise;  $f_i$  is the fraction of attention devoted to the  $i$ th display;  $\sigma_{y_i}$  is the standard deviation of the  $i$ th displayed quantity;  $N$  is the describing function for the dead zone element of width  $2\sigma_{y_i}$ ; and  $\bar{y}_i$  is the multiplication noise/signal ratio which has been found to describe human performance under full-attention, fixed-base, visual IMC tracking. It has been found that a value of  $\bar{y}_i = -20$  dB (or  $.01$ ) provides a good description of the observed results.

One element of the model which is not shown in the block diagram is the quadratic functional which is minimized by the choice of the control gains,  $L$ . In its most general form this is

$$J = E \left\{ \int_0^{\infty} (y'Q_y y + x'Q_x x + \dot{u}'Q_{\dot{u}} \dot{u} + u'Q_u u) dt \right\}^2 \quad (2)$$

where  $Q_y$ ,  $Q_x$ ,  $Q_{\dot{u}}$ , and  $Q_u$  are weightings on the displays, state, control rate, and control, respectively. In practice, it has usually been sufficient to weight the display deviations from nominal and ignore weights on the state  $x$  and control displacement,  $u$ . The weights on control rate are chosen to provide a neuromuscular time constant ( $T_N$  in Figure 1) consistent with the manipulator, with a value of  $T_N = .1$  second being typical.

In spite of its seeming complexity, there are few free parameters in the model: for fixed-base IMC control tasks, these parameters are the display weights and display thresholds. A good prediction of control performance under these conditions can be obtained by weighting the display deviations inversely proportional to the square of their maximum values, and choosing thresholds consistent with an indifference value, i.e., a value a pilot is likely to accept without taking corrective action.

To extend the use of this model to incorporate motion cues, we first assume that the semi-circular canal and otolith signals can be represented by an equivalent set of vestibular organs aligned with the body axes, i.e., the coordinate transformations required would all be performed internally. Following Reference 3, we use the following transfer functions between the physical stimulus and the afferent firing rate (expressed in terms of the stimulus units):

Semi-circular canal

$$y_{scc}/\dot{\theta} = \frac{.0069 s^3 (s + 50)}{(s + .0555)(s + .0333)} \quad (3)$$

(deg/sec<sup>2</sup>)/(deg/sec<sup>2</sup>)

Otolith

$$y_{oto}/f = \frac{2.024 (s + .0988)}{(s + .20)} \quad (4)$$

These transfer functions represent the effects of the vestibular "displays" shown in the block diagram in Figure 1, with the dynamics of the vestibular sensors incorporated in the equations of the system dynamics.

To examine the effects of the noise to signal ratio for vestibular only measurements, the rms predictions of the model were compared with the experimental data described in Reference 5 for five typical plants. The shelf spectrum used in Reference 5 was approximated by a fourth-order filter as described in Reference 4. Figure 2 compares the

rms model predictions with the experimental data for noise to signal ratios. For all of these data, the motor noise was set at the recommended noise/signal ratio of -25 dB. At the present time the only explanation for the somewhat deviant behavior of the control plants  $k/s$  and  $k/(s^2 + 10)$  is the interaction of the motion with the manipulator, which might be accounted for by decreasing the motor noise for  $k/s$  and increasing it for  $k/(s^2 + 10)$ . Based on these comparisons, however, a representative noise to signal ratio for vestibular measurements appears to be approximately -18 dB, compared to the -20 dB typically used for visual inputs.

To test the model with these motion cues incorporated, it was used to predict the performance in a VTOL hovering task. This hovering task was run under three motion conditions: fixed base; angular cues only; and angular and linear cues. The dynamics were programmed in accordance with the simulation description (Reference 6). The weighting coefficients and indifference thresholds for the visual and vestibular inputs are shown in Table 1. No weights were applied on the vestibular outputs, i.e., the vestibular outputs were used as measurements only and were not to be nullified. The vestibular threshold levels were taken as three times the typical laboratory-determined thresholds, to account for masking and effects of the simulator. Using these parameters in the model resulted in the rms performance predictions shown in Figure 3, which also indicates the range of means of the three subjects. Figure 3 clearly demonstrates that there is good agreement, both qualitatively and quantitatively, between the model predictions and the results for the three subjects (a small population). Both the model and the experimental data show little difference between fixed-base and moving-base conditions because the simulator seemed to be operating near the vestibular thresholds much of the time (Reference 6).

Table 1. Weighting Coefficients and Indifference Thresholds, VTOL Hovering Task

Display Variables	Display Gain	Weighting Coefficient	Indifference Threshold
$x, y$	$1 \text{ in}/9.1 \text{ ft}$	$1/(1 \text{ in})^2$	.2 in
$u, v$	$(1 \text{ in/sec})/(9.1 \text{ fps})$	$(5 \text{ sec}/1 \text{ in})^2$	.2 in/5 sec
$\dot{\theta}, \dot{\phi}$	$5(180 - \pi) \text{ deg/rad}$	$1/(10 \text{ deg})^2$	2 deg
$\ddot{\theta}, \ddot{\phi}$	$5(180 - \pi) \text{ deg/sec}^2$	$(1 \text{ sec}/10 \text{ deg})^2$	2 deg/1 sec
$z$	1.0	$1/(10 \text{ ft})^2$	2 ft
$w$	1.0	$(5 \text{ sec}/10 \text{ ft})^2$	2 ft/5 sec
SCC	1.0	0	.57 deg/sec <sup>2</sup>
OTO	1.0	0	.015 g

### III. VMC Cues

The primary difference between IMC and VMC cues (as reported anecdotally) seems to be that the pilot is willing to tolerate larger excursions of attitude angle to more closely control position (Reference 6) or to use higher bank angle rates to null position error (Reference 7). There are several places in the model where this might be accounted for: decreased noise or threshold on angular rate because of increased peripheral stimulation, or by decreased weighting on attitude rate to reflect different pilot strategy. Both of

To determine the effects of these VMC cues in a more complicated condition, the model was used to predict the pilot describing function determined from in-flight experiments in a VMC roll control task as described in Reference 7. In comparing the predicted describing function and the measured values, we found good agreement except at low frequencies (a not uncommon characteristic of the model). The primary discrepancy between the predictions and the data lies in a low frequency fall off in gain and a corresponding increase in phase lead, whereas the pilots maintained the gain with no phase lead at frequencies below .3 radians per second. At the present time there is no adequate explanation for the difference between the model predictions and the data, since changing the weights on canals and otolith measurements in comparison to the visual display has only minor effect on the pilot describing functions shown here. The primary difference in the complete forward loop transfer function is that the model looks like a high gain first-order system at low frequencies, whereas the data imply that the forward transfer function behaves more like an integrator at these low frequencies.

The optimal control of the pilot has been extended to incorporate motion and visual cues outside the cockpit. The vestibular measurements appear to be adequately accounted for by incorporating their dynamic properties in the controlled element dynamics, and including their different signals as measurements with noise to signal ratios of approximately  $-17$  to  $-18$  dB. Using this approach we have accurately predicted the difference between fixed-base and differing moving-base cues in a VTOL hovering task both on an absolute and a relative basis. The incorporation of VMC cues in attitude control rates appears to be modeled by a change in the weighting coefficients of the quadratic cost functional, which are equivalent to raising the maximum value of attitude rate. Using this technique to predict pilot describing function data for both motion and VMC cues provides excellent agreement at the mid- to high-frequency range, but as yet there is no adequate explanation for the discrepancy between the model and reported data at low frequencies ( $1-3$  radians per second). In spite of this, it appears as though the model as it currently stands is capable of providing an excellent prediction of changes in pilot performance with the addition of motion and VMC cues.



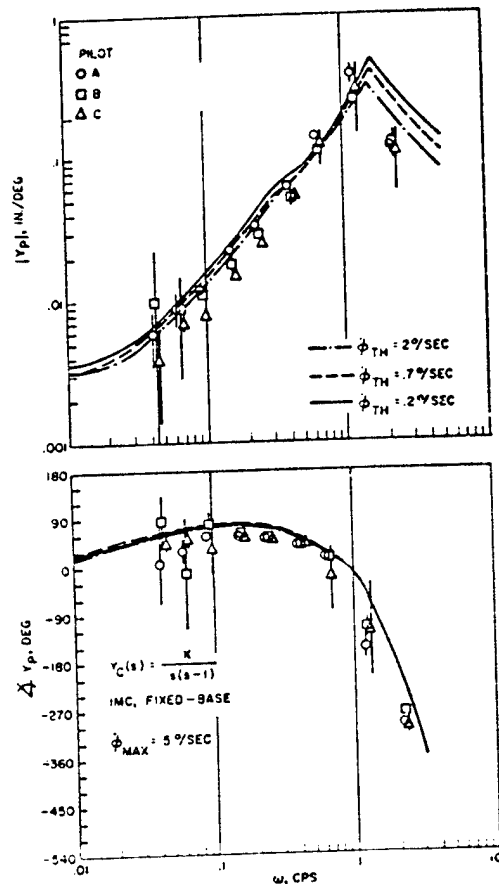


Figure 4. Effect of Attitude Rate Threshold on Pilot Describing Function (Reference 7).

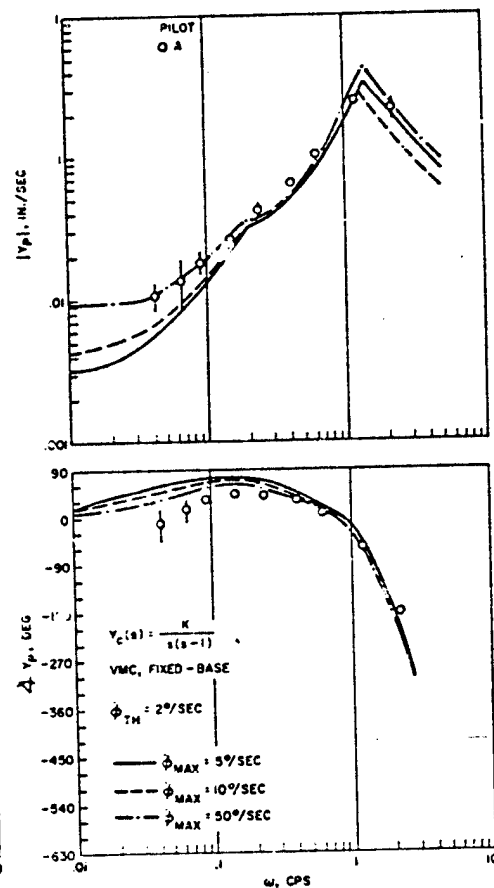


Figure 5. Effect of Attitude Rate Cost Weighting on Pilot Describing Function (Reference 7).

#### References

1. McRuer, D. T.; and Krendall, E. S.: Mathematical Models of Human Pilot Behavior. AGARDograph No. AG-188, January 1974.
2. Kleinman, D. L.; Baron, S.; and Levison, W. H.: A Control Theoretic Approach to Manual Vehicle Systems Analysis. IEEE Transactions on Automatic Control, AC-16, December 1971.
3. Stapleford, R. L.; Peters, R. A.; and Alex, F. R.: Experiments and a Model for Pilot Dynamics with Visual and Motion Inputs. NASA CR-1325, May 1969.
4. Dillow, J. D.; Picha, D. G.; and Anderson, R. O.: Slushy Weightings for the Optimal Pilot Model. Proceedings of the Eleventh Annual Conference on Manual Control, NASA TM X-62,464, May 1973.
5. Shirley, R. S.: Motion Cues in Man-Vehicle Control. Ph.D. Dissertation, Massachusetts Institute of Technology, Department of Aeronautics and Astronautics, January 1967.
6. Rineand, R. F.; Stapleford, R. L.; and Magdaleno, R. E.: Motion Effects on IFR Hovering Task - Analytical Predictions and Experimental Results. NASA CR-1933, November 1971.
7. Newell, F. D.; and Smith, H. J.: Human Transfer Characteristics in Flight and Ground Simulation for a Roll Tracking Task. NASA TN D-5007, February 1969.
8. Crmsby, C. C.: Model of Human Dynamics Orientation. NASA CR-132537, January 1974.

# THE EVALUATION OF PERIPHERAL DISPLAY UNITS IN A

## FIXED BASE SIMULATOR

by Lloyd D. Reid and Andrew J. Fraser

University of Toronto  
Institute for Aerospace Studies

### SUMMARY

As part of the design of a fixed base hovercraft simulator a peripheral display unit has been constructed. This unit operates in conjunction with a central computer generated perspective view of a roadway lined with poles and a horizon line. The peripheral display is controlled by the computer in such a manner as to duplicate the passage of the poles through the pilot's peripheral field of view.

In order to assess the effectiveness of the peripheral display, an automobile simulation was implemented and a tracking task carried out. The observed improvement in tracking performance with the displays operating was found to be statistically significant. In addition, subjective comments from those involved in the test program indicated that the peripheral displays aided much to the realism of the simulation.

### INTRODUCTION

The present display development has been undertaken as part of a program at our Institute to study air cushion vehicle technology. My interest is in putting together a fixed base simulator capable of performing useful air cushion vehicle control studies. In particular we intend to investigate the control of air cushion vehicles of modest size during cruise conditions when operated over restricted pathways. Such situations arise in river or overland applications in the Canadian North.

### GENERAL SYSTEM DETAILS

In order to achieve a suitable simulation of this task it is necessary to develop a display incorporating the essential visual cues. Based on a limited budget it was felt that this could best be achieved by using our mini-computer to generate a CRT display. The system is based on an HP 2100 driving an electronic X-Y plotter with an 20 x 28 cm CRT through a high speed 8 bit digital-to-analog converter. This results in a 256 x 256 dot matrix display. A TR-48 analog computer is used to simulate the vehicle

equations of motion.

The work station was configured with suitable vehicle controls. It was decided to augment the central display with a peripheral display in order to provide additional velocity cues and added realism.

#### CENTRAL DISPLAY

The format of the central display was selected to represent a straight pathway lined with marker poles. See Figure 1. This is a view, in perspective, of the scene as observed out the front cab window. The sides of the pathway provide lateral position cues, the poles provide velocity cues, and the vanishing point heading cues. A horizon line completes the picture and provides pitch and roll attitude cues. The amount of detail must be restricted to allow the mini-computer to maintain a display update rate sufficient to achieve smooth display motion. The present system is updated with a newly computed picture at a rate of 25 per second.

Figure 2 represents the display with non-zero vehicle attitude variables.

#### PERIPHERAL DISPLAY

The peripheral display units are located on either side of the central display. See Figure 3. As a pole leaves the central display it is picked up on the peripheral display at the appropriate time and, under mini-computer control, traverses the display screen. The correct angular position of the pole in the field of view is achieved through suitable software. The total field of view of the display is 170 when the viewer's eyes are 18 in. from the central display.

The mechanical features of the peripheral display units are shown in Figure 4. The front face of the unit is a translucent plexiglass screen. A single pole is projected on to the rear of the screen by using a vertical line light source. Motion of the pole is achieved by employing a galvanometer mounted mirror. The galvanometer deflection is controlled by a 12 bit high speed digital-to-analog converter that is part of the mini-computer system. The left and right hand units are under independent computer control. The poles can move, if required, either forward or backward since the system is based on position information. Each unit, however, is restricted to the display of a single pole. If a situation arises where two poles lie in the field of view represented by a single peripheral display unit then only the pole closest to the central CRT is displayed.

When a pole leaves the peripheral display the light beam is parked out of sight at the front end of the unit by driving the galvanometer at its maximum rate to this position. No detectable light beam motion results from this flyback operation. An alternative to this approach, namely the use of a shutter to blank the light source, was deemed to be too complex and unnecessary.

### DISPLAY EVALUATION

In order to evaluate the display it was first necessary to simulate some vehicle on the analog computer. Because the equations of motion for the air cushion vehicle were not yet available it was decided to simulate a car driving task. See Figure 5. This also simplified the job of finding qualified operators at this stage in the program. The equations of motion employed represent a standard North American sedan travelling at 30 mph (reference 1). A steering ratio of 20:1 was employed along with a 3° steering wheel deadband.

A task disturbance signal was incorporated in the form of a road wheel angle perturbation. This signal was made up of a sum of 4 sine waves with frequencies between 0.5 and 6.28 rad./sec. The dc level was zero and the rms corresponded to 3.25° of steering wheel angle. The diagram of Figure 6 represents the analog computer implementation of this system. (Note that  $Y_r$  has been dropped from the equations because  $V \gg Y_r$ .)

During the tests 3 display configurations were evaluated:

- Mode A: full central display and peripheral units.
- Mode B: full central display without peripheral units.
- Mode C: partial central display (poles absent) without peripheral units.

In the case of the latter (Mode C) no forward motion cues are present.

Over a period of several days, 3 subjects underwent a series of sessions in the simulator lasting about 45 min. each. The first few sessions were used for training, while the last three formed the data base for the experimental test results. The number of training sessions per subject was adjusted to ensure that each individual's learning curve had flattened out.

### TEST RESULTS

Typical tracking records are shown in Figure 7. Here  $\delta_d$  is the road wheel disturbance signal,  $\alpha_s$  is the steering wheel position,  $\psi$  is the

heading angle and  $T_y$  is lateral displacement from the center of the road. The task was to drive down a straight road in the presence of the disturbance signal. The car's speed was maintained at 30 mph by the computer. Tracking score was measured as the standard deviation of lateral position. After the training period and after the last test session, the subjects were questioned about their impressions of the simulator, and suggestions for improvements were invited.

Figure 8 gives the tracking scores achieved by the subjects based on 6 replicates per data point. The average of the scores achieved by all 3 subjects shows a 9% improvement in going from Mode B to A and a 14% improvement in going from Mode C to A. An analysis of variance performed on these data indicated that display mode effects were significant at the 5% level.

The following observations were made concerning the present simulation: An initial tendency to fixate on the motion of the vanishing point to the exclusion of road side line cues resulted in inadvertent control reversal, which was most pronounced (and persistent) in the Mode C display with its lack of forward motion cues. With training, subjects found they used an aiming point 60 to 90cm down the road and were then better able to utilize the display. During Mode C tests subjects stated that they lost all realism, and felt they were merely controlling an instrument. In general they felt that the motion cues provided by the poles on the central display were essential to the simulation and that the peripheral displays enhanced their ability to interpret the display as a real world situation.

#### CONCLUSION

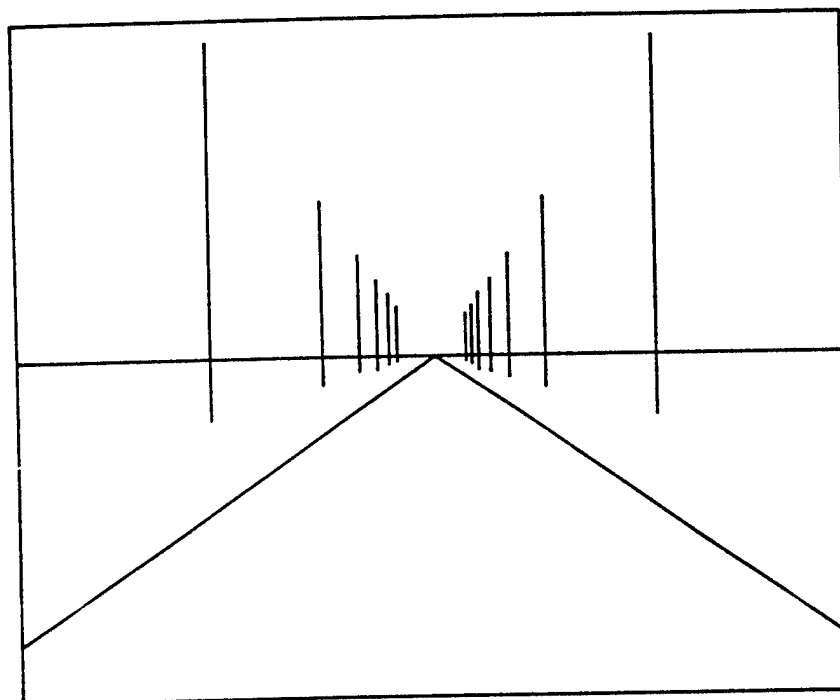
Use of peripheral displays to complement the motion depicted on a small two dimensional screen creates a more compelling simulation of the real world. Human operator performance improves under these conditions and they are more easily able to project into the task. In effect, the use of peripheral displays can generate a larger simulator display without greatly increasing system complexity.

(Further details concerning this project are contained in reference 2).

#### REFERENCES

1. Allen, R.W.; Jex, H.R.; McRuer, D.T.; and Di Marco, R.J.: Alcohol Effects on Driving Behaviour and Performance in a Car Simulator. IEEE Transactions on Systems, Man, and Cybernetics, Vol. SMC-5, No. 5, September 1975, pp. 498-505.

2. Fraser, A.J.: Development and Testing of a Fixed-Base Hovercraft Simulator. UTIAS Tech. Note. No. 197, December 1975.

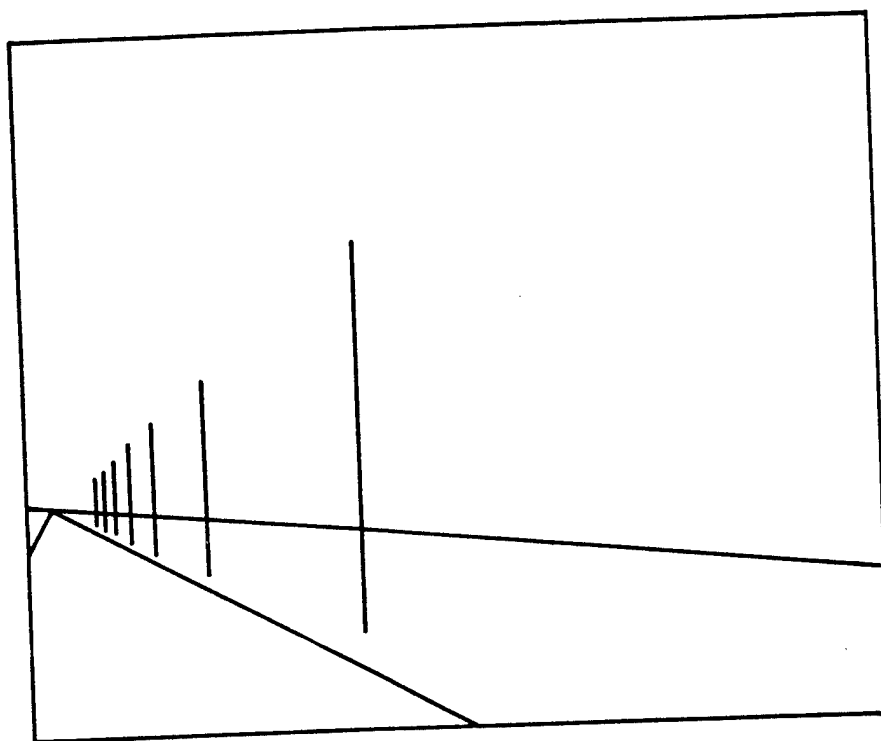


$\theta = 0$   
 $\phi = 0$   
 $\psi = 0$   
 $\chi = 0$

#### SIMULATION CONSTANTS

Pathway width	12 ft.
Distance-edge of road to pole	9 ft.
Distance to furthest pole	700 ft.
Distance between poles	100 ft.
Height of poles	25 ft.
Eye level	4 ft.

FIGURE 1



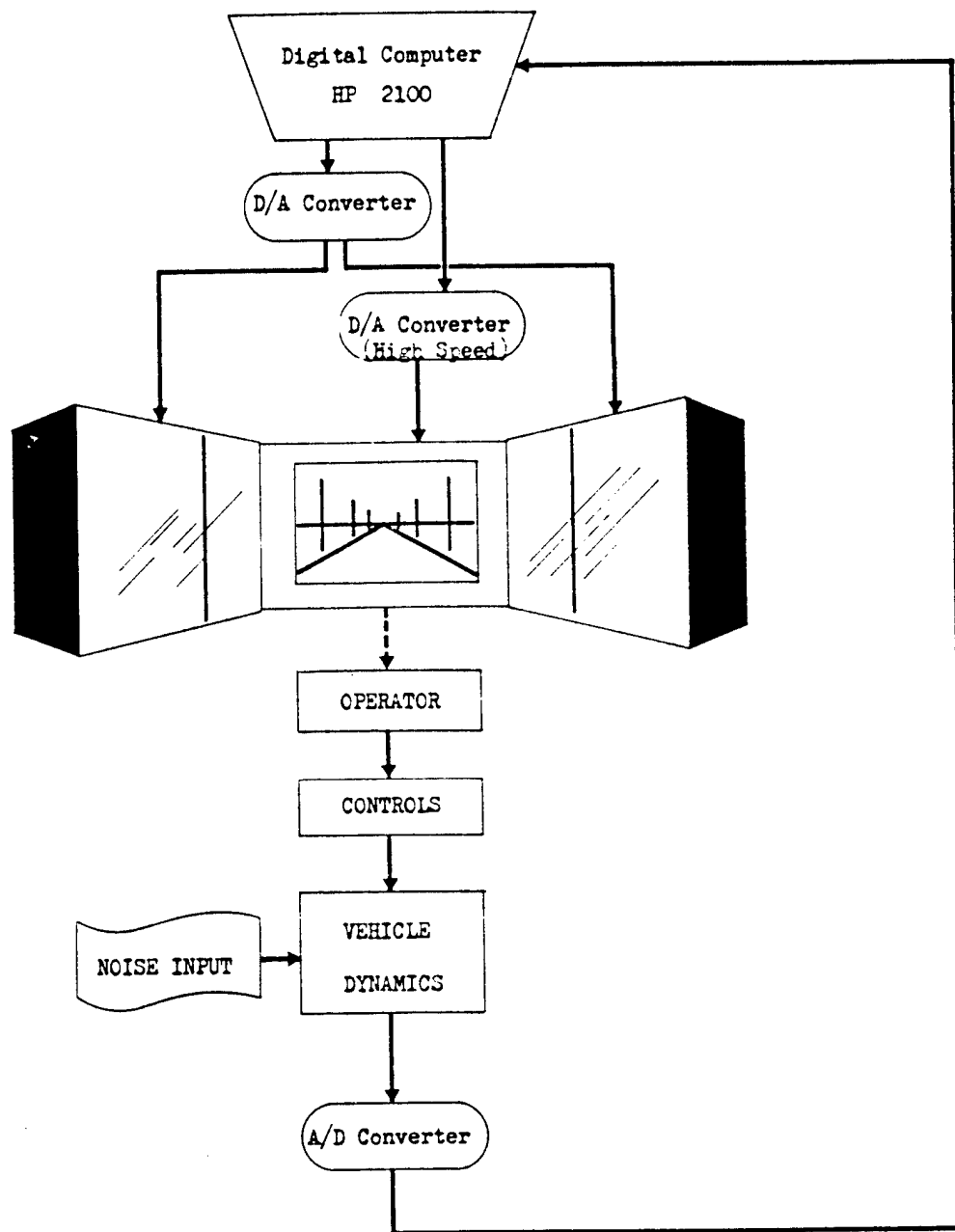
$\phi = - 0.1 \text{ rad.}$   
 $\theta = 0.1 \text{ rad.}$   
 $\psi = 0.25 \text{ rad.}$   
 $T_y = - 4.0 \text{ ft.}$

#### SIMULATION CONSTANTS

Pathway width	12 ft.
Distance-edge of road to pole	9 ft.
Distance to furthest pole	700 ft.
Distance between poles	100 ft.
Height of poles	25 ft.
Eye level	4 ft.

FIGURE 2





Simulation Control Flow

FIGURE 3

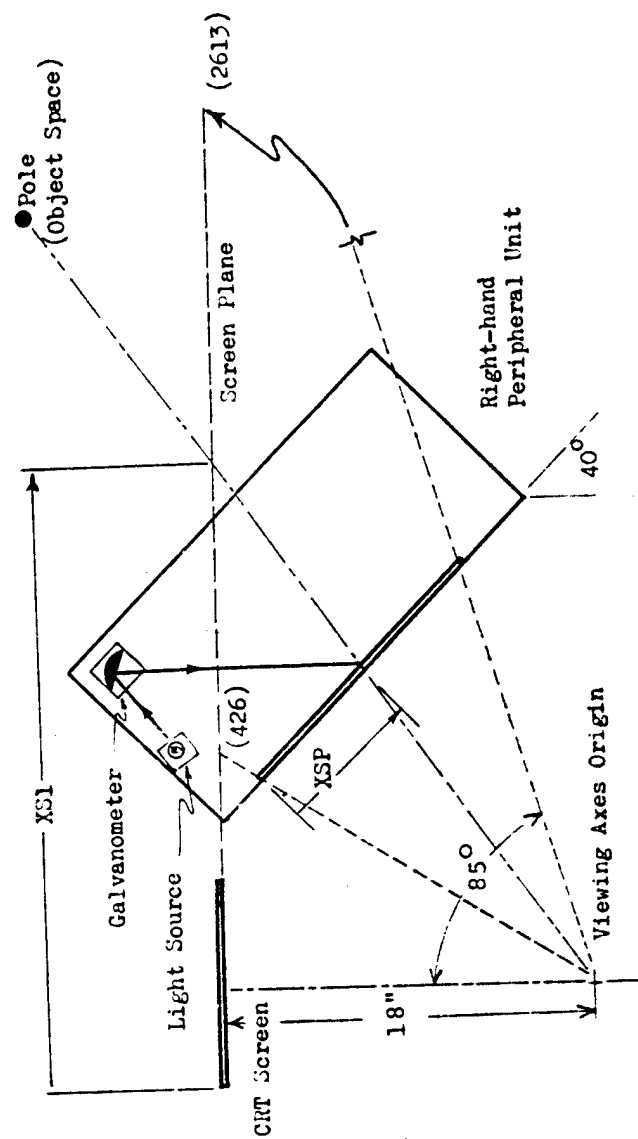
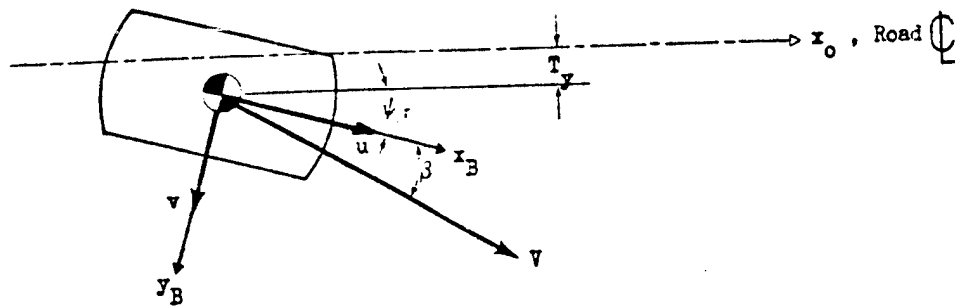


FIGURE 4



Automobile Motion Vectors

$$\begin{bmatrix} s - Y_v & V - Y_r \\ -N_v & s - N_r \end{bmatrix} \begin{bmatrix} v \\ r \end{bmatrix} = \begin{bmatrix} Y_\delta \\ N_\delta \end{bmatrix} \delta$$

Automobile Lateral-Directional Matrix

$$G_\delta^T = \frac{90.9(s^2 + 2(.36)(7.6)s + 7.6^2)}{s^2(s^2 + 2(.94)(5.6)s + 5.6^2)}$$

$$G_\delta^\psi = \frac{19.5(s + 6.1)}{s(s^2 + 2(.94)(5.6)s + 5.6^2)}$$

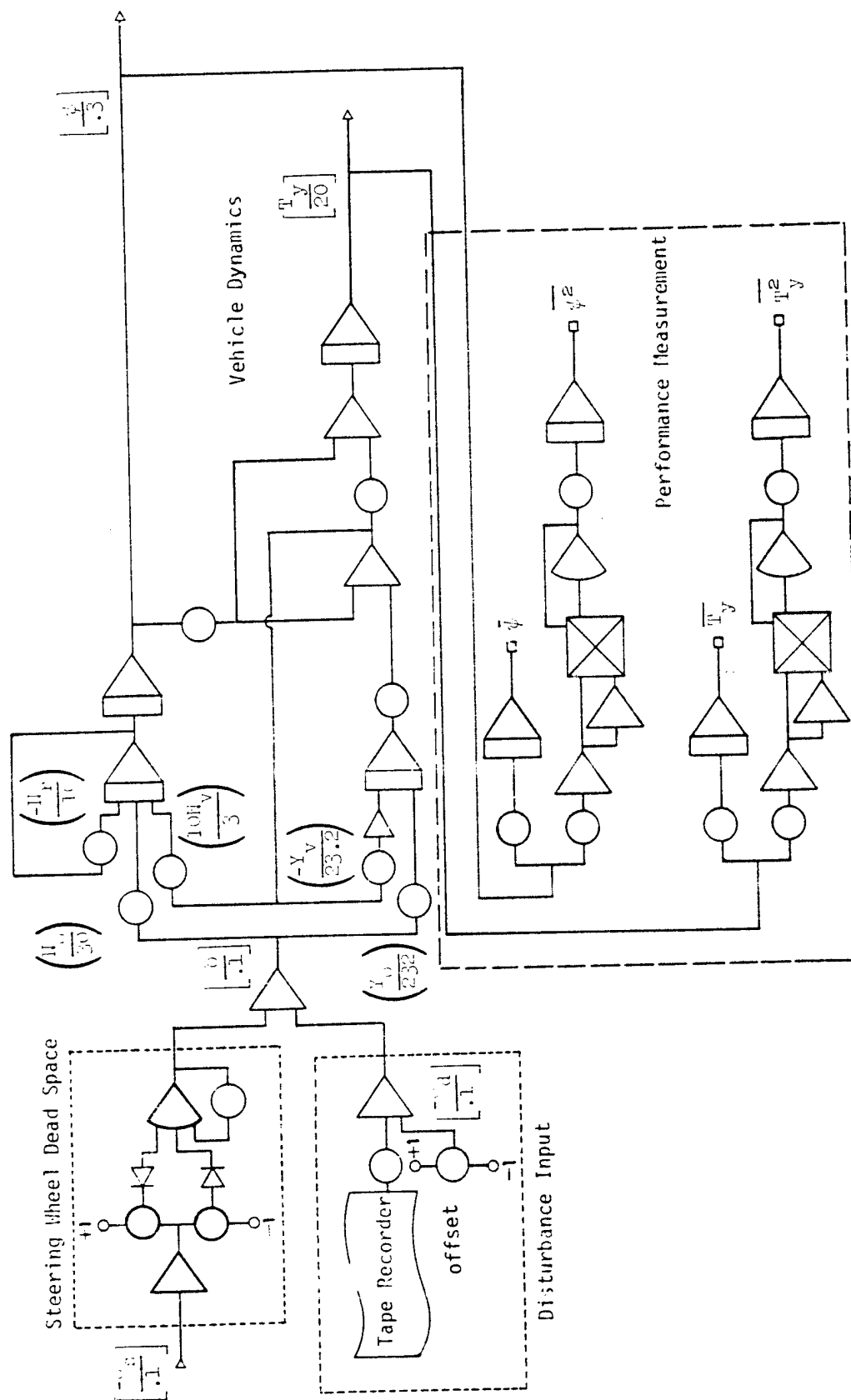
Automobile Transfer Functions

Vehicle: North American Sedan

Speed	44 fps
$Y_\delta$	90.9 ft/sec <sup>2</sup> - rad
$Y_v$	-5.6 sec <sup>-1</sup>
$Y_r$	2.87 ft/sec - rad
$N_\delta$	19.5 sec <sup>-2</sup>
$N_v$	0.094 rad/ft - sec
$N_r$	-4.86 sec <sup>-1</sup>

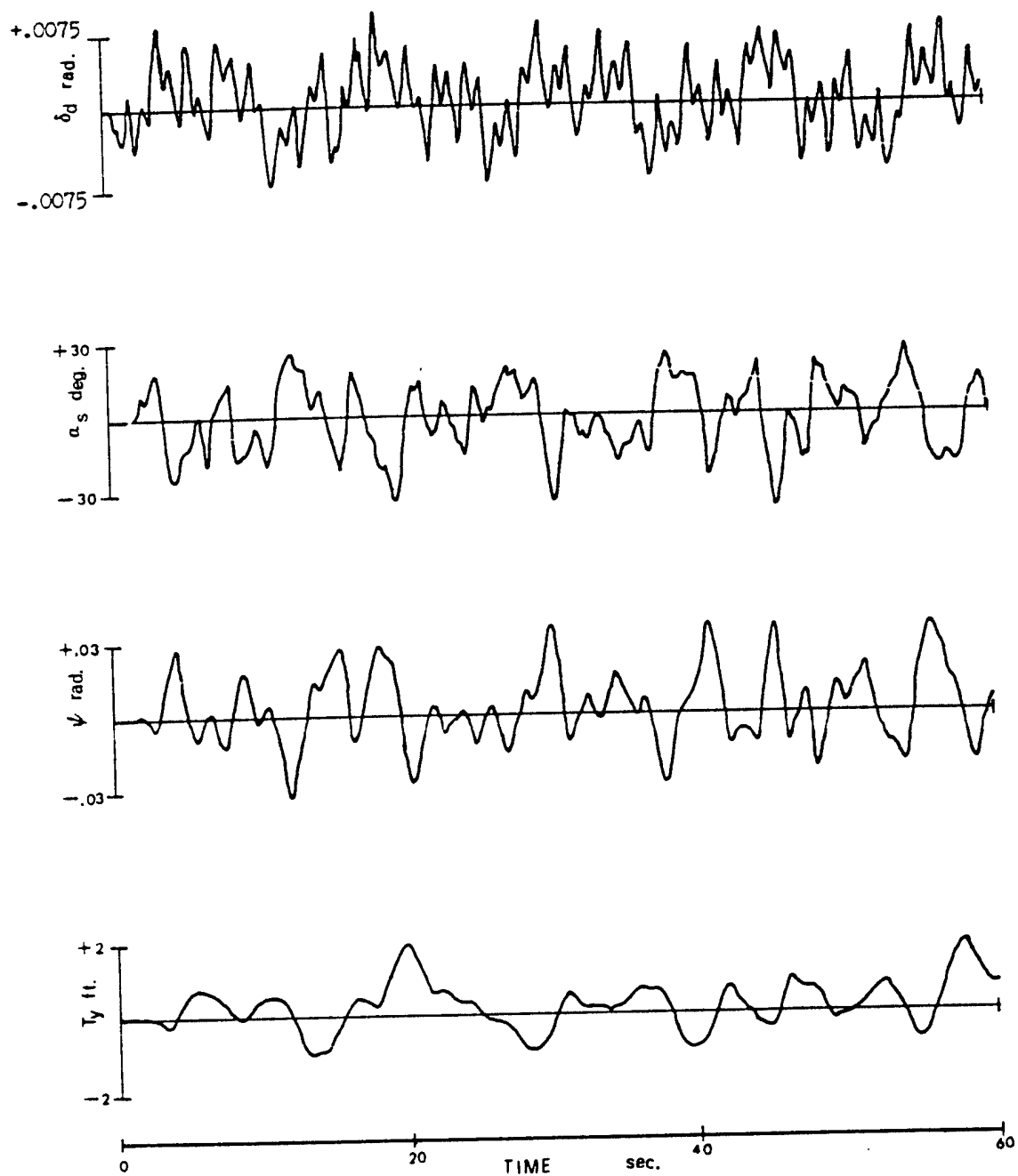
Automobile Dynamic Parameters

FIGURE 5



AUTOMOBILE SIMULATION ANALOGUE PROGRAMMING

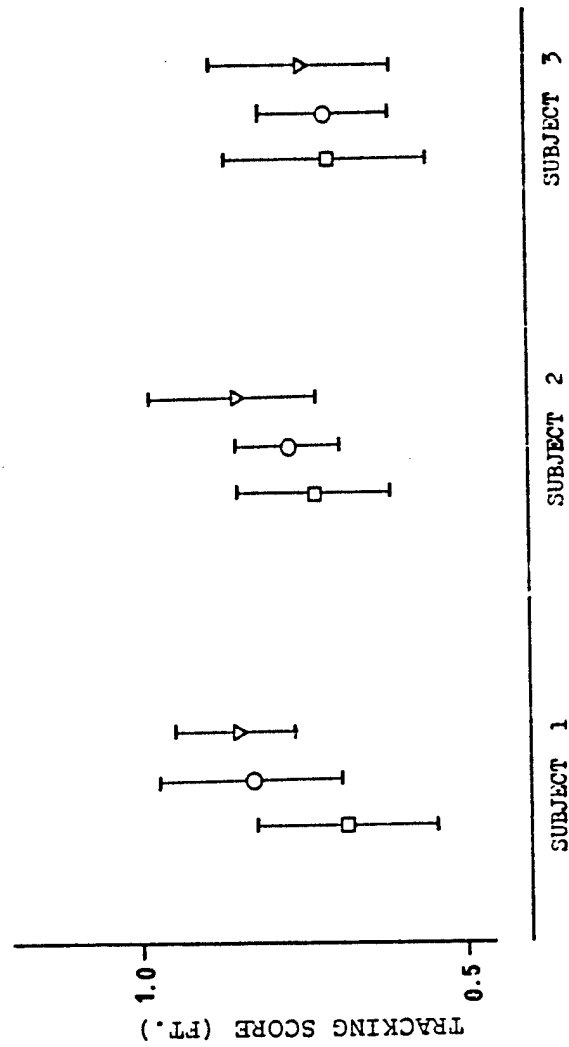
FIGURE 6



Time Trace of Subject Performance

FIGURE 7

□ MODE A: FULL CENTRAL DISPLAY AND PERIPHERAL UNITS.  
 ○ MODE B: FULL CENTRAL DISPLAY WITHOUT PERIPHERAL UNITS.  
 ▽ MODE C: PARTIAL CENTRAL DISPLAY (POLES ABSENT) WITHOUT PERIPHERAL UNITS.



Mean Performance Scores by Subject & Mode  
 (Bars Indicate Standard Deviation)

FIGURE 8

## ROLL AXIS TRACKING IMPROVEMENT RESULTING FROM

### PERIPHERAL VISION MOTION CUES

Thomas E. Moriarty, Air Force Institute of Technology  
Andrew M. Junker, Aerospace Medical Research Laboratory  
Don R. Price, Aeronautical Systems Division

#### SUMMARY

Subjects performed a compensatory roll-axis tracking task, with and without peripheral vision motion cues. Controlled vehicle dynamics, of the general forms  $K/S^2$  and  $K/S^3$ , were simulated on an analog computer. Control was commanded via a force stick in a stationary cockpit mockup. Plant roll rate, in the form of vertically moving black and white grid lines, was displayed on television screens positioned on either side of the cockpit. The target aircraft's motion was simulated by a sum-of-sines input forcing function.

Roll axis tracking performance is shown to improve marginally stable plants of the general form  $K/S^3$ , when peripheral plant roll rate information is provided. Subject-controlled plant describing functions are compared for both plants, with and without the peripheral motion cues. Subject describing functions are also compared. The tracking error spectra are broken into correlated and remnant contributions, and are compared for all four conditions.

#### INTRODUCTION

In the last ten years, research has been performed which indicates that peripheral vision cues might be used to assist in accomplishing manual control tasks (Ref 1, 2, 3). This is particularly attractive from the viewpoint of allowing the human controller to have additional information without increasing the complexity of his foveal display. Another motivating factor for research into peripheral vision cues is the possibility of substituting, at least in part, peripheral vision displays for actual moving base capabilities in simulation.

The Aerospace Medical Research Laboratory at Wright-Patterson AFB, Ohio is presently engaged in a long term study of the effects of motion on the human operator, including the effects of both peripheral vision motion cues and actual moving base cues for roll-axis tracking tasks. This experimental study, performed by personnel at the Air Force Institute of Technology at Wright-Patterson AFB, is in support of the laboratory's overall effort and addresses the specific question of whether a stationary operator's performance of roll-axis compensatory tracking is improved when controlled plant roll

rate, in the form of vertically moving black and white grid lines, is displayed in the human operator's field of vision. Implicit in this study is an analysis of the operator's control strategy and performance characteristics.

#### LIST OF SYMBOLS

$Y_c$ - controlled plant transfer function	$\phi_{ee_c}$ - correlated error power spectrum
$Y_s$ - subject describing function	$\phi_{ee_r}$ - remnant error power spectrum
$\phi_m$ - phase margin	$\omega_c$ - system gain crossover frequency

#### EXPERIMENT DESCRIPTIONS

Subjects were given a roll axis tracking task in a fixed-base simulation shown schematically in Figure 1. In particular, the subjects were asked to follow a target aircraft in the roll axis by minimizing the centrally displayed angular error. The task was accomplished both with and without peripheral display units which provided the subject with the plant roll rate.

Controlled Plant Dynamics. Two different controlled plants were used in the experiment. The choice of plant dynamics permitted a comparison of peripheral vision motion cue effects on human operator control strategy for different levels of task difficulty. The "easy" plant had a transfer function of

$$G(s) = \frac{135}{s(s+1)(s+10)}$$

and was considered to be an easy plant to control ( $\sim \frac{K}{s}$ ). The "difficult" plant was designed to be more difficult to control ( $\sim \frac{K}{s^3}$ ) and consisted of

$$G(s) = \frac{63.75}{s^2(s+0.5)(s+10)}$$

Figures 2 and 3 show the frequency responses of the easy and difficult plants respectively. The characteristics were similar to two of the plants used in a motion effects study performed by Junker and Replogle (Ref 4:819-822).

Sum-of-Sines Tracking Input. A different sum-of-sines input signal was used with each of the two controlled plants. The input for the easy plant was the sum of 12 sinusoidal components with a bandwidth of 1.25 radians/sec and a 20 degree RMS amplitude, and is shown on Figure 2. For the difficult



plant, the 12 components had a bandwidth of 0.5 radians/sec and an RMS amplitude of 40 degrees. Figure 3 shows the input power spectrum for the difficult plant. Table 1 contains a list of the twelve input frequencies.

Table 1

Input Forcing Function Frequencies (rad/sec)

$\omega_1 = 0.077$	$\omega_7 = 1.572$
$\omega_2 = 0.192$	$\omega_8 = 2.378$
$\omega_3 = 0.307$	$\omega_9 = 3.567$
$\omega_4 = 0.460$	$\omega_{10} = 5.369$
$\omega_5 = 0.690$	$\omega_{11} = 8.053$
$\omega_6 = 1.035$	$\omega_{12} = 12.080$

EQUIPMENT & FACILITIES

The controlled plant dynamics were simulated on analog computers which accepted inputs from a side-mounted force stick and produced output signals to drive the central and peripheral display units. A digital computer was used to generate the sum-of-sines input forcing function, and was also used for data collection and frequency analysis computations. The subject was seated in a stationary fighter-type cockpit mockup which was, in turn, in an isolated room with a low light level. The central and peripheral displays were positioned as shown in Figure 4.

Central (Foveal) Display. The foveal display was presented on a  $12\frac{1}{2}$  in by  $12\frac{1}{2}$  in square area of a television monitor. The inside-out display consisted of a  $1\frac{7}{8}$  in long rotating line whose center was superimposed upon a stationary horizontal line, as shown in Figure 5. Upright orientation was provided by a  $1/8$  in perpendicular line at the center of the rotating line. The angle between the rotating and stationary lines,  $\phi_e$ , depicted the difference between the controlled plant roll angle and the forcing function roll angle.

Peripheral Display. The peripheral display was presented on two 21 inch televisions placed on opposite sides of the cockpit mockup as shown in Figure 4. The two television screens were vertically located such that their midpoints were within  $1\frac{1}{2}$  degrees of subject eye level. The horizontal position of the screens was such that the peripheral viewing field went from 40 degrees nasal to 90 degrees nasal.

The peripheral display presented plant roll rate in the form of vertically moving alternate black and white bars  $2 \frac{3}{4}$  in wide. The bar motion was scaled such that

$$V_p = 16.5 \omega$$

where  $V_p$  was the display pattern vertical velocity in in/sec and  $\omega$  is the instantaneous plant roll rate in rad/sec. The distance between the center-line of the foveal display and each peripheral display is 16.5 in. Polarity was such that the motion of the lines represented the apparent background motion that would result from cockpit motion.

#### EXPERIMENTAL PROCEDURE

Four experimental conditions were experienced by each subject. The subjects were divided into two groups, denoted as "morning" and "afternoon" and then briefed on the experimental task. The three subjects in the morning group first experienced the "easy" plant without peripheral display; and daily replications were accomplished until the RMS error scores indicated that the subjects had reached a sustained level of task proficiency. After the subjects had "learned" the task, signals were recorded for subsequent analysis. The peripheral display was then added and the morning subjects performed the task until learning had been achieved and data could be recorded. The afternoon group of three subjects performed the same tasks but were exposed first to the easy plant with peripheral display and then to the task without the peripheral units.

The experimental procedure for the "difficult" plant was changed somewhat due to subject limitations. The number of subjects was reduced by one and they were combined into one group. In an attempt to insure that separate control strategies could be developed without biasing, each subject experienced alternating tasks of one run with peripheral followed by one run without the peripheral display.

#### Data Recording

RMS error scores were computed from digitized data for each subject and each run. Once the RMS error scores indicated that the subjects of an experimental group had "learned" the tracking task for a given experimental condition, time histories were digitized and recorded for use in analyzing subject control strategy. The time histories from the last 4 replicates for each subject in each condition consisted of input forcing function, error, stick, and controlled plant output signals.

## DATA ANALYSIS

A Fast Fourier Transform (FFT) technique was used to convert the raw digital data into useful performance measures. Power spectral densities were generated for both correlated and remnant components of the input, error, stick (subject) and plant signals. Transfer characteristics (describing functions) were calculated for the subject and the subject-plant combination.

The analysis methods used in this study are based upon those presented in Ref 5, and will be briefly summarized here.

For a 12 component sum-of-sines input, correlated power can only exist at the twelve nominal input frequencies. Thus, any power observed at non-input frequencies is directly identifiable as remnant under the usual definition (Ref 6, 7, 8). For each recorded experiment run, the remnant power was calculated at the FFT frequencies (base frequency  $\omega_0 = 0.038$  rad/sec) over a frequency band encompassing 0.125 octaves on either side of, but not including, each nominal frequency. Correlated power at the nominal frequency was then computed as the difference between the total power at the nominal and the average remnant in the corresponding band.

The experimental results were combined by groups for presentation and the statistical significance of apparent group mean data was determined by means of a small sample t-test (Ref 9). The group means along with an indication of plus-or-minus one standard deviation were used for graphical presentation.

## RESULTS AND CONCLUSIONS

The results and conclusions are presented with emphasis upon determining if the peripheral motion cues improved subject performance in the compensatory tracking task and, when performance was improved, determining how the peripheral cues were used. Overall subject performance is presented first, using RMS error scores of the tracking task as the performance metric. Analysis of subject control strategy follows and is performed in the frequency domain.

### RMS Tracking Error

Figures 6 and 7 show the group RMS tracking error scores for the "easy" and "difficult" tasks respectively. The means (indicated by circles) and standard deviations are plotted by day for each of the two experimental conditions encountered for each plant.

The morning groups performance for the easy plant is not shown because a circuit malfunction in the analog computer plant simulation made it difficult to validly compare the peripheral to nonperipheral condition tracking

error scores.

The afternoon group "easy" plant tracking error, shown in Figure 6, indicates that after learning has occurred there is little improvement to be obtained by providing peripheral roll rate information. Applying a t-test to the last four runs with peripheral and the last four runs without peripheral resulted in no significant difference between the population samples ( $< 0.6$  level).

The "difficult" plant results, shown in Figure 6, show that the use of the peripheral plant roll rate display yields a significant ( $> 0.001$  level) reduction in the RMS tracking error.

It can thus be concluded that for more difficult plants ( $K/s^2$ -type controlled plant dynamics) roll-axis tracking performance of a static human controller is significantly improved when plant roll rate information, in the form of vertically moving black and white horizontal grid lines, is displayed in the peripheral field of vision. Tracking performance is not significantly improved by displaying plant roll rate in the human operator's peripheral field of vision when the controlled plant is stable with control dynamics of the form  $K/s^2$ .

#### Frequency Domain Analysis

Frequency domain data and analysis of the tracking task results are presented separately for the two controlled plants with the "easy" plant results treated first. In order to assess the effect of the peripheral display upon the correlated portion of the subject's response, the group mean subject-controlled plant describing functions ( $Y_s Y_c$ ) are compared for the two conditions of with and without peripheral displays. The group mean subject describing functions ( $Y_s$ ) are then compared and finally the associated error signal power spectra ( $\dot{e}_{ec}$  and  $\dot{e}_{er}$ ) are examined. All data plots depict group mean values in circles with an indication of plus or minus one standard deviation.

"Easy" Plant. Figures 8 and 9 show the  $Y_s Y_c$  describing function for the two conditions of with peripheral display and without peripheral display respectively. A visual comparison of the two describing functions yields little noticeable difference and since  $Y_c$  is constant over the two conditions, the subject describing function  $Y_s$  should yield a more direct indication of different control strategies. Figures 10 and 11 are plots of the group mean describing functions without and with the peripheral roll rate display. The  $Y_s$  data agrees with the  $Y_s$  characteristics implied by the  $Y_s Y_c$  describing functions. The  $Y_s$  data points which differ the greatest in value for the two experimental conditions were at  $\omega = 1.035$  rad/sec, the

difference was not significant at the 0.1 level. Both group  $Y_s$  describing functions exhibit similar adjustment characteristics. First order lead was applied over the measurement range through the crossover frequency, but the accompanying phase angles indicate lag/time-delay effects below the measurement range. Additional lead was applied at frequencies beyond crossover prior to the well known high frequency neuromuscular lag effects appearing between  $\omega=5$  and  $\omega=10$  rad/sec.

Easy plant group error power spectra averages are presented in Figures 12 and 13. Included on the figures are the average percentages of total error power, and one standard deviation, calculated for correlated and remnant error contributions. In both cases, the remnant error power was less than 25 percent of the total error power. Correlated error power magnitudes were relatively constant at nominal input frequencies up to slightly beyond the system crossover frequency and fell off sharply thereafter. The two correlated error spectra show no appreciably different characteristics.

The two continuous remnant power spectra were similar in waveform shape with the greatest values of remnant power occurring at the lower frequencies of the measurement band. In each case, a lower magnitude plateau is evident for a frequency band that includes the system crossover frequency, and a high frequency roll-off is observed similar to that noted for the correlated error signal.

"Difficult" Plant. Subject - controlled plant describing functions with the difficult plant as the controlled element are presented in Figures 14 and 15. The  $Y_s Y_c$  describing functions differ in amplitude slope and phase angle at the lower frequencies but are strikingly similar at the higher nominal input frequencies. The crossover frequency is about  $\omega=1.4$  rad/sec in each case but the phase margin ( $\phi_m$ ) is about 38 degrees with the display and about 22 degrees without the display.

Group averaged subject describing functions,  $Y_s$ , are shown in Figures 16 and 17. The  $Y_s$  describing functions indicate that considerably more low frequency lead was generated with the peripheral display present. The phase angle differences were significant at less than the .001 level for measurement frequencies  $\leq 1.572$ . The describing functions both reflect a 40 db/decade slope at and somewhat above the crossover frequency with higher frequency lag effects above  $\omega=5$  rad/sec.

Figures 18 and 19 show the error power spectra without and with the peripheral display respectively. The spectra present the same general characteristics for the two conditions but they do differ in magnitude. Annotations on the figures indicate the significantly higher percentage of correlated error present when the peripheral information was available. Error correlated power is comparable for both conditions except at the frequencies near crossover where error levels for the peripheral display condition is somewhat less. Both remnant spectra are relatively flat through  $\omega_c$  and roll off sharply at higher frequencies, similar to the corre-

lated power high frequency decrease. Remnant power with the peripheral display present is consistently 4 to 6 db less at frequencies below gain crossover.

### CONCLUSIONS

The  $Y_{s_c}$  and  $Y_s$  describing functions did not indicate any appreciable differences in subject control strategy due to peripheral display effects for the easy plant. Minor differences can be observed, but since there was no apparent improvement in tracking performance or changes in error spectra, the overall conclusion is that peripheral rate display has little effect upon the subject's roll axis tracking performance for the easy ( $\frac{K}{s}$ ) plant.

For the more difficult plant, the presence of peripheral rate information allowed the subjects to insert more low frequency lead. Above crossover, there were essentially no difference between the describing functions for the two conditions. The correlated error power spectra showed minor differences but the remnant contribution to total power was appreciable reduced in the peripheral display condition. The remnant power was reduced mostly in the frequency range below crossover. Thus, it can be concluded that for the difficult ( $\frac{K}{s}$ ) controlled plant, the roll-axis tracking performance of a static human controller is significantly improved when plant roll rate information, in the form of vertically moving black and white horizontal grid lines, is displayed in the peripheral field of vision.

### REFERENCES

1. Vallerie, L. L. Peripheral Vision Displays. NASA CR-808. Washington: National Aeronautics and Space Administration, June 1967.
2. Rogers, J. G. "Peripheral Contrast Thresholds for Moving Images." Human Factors, 14:199-205, (June 1972).
3. Emer, E. L. A Study of Pilot Performance During a Glide-Slope Approach When Rate Information is Supplied Via the Peripheral Vision. AFIT Thesis GE/MA/74D-2, W-PAFB, Ohio: Air Force Institute of Technology, December 1974. AD A005284
4. Junker, A. and C. Replogle. "Motion Effects on the Human Operator in a Roll Axis Tracking Task." Aviation, Space, and Environmental Medicine, 46:819-822 (June 1975).

5. Levison, W. H. Techniques for Data Analysis and Input Waveform Generation for Manual Control Research. BBN Technical Memorandum CSD-75-2. Cambridge: Bolt, Beranek, and Newman, Inc., January 1975.
6. McRuer, D. T., et al. Human Pilot Dynamics in Compensatory Systems, Theory, Models, and Experiments with Controlled Elements and Forcing Function Variations. AFFDL-TR-65-15. W-PAFB, Ohio: Air Force Flight Dynamics Laboratory, July 1965.
7. Levison, W. H. and D. L. Kleinman. "A Model for Human Controller Remnant." Fourth Annual NASA-University Conference on Manual Control. 3-14, NASA SP-192. Washington: National Aeronautics and Space Administration, 1969.
8. Jex, H. R., et al. Display Format Effects on Precision Tracking Performance, Describing Functions, and Remnant. AMRL-TR-71-63. W-PAFB, Ohio: Aerospace Medical Research Laboratory, August 1972.
9. Chapanis, A. Research Techniques in Human Engineering. Baltimore: The John Hopkins Press, 1959.

# SIGNAL DEFINITIONS

$\Phi_i$  = INPUT FORCING FUNCTION (TARGET ROLL ANGLE)

$\Phi_e$  = ROLL ANGLE ERROR

$\dot{\Phi}_c$  = CONTROL STICK OUTPUT

$\Phi_p$  = PLANT ROLL ANGLE

$\dot{\Phi}_p$  = PLANT ROLL RATE

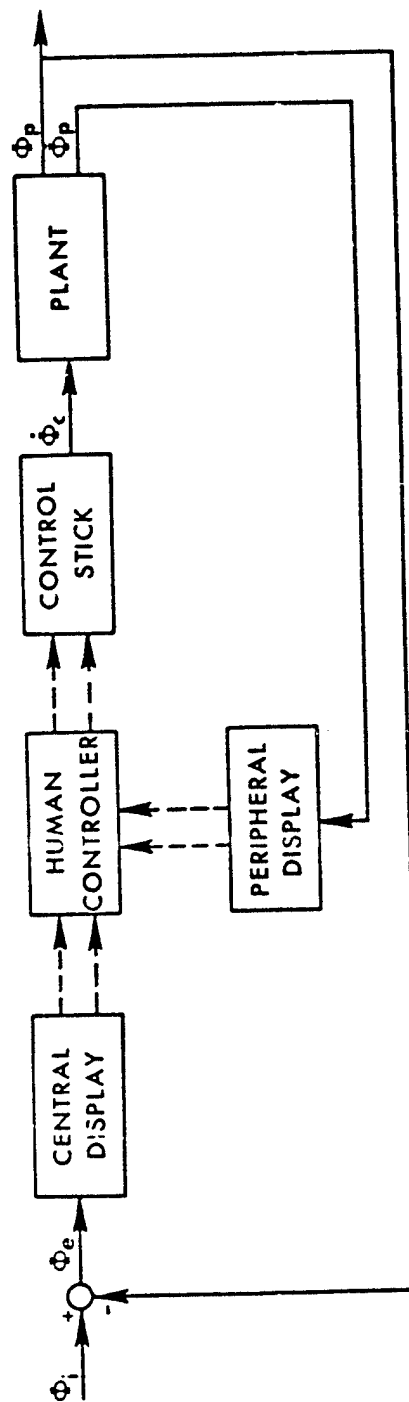


Figure 1. Simulation Block Diagram for Roll Axis Tracking Task



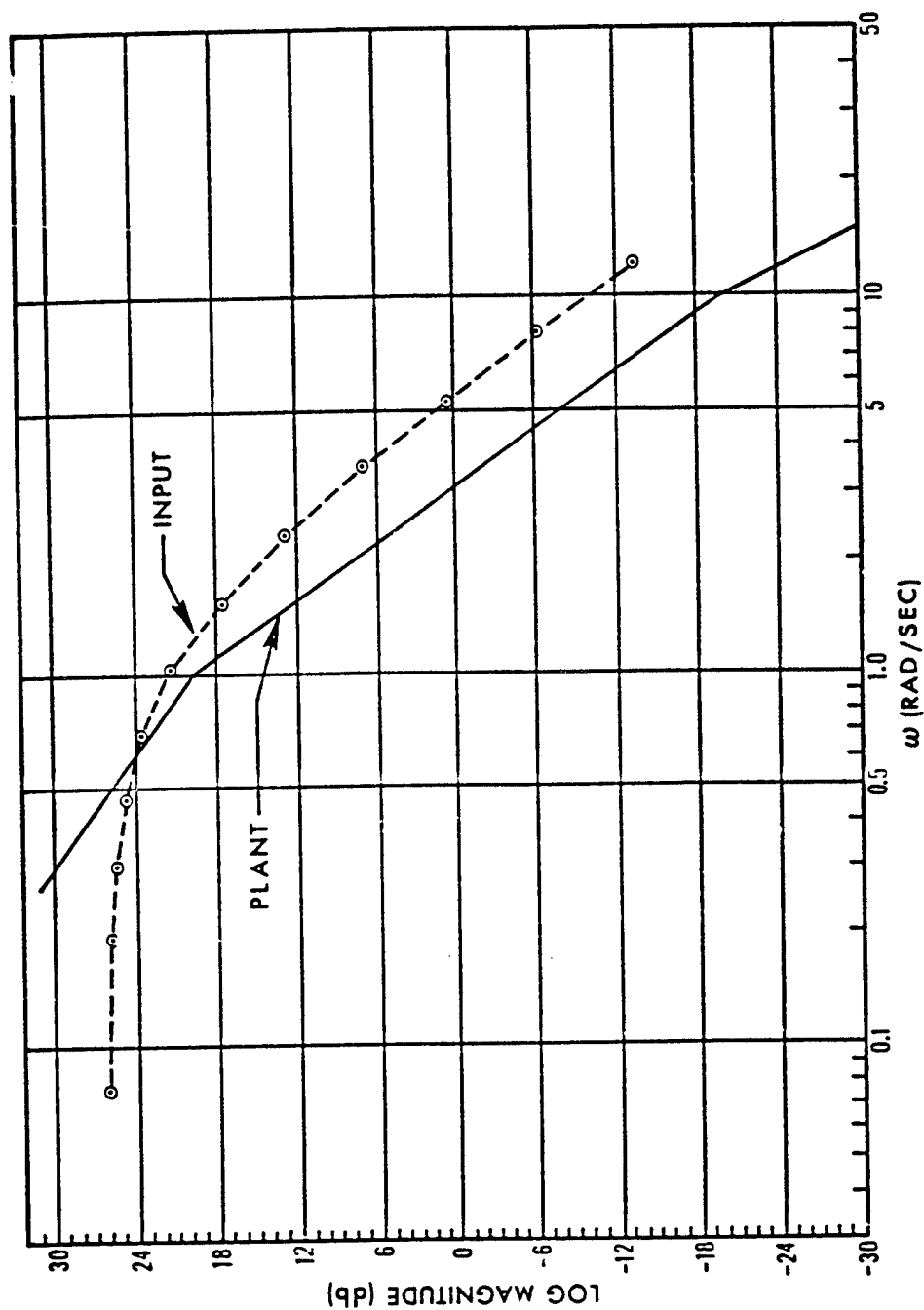


Figure 2. Easy Plant Frequency Response and Input Power Spectrum  
(Frequency Components Denoted by Circles)

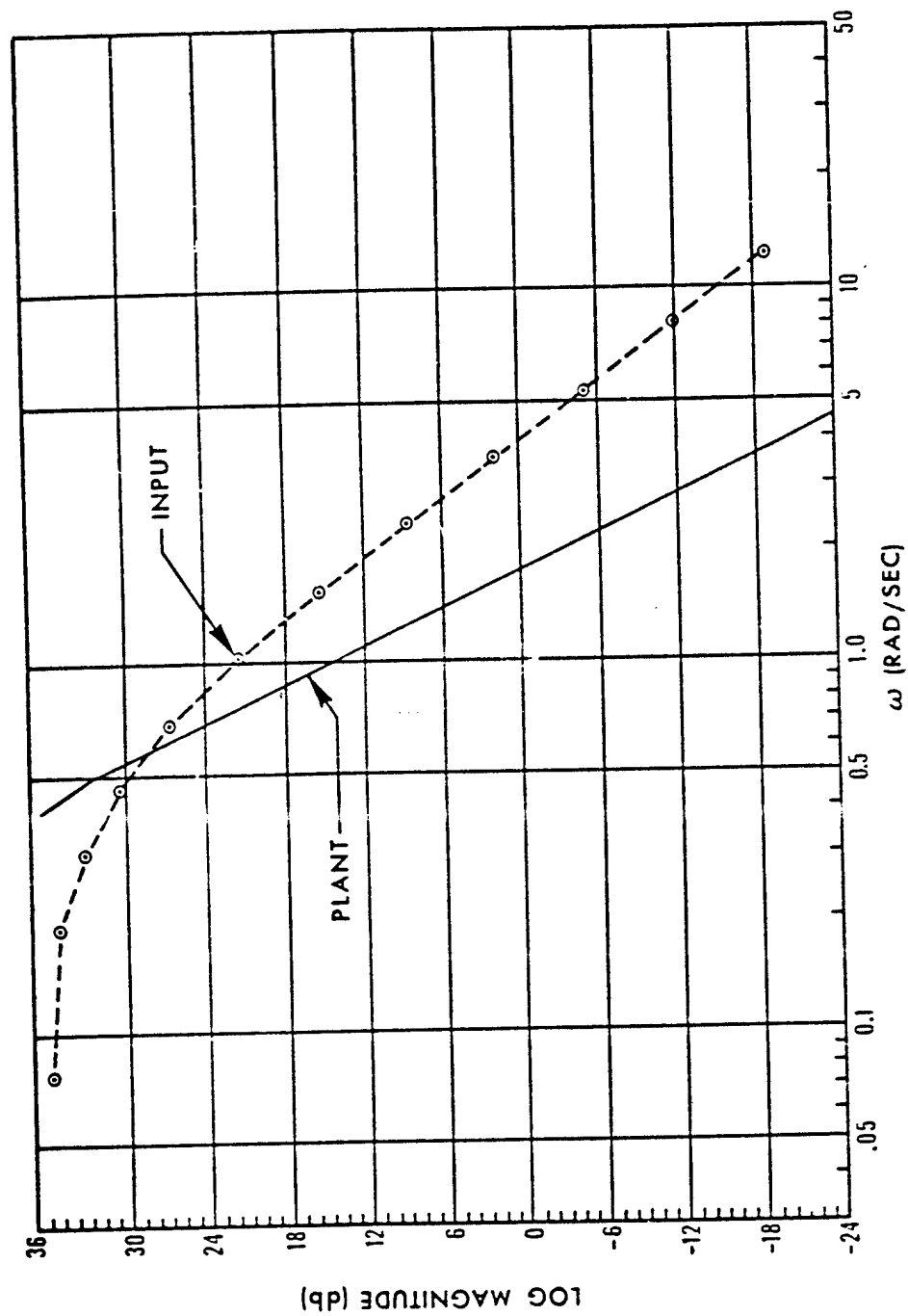


Figure 3. Difficult Plant Frequency Response and Input Power Spectrum  
(Frequency components denoted by Circles)

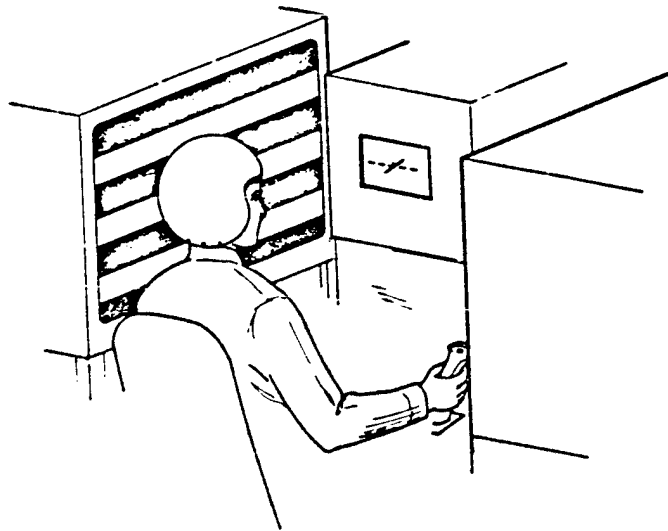


Figure 4. Display Layout

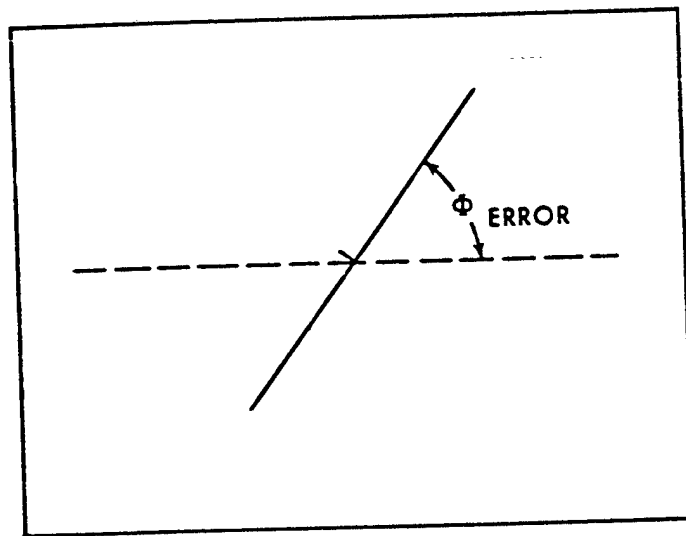


Figure 5. Central Display

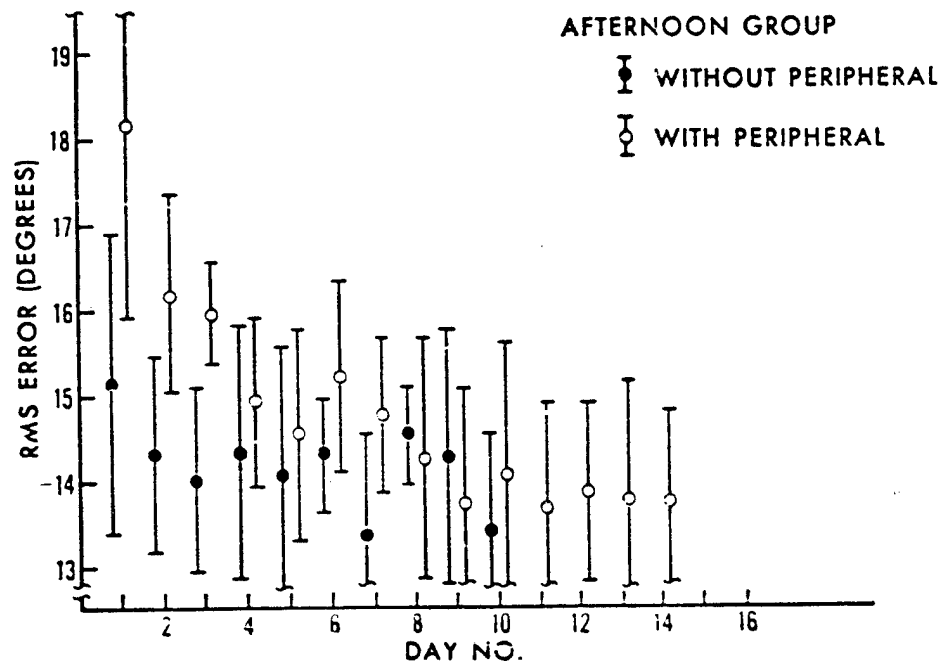


Figure 6. RMS Error Scores for Easy Plant

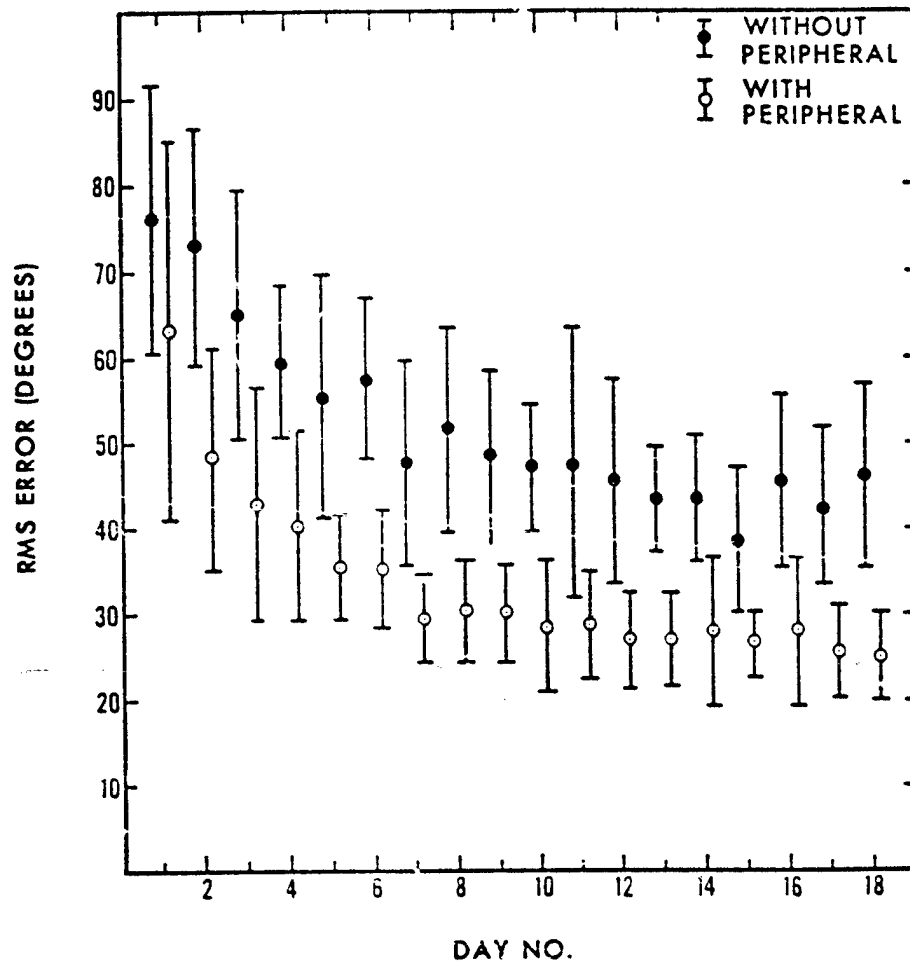


Figure 7. RMS Error Scores for Difficult Plant

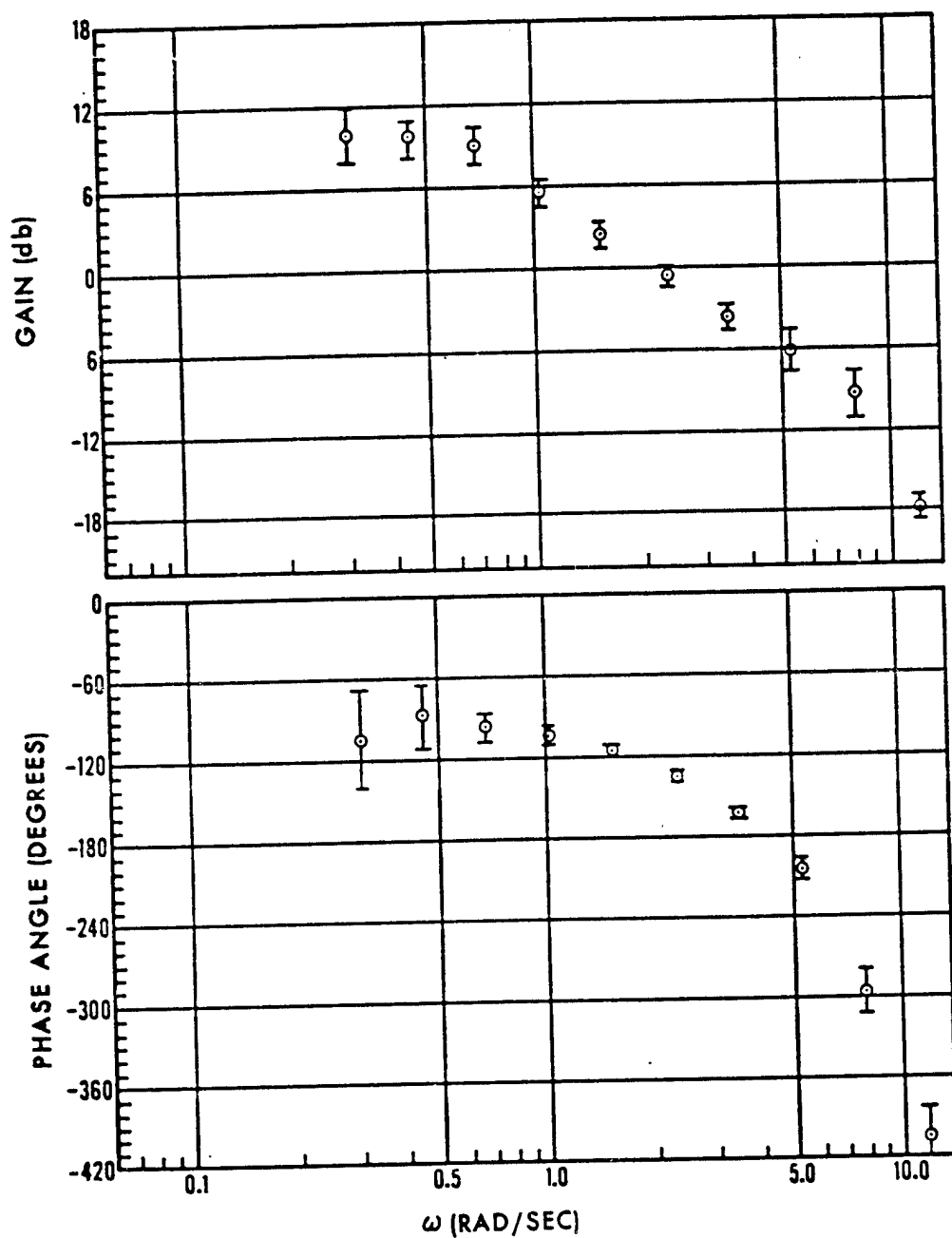


Figure 8. Group Mean Subject-Controlled Plant Describing Function for Afternoon Group and Easy Plant - Without Peripheral Display

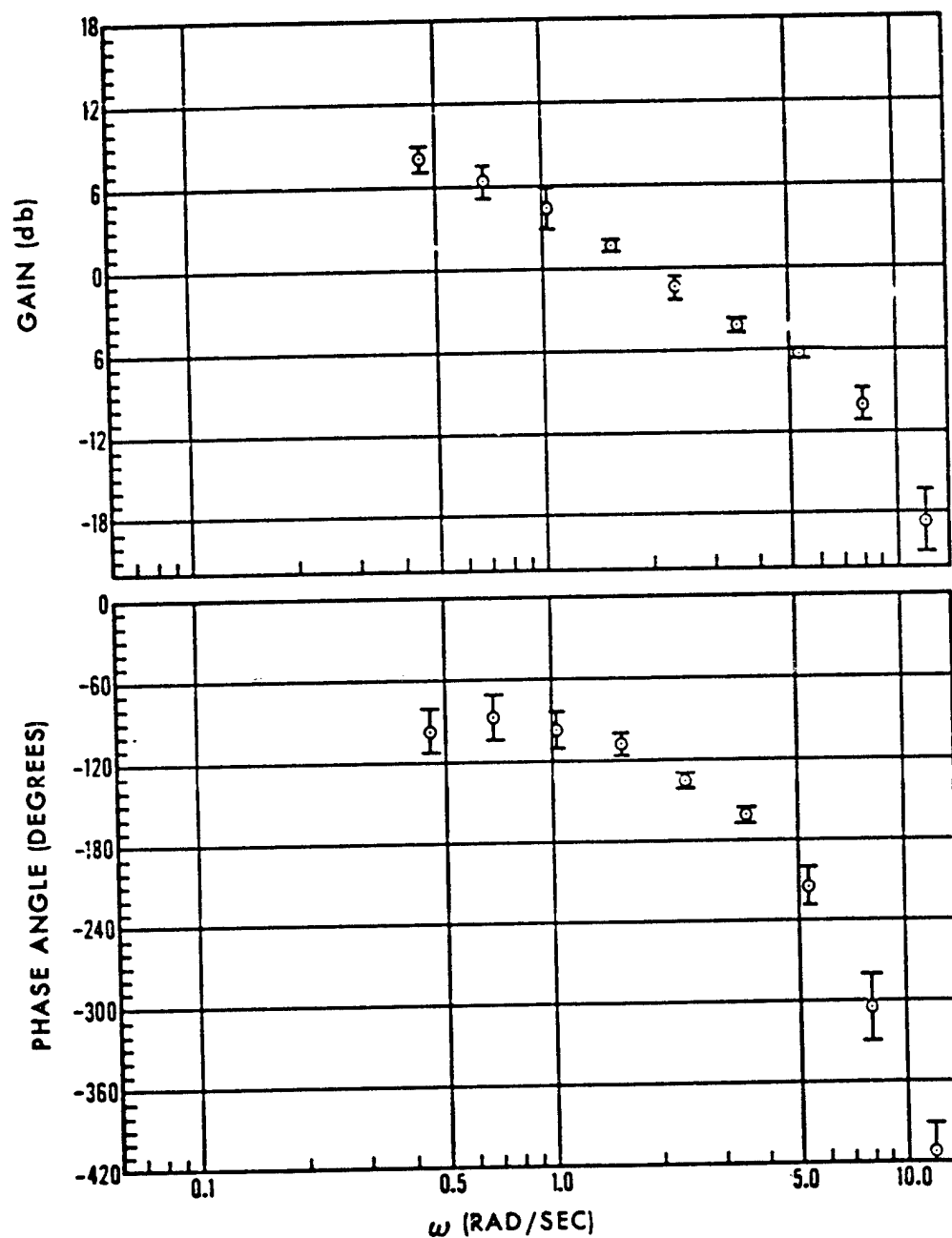


Figure 9. Group Mean Subject-Controlled Plant Describing Function for Afternoon Group and Easy Plant - Peripheral Display Present

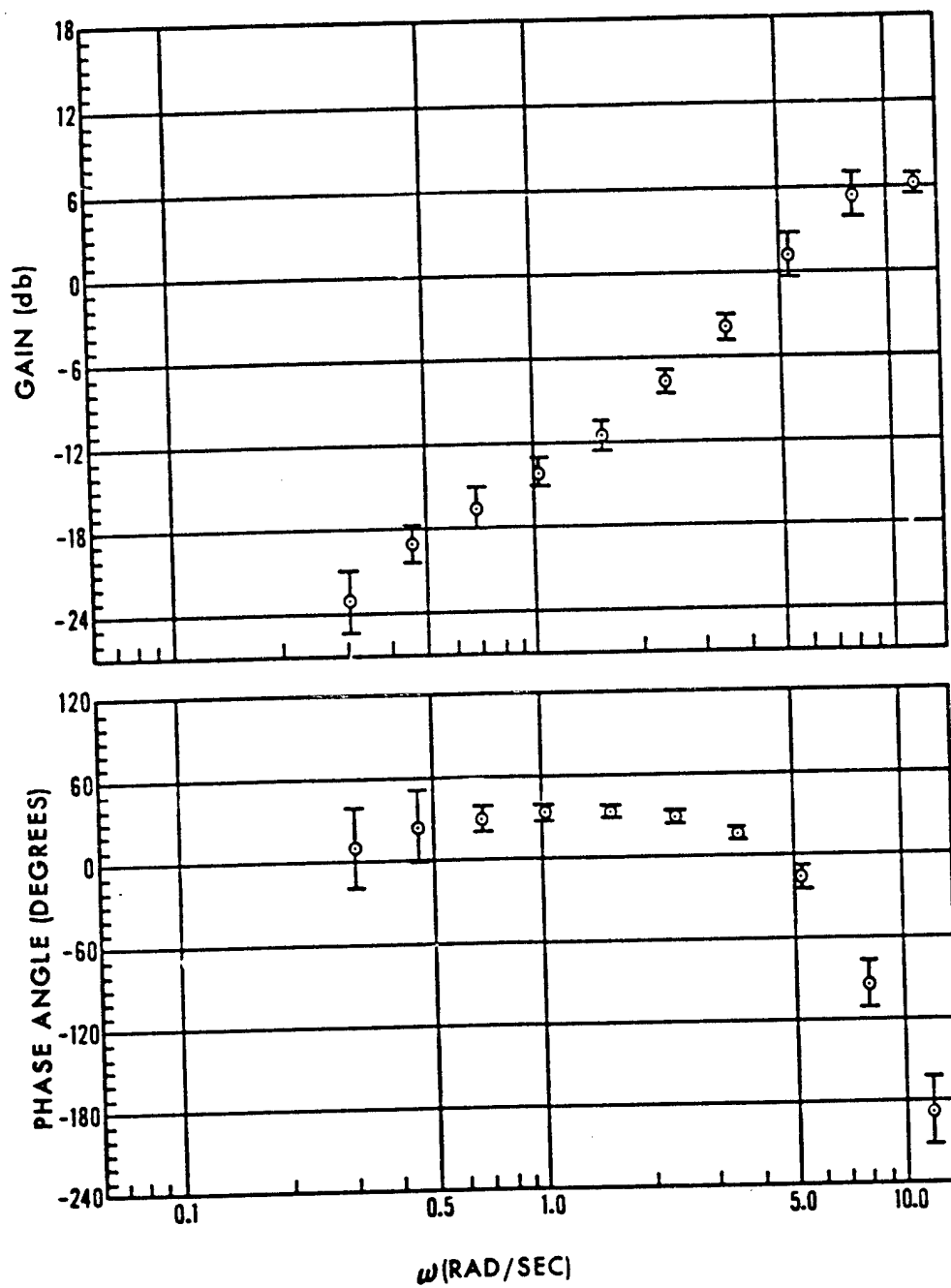


Figure 10. Afternoon Group Mean Subject Describing Function  
- Without Peripheral Display (Easy Plant)



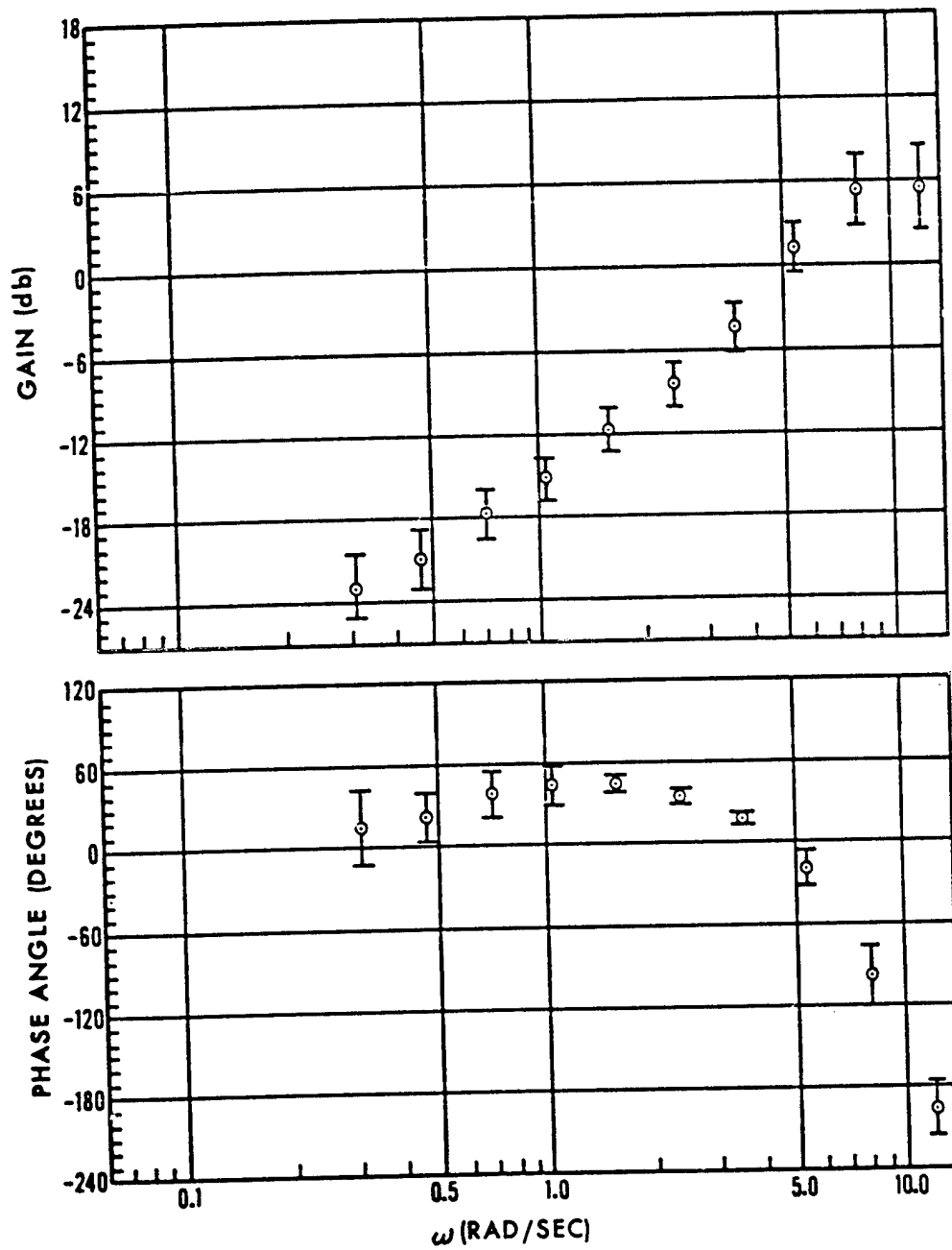


Figure 11. Afternoon Group Mean Subject Describing Function  
- Peripheral Display Present (Easy Plant)

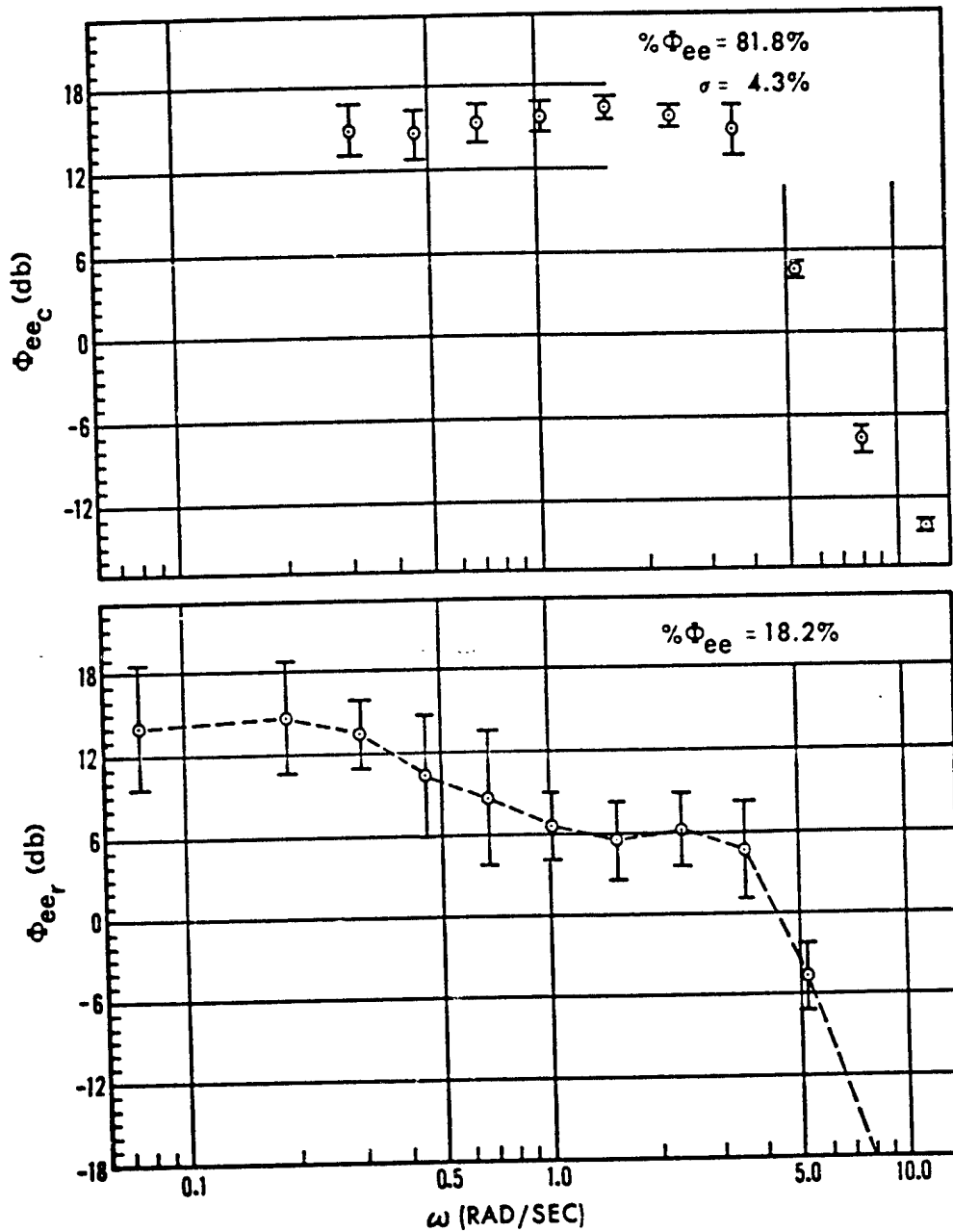


Figure 12. Averaged Afternoon Group Error Power Spectra  
- Without Peripheral Display (Easy Plant)

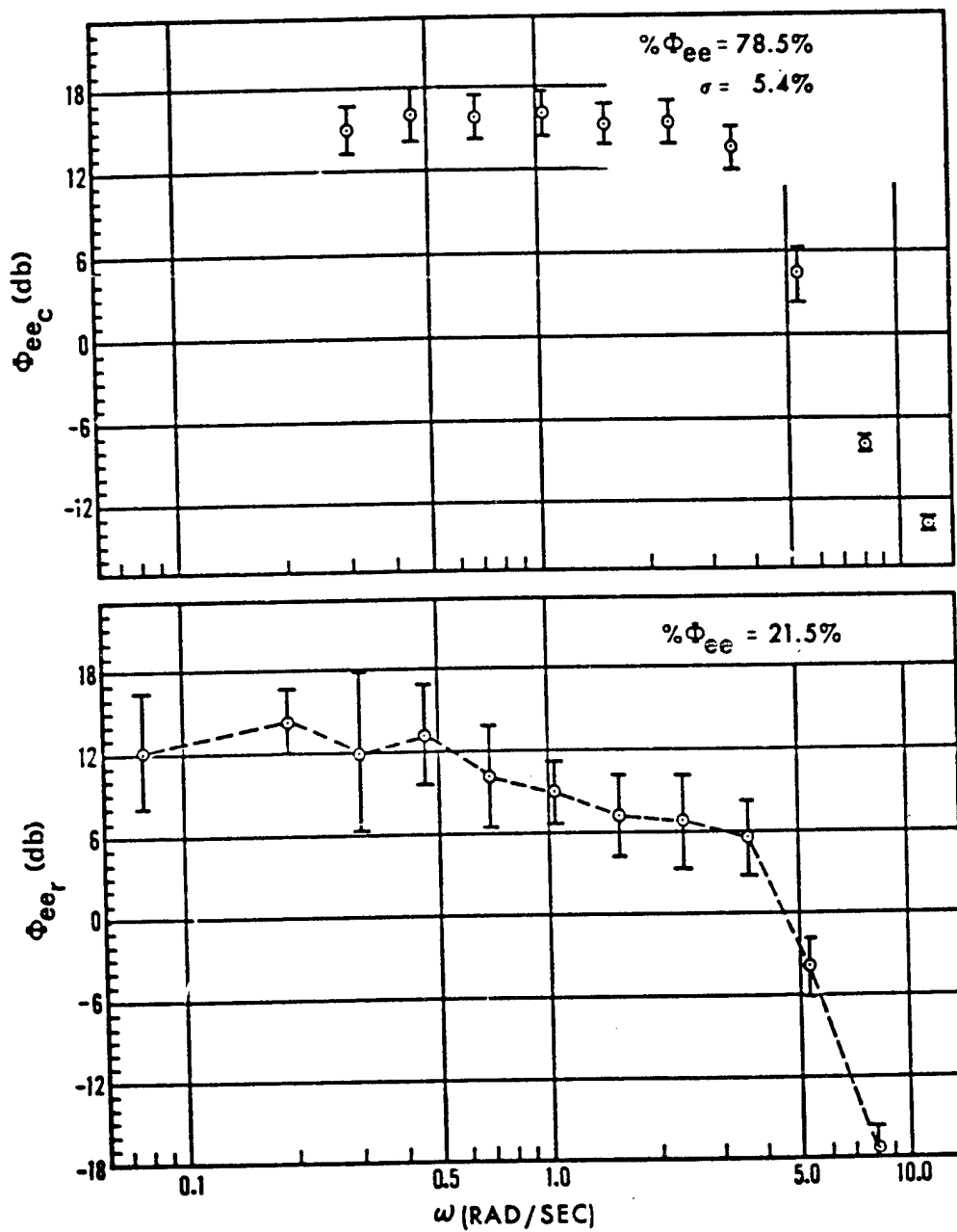


Figure 13. Averaged Afternoon Group Error Power Spectra-Peripheral Display Present (Easy Plant)

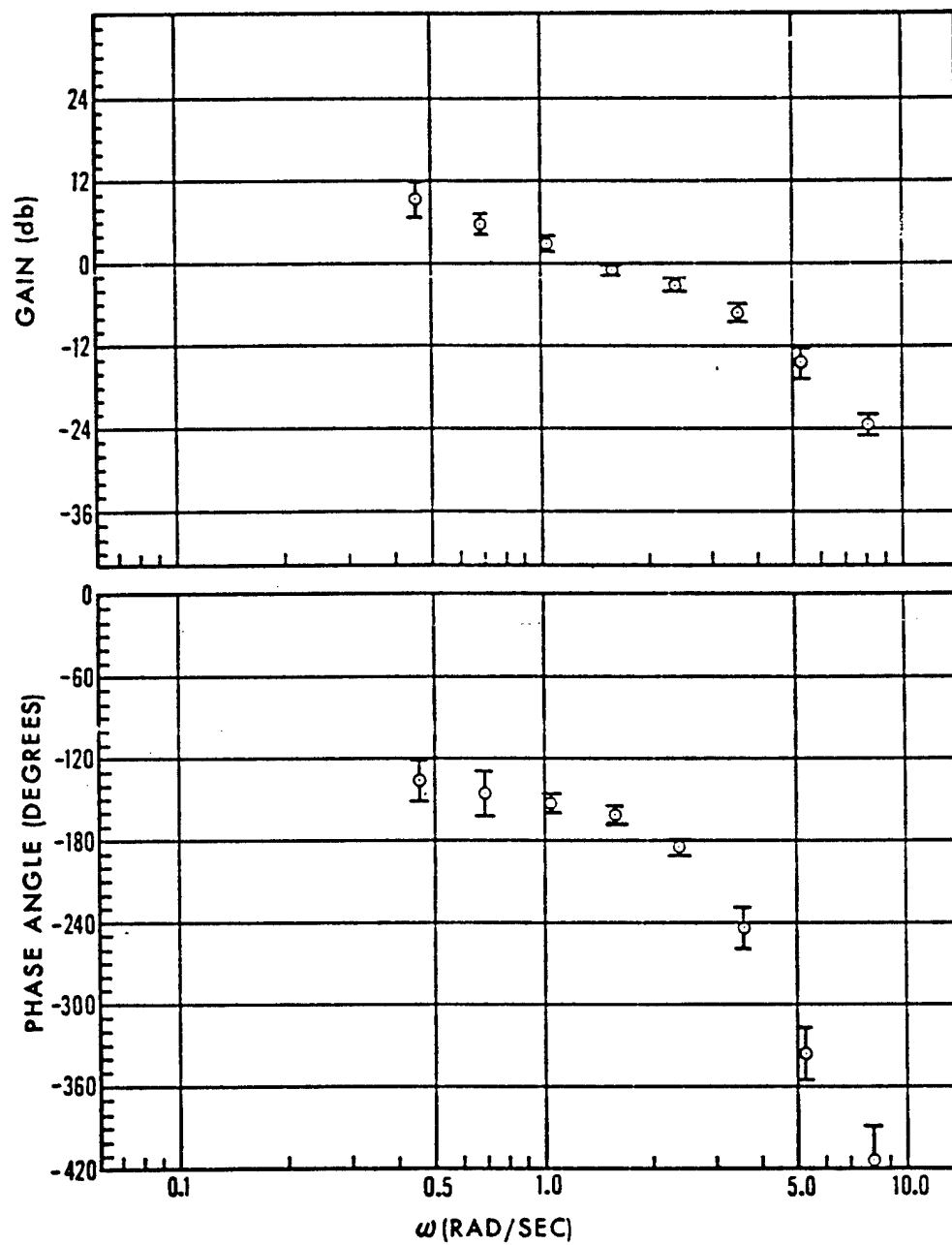


Figure 14. Group Mean Subject-Controlled Plant Describing Function with Difficult Plant - Without Peripheral Display

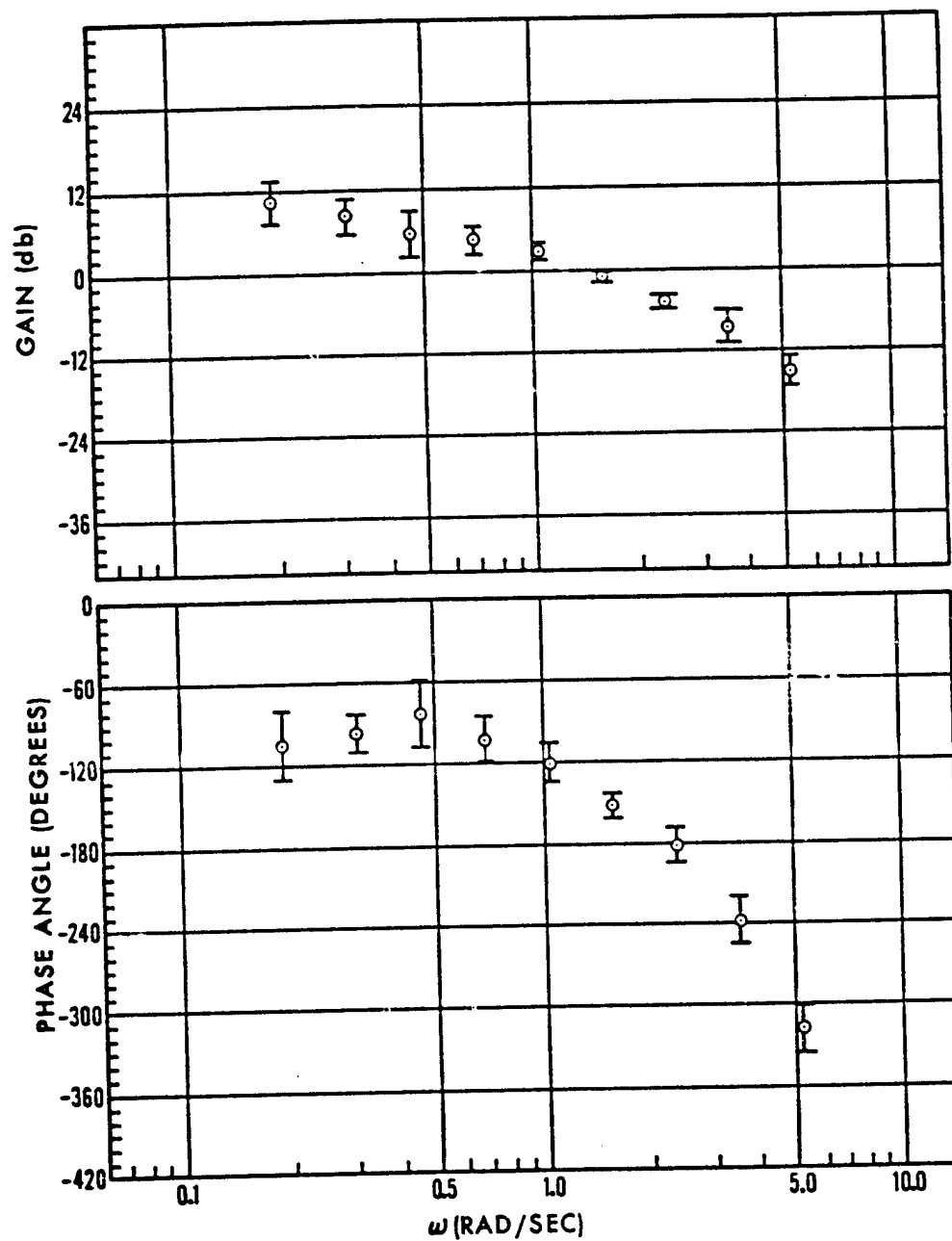


Figure 15. Group Mean Subject-Controlled Plant Describing Function with Difficult Plant - Peripheral Display Present

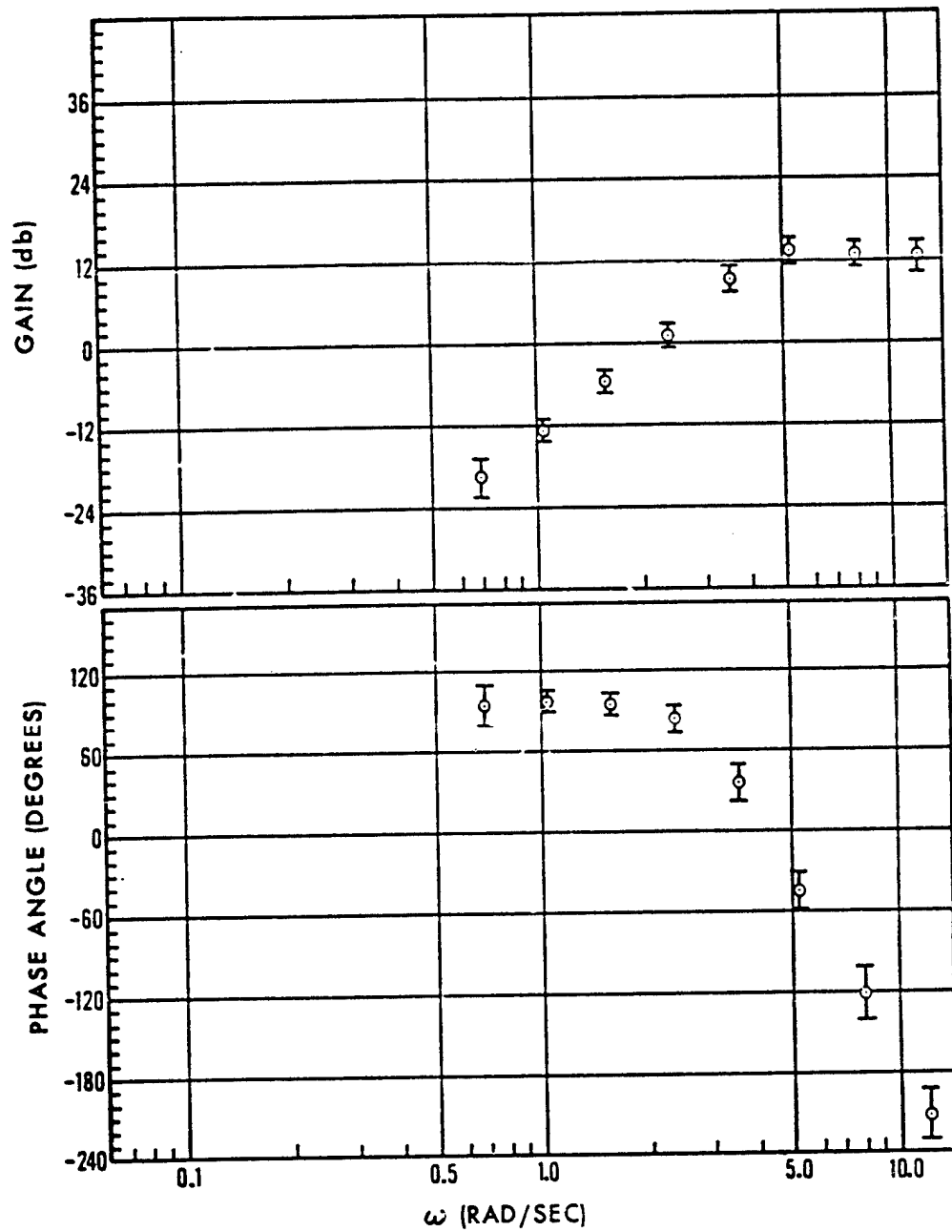


Figure 16. Group Mean Subject Describing Function,  
Difficult Plant - Without Peripheral Display

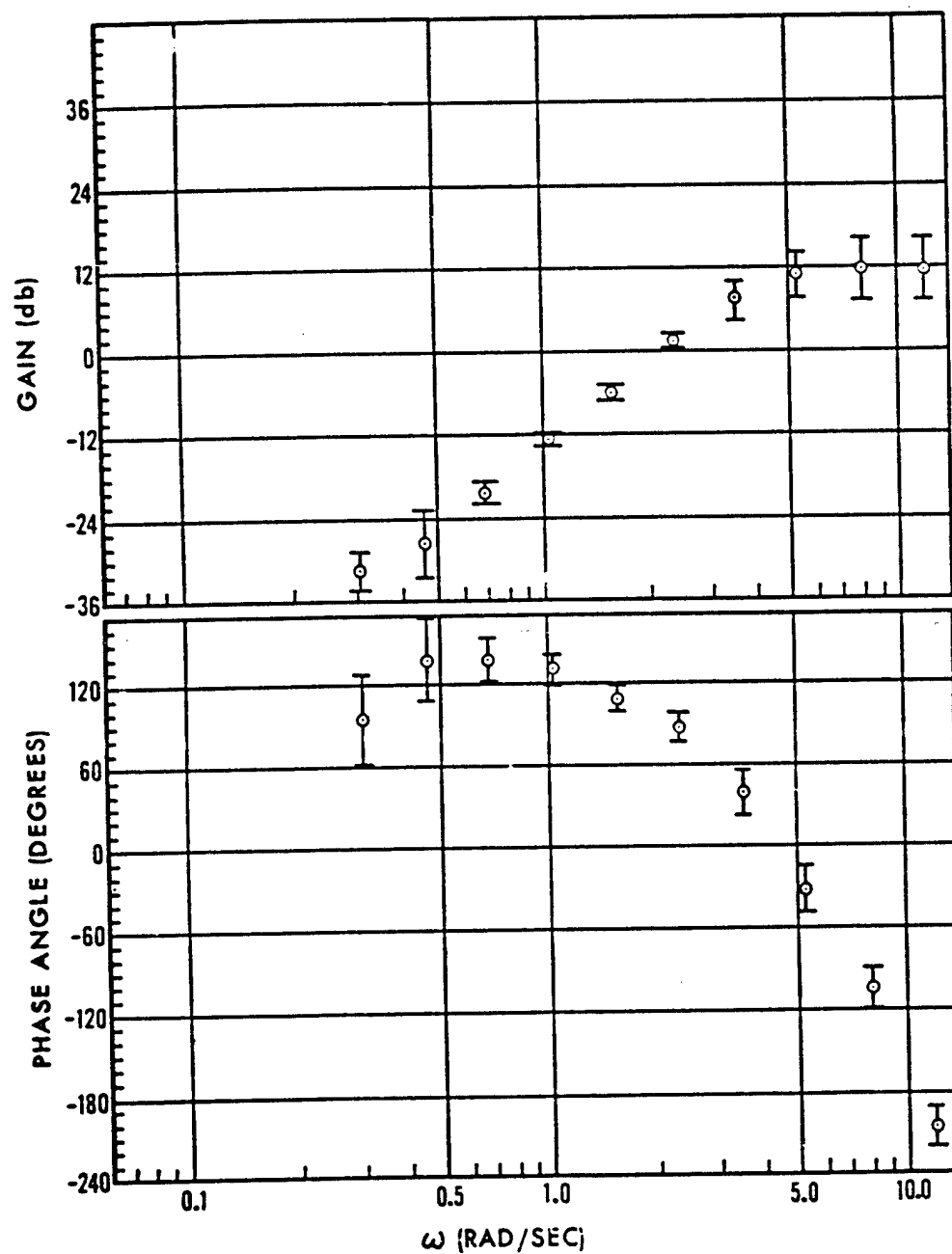


Figure 17. Group Mean Subject Describing Function,  
Difficult Plant - Peripheral Display Present

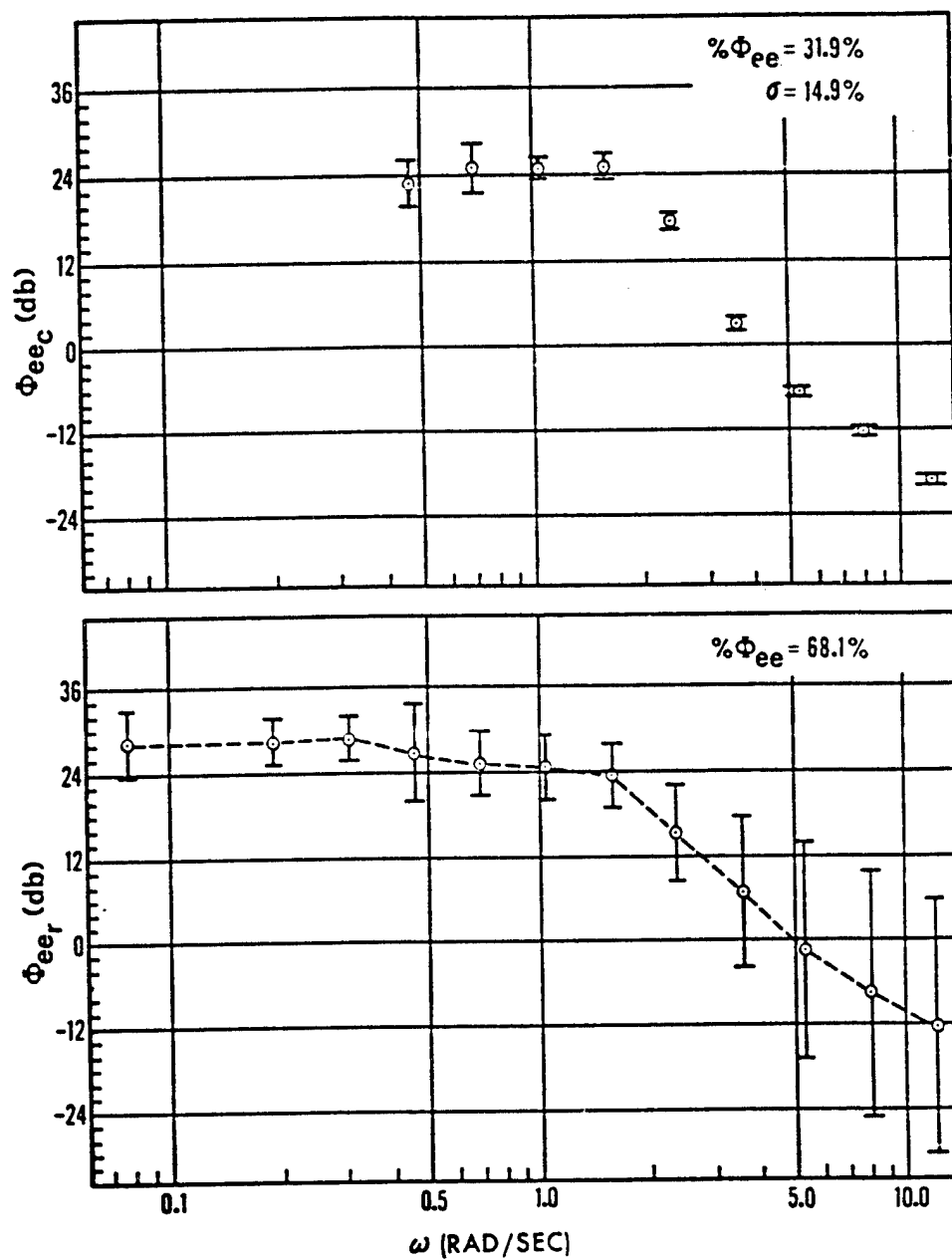


Figure 18. Averaged Group Error Power Spectra, Difficult Plant - Without Peripheral Display



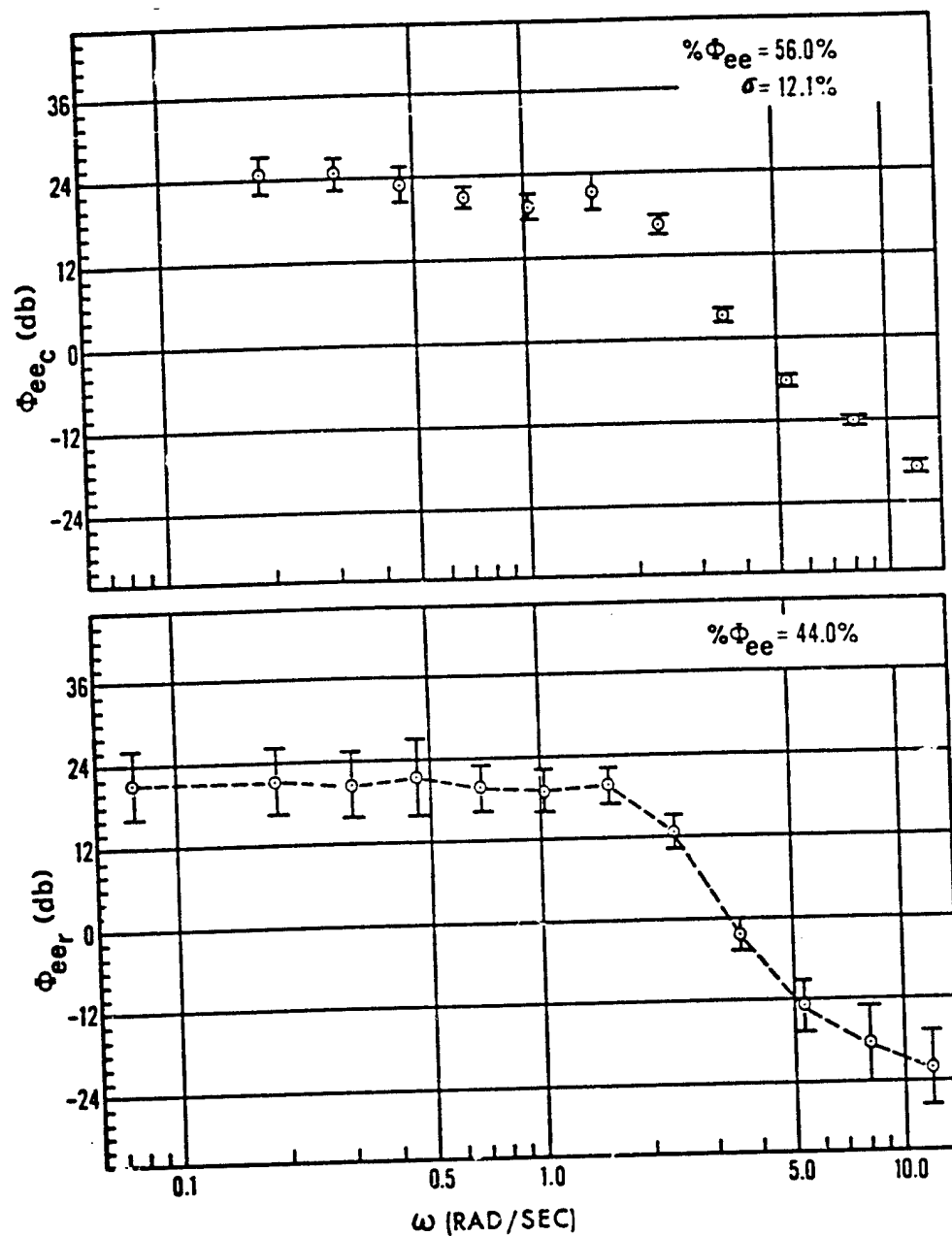


Figure 19. Averaged Group Error Power Spectra,  
Difficult Plant - Peripheral Display Present

## USE OF MOTION CUES IN STEADY-STATE TRACKING\*

by

William H. Levison  
Bolt Beranek and Newman Inc  
Cambridge, Massachusetts

Presented at the Twelfth Annual Conference on  
Manual Control, May 25-27, 1976, University of  
Illinois at Urbana-Champaign

### ABSTRACT

Data obtained in an experimental study of roll-axis tracking are analyzed. The effects of motion cues on tracking performance are modeled by (a) an increment of 0.05 seconds to the pilot time delay, and (b) inclusion of sensory variables that are likely to be provided by motion cues (position, rate, and acceleration of the vehicle roll angle in these experiments). The model replicates the important experimental results; namely, that motion cues cause (a) an increase in low-frequency phase lead, (b) an increase in high-frequency phase lag, (c) no change in man-machine gain-crossover frequency, (d) a reduction in rms tracking error only for the more difficult plant. Modeling of motion-sensor dynamics is not required.

### INTRODUCTION

This paper reviews the results of an analytical and experimental study to explore the use of motion cues in a simulated roll-axis tracking task. The experiments were performed at the Aerospace Medical Research Laboratory (A<sup>2</sup>RL), Wright-Patterson Air Force Base. Primary data reduction was performed by the Air Force; statistical analysis and modeling were performed by Bolt Beranek and Newman Inc (BBN). The results of this study are documented in greater detail in Levison, Baron, and Junker (1).

This paper is concerned with the use of motion-related sensory information for continuous flight control. Other potential effects of motion, such as providing alerting cues to the pilot or providing "realism" to aircraft simulations, are not considered here.

Analysis of the A<sup>2</sup>RL experimental results was directed towards developing a generalized description of the manner in which the pilot uses motion

\*This work was performed in part under AFOSR Contract No. F44620-75-C-3600 Lt. Col. William Wisecup of the Air Force Office of Scientific Research was contract monitor. Mr. Andrew Junker of the Aerospace Medical Research Laboratory directed the experimental study of which some of the results are summarized in this paper.

cues, with the ultimate goal of providing a model that can predict the effects of motion cues on system performance in a variety of control situations. Such a model would have a number of important applications; for example, one might use the model to:

- (1) determine whether or not motion cues are used by the pilot in a particular control situation;
- (2) extrapolate the results of fixed-base simulation to a motion environment;
- (3) facilitate the design of ground-based simulators;
- (4) identify situations where misinterpretation of motion cues is likely to cause a pilot response that seriously degrades system performance.

Although a number of experimental studies have been conducted to determine the effect of motion cues on pilot response behavior (2-5), a generalized model has not been developed and tested. Rather, the conclusions reached in these studies have been restricted to the context of the experiments yielding the data.

Perhaps the most comprehensive study of the effects of motion cues on tracking performance was conducted by Shirley (4). He explored overall system performance and pilot response behavior in a series of tasks that included a wide range of vehicle dynamics. Most of his results conformed to the following set of rules:

1. The human operator uses motion to generate additional lead at high frequencies, which permits an increase in pilot gain and therefore an increase in the gain crossover frequency of the man-machine system.
2. Greatest percentage reduction in rms error scores with motion is achieved for systems that respond to inputs above 3 rad/sec. That is, improvement is greater for low-order than for high-order systems.
3. Motion is used to greatest advantage in marginally stable or unstable systems.

Stapleford et al (3) also found that high-frequency phase lag decreased and gain crossover frequency increased when motion cues were present; furthermore, these effects generally decreased as the vehicle dynamics increased in difficulty. In contradiction to Shirley they found that, on the average, the effects of motion cues on error score increased for increasing vehicle difficulty.

Because the effect of motion simulation on tracking performance is highly dependent on the details of the tracking task, generalizations of the type reviewed above cannot be reliably extended beyond situations similar to those studied experimentally. Therefore, an alternative philosophy has been suggested and partially explored: namely, to account for the pilot's use of motion cues by including additional sensory feedback paths in the pilot model (2). Given a model structure that allows one to predict the influence of these feedbacks on pilot response as a function of task parameters, one may then extend

experimental results to a variety of control situations. The "optimal-control" pilot model developed by BBN appears to contain the desired structure, and application of this model to the AMRL roll-axis study is reviewed in this paper.

## EXPERIMENTAL PROCEDURES

The experimental data analyzed by BBN were only a portion of the data obtained in a larger study of the pilot's use of visual and motion cues in manual control tasks; we review below those aspects of the experimental program that pertain to the analysis performed by BBN.

### Description of the Tracking Task

The tracking task was mechanized similarly to that used in a previous study (6). Briefly, the closed-loop roll-axis motion simulator consisted of a drive system, aircraft seat, central visual display, and motion controls. The rotating system dynamics were identified and simulated on a hybrid computer. A block diagram of the resulting system is shown in Figure 1. The task was to follow a target aircraft in the roll axis. The difference between the target roll angle and the controlled plant position was provided to the human operator on a television monitor in the format shown in Figure 2. The angle between the rotating and stationary lines,  $e$ , depicted the difference between the controlled plant roll angle and the target roll angle.

### Plant Dynamics

Data were obtained for two sets of plant dynamics. "Task 1" used a plant that had approximate second-order response characteristics over much of the measurement bandwidth, whereas "Task 2" employed dynamics that were approximately third-order. Previous experimental results indicated that performance on Task 1 would be relatively unaffected by the presence of motion cues, while the presence of motion cues would appreciably enhance performance on Task 2. These two tasks were explored to provide a check on the consistency of the model developed to account for the pilot's use of motion cues.

Because of the complex dynamics and nonlinearities of the rotating machinery, the plant dynamics did not conform exactly to the desired theoretical response behavior. In order to minimize difference in plant dynamics between the motion and static (i.e., fixed-base) conditions, an effort was made to simulate the rotating dynamics in the static cases.

Figure 3 shows the transfer functions of the two plants as derived from the experimental data, along with analytic ("model") fits to these transfers. Plant dynamics for corresponding static and motion conditions are nearly identical over most of the measurement range, but differences appear at the highest frequencies. As these frequencies are well above the gain crossover frequency of the combined man-machine system, differences between static and motion plant dynamics were expected to have little effect on pilot behavior and system performance.

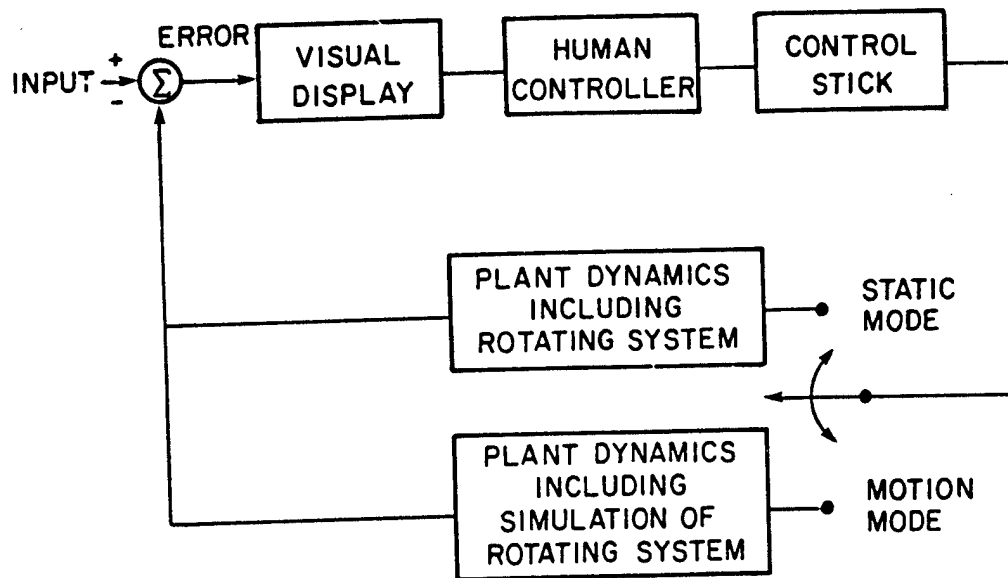


Figure 1. Block Diagram of Tracking Task.

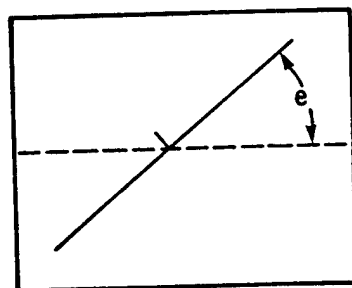


Figure 2. Sketch of Tracking Display.

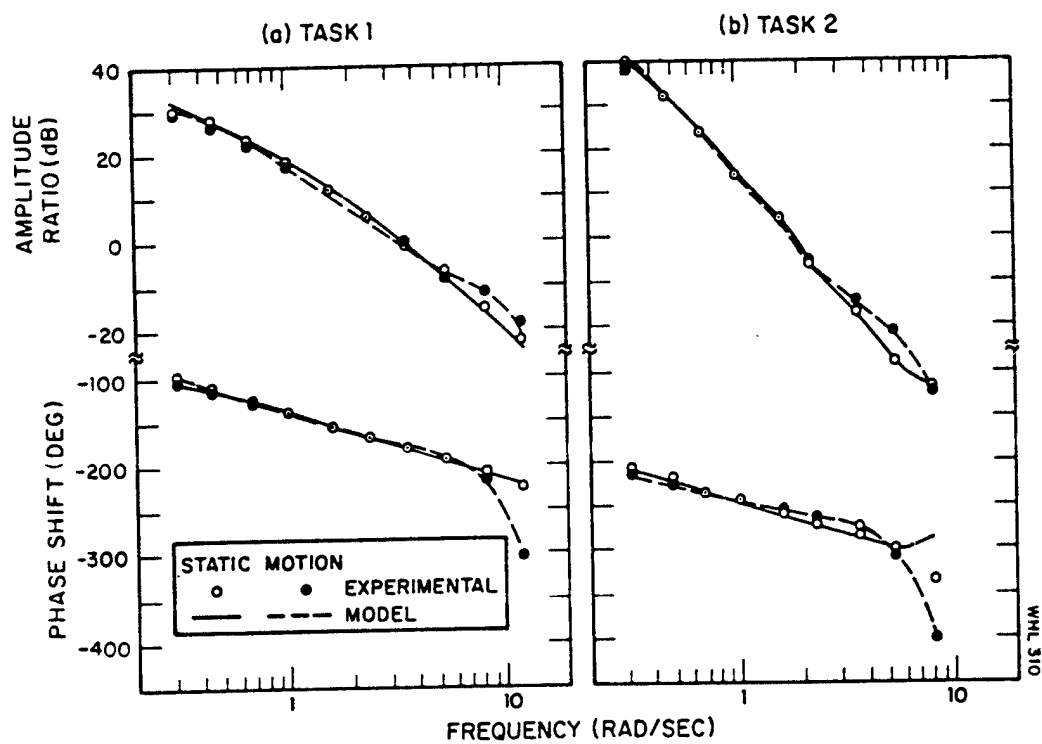


Figure 3. Frequency Response of the Controlled Plants.  
0 dB represents 1 degree of roll angle per  
in-lb of control torque

A side-mounted force stick was used for all tracking runs. A comfortable stick gain was selected at the beginning of the experiment and maintained throughout so that the same stick gain was used for all subjects for all runs.

#### Input Forcing Function

The target roll angle was driven by a random-appearing input signal that consisted of 12 sine waves with frequencies and amplitudes chosen to approximate the power density spectrum of Gaussian white noise passed through a second-order low-pass filter having a double pole. The properties of the input signal were varied from one controlled plant to the next so that the subjects were always provided with a challenging tracking task, but one that did not severely restrict the bandwidth of the pilot's response. Rms amplitudes and (simulated) critical frequencies for the input signals were 20 degrees roll angle and 1.25 rad/sec for Task 1, and 40 degrees and 0.5 rad/sec for Task 2.

#### Training and Data-Collection Procedures

The same three subjects provided data for both Tasks 1 and 2; data from a fourth subject was analyzed for Task 2. All subjects were young, healthy adults between the ages of 18 and 21 with previous tracking experience on the simulator in both the static and motion modes. Since this tracking experience was not for the plants explored in this study, additional training was required.

Training and data collection were completed first for Task 1; tracking performance on Task 2 was then studied. In both phases of the experimental study, the training procedure consisted of tracking in the static and motion modes until the rms error scores appeared to reach asymptotic levels. The subjects were provided their rms error scores after each tracking trial. To maintain subject motivation, subjects were also informed of each other's performance scores.

During both training and data collection, each subject performed four tracking runs per day. These consisted of two static and two motion runs of about 164 seconds duration. Each subject experienced two consecutive runs at a time - one static and one motion - with the order randomized. After the final subject in the group accomplished his second run, the subjects completed the session by experiencing two additional replicates of the tracking task in the same subject sequence as before. In order to prevent the subjects from learning the input waveforms, a random number generator was used to vary the phase relationships of the input sinusoids from one experimental trial to the next.

## EXPERIMENTAL RESULTS

#### Analysis Procedures

Variance scores were computed for each experimental trial for the tracking error, tracking error rate, plant position, plant rate, control, and control rate. These variance scores were averaged across the four replications of

a given experimental condition within each subject. The square root was taken of each subject mean to yield an rms performance measure\*, and the mean and standard deviation of the subject means pertaining to the same experimental condition were then computed. In order to test for significant differences between motion and static conditions, paired differences were formed from corresponding subject means; these differences were subjected to a two-tailed t-test. Difference scores significant at the 0.05 confidence level or smaller were considered "significant".

Analysis procedures were similar to those used in previous studies of manual control (7-10). Fast-Fourier transform techniques allowed computation of pilot describing functions and signal spectra, with the spectra being partitioned into input-correlated and remnant-related components (where "remnant" is defined as signal power not linearly correlated with the input forcing function). The pilot describing function was computed by dividing the Fourier transform of the control response by the transform of the tracking error. This response measure, therefore, included response to both visual and motion cues.

Means and standard deviations were computed for the describing function amplitude ratio (in dB), for the describing function phase shift (in degrees), and for spectral quantities (in dB). Statistics were computed at each input frequency; in the case of spectra, statistics were computed separately for input-correlated and remnant-related components. T-tests were performed on paired differences of selected frequency-response measures to determine the significance of motion cues on these quantities.

The input-correlated spectral components, which were discrete spectra because of the sum-of-sines inputs, were converted to equivalent continuous-frequency spectral density functions to be compatible with the spectral densities generated by the pilot/vehicle model. The conversion scheme is described in (1). For notational conciseness, all power spectral density functions, whether theoretical or derived from experimental data, are referred to in this paper simply as "spectra".

#### RMS Performance Scores

Variables for which rms performance scores were computed, their units, and their symbolic notation are shown in Table 1. Average rms performance scores are shown in Figure 4, with significant static-motion differences indicated by the arrows.

\*More precisely, the resulting scores should be termed "standard deviation scores", since the contributions of mean components, if any, were removed. However, to avoid confusion we restrict the usage of the term "standard deviation" to indicate subject-to-subject variability.



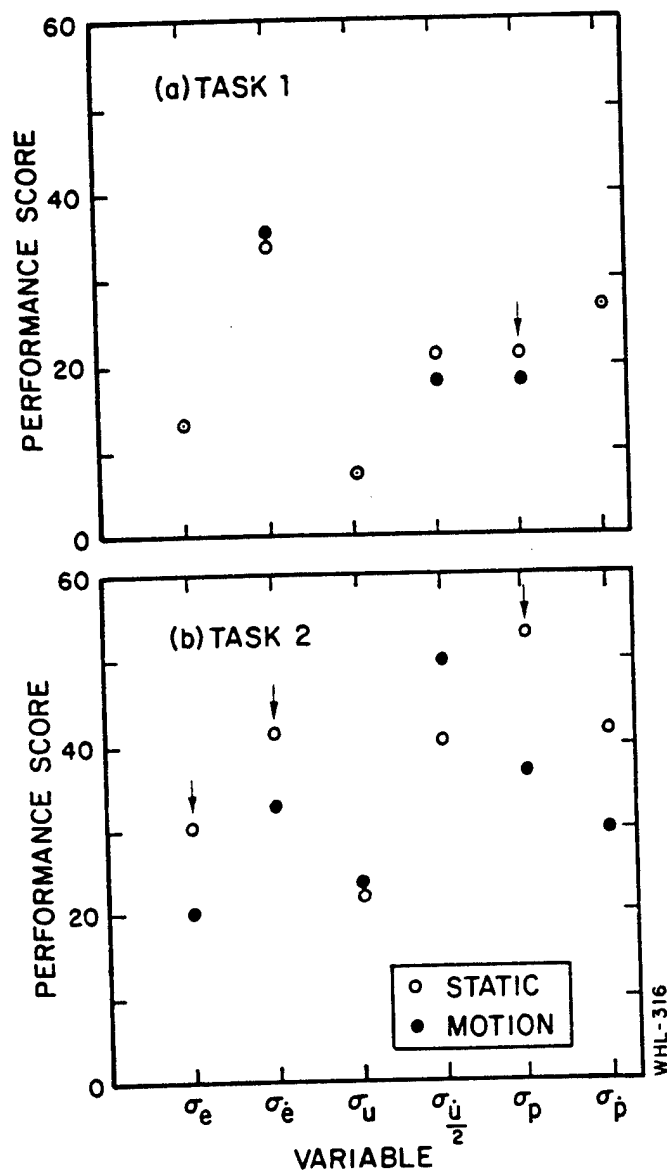


Figure 4. Effect of Motion Cues on Average RMS Performance Scores.

Table 1  
Tracking Variables Analyzed

Variable	Symbol	Units
Tracking Error	$e$	degrees
Tracking Error Rate	$\dot{e}$	degrees/sec
Plant Position	$p$	degrees
Plant Rate	$\dot{p}$	degrees/sec
Control	$u$	in-lb
Control Rate	$\dot{u}$	in-lb/sec

Error and control variables were virtually unchanged by the presence of motion cues in Task 1. Only rms plant position was significantly influenced by motion cues and was about 12% less when motion was present. When the third-order plant (Task 2) was controlled, however, motion simulation allowed large and significant reductions in rms tracking error, error rate, plant position, and plant rate. Rms control torque was essentially unaffected by motion. Although rms control rate increased by about 23% on the average when motion was simulated, this change was not statistically significant.

#### Frequency Response

Figure 5 shows average pilot frequency-response behavior. The four sets of curves shown for each tracking task are, from top to bottom, the amplitude ratio of the pilot describing function, the phase shift of the pilot describing function, the input-correlated component of the spectrum of the pilot's control response, and the remnant-related component of the control spectrum. The presence of apparent "system noise" associated with the motion simulation in Task 2 prevented reliable estimates of pilot remnant at the lowest three measurement frequencies shown in Figure 5. Therefore, estimates of remnant at these frequencies are not plotted for the Task 2 motion simulation.

The effect of motion cues on performance in both tasks was to increase low-frequency phase *lead* while also increasing high-frequency phase *lag*. In addition, motion simulation in Task 2 significantly modified the control spectrum. Input-correlated and remnant-related components were reduced at frequencies corresponding to gain-crossover and lower. No significant changes occurred in the correlated power at high frequencies, whereas remnant increased. No motion-related changes in amplitude ratio were observed in the region of gain-crossover for either task.

The "open-loop" describing functions shown in Figure 6 give a more direct

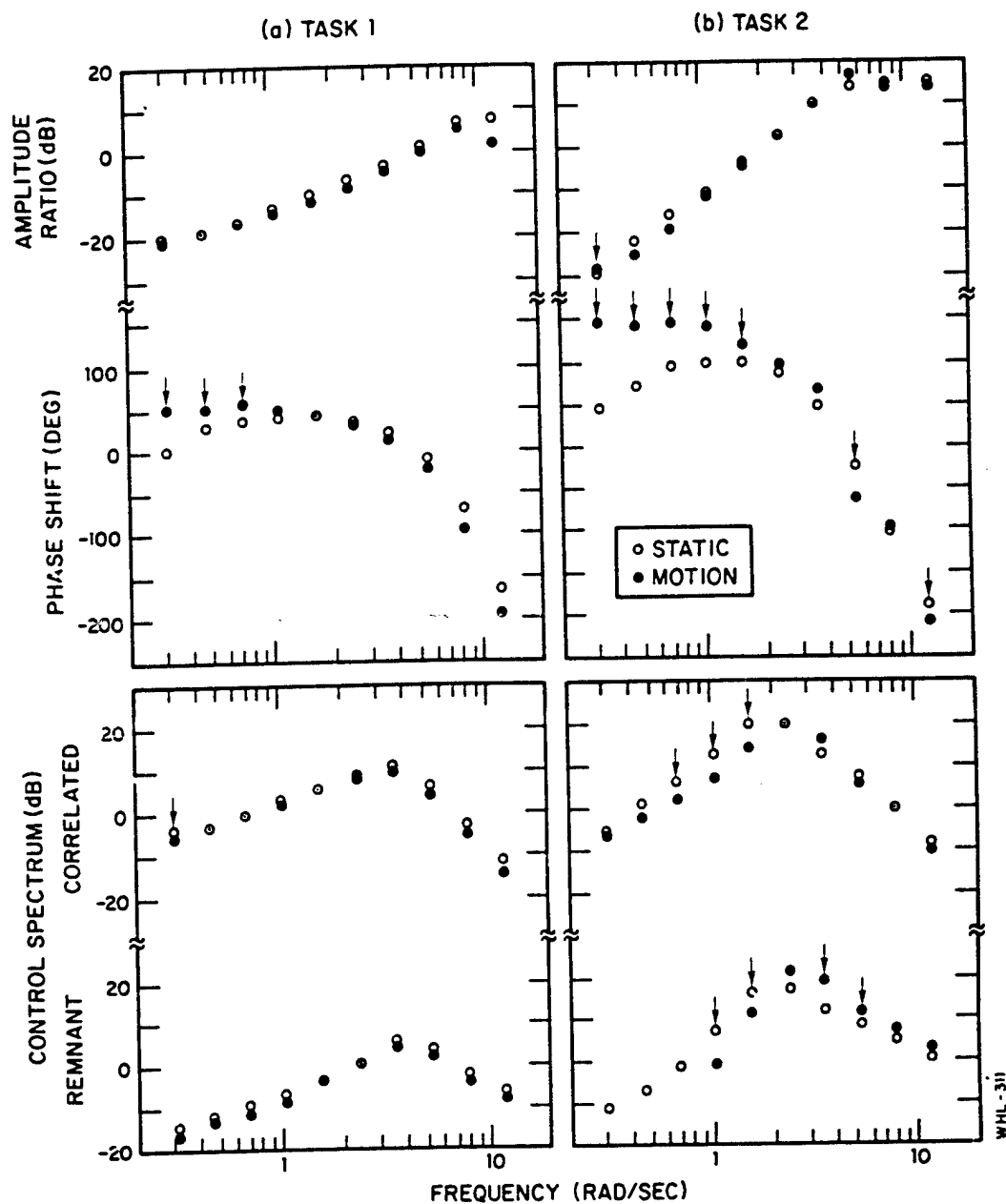


Figure 5. Effect of Motion Cues on Average Pilot Frequency Response

0 dB represents 1 in-lb control torque per degree roll for the amplitude ratio and 1 (in-lb)<sup>2</sup>/(rad/sec) for control power

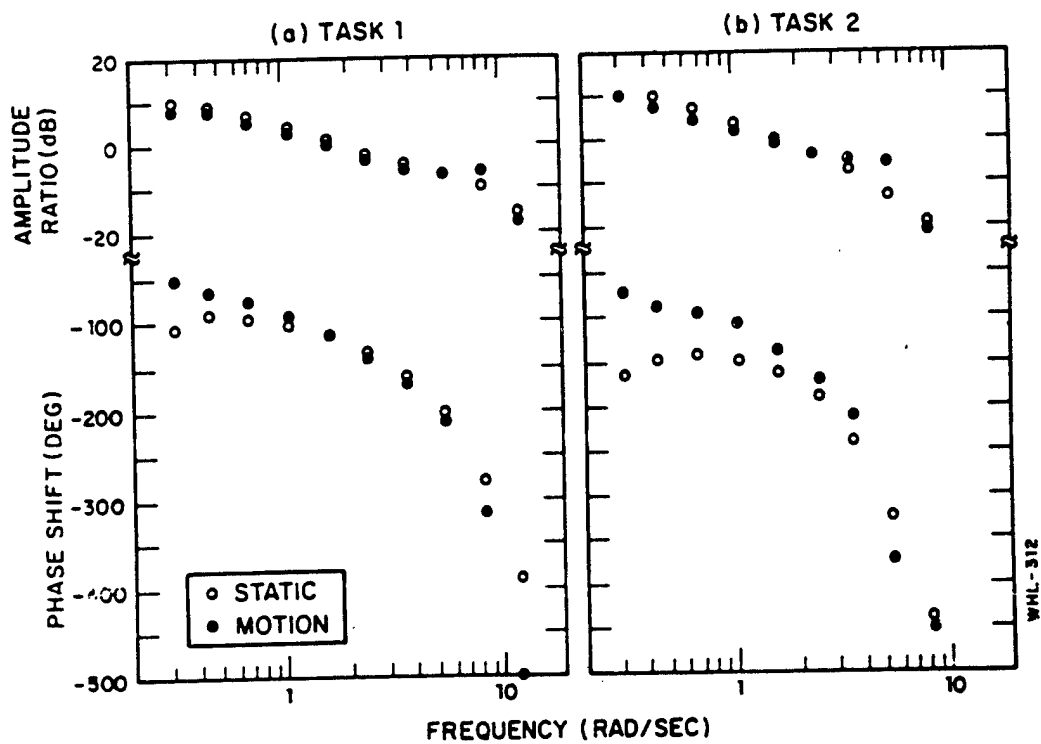


Figure 6. Effect of Motion Cues on Open-Loop Describing Function.  
 0 dB = 1 (dimensionless)

indication of combined man-machine response capabilities. The gain-crossover frequency is in the range of 1.5-1.8 rad/sec and is little affected by either plant dynamics or by the presence of motion cues. The phase margin, on the other hand, is quite variable. Phase margin is about 60-70 degrees for Task 1. Phase margin is reduced to about 40 degrees for Task 2 with motion simulation and to about 20 degrees for Task 2 in the static mode. Apparently, the increase in phase margin, combined with the reduction in controller remnant at frequencies below crossover, account for the reduced error score in the Task 2 motion simulation.

#### Comparison with Previous Experimental Results

The experimental results presented here appear to conflict with the findings of others regarding the effects of motion cues on tracking performance. Both Shirley (4) and Stapleford et al (3) concluded that the addition of motion cues allows the pilot to generate greater lead at high frequencies, thereby permitting an increase in gain-crossover frequency. Furthermore, Shirley concluded that motion cues were relatively more beneficial for tracking tasks involving low-order plants than for those involving high-order dynamics. On the contrary, the results presented above show that motion cues result in more high-frequency phase lag (rather than lead), no appreciable change in gain crossover, and greater relative improvement with the higher-order plant.

These apparent contradictions do not necessarily indicate that the AMRL experimental subjects used motion cues in a manner different from the subjects who participated in the studies of Shirley and of Stapleford et al. There were some important differences between the AMRL experiments and the earlier studies. Both Shirley and Stapleford et al applied the input disturbance in such a manner that both the visual display and the motion simulator were driven by the input. (That is, the input was applied essentially in parallel with the pilot's control.) In the AMRL/BBN study, the input was purely a command signal; the plant was driven only by the subject's control input. Thus, in the latter study, motion cues provided direct perceptions of vehicle response behavior; this was not the case in the earlier studies. In addition, the dynamics used in Task 2 of the AMRL/BBN study were higher order than those explored in the previous studies.

Because of the strong interaction between pilot response behavior and task parameters, we cannot tell from experimental data alone whether or not subjects participating in two different experiments obeyed the same set of rules with regard to the use of motion cues. A model is needed to account both for the limitations inherent in the human's use of perceptual information and for the interaction between task parameters and human response. Given this model, we can then try to find a consistent set of rules for selecting pilot-related parameters that accounts for the use of motion cues across a variety of task conditions.

The results of model analysis applied to the AMRL experimental data are described below.

## MODEL ANALYSIS

### Model Structure

The model applied to the foregoing experimental results was a modified version of the "optimal-control" pilot/vehicle model that has been applied in numerous previous studies of manual control (11-18). The modification to the model described in the literature consisted of the following revised treatment of motor-related sources of pilot remnant: (1) "motor noise" was treated as a wide-band noise process added to control rate, rather than to commanded control, and (2) the concept of "pseudo" motor noise was introduced to allow a differentiation between the actual noise driving the system ("driving" motor noise) and the pilot's internal model of this noise (the "pseudo" noise). No modifications were made to the model structure specifically to treat the pilot's use of motion cues.

Injecting motor noise to control rate allowed the model to reproduce the low-frequency "phase droop" exhibited by most pilot describing functions. Although tracking performance is generally little affected by low-frequency phase response, it was necessary to obtain an accurate model of this aspect of controller behavior because of the importance of low-frequency phase characteristics on performance in the AMRL/BBN roll-axis tracking study. By introducing the concept of pseudo motor noise, we gained added flexibility in representing pilot uncertainties about his own control behavior and about vehicle response. The mathematical implications of this model revision, as well as applications of the revised model to previous laboratory tracking results, are documented in Levison, Baron, and Junker (1).

The focus of the modeling effort was to represent the effects of motion primarily by appropriate definition of the sensory variables assumed to be available to the pilot. Thus, static-mode tracking was modeled with a two-element "display" vector consisting of tracking error and error rate. In the case of motion tracking, the display vector was augmented to include quantities that would be provided by the pilot's motion-sensing capabilities; specifically, plant position (i.e., roll angle), plant rate, and plant acceleration. These motion-related variables were considered individually and in combination.

Because we were dealing with steady-state tracking signals of moderate bandwidth, we did not expect motion-sensor dynamics to have an important effect on tracking performance. Therefore, sensor dynamics were not included in the pilot model: informational quantities included in the display vector were assumed to be corrupted only by observation noise and not by bandwidth limitations.

### Identification Procedure

The primary goal of the model analysis was to seek a consistent set of rules for selecting pilot-related model parameters that would allow reliable predictions of the effects of motion cues in a variety of control tasks. A second (and related) goal was to determine the specific motion-related cues that the subjects had used in the AMRL/BBN experimental study.

The identification scheme employed in this study was similar to that used by BBN in previous studies (7, 9) and was applied to reduced data rather than to time histories. Parameter values were sought that would simultaneously provide a good match to performance scores, describing functions, and control spectra. A quantitative "matching error" was defined as described in (1), and pilot-related model parameters were selected to minimize this error.

A number of iterations were required to arrive at a set of pilot-related parameter values that would explain the maximum amount of data with minimum variations in parameters. The logical (if not entirely chronological) steps in the identification procedure were as follows: (1) analysis of previous laboratory tracking experiments provided an initial set of values for pilot-related parameters; (2) the Task 1, static-mode data were matched to determine modifications, if any, to these parameter values for the roll-axis tracking results; (3) the data of Task 2, both static and motion, were matched to test specific hypotheses concerning the use of motion cues; (4) the results of Step 3 were then applied to the static and motion data from Task 1 to verify the consistency of the treatment of motion cues, and (5) iterations on Steps 3 and 4 led to the final selection of model parameters.

#### Primary Results of the Model Analysis

Parameter values identified from the roll-axis tracking data are given in Table 2. The following considerations were involved in arriving at this set of parameter values:

*Control-rate Cost Coefficient:* We initially attempted to match experimental results with control-rate cost coefficients corresponding to a motor time constant of 0.1 seconds, in keeping with previous model applications. We found, however, that weightings so chosen yielded rms control-rate scores that were much greater than those observed experimentally; accordingly, weightings were re-adjusted to provide a better overall match to the data. (Predicted rms error scores were relatively insensitive to the choice of control-rate cost coefficient.)

*Time Delay:* A time delay of 0.2 seconds was selected on the basis of previous studies and provided a good match to the static results. It was necessary to increase the delay to around 0.25 seconds, however, to account for the greater high-frequency phase shift observed in the motion experiments.

*Motor Noise:* Motor noise was neglected as a source of direct input to the control system. Pseudo-motor noise, reflecting the subject's uncertainties about the system as well as uncertainty about his own control action, was adjusted to match the low-frequency portion of the pilot's phase characteristics.

*Observation Noise:* An observation noise/signal ratio of -20 dB was adopted as the noise level corresponding to nominal "full attention".\*

\* On the basis of previous studies, the observation noise/signal ratio was assumed to vary inversely with "attention" (7, 17, 18).

Table 2

Identified Model Parameter Values

Model Parameter	Task 1		Task 2	
	Static	Motion	Static	Motion
Control-Rate Cost Coefficient	0.02	0.02	0.08	.01
Motor Time Constant (sec)	0.126	0.130	.193	.145
Time Delay (sec)	0.20	0.25	0.20	0.25
Driving Motor Noise/Signal Ratio (dB)	Negl.	Negl.	Negl.	Negl.
Pseudo Motor Noise/Signal Ratio (dB)	-35	-35	-35	-35
Observation Noise/Signal Ratio (dB)	-20	-20	-20	-20
Attention to Error Displacement	0.1	0.095	0.1	0.07
Attention to Error Rate	1.0	0.95	1.0	0.70
Attention to Motion Variables	-	0.05	-	0.30

On the basis of the re-examination of previous  $K/s^2$  tracking results, attention to error displacement was assumed to be only one tenth the attention to error rate (1). Thus, "full attention" to visual display variables was modeled by observation noise/signal ratios of -10 dB on error displacement and -20 dB on error rate. The model parameters relating to attentional allocation in Table 2 reflect the hypothesis that attention must be shared between visual variables as a group and motion variables as a group. All motion cues (plant position, rate, and acceleration) were assumed available, and there was assumed to be no interference among these informational quantities.

Model-generated rms performance scores were compared with experimental results in Figure 7. The left-hand graphs show the results for "displacement" (i.e., zero derivative) variables, whereas rate variables are diagrammed in the right-hand graphs. With one exception, model results show a near-perfect match to experimental scores for displacement variables. The match is less good for rate variables, but (again with one exception) the model correctly predicts the influence of motion cues on the trends of the performance measures.



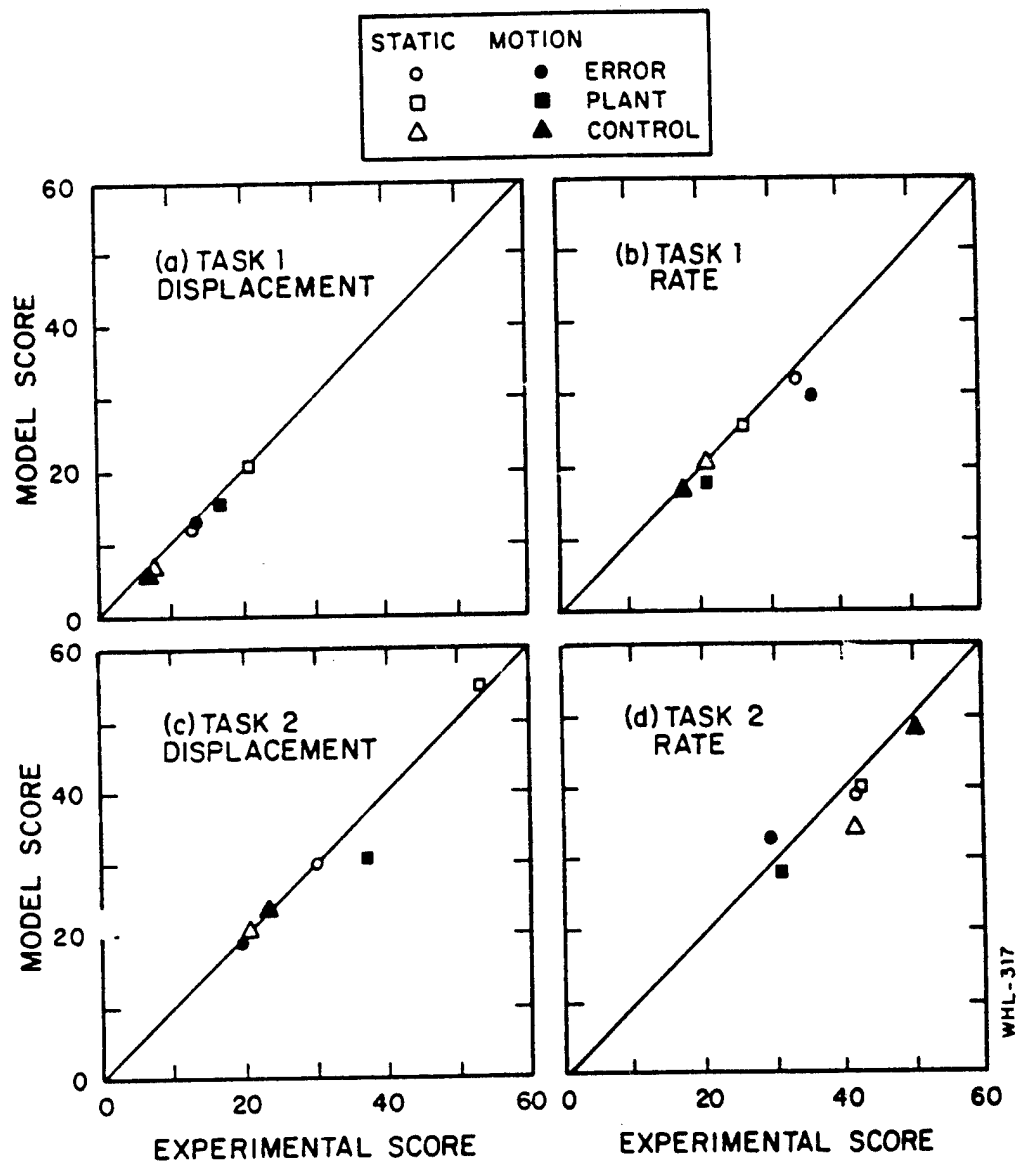


Figure 7. Comparison of Model and Experimental RMS Performance Scores.

Comparisons of model and experimental frequency-response curves are provided in Figure 8. In general, model response curves closely match experimental measures. Most importantly, the major effects of motion cues--the increase in low-frequency phase lead and the reduction in pilot remnant at low frequencies--are mimicked by the model, as is the constancy of the gain-crossover frequency between static and motion conditions.

Having quantified the effect of motion cues on pilot-related model parameters, we can now use the model to extrapolate the experimental results to situations beyond those studied in the laboratory. A particularly useful application of the pilot/vehicle model is to predict performance-workload tradeoffs (17, 18), especially as it is very difficult to obtain objective measures of workload experimentally.

Figure 9 shows predicted rms tracking error as a function of attention to the tracking task, where "attention" is related to the observation noise/signal ratio as described in Section 2. A relative attention of unity corresponded to -20 dB in this analysis.

Although not apparent from Figure 9, attentional allocation between visual and motion perceptual variables was readjusted to achieve minimum performance cost at different levels of overall attention. For both Task 1 and Task 2, decreasing overall attention required that an increasing fraction of available attention be devoted to motion variables.

Motion cues affect the predicted tradeoff curves differently for the two experimental tasks explored in the AMRL/BBN study. The dependency of rms error on attention is similar for Task 2 static and motion conditions, with error being consistently lower for the motion case. The effect of motion cues for Task 1 is basically to reduce the sensitivity of performance to workload at low levels of workload. That is, performance is about the same for moderate to high workload levels; at low workload, motion cues apparently provide stabilizing information that prevents severe deterioration of performance.

#### Discussion of Model Results

As we noted in the discussion of experimental results, the AMRL roll-axis experiments produced results different from those observed in previous studies. Specifically, gain-crossover frequency remained virtually constant, high-frequency phase shift changed in the direction of more lag, low-frequency phase lead increased, and the benefits of motion cues were greater for the high-order (i.e., low-bandwidth) plant; most of the Stapleford et al and Shirley data showed opposite trends.

Except for the greater high-frequency phase lag, the effects of motion in the AMRL/BBN study are accounted for by a straightforward information analyses. The increase in high-frequency phase lag is modeled best by an increase in effective pilot time delay. One possible cause of the apparent increase in delay is the lag introduced by the dynamics associated with information processing by the semi-circular canals (19, 20).

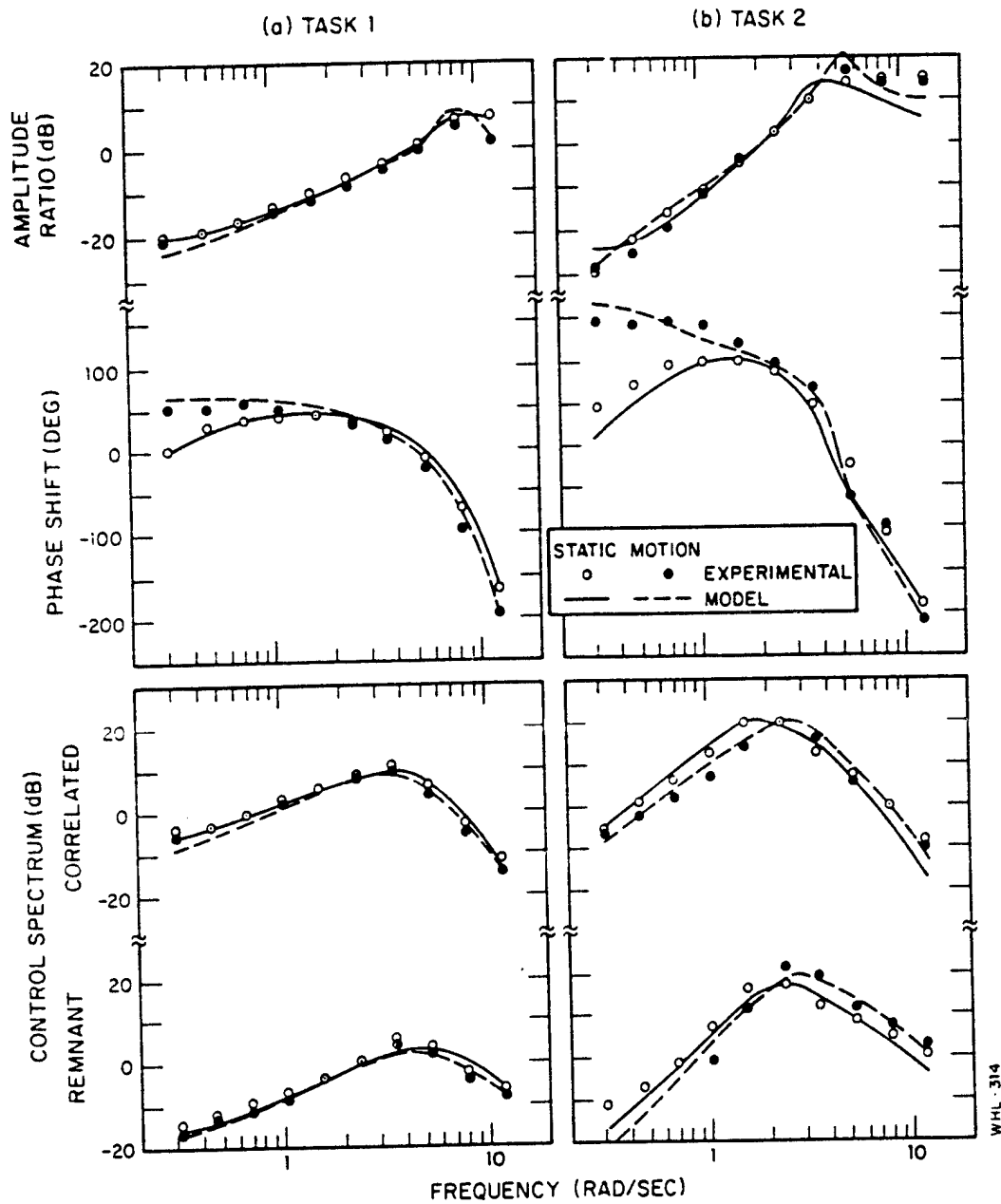


Figure 8. Comparison of Model and Experimental Frequency Response.

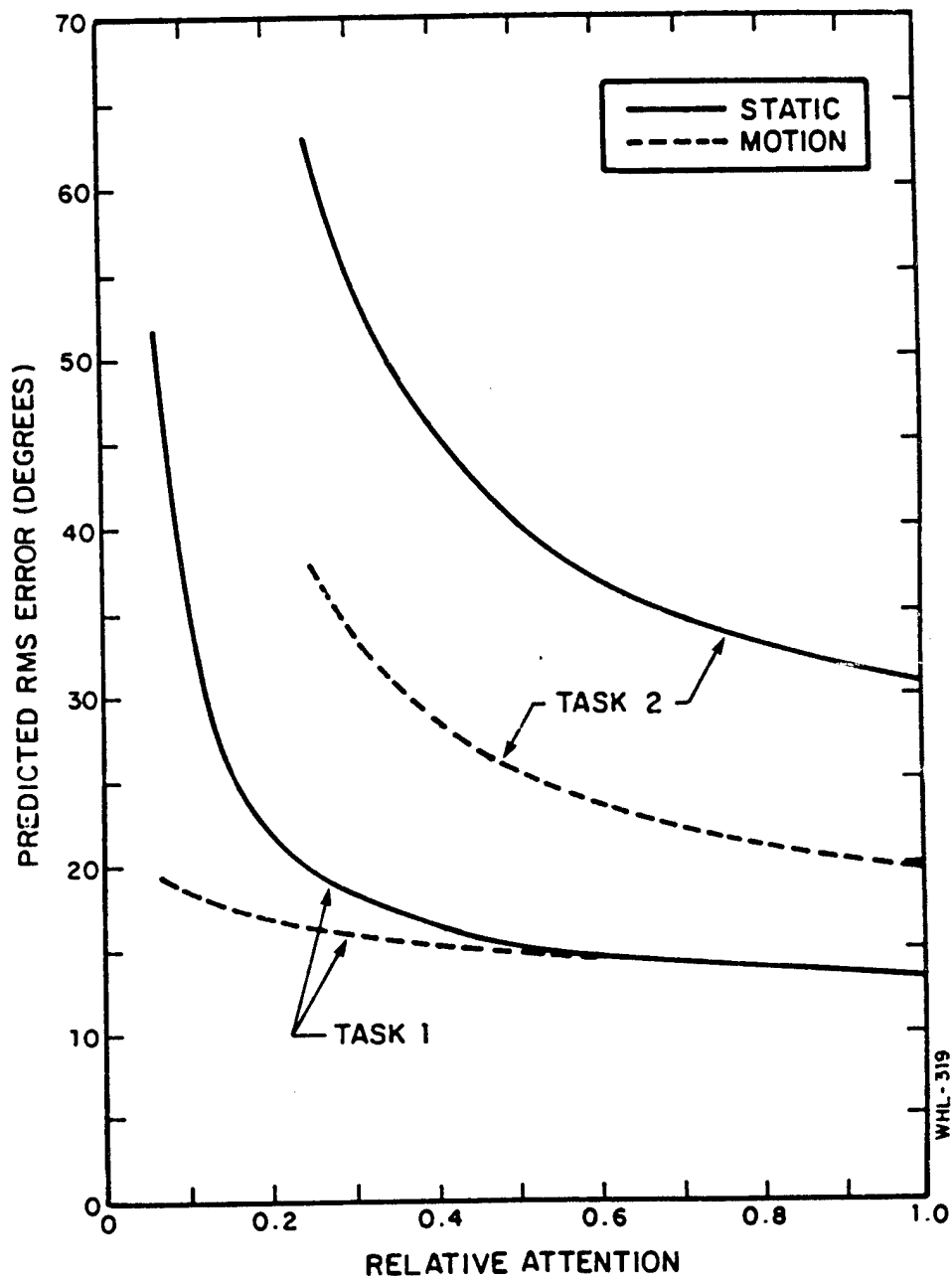


Figure 9. Effect of Motion Cues on Predicted Performance - Workload Tradeoff.

The time delay increase may also be related to limb motion induced by simulator motion. Recent studies of tracing in vibration environments have shown that effective pilot delay increases under vibration conditions (8, 9). Large increases in motor diving noise were also associated with vibration, however; similar effects were not observed in the AMRL/BBN study.

The model results shown in Figures 7 and 8 are consistent with the hypothesis that (a) the pilot obtains position, rate, and acceleration cues from the motion simulation, and (b) visual and motion-related sensory information mutually interfere. Other hypotheses were also tested; in particular, that (a) only rate information is obtained, and (b) there is no interference between visual and motion information.

As documented in (1), these various hypotheses yielded similar matching error scores. Thus, analysis did not provide a clear-cut choice of hypotheses concerning the use of motion cues in the roll-axis experiments, and some subjective judgement was required to select a modeling philosophy. Since there is a physiological basis for assuming that position, rate, and acceleration information will be provided in a moving environment (at least in combination, if not as distinctly separate sensations), we adopt the more general hypothesis that all these cues are obtained; we let the model then determine the extent to which the available cues will be used in a specific tracking situation.

There is some supporting evidence to indicate that attention is shared between motion and visual cues. The attentions shown in Table 2 were derived on the basis of providing the best quantitative match to the experimental data. The model was also used in a purely predictive manner to find the allocation of attention (assuming interference) that would provide the lowest cost, where "cost" was defined as a weighted sum of error and control-rate variances. The attentional allocation that yielded least cost was very close to the allocation that best matched experimental data.

As documented in Levison, Baron, and Junker (1), additional model analysis was performed to search for a consistent set of rules for selecting control-related cost weightings. In the case of the roll-axis tasks discussed in this paper, the subjects appeared to operate at a point where the slope of the error-vs-control-rate curve reaches a minimum. This finding suggests a notion of physical workload that is similar to the ideas of attentional workload offered various researchers (7, 21); namely that the pilot will operate in a region in which additional improvement in overall system performance is offset by the additional cost of the effort required (where "cost" is defined in terms of pilot noise/signal ratios in the case of attentional workload and control or control rate activity in terms of physical workload).

## CONCLUSIONS

The principal results of this study may be summarized as follows:

1. The effects of motion cues on roll-axis tracking performance obtained by AMRL can be modeled by (a) an increment of 0.05 seconds to the pilot time delay, and (b) inclusion of sensory variables that are likely to be provided by motion sensors (position, rate, and accel-

eration of the plant roll angle in these experiments). Modeling of dynamics associated with motion sensing is not required.

2. The experimental results do not allow us to determine whether motion and visual cues are processed in parallel, or whether the pilot must "share attention" between modalities. Furthermore, we are unable to determine whether the pilot obtains only rate cues from his motion sensors, or whether he uses a combination of position, rate, and acceleration cues.
3. If we assume that attention is shared between modalities, tracking performance is consistent with the notion that attention is shared optimally. Moreover, optimal allocation of attention between motion and visual sensory variables is different for the two control systems explored in the AMRL study.
4. Although tracking error is not greatly affected by the selection of a relative "cost coefficient" on control-rate activity, a good match to control scores requires that this weighting be readjusted for the two plants explored in this study; furthermore, different weightings are found for motion and static tracking for the more difficult plant.
5. The results of the AMRL experiment are different in certain respects from earlier studies of motion-based tracking. The AMRL study shows that motion cues result in an increase in low-frequency phase lead, an increase in high-frequency phase lag, and no important change in gain-crossover frequency; whereas other studies have shown that motion has little effect on low-frequency phase lead, reduces high-frequency phase lag, and allows an increase in gain-crossover frequency.
6. Although motion cues did not enhance tracking performance for the less difficult plant explored in the AMRL study, model analysis predicts that motion will enhance performance on this task if the pilot is required to allocate a substantial fraction of his attention to another task. That is, the less attention paid to the tracking task, the greater the relative benefit of motion cues.

The results of this study suggest a number of areas for future research, some of which are likely to be the subject of a follow-on to the study described herein. Recommended areas include:

1. application of the model to tracking situations explored in preceding studies of motion cues to determine whether or not a consistent modeling philosophy accounts for the use of motion cues in a variety of steady-state tracking situations;
2. consideration of vestibular dynamics in the pilot model, specifically to determine whether or not the apparent increase in time delay can be accounted for by the lags associated with vestibular dynamics;

3. effects of motion cues on performance in a high workload environment;
4. effects of motion cues in tracking tasks with transient inputs, especially in situations where visual/motion conflicts may be important; and
5. a controlled study of the effects of control gain and system bandwidth to help refine the motor aspects of the pilot/vehicle model.

#### REFERENCES

1. Levison, William H., S. Baron and A. M. Junker, "Modeling the Effects of Environmental Factors on Human Control and Information Processing," BBN Report No. 3258, May 1976.
2. Ringland, R. F., R. L. Stapleford, and R. E. Magdaleno, "Motion Effects on an IFR Hovering Task--Analytical Predictions and Experimental Results," NASA CR-1933, November 1971.
3. Stapleford, R. L., R. A. Peters, and F. Alex, "Experiments and a Model for Pilot Dynamics with Visual and Motion Inputs", NASA CR-1325, May 1969.
4. Shirley, R. S., "Motion Cues in Man-Vehicle Control", M.I.T., Cambridge, Mass., Sc.D. Thesis, January 1968.
5. Ringland, R. F. and R. L. Stapleford, "Experimental Measurements of Motion Cue Effects on STOL Approach Tasks", NASA CR-114458, April 1972.
6. Junker, A. and C. Replogle, "Motion Effects on the Human Operator in a Roll-Axis Tracking Task", Aviation, Space and Environmental Medicine, Vol. 46, pp. 819-822, June 1975.
7. Levison, W. H., J. I. Elkind and J. L. Ward, "Studies of Multivariable Manual Control Systems: A Model for Task Interference", NASA CR-1746, May 1971.
8. Levison, W. H. and P. D. Houck, "Guide for the Design of Control Sticks in Vibration Environments", Aerospace Medical Division, Wright-Patterson Air Force Base, Ohio, AMRL-TR-74-127, February 1975.
9. Levison, W.H., "Biomechanical Response and Manual Tracking Performance in Sinusoidal, Sum-of-Sines, and Random Vibration Environments", AMRL-TR-75-94, Aerospace Medical Division, Wright-Patterson Air Force Base, Ohio, April 1976.
10. Levison, W. H., "The Effects of Display Gain and Signal Bandwidth on Human Controller Remnant", Wright-Patterson Air Force Base, Ohio, AMRL-TR-70-93, March 1971.

11. Baron, S., D. L. Kleinman, et al., "Application of Optimal Control Theory to the Prediction of Human Performance in a Complex Task", AFFDL-TR-69-81, March 1970.
12. Kleinman, D. L., S. Baron and W. H. Levison, "An Optimal-Control Model of Human Response, Part 1: Theory and Validation", Automatica, Vol. 6, pp. 357-369, 1970.
13. Kleinman, D. L. and S. Baron, "Manned Vehicle Systems Analysis by Means of Modern Control Theory", ASA CR-1753, June 1971.
14. Kleinman, D. L., S. Baron and W. H. Levison, "A Control Theoretic Approach to Manned-Vehicle Systems Analysis", IEEE Trans. on Auto. Control, Vol. AC-16, No. 6, December 1971.
15. Baron, S. and D. L. Kleinman, et al., "An Optimal Control Model of Human Response - Part II: Prediction of Human Performance in a Complex Task", Automatica, Vol. 6, pp. 371-383, Pergamon Press, London, England, May 1970.
16. Baron S. and W. H. Levison, "Analysis and Modelling Human Performance in AAA Tracking", BBN Report No. 2557, Bolt Beranek and Newman Inc., Cambridge, Mass., March 1974.
17. Baron, S. and W. H. Levison, "A Manual Control Theory Analysis of Vertical Situation Displays for STOL Aircraft", NASA CR-114620, April 1973.
18. Baron, S. and W. H. Levison, "An Optimal Control Methodology for Analyzing the Effects of Display Parameters on Performance and Workload in Manual Flight Control", IEEE Trans. on Systems, Man, and Cybernetics, Vol. SMC-5, No. 4, July 1975.
19. Young, L. R., "The Current Status of Vestibular System Models", Automatica, Vol. 5, pp. 369-383, 1969.
20. Peters, R. A., "Dynamics of the Vestibular System and Their Relation to Motion Perception, Spatial Disorientation, and Illusions", NASA CR-1309, April 1969.
21. Wewerinke, P. H., "Human Operator Workload for Various Control Situations", Proceedings of the Xth Annual Conference on Manual Control, Wright-Patterson Air Force Base, Ohio, April 1974.



THE INFLUENCE OF LOSS OF VISUAL CUES ON PILOT PERFORMANCE DURING THE FINAL  
APPROACH AND LANDING PHASE OF A REMOTELY PILOTED VEHICLE MISSION

James C. Howard

NASA-Ames Research Center  
Moffett Field, California 94035

SUMMARY

Remotely piloted research vehicles (RPRVs) are currently being flown from fixed-base control centers, and visual information is supplied to the remote pilot by a TV camera mounted in the vehicle. In these circumstances, the possibility of a TV failure or an interruption in the downlink to the pilot must be considered. To determine the influence of loss of TV information on pilot performance during the final approach and landing phase of a mission, an experiment was conducted in which pilots were asked to fly a fixed-base simulation of a Piper PA-30 aircraft with loss of TV information occurring at altitudes of 15.24, 30.48, and 45.72 m (50, 100, and 150 ft). For this experiment, a specially designed display configuration was presented to four pilots in accordance with a Latin square design. Initial results indicate that pilots could not ensure successful landings from altitudes exceeding 15.24 m (50 ft) without the visual cues supplied by the TV picture.

INTRODUCTION

To facilitate control of remotely piloted research vehicles (RPRVs), visual information is supplied to the remote pilot by a TV camera mounted in the vehicle as shown in figures 1 and 2. Because of the possibility of TV failure, an experiment was conducted to determine the influence of loss of visual cues on pilot performance during the final approach and landing phase of a mission. A recent study (ref. 1) established that the display of state variables shown in figure 3, was an effective configuration for RPRV pilots. In the configuration used, the basic display consisted of a TV picture of the terrain and runway, a horizon bar, and an aircraft symbol. Pilot opinion and experimental evidence indicated that pitch attitude, glide slope information, and a chevron combined with digital readouts of airspeed, altitude, and vertical velocity were the most useful additions to the basic display. The chevron, which is a sensitive indicator of altitude and sink rate, is shown separately in figure 4. It enables the RPRV pilot to control these variables with the precision necessary for successful landings. In all simulated landings, the chevron appeared on a head-up display at an altitude of 30.48 m (100 ft). In the present experiment, the TV picture was blacked out at altitudes of 15.24, 30.48, 45.72 m (50, 100, and 150 ft), and pilot performance was measured as a function of loss of visual information.

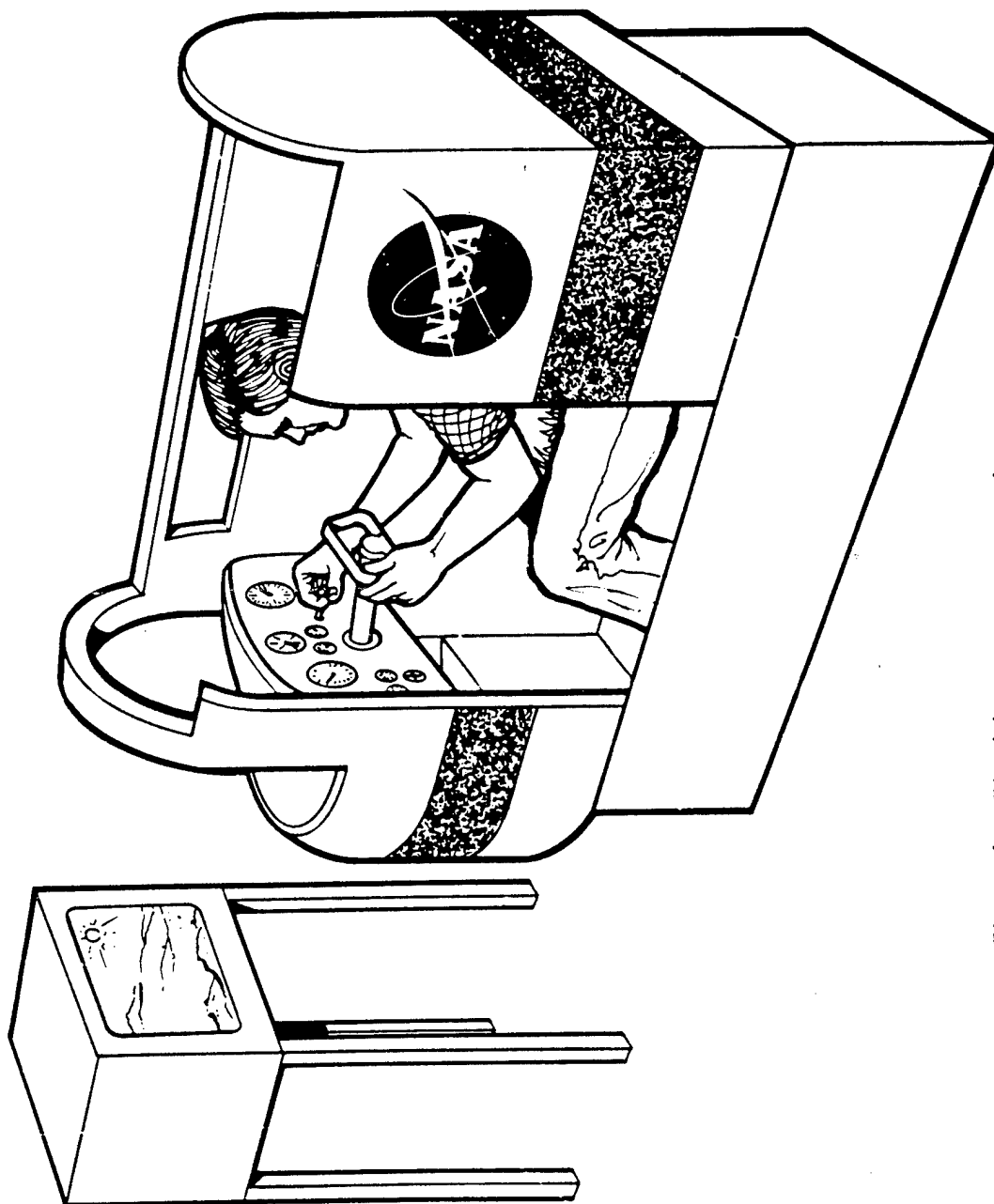


Figure 1.- Fixed-base remote control center.

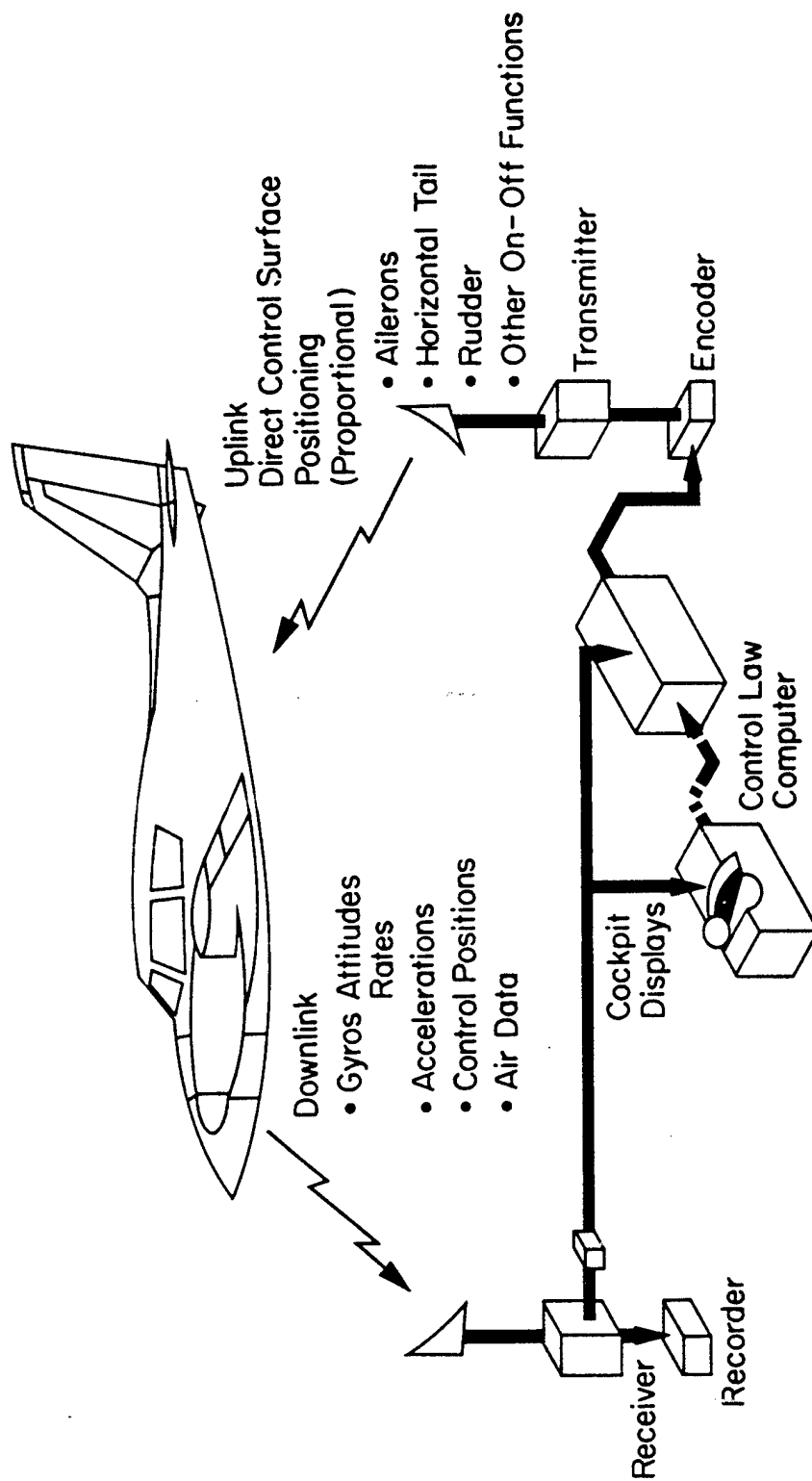


Figure 2.- Avionics link used in the NASA remotely piloted research vehicle.

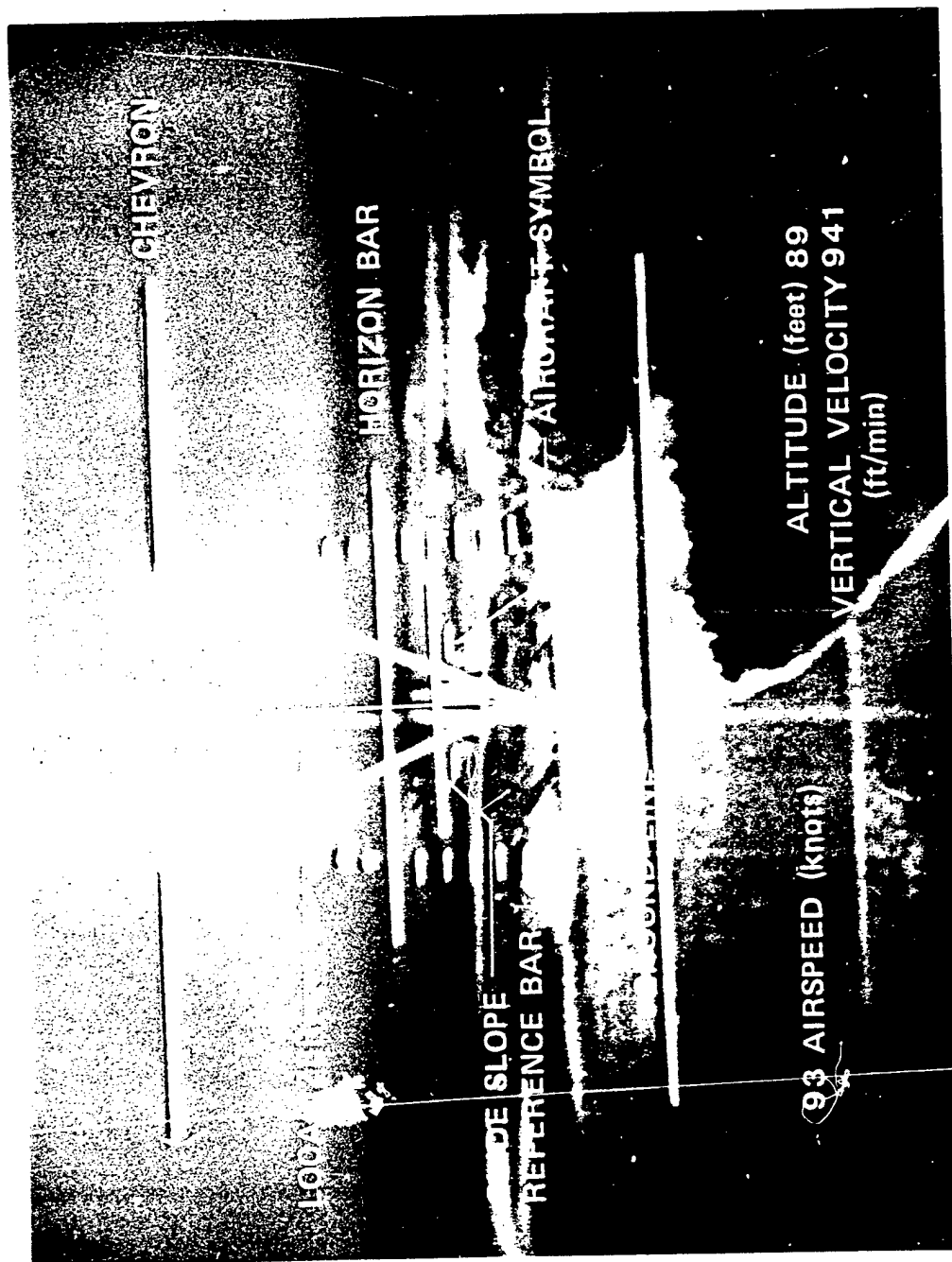


Figure 3.- Display configuration.

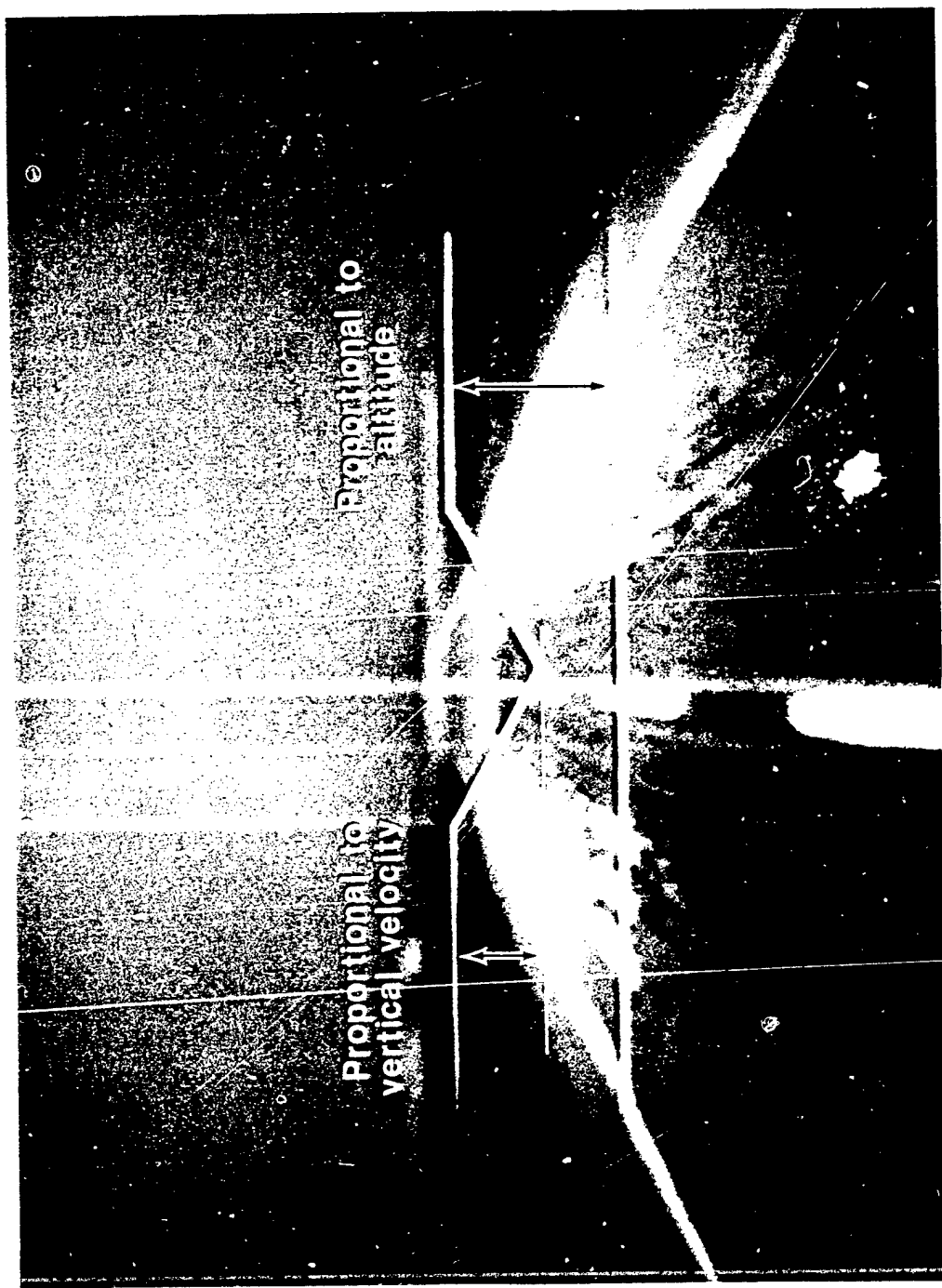


Figure 4.- Chevron characteristics.

## EQUIPMENT AND METHOD

### Aircraft Description

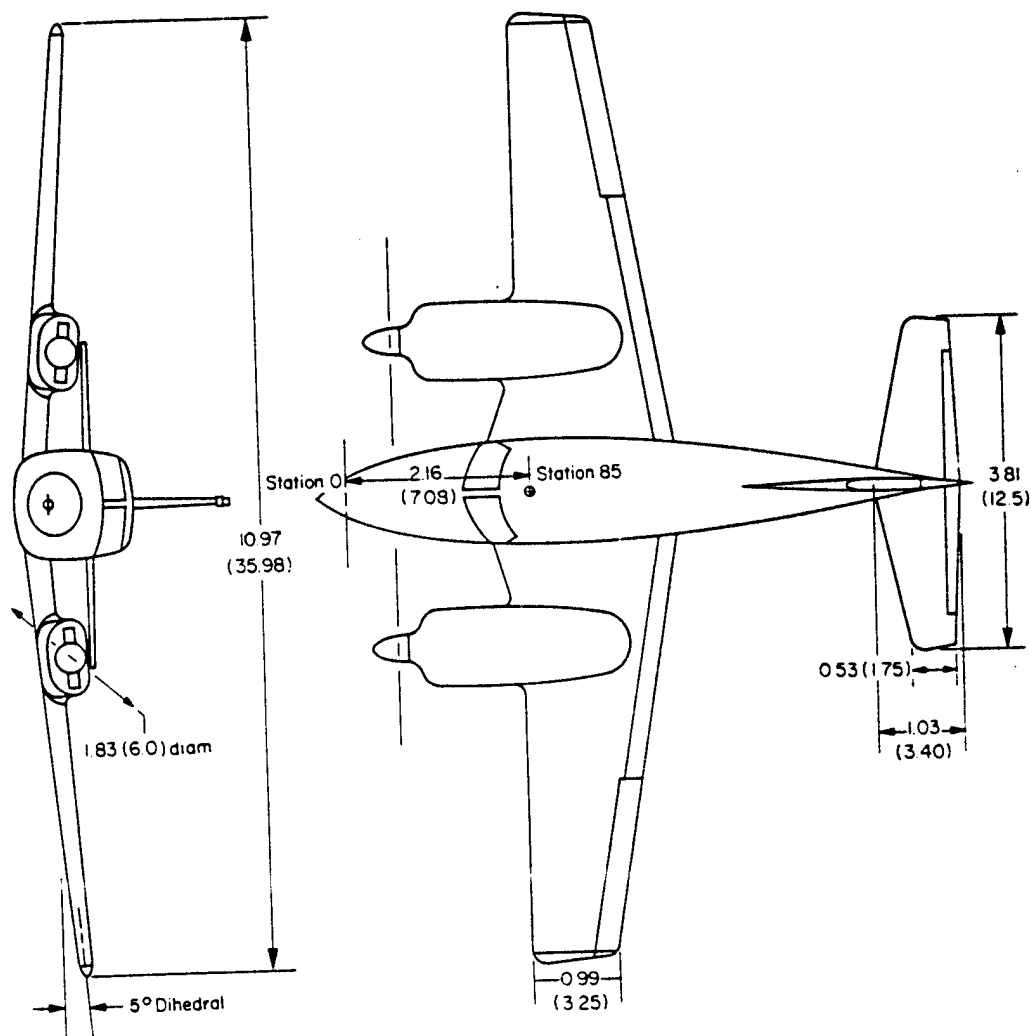
A Piper PA-30 aircraft was simulated for this experiment. This aircraft was chosen because it is currently being used at NASA's Flight Research Center for RPRV flight test experimentation. It is a low-wing monoplane, powered by two Lycoming, four cylinder, aircooled engines, each capable of delivering 160 rated horsepower. Figure 5 gives the principal dimensions. The airplane has a wing span of 10.97 m (35.98 ft), a wing area of 16.54 m<sup>2</sup> (178 ft<sup>2</sup>), an aspect ratio of 7.3, and a mean aerodynamic chord of 1.52 m (5 ft) (ref. 2). The airplane has the standard three-control system. The horizontal tail is the all-movable type with a control deflection range of 4° to -14°. The tail has a trailing-edge tab which moves in the same direction as the tail, with a deflection ratio (tab deflection to tail deflection) of 1.5. The control deflection on each aileron is from 14° to -18°. The rudder control deflection range is ±27° (ref. 2).

### Simulator and Vehicle Model

The Piper PA-30 aircraft was simulated on a Systems Engineering Laboratory (SEL) 840 digital computer. The final-approach model was based on available data from FRC's simulation model and references 2 and 3. The model consisted of the rigid body, six-degrees-of-freedom equations of motion that are perturbation equations in the stability axis system (ref. 3). After passage through a digital to analog converter (DAC), the output from the SEL 840 computer was used to drive a visual-flight attachment via an Applied Dynamics, Inc. (ADI) 256 analog computer. The output from the SEL 840 computer was also used to drive an Evans and Sutherland (E and S) LDS-2 display generator, which was mounted in parallel with the visual-flight attachment. The E and S display generator was used to superimpose geometric representations of state variables on the pictorial scene of terrain and runway generated by the visual-flight attachment. The visual-flight attachment used in this experiment was a General Precision Systems (GPS) model. The essential components of this attachment are a servo-driven television camera, an optical probe, and a TV monitor (ref. 4). A fixed-base simulator, consisting of a pilot's cab equipped with a conventional cockpit display and augmented with the GPS visual scene, was used to assess the importance of the E and S generated displays in assisting RPRV pilots to execute the final approach and landing phase of a mission without a TV picture of the terrain.

## EXPERIMENTAL DESIGN

The configuration shown in figure 3 was used as a head-up display superimposed on a picture of the terrain. The picture of the terrain represents the visual information supplied to the RPRV pilot by the TV camera mounted in the vehicle. Four landing conditions were devised, three with loss of TV information at different altitudes and one with no loss of TV information. The



ORIGINAL PAGE IS  
OF POOR QUALITY

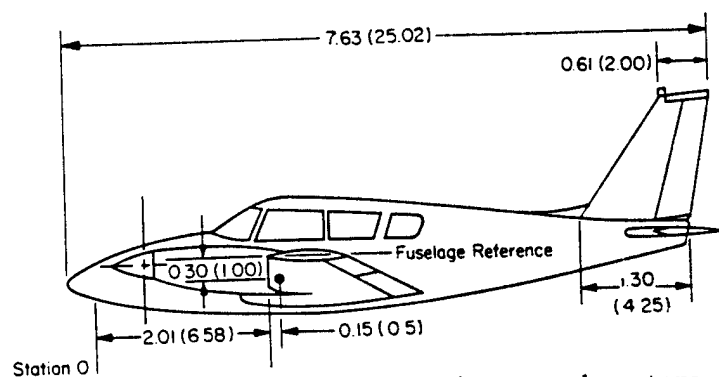


Figure 5.- Three-view drawing of airplane. All dimensions are in meters (feet).

resulting tasks were given to four pilot subjects in accordance with a Latin square design. If a Latin square with four displays is used, the error mean square will have only six degrees of freedom. To obtain an estimate of error with a larger number of degrees of freedom, the experiment was replicated using eight Latin squares. Each Latin square was then treated as a block in a randomized block design, with the square X display sum of squares corresponding to the block X treatment sum of squares in a randomized block design.

In the applications to which the Latin square has been typically applied in the fields of psychology, physiology, and drug research, each row of a square corresponds to a single subject, with the columns corresponding to successive periods or tests. This procedure was followed in the present design, where the element in a given Latin square gives the performance measure obtained during a test run with the corresponding display.

Each pilot was instructed to execute final approaches and landings starting from an initial distance of 2743 m (9000 ft) from the runway threshold, and an initial altitude of 152 m (500 ft). For each series of runs, the Latin square design assures that a subject never encounters the same order of presentation more than once, and that the order effect, whether it be practice, fatigue, boredom, etc., is independent of particular displays.

During each run the following performance measures were taken for subsequent statistical evaluation: sink rate at touchdown, root mean square (rms) of sink rate, rms of stick activity during the final 30.48 m (100 ft), and rms of distance from runway centerline.

## RESULTS AND DISCUSSION

### Sink Rate at Touchdown

The influence of loss of visual information on pilot performance may be seen by tabulating the sink rate at touchdown for each condition. In the following matrices of performance measures, S denotes subject, L the Latin square, and C the condition. Condition 1 is the condition without loss of TV visual information. Conditions 2, 3, and 4 represent loss of visual information at altitudes of 15.24, 30.48, and 45.72 m (50, 100, and 150 ft), respectively. The elements of the matrices are measures of sink rate at touchdown in ft/sec.

S = 1				
C =	1	2	3	4
L = 1	-2.53000	-1.66400	-3.07900	-0.60400
2	-1.79900	-0.78000	-0.90300	-0.59100
3	-1.95200	-1.04600	-1.46200	-1.76100
4	-1.84200	-0.77900	-1.21000	-1.48900
5	-1.76500	-1.82300	-1.72300	-1.42900
6	-1.86600	-1.31700	-0.76700	-0.95100
7	-1.87800	-1.15200	-1.24300	-1.26000
8	-1.62200	-1.12800	-1.11700	-1.77700



S = 2				
C =	1	2	3	4
L = 1	-4.88000	-3.35400	-2.18200	-1.91900
2	-3.50800	-5.20800	-7.84600	-3.66900
3	-4.12400	-0.83700	-6.55600	-3.64200
4	-4.33100	-2.65200	-2.32100	-2.03900
5	-4.00300	-2.82300	-1.48300	-4.64600
6	-4.06800	-1.15800	-0.79800	-3.17200
7	-2.59000	-6.17300	-1.62100	-4.66800
8	-2.93900	-0.63400	-0.94100	-1.78200

S = 3				
C =	1	2	3	4
L = 1	-0.93200	-2.91900	-4.09000	-2.10800
2	-3.30600	-1.63500	-2.52300	-1.86800
3	-2.82900	-3.10100	-1.47900	-2.75400
4	-1.60300	-2.23200	-4.27900	-4.22900
5	-1.51800	-1.40300	-8.47300	-1.28400
6	-1.20400	-2.29900	-1.86800	-2.54900
7	-1.75900	-0.80800	-2.06900	-7.27100
8	-1.73000	-1.15500	-0.91400	-0.74700

S = 4				
C =	1	2	3	4
L = 1	-1.41100	-3.06000	-1.01800	-6.52400
2	-3.20000	-1.19300	-2.05300	-3.62200
3	-1.52300	-0.68100	-5.54500	-1.67500
4	-1.42300	-1.33100	-1.14000	-1.40000
5	-0.69000	-0.69100	-1.62500	-2.05400
6	-0.37500	-0.91400	-3.82400	-0.71000
7	-0.86000	-1.10300	-3.37600	-0.84500
8	-1.22400	-0.83300	-1.84700	-0.77100

The computed value of the variance for the four conditions was 3.24. An error variance of 2.08 gave rise to an F ratio of 1.6. For a significance level of 0.05, the critical value of F for a condition variance with three degrees of freedom and an error variance with nine degrees of freedom is 3.86, and it is evident that the experimental value is not statistically significant.

#### rms Values of Sink Rate

To assess the influence of loss of visual information on pilot performance, as measured by rms values of sink rate, this parameter was computed during the final 30.48 m (100 ft) of altitude. The mean rms value of sink rate for all subjects and all error conditions was 1.9 m/s (6.24 ft/sec). As in the case of sink rate at touchdown, the rms values of sink rate were tabulated for each landing condition and are presented in the matrices below. The elements of the following matrices are rms values of sink rate, calculated during the final 30.48 m (100 ft) of altitude.

---

S = 1				
C =	1	2	3	4
L = 1	5.52900	6.32900	4.66000	5.02100
2	5.56400	4.65300	5.61100	5.42800
3	5.52200	4.85200	5.14200	5.20800
4	5.85000	6.25700	5.50800	5.07500
5	6.30900	5.75800	5.00800	5.81200
6	5.89200	5.90300	5.73000	5.88900
7	6.10300	6.32100	6.02800	5.81700
8	6.71100	5.73100	6.58100	5.92200

---

S = 2				
C =	1	2	3	4
L = 1	5.38800	5.90100	7.59300	6.86600
2	5.26900	7.20300	27.47600	6.28000
3	7.38000	7.14700	8.69200	7.33400
4	7.09000	6.57400	8.50800	6.22200
5	6.77900	8.47500	6.82600	7.48000
6	7.33600	5.90700	9.12400	7.02900
7	6.17800	9.79200	7.37500	7.66600
8	6.96200	6.48700	7.98700	8.24400

---

S = 3				
C =	1	2	3	4
L = 1	6.51300	5.82200	5.65900	6.41800
2	4.60200	6.44900	3.76000	4.04800
3	5.70600	4.20300	4.45500	5.57700
4	4.87800	4.55400	3.93900	5.33500
5	4.92600	5.88200	5.28100	5.54900
6	4.73600	3.30900	4.77500	4.51300
7	5.31400	5.06000	4.47300	4.56700
8	4.58700	5.03800	6.20800	4.09100

---

S = 4				
C =	1	2	3	4
L = 1	5.25900	6.20000	7.01000	9.07200
2	5.32100	6.21400	6.41900	7.65600
3	5.43000	6.67900	8.15900	6.30600
4	5.05000	5.47300	5.74400	5.41900
5	5.59300	5.31500	6.37900	6.59300
6	6.14500	7.49800	8.18100	6.68200
7	5.13300	6.03400	7.37300	6.67900
8	5.11000	6.18800	7.69200	5.84000

---

The computed value of the variance for the four landing conditions was 8.71. An error variance of 7.2 gave rise to an F ratio of 1.21. For a significance level of 0.05, the critical value of F for a condition variance with three degrees of freedom and an error variance with nine degrees of freedom is 3.86. It is evident that the experimental value obtained on the basis of rms values of sink rate measures is not statistically significant.

### rms Values of Stick Activity

In order to determine the influence of loss of visual cues on pilot work load, as measured by rms values of stick activity, this parameter was measured during the final 30.48 m (100 ft) of altitude. The mean rms value of stick activity for all subjects and all conditions was 0.39 in.

As in the case of sink rates, the rms values of stick activity were tabulated for each condition. In the matrices of performance measures, the same notation applies here as in the preceding two cases, and the range of conditions is the same. The elements of the following matrices are rms values of stick activity measured during the final 30.48 m (100 ft) of altitude.

---

S = 1				
C =	1	2	3	4
1	0.14900	0.14800	0.29300	0.19400
2	0.15600	0.26600	0.18800	0.14900
3	0.13800	0.19400	0.18100	0.15600
4	0.13100	0.14300	0.16300	0.18400
5	0.12000	0.14900	0.17600	0.16600
6	0.11500	0.16100	0.13100	0.12500
7	0.12700	0.12200	0.12500	0.13100
8	0.10500	0.14200	0.12600	0.15300

---

S = 2				
C =	1	2	3	4
1	0.31300	0.21000	0.15400	0.36600
2	0.21100	0.40200	0.10100	0.21800
3	0.21400	0.17100	0.34700	0.24700
4	0.19900	0.17400	0.33300	0.12800
5	0.20500	0.14100	0.18800	0.13700
6	0.17700	0.11800	0.20200	0.21400
7	0.15400	0.12600	0.19300	0.18500
8	0.14300	0.25200	0.14000	0.12000

---

S = 3				
C =	1	2	3	4
1	0.77900	0.85000	1.30300	1.42800
2	0.54900	1.51500	1.02500	1.13900
3	0.24500	1.56500	0.49000	0.89100
4	0.57600	1.52000	1.98700	0.56300
5	0.73900	1.90900	1.92800	0.42200
6	0.52000	0.49300	0.58400	1.37900
7	0.52200	0.72300	0.32500	2.25800
8	0.72600	0.63500	0.71600	1.41000

---

S = 4				
C =	1	2	3	4
1	0.23300	0.21600	0.17700	0.21200
2	0.23400	0.17100	0.15400	0.15400
3	0.20700	0.25500	0.11800	0.21500
4	0.23200	0.20200	0.17200	0.20700
5	0.18900	0.22500	0.29300	0.15600
6	0.19600	0.14500	0.11300	0.14900
7	0.25400	0.23000	0.10700	0.13500
8	0.21300	0.17000	0.10400	0.18700

The computed value of the variance of stick activity for all conditions was 0.15. An error variance of 0.16 gave rise to an F ratio of 0.97. As in the preceding two cases, the critical value of F for a significance level of 0.05 is 3.86. It is evident that the variation of workload with loss of visual cues, is not statistically significant.

#### Lateral Offset from Runway Centerline

The data obtained indicate that with the head-up display configuration used, the absence of a TV picture of the terrain made no significant difference to the pilot's ability to control sink rate. Moreover, landing under these conditions imposed no additional workload on the pilots. However, the disappearance of the visual scene provided by the TV camera impaired the pilot's ability to land on the runway. In terms of distances from the runway centerline, the performance data assumed the following form:

S = 1				
C =	1	2	3	4
L = 1	-16.19398	39.46399	-90.33099	13.10200
2	-15.98100	-60.21599	30.13300	6.74900
3	-11.48700	-33.71100	26.88399	14.50500
4	0.81300	-18.58699	-12.41300	-99.40199
5	2.48700	5.56700	-62.53600	-83.81200
6	-9.32900	-20.62399	-157.37900	-65.90500
7	-8.54200	21.83099	-139.63100	17.70599
8	-0.42100	-0.24400	-123.98499	-108.51999

S = 2				
C =	1	2	3	4
L = 1	1.49000	28.60500	-136.31799	-143.21199
2	-1.18900	-121.96199	-19.43799	4.77600
3	12.89300	-35.34799	-83.18599	46.59299
4	22.04599	2.92600	-67.99300	76.88899
5	2.95300	-6.29400	-43.64899	81.21599
6	5.96100	31.53699	-69.62900	52.13899
7	5.27100	-9.15000	-133.36800	-69.99599
8	-6.56800	2.72700	-149.36899	-219.23499

S = 3				
C =	1	2	3	4
L = 1	-13.77200	7.39100	-32.41599	158.53600
2	14.23500	-3.22000	64.41699	-77.44899
3	8.16900	-234.73499	-19.11499	-10.81500
4	10.01300	24.25000	-237.16800	-15.80800
5	4.97700	57.75000	115.48999	-22.53899
6	14.15400	13.89200	-0.06200	-45.82999
7	6.12600	4.43200	20.12399	-62.76299
8	-10.66700	0.91000	13.35600	-46.70200

S = 4				
C =	1	2	3	4
L = 1	-26.34999	52.68100	16.80499	-29.35300
2	-33.31799	51.51299	-3.57100	24.44398
3	-10.27100	39.03400	-11.63700	19.67899
4	-8.64900	24.05399	45.72299	-4.87100
5	-13.30500	25.73199	75.36400	19.04199
6	-11.76900	1.32400	-2.29400	23.49399
7	8.50900	-27.18500	-22.34698	-26.70599
8	-19.03799	-14.80900	-15.26000	18.64999

Since these data clearly indicate the influence of TV information on the pilot's ability to land on the runway, there is no need to perform an analysis of variance. However, to facilitate the interpretation of these data, the rms values of lateral offset from runway centerline in feet are shown in the following table for each pilot and each condition.

Subject	Condition			
	1	2	3	4
1	3.08 m (10.10 ft)	9.39 m (30.82 ft)	29.22 m (95.85 ft)	19.80 m (64.97 ft)
2	3.00 m (9.83 ft)	14.49 m (47.53 ft)	29.97 m (98.33 ft)	32.49 m (106.59 ft)
3	3.30 m (10.82 ft)	26.24 m (86.10 ft)	29.66 m (97.30 ft)	21.61 m (70.91 ft)
4	5.64 m (18.49 ft)	10.31 m (33.82 ft)	10.19 m (33.42 ft)	6.68 m (21.92 ft)

The number of times each pilot failed to land on the runway, for each condition, is shown in the following table.

Subject	Condition			
	1	2	3	4
1	0	0	4	3
2	0	1	4	4
3	0	1	2	2
4	0	0	1	0

## CONCLUSIONS

Statistical evaluation of the data obtained indicates that for the range of conditions considered, there is no significant difference in landing performance, as measured by sink rate, that can be attributed to the absence of a TV picture of the terrain. Workload, as measured by stick activity, did not increase significantly when the pilot was deprived of visual cues. However, there appeared to be increased rudder activity as the pilot attempted to control heading without the visual scene. The sudden transition from visual to instrument reference conditions was disconcerting to the pilots, and when this occurred at 30.48 m (100 ft) or more, the probability of drifting off the runway increased, particularly if the transition occurred when the localizer error was large.

## REFERENCES

1. Howard, James C.: Display Requirements for the Final Approach and Landing Phase of an RPV Mission. NASA TM X-62,346, 1974.
2. Funk, Marvin P.; and Freeman, Delma C., Jr.: Full Scale Wind-Tunnel Investigation of Static Longitudinal and Lateral Characteristics of a Light Twin-Engine Airplane. NASA TN D-4983, 1969.
3. Koziol, Joseph S., Jr.: Simulation Model for the Piper PA-30 Light Maneuverable Aircraft in the Final Approach. Transportation Systems Center Technical Memorandum, July 1971.
4. Chase, Wendell D.: Evaluation of Several TV Display Systems for Visual Simulation of the Landing Approach. NASA TN D-6274, 1971.

SIMULATION OF CONVENTIONAL AIRCRAFT APPROACH AND LANDING:  
THE EFFECT OF WITHHOLDING MOTION OR INSTRUMENT CUES

By R.V. Gressang, Capt, USAF

AF Flight Dynamics Laboratory

SUMMARY

The results of two experiments conducted using the multicrew cab simulator of the Flight Control Division, Air Force Flight Dynamics Laboratory are presented. The first experiment was concerned with the effect upon approach and landing performance of fixed base versus moving base operation. The second experiment was concerned with the effect of denying instrument information upon approach and landing performance in a simulator. For this experiment, the instruments were frozen at their initial trim values, and the pilot had to land the simulator using only visual, motion, and sound cues.

The aircraft simulated was a four engine jet transport of about 180,000 pounds. During the experiments, the aircraft was simulated both with and without its stability and control augmentation system (SCAS).

The first experiment established that performance changes due to fixed base versus moving base operation were slight, and were much smaller than changes induced by turning off the SCAS system. In this simulator, the pilot could achieve a credible landing without using the instruments, but he had more difficulty if the SCAS was off. If instrument information were denied, he flew a lower, slower approach.

INTRODUCTION

The simulation of aircraft approaches and landings has recently become important because of the low cost, safe, flexible opportunities it presents for aircrew training, pilot/aircraft system research and engineering [1], [2], [3]. For these applications to be feasible, it is necessary to know how simulation results and performance compare with actual results and performance for the appropriate task. It is also necessary to know that the pilot does not significantly change his behavior in going from an actual aircraft to a simulation of that aircraft, and to know what cues must be provided in the simulator to allow the pilot to fly the simulator without changing his basic behavior pattern for the task being simulated.

Experience to date indicates that it is difficult to simulate landing an aircraft in such a way that the touchdown performance is comparable to the performance achieved by a pilot in a real aircraft [2-8]. The statistic most commonly reported about landing simulations is the mean sink rate at

touchdown, which is generally significantly higher in the simulation than it would be for an actual aircraft. This has been observed in over fourteen different simulations, involving at least four different aircraft, both fixed base and three degree of freedom moving base, and at least five different types of visual display. [2-8]

Experimental investigations of the differences between simulator landing performance and aircraft landing performance have not determined any specific single factor which contributes most of the difference between simulator and aircraft performance. Since no single specific factor has been related to the difference between simulator and aircraft performance, and since attaining maximum realism of cues in a simulator is limited by necessary physical limitations (such as the amount of travel allowed in motion drive systems) and the economic law of diminishing returns, the objective of attaining realistic pilot behavior in landing simulations must be obtained by carefully determining the sensitivity of the pilot's performance to the various cues.

One approach to attaining realistic performance has been to thoroughly familiarize the pilot with the simulation, giving him several hours of simulation time before the experiment is started and data collected. However, it has been objected that this results in training the pilot to fly the simulator as a simulator rather than as an aircraft. An alternate approach is to analyze what cues are used by the pilot to accomplish the landing task, and then concentrate on providing accurately only the minimum cues necessary. The difficulty with this approach is that no clear consensus exists as to what cues are used during landing, and what their relative importance is.

The experiments reported on in this paper provide information useful to either of the above approaches. Information was obtained on how many simulation runs would result in stabilized touchdown sink rates, while the effect of freezing the instruments (thus preventing the pilot from flying the simulator using only the instruments) was studied. Similarly, the effect of the limited motion cues available upon touchdown performance was studied. When the instruments were frozen, it was determined that visual and limited motion cues were sufficient to land the simulator. The pilot did succeed in landing the simulator with sink rates representative of real aircraft, but his behavior was slightly modified from what it would have been in a real aircraft.

#### DESCRIPTION OF THE SIMULATION

The objectives of the experiments reported on in this paper were to investigate the effects of visual and motion cues upon simulated aircraft landings. The pilot's task was to execute a conventional Visual Flight Rules (VFR) approach and landing, depending mainly upon the visual display for flight path guidance. All approaches were conducted under simulated clear air daylight conditions. Each experimental run began from trim conditions at 750 feet on a three degree glide slope. The pilot used visual path information to fly a nominally three degree glide slope approach to the runway, flare, and touch the aircraft down. The run was terminated after touchdown.



The aircraft used for this simulation was modeled by six degree of freedom nonlinear equations of motion on a hybrid computer<sup>[9]</sup>. The aircraft was a four engine jet transport of approximately 180,000 pounds gross weight. The aircraft had conventional aileron, elevator, rudder, and throttle controls. It also had a direct lift control obtained by using spoilers, and blown flaps. The blown flaps resulted in considerable powered lift. Longitudinal control was accomplished through the direct lift control and pitch trim button, while lateral control was accomplished using the ailerons. In normal configuration, the aircraft had an extensive stability and control augmentation system (SCAS). Certain runs were made with the SCAS on, and other runs made with the unaugmented aircraft.

The instrument panel was organized in a conventional manner. No flight director was used. The cockpit was a C-135 cockpit that had been modified for research and development use. It was mounted upon a three degree of freedom (roll, pitch, heave) motion base<sup>[10]</sup>. Sound cues duplicating four turbo-jet engines were generated.

Visual cues simulating real world changes in size and perspective with respect to aircraft motion were produced using a three dimensional illuminated terrain model and television camera-screen projection system. The field of view of the screen was 60 degrees diagonally. The view was large enough to present a realistic scene through the front windows, but there were no peripheral cues. During an approach, the pilot saw a daylight rural terrain with an airport complex.

Turbulence inputs were inserted into the simulation. These inputs corresponded to light turbulence of the Dryden spectra of MIL-F-8785B<sup>[11]</sup>.

#### DESCRIPTION OF THE EXPERIMENTS

Two experiments were conducted, with the following objectives:

1. Does the motion system affect landing performance?
2. Can the simulator be landed as a conventional aircraft without the use of the cockpit instruments?
3. Can the simulator be landed as a conventional aircraft with realistic values of sink rate at touchdown?

The first experiment was to answer objective 1, and was a 2x2x10 factorial experiment. The factors were motion system on or off, SCAS on or off, and replication (10 replications). Before the experiment began, the pilot executed 10 practice runs. During the experiment, the various conditions were presented to the pilot randomly.

The second experiment consisted of 20 simulated approaches and landings, made with the cockpit instruments frozen at their initial trim values. Half of these runs were made with the SCAS on, and half with the SCAS off. SCAS on or off was presented randomly to the pilot.

The third objective was satisfied by recording the touchdown sink rates of all the approach and landing runs that the subject pilot made. On each simulation run, data were collected both at the instant of touchdown and during the approach. The data collected at touchdown consisted of the instantaneous values of  $x$ ,  $\dot{x}$ ,  $z$ ,  $\theta$ ,  $q$ ,  $y$ ,  $\dot{y}$ ,  $\phi$ ,  $\psi$ ,  $p$ , and  $v$ . During the approach the means and standard deviations of  $\theta$ ,  $q$ ,  $h$  (glide slope deviation in feet),  $\alpha$ ,  $\phi$ ,  $p$ ,  $\psi$ ,  $r$ ,  $y$  (localizer deviation in feet) and  $\beta$  were computed in real time for all points on the approach lying between 500 feet altitude and 50 feet altitude.

The subject pilot for these experiments was an Air Force pilot with 1700 hours total flying time. He was briefed on the purpose of the experiments, and conducted the simulated approaches and landings alone, without the assistance of a copilot. He had no tasks to perform in addition to landing the aircraft.

#### RESULTS OF THE EXPERIMENTS

The data collected during the experiments are presented in Tables 1 through 4. Table 1 presents the longitudinal touchdown data, Table 2 presents the lateral touchdown data, Table 3 presents the longitudinal approach data, and Table 4 presents the lateral approach data. The classification scheme used for the data denotes the (SCAS, motion) combination as A, (SCAS, no motion) as B, (No SCAS, motion) as C, (No SCAS, no motion) as D, (SCAS, no instruments) as E, and (No SCAS, no instruments) as F.

A complete statistical analysis of the data, using  $t$  tests,  $F$  tests,  $M$  tests for homogenous variances, and analysis of variance can be found in reference 12. The results of this analysis are summarized in the following paragraphs.

The largest effects observed during the experiments were due to the control system (SCAS). The aircraft was more difficult to fly when the control system was off, and this was reflected in more scatter in the aircraft variables during the approach and at touchdown.

The only effects observed due to motion cues were a lesser tendency to "duck under" the nominal glide slope when the motion was off combined with a tendency to land further down the runway. However, the tendency to land further down the runway was in conjunction with a similar but more prominent tendency associated with the control system being off.

When the pilot was forced to fly the simulator using only the visual display, he flew more slowly and had more difficulty in controlling airspeed. He "ducked under" the nominal glide slope to a greater extent, and the control system being off increased the scatter in the aircraft variables, especially the lateral variables. Despite these differences, the pilot was able to fly and land the simulator as an aircraft.

The lack of an appreciable effect due to the motion system being on or

off is not unexpected for the landing task. The standard deviations of  $p$ ,  $q$ , and  $r$  are all of the same magnitude or smaller than the thresholds for human sensing of these angular velocities, so motion cues would not be expected to be important in the task simulated.

The data available for studying whether the simulator can be landed as a conventional aircraft with realistic values of sink rate at touchdown consisted of values of the sink rate at touchdown on 128 simulated landings by the same pilot. These 128 sink rate values were listed chronologically, examined for learning behavior and the effects of changing experiments, and classified as to the various landing strategies used by the pilot. The data most readily available concerning landing sink rates of actual aircraft is in the form of a nominal sink rate, and sometimes a standard deviation. Typical values are -2 ft/sec mean and a standard deviation of .5 ft/sec.

The mean and standard deviation of the simulation touchdown sink rates were computed for groups of 10 runs, with the division into groups being on a chronological basis. The exceptions to this were the last two groups, which were of 7 and 11 runs respectively, and so divided because of a change in pilot strategy. The means and standard deviations for each group are given in Table 5.

Examining the data in Table 5, a learning effect is present throughout the first 40 runs, and terminates in a sudden step improvement in performance about run 40. The duration of the learning period agrees well with the data in references 8 and 13. The pilot's performance then plateaued until about run 80, when either a three-week layoff or changing experiment conditions resulted in the pilot having to relearn to his previous level of proficiency. The sink rate performance then approaches the previous level until run 118.

The most interesting part of the data is the sudden decrease in sink rate starting at Run 118, as it is associated with the pilot saying he changed his landing strategy. The first strategy used by the pilot involved trading off longitudinal touchdown position for sink rate. During the flare, the pilot would retard the throttles as would be normal in an aircraft. The change that resulted in the second strategy was that the pilot waited until after touchdown to chop the throttles. This change resulted in a mean and standard deviation of touchdown sink rate which compares very well with the values for actual aircraft. Since the only change in the pilot's behavior which occurred and resulted in the agreement with actual aircraft sink rates was in the timing of the throttle chop, the possibility is raised that simulator sink rate problems during landing may be due to either pilot difficulty in judging height, or due to poor models of engine thrust dynamics.

#### CONCLUSIONS

The overall conclusions of these experiments are that:

1. The limited motion system used in these experiments had minimal effect upon the pilot's landing performance.

2. The simulator can be landed as a conventional aircraft without instrument cues.

3. The simulator can be landed as a conventional aircraft with realistic values of sink rate at touchdown provided the pilot cuts the throttles after touchdown.

4. Changing the aircraft dynamic response has a much greater effect upon the pilot's landing performance than turning off the motion system.

#### REFERENCES

1. Laynor and Roberts. A Wind Shear Accident as Evidenced by Information from the Digital Flight Data Recorder. SASI International Seminar, Ottawa, Canada, 7-10 October 1975.
2. Gressang, Stone, Kugel and Pollard. Low Visibility Landing Pilot Modeling Experiment and Data. AFFDL TR 75-41, December 1975.
3. Gressang. Low Visibility Landing Pilot Modeling Experiment and Data, Phase II. AFFDL TR 75-57, August 1975.
4. Armstrong. Difficulties with the Simulation of Aircraft Landings. RAE TR 68116, May 1968.
5. Brown. A Preliminary Simulator Investigation of the Problems of Category II Operation. RAE Tech Memo, BLEU 135, May 1968.
6. Brown. An Examination of Simulator Landing Problems. RAE Tech Memo Avionics 49, March 1970.
7. Armstrong and Musker. Training for Low Visibility Landings. RAE TR 70225, November 1970.
8. Falmer and Cronn. Touchdown Performance with a Computer Graphics Night Visual Attachment. Unpublished paper, NASA Ames Research Center.
9. Bankovskis. Equations of Motion and Constants for the AFFDL Hybrid Simulator. AFFDL TM 75-98-FGD, June 1975.
10. Naylor. Proposed Methods of Driving AFFDL Engineering Flight Simulator Motion Systems. AFFDL TM 75-22-FGD, February 1975.
11. Chalk, Neal, Harris, Pritchard, and Woodcock. Background Information and User Guide for MIL-F-8785B(ASG), "Military Specification--Flying Qualities of Piloted Airplanes". AFFDL TR 69-72, August 1969.

12. Gressang. Landing Simulation Experiments: Fixed Versus Moving Base and Purely Visual Approach. AFFDL Draft Technical Report.

13. Parrish, Rollins, and Martin. Visual-Motion Simulation of CTOL Flare and Touchdown Comparing Data Obtained from Two Model Board Display Systems. AIAA Visual and Motion Simulation Conference, Dayton, Ohio, 26-28 April 1976.

TABLE 1: LONGITUDINAL TOUCHDOWN PARAMETERS

VARIABLE		CONFIGURATION					
		A	B	C	D	E	F
x	Mean	83.02	191.87	450.86	902.13	27.5	679.2
	Std. Dev.	556.5	457.42	679.92	999.02	919.21	869.44
$\dot{x}$	Mean	185.44	187.07	182.61	179.79	169.93	166.93
	Std. Dev.	3.37	6.33	5.27	6.36	19.91	8.19
$\dot{z}$	Mean	-4.64	-4.30	-5.47	-5.96	-5.86	-5.29
	Std. Dev.	2.15	1.90	2.51	2.48	3.99	1.59
$\theta$	Mean	4.27	4.72	5.88	5.30	8.07	9.10
	Std. Dev.	.67	2.39	2.50	2.40	3.89	1.98
q	Mean	.45	.50	1.56	.79	.34	1.58
	Std. Dev.	.76	.58	.84	2.07	.82	1.36

Table 1: Units are ft., ft/sec., deg., deg/sec.

TABLE 2: LATERAL TOUCHDOWN PARAMETERS

VARIABLE		CONFIGURATION					
		A	B	C	D	E	F
y	Mean	15.11	14.77	-4.31	1.94	15.87	1.87
	Std. Dev.	16.22	21.07	13.50	25.08	26.59	27.52
$\dot{y}$	Mean	-.63	.20	.85	1.07	-.10	-1.19
	Std. Dev.	2.86	4.75	3.53	2.99	1.27	3.58
$\phi$	Mean	.45	.80	.47	1.04	-.29	.68
	Std. Dev.	1.18	1.62	3.73	6.05	.77	3.12

TABLE 2 (Continued)

VARIABLE		CONFIGURATION					
		A	B	C	D	E	F
$\psi$	Mean	89.49	89.36	88.94	88.19	90.19	90.06
	Std. Dev.	.60	1.16	1.59	2.39	.95	1.62
p	Mean	-.43	1.29	.78	-.95	-.01	-.30
	Std. Dev.	2.15	1.88	2.13	3.25	1.14	2.19
r	Mean	0.57	-.27	.29	-.05	.30	-.38
	Std. Dev.	1.08	1.00	1.43	1.72	1.47	.93

Table 2: Units are ft., ft/sec., deg., deg/sec.

TABLE 3: LONGITUDINAL APPROACH STATISTICS

VARIABLE		CONFIGURATION					
		A	B	C	D	E	F
$\theta$	Mean	1.622	1.948	1.555	2.102	3.408	2.652
	Std. Dev.	.478	.502	.993	1.077	1.156	1.011
q	Mean	-.0035	-.004	-.002	.007	.039	-.013
	Std. Dev.	.309	.348	.866	.888	.375	.727
h	Mean	-24.6	-14.6	-27.6	-13.7	-34.07	-29.67
	Std. Dev.	9.36	11.38	11.77	13.67	14.75	12.95
$\alpha$	Mean	4.716	4.880	4.442	5.131	6.581	5.652
	Std. Dev.	.628	.653	.936	.964	.989	.819

Table 3: Units are ft., deg., deg/sec.

TABLE 4: LATERAL APPROACH STATISTICS

VARIABLE		CONFIGURATION					
		A	B	C	D	E	F
φ	Mean	.449	.597	1.074	1.096	.097	.513
	Std. Dev.	1.185	1.747	3.387	3.281	.830	4.555
p	Mean	-.031	.035	.032	.018	-.035	-.033
	Std. Dev.	1.598	1.814	2.375	2.478	.887	2.472
ψ	Mean	89.525	88.921	88.434	88.392	90.095	89.315
	Std. Dev.	.992	1.098	1.315	1.527	.900	1.381
r	Mean	.044	.002	.069	.013	.018	-.005
	Std. Dev.	.827	.862	1.193	1.243	.507	1.042
y	Mean	-4.4	22.8	-4.5	-3.3	17.9	17.4
	Std. Dev.	27.0	31.9	25.4	19.6	21.3	38.1
β	Mean	.394	.921	1.476	1.598	-.147	.392
	Std. Dev.	1.033	1.285	1.846	1.933	.686	2.069

Table 4: Units are ft., deg., deg/sec.

TABLE 5: TOUCHDOWN SINK RATE MEANS AND STANDARD DEVIATIONS

RUNS	MEAN $\dot{z}$	$\dot{z}$ STANDARD DEVIATION
1 to 10	-7.81	3.18
11 to 20	-6.63	2.16
21 to 30	-6.34	2.37
31 to 40	-6.00	2.31
41 to 50	-4.04	1.37
51 to 60	-4.09	1.97
61 to 70	-4.38	1.59
71 to 80	-4.76	1.75
81 to 90	-6.58	3.67
91 to 100	-6.37	2.59
101 to 110	-4.71	2.39
111 to 117	-4.51	1.15
118 to 128	-1.94	.57

Table 5: Units are ft/sec.

# EFFECTS OF DIFFERING MOTION SYSTEM DRIVES ON

## SIMULATION OF APPROACH AND LANDING

Capt Joseph Pollard  
Air Force Flight Dynamics Laboratory

### SUMMARY

A discussion of simulator testing for motion response is coupled with a scientific experiment to determine the effects of differing motion drive equations on approach and landing of a heavy aircraft. The conditions of no motion, motion driven by linear combinations of rate and attitude, and motion driven by linear accelerations are tested to determine if significant statistical differences exist between systems. All other factors were held constant. The simulation was performed at the Flight Control Development Laboratory utilizing the Multicrew Cab. The results of the simulation analysis are clearly shown to be affected by the required choice of motion drive equations in simulation design. Specific performance variables are indicated as most seriously affected.

### INTRODUCTION

One of the tasks most often investigated at the Flight Control Development Laboratory is that of landing including power approach flare, and touchdown. A simple experiment was designed to investigate the sensitivity of pilot performance to changes in the drive equations applied to the limited motion base simulator. The tracking performance of the pilot during power approach was found to be relatively insensitive; however, the variations in many of the aircraft states at touchdown were found to be statistically significant. [1]

### SYMBOLS

The following symbols are used throughout this paper. The most commonly used units are given for presentation with this paper.

$a_x, a_y, a_z$	Aircraft inertial earth axis accelerations, ft/sec <sup>2</sup>
$\dot{u}, \dot{v}, \dot{w}$	Aircraft body axis linear accelerations, ft/sec <sup>2</sup>
$\dot{p}, \dot{q}, \dot{r}$	Aircraft body axis rotational accelerations, deg/sec <sup>2</sup>
$\theta$	Aircraft pitch angle, deg



$\phi$	Aircraft roll angle, deg
$\psi$	Aircraft heading angle, deg
$p$	Aircraft roll rate, deg/sec
$q$	Aircraft pitch rate, deg/sec
$r$	Aircraft yaw rate, deg/sec
$\theta_o$	Aircraft nominal pitch angle, trim, deg
$l_x, l_y, l_z$	Offsets from aircraft center of gravity to the pilot's station, ft
$g$	Acceleration due to gravity, 32.2 ft/sec <sup>2</sup>
$s$	Laplace operator
$\alpha$	Confidence level assigned to statistical testing
$F$	A ratio of variances used in statistical tests

#### THE SIMULATOR

A three degree of freedom motion base simulator with a multicrew cab instrumented as an AMST aircraft was used for the experiment. The motion system is a scissors configuration utilizing two forward hydraulic cylinders and one aft. The forward cylinders are identical and have a stroke of  $\pm 12$  inches while the rear cylinder has a travel of  $\pm 18$  inches. Hydraulic power was supplied by a 60 gpm pumping system at 3000 psi. Each actuator was flow limited to 10 gpm. The motion base was programmed so that all three cylinders provided heave while the two forward cylinders were operated asymmetrically to produce roll. The rear cylinder was operated alone to produce pitch. Figure 1 shows an exterior view of the simulator. Each of the three cylinders was also electrically and mechanically safety limited.

The motion base was instrumented with three accelerometers located at the pilot's station to measure  $a_x$ ,  $a_y$ , and  $a_z$ . The pitch rate and roll rate were detected using gyros.

A Redifon terrain board projection visual system was used to provide visual cues to the pilot. The full color projection is  $48^\circ \times 36^\circ$ . Landing lights were provided to the pilot.

## THE AIRCRAFT SYSTEM AND TASK

An AMST similar aircraft was utilized as the system airframe. These dynamics were heavily and nonlinearly augmented. The pilot was asked to land the aircraft in a conventional manner utilizing a 3° ILS. A matrix of 30 runs was then accomplished with each of two motion drive systems and no motion drive being the experimental factor tested. This matrix provided ten replications of each motion condition. No other factors were willfully changed. Light turbulence (4 ft/sec rms) was applied to the aircraft dynamics for each run. Each approach took about 90 seconds at 120 knots. Initial altitude was 750' AGL.

## THE MOTION DRIVES

Drive system A is depicted graphically in Figure 2. This system was a blend intended to present angular and angular rate information to the pilot. The heave axis was driven by a blend of  $q$  and  $\dot{h}$ . All signals were passed through washout circuits. For each system component the time constants used are shown in Table 1.

### Washout Time Constants Drive A

Pitch  $\tau = 4$

Roll  $\tau = 2.86$

Heave  $\tau = 4$

Table 1

Motion fade and cab leveling circuits are also included to provide a means of initializing the simulator.

Drive System B was designed to present linear acceleration data to the pilot. Linearized equations expressing these accelerations are given by:

$$a_x = \dot{u} - l_y \dot{r} + l_z \dot{q} + \sin \theta \quad (1)$$

$$a_y = \dot{v} - g\phi \cos \theta_0 - l_x \dot{r} - l_z \dot{p} \quad (2)$$

$$a_z = \dot{w} + g\theta \sin \theta_0 - l_x \dot{q} \quad (3)$$

For purposes of implementation, these were simplified to:

$$a_x = \dot{u} + l_z \dot{q} \quad (4)$$

$$a_y = \dot{v} - g\phi + l_x \dot{r} - l_z \dot{p} \quad (5)$$

$$a_z = \dot{w} - l_x \dot{q} \quad (6)$$

For washout circuits, a model similar to that representing the otoliths of the ear was used since it is assumed that they are the primary means of motion perception. A typical model is

$$G(s) = \frac{k(t_3 s + 1)}{(t_1 s + 1)} \frac{1}{t_2 s + 1} \quad (7)$$

where  $t_3$  is large compared to  $t_2$  and  $t_1$ .

Thus the model is simplified to the washout plus filter given by:

$$G_1(s) = \frac{1.5s}{(s+1.5)(s+.19)} \quad (8)$$

Due to inherent 400 Hz noise in the hybrid simulator the acceleration rate terms were filtered before use by

$$G_2(s) = \frac{10}{s+10} \quad (9)$$

Further each actuator was determined to be accurately modeled by

$$G_3(s) = \frac{2\pi(.4)}{s+.4(2\pi)} \approx \frac{2.51}{s+2.51} \quad (10)$$

Therefore a compensator of the form

$$G_4(s) = \frac{10(s+.251)}{(s+2.51)} \quad (11)$$

was inserted to pre-emphasize each drive signal. Figure 3 shows a block diagram of the system called Drive B.

## DATA COLLECTED

The data collected can be divided into two types: statistical and discrete point. Time average statistics (mean and standard deviation) were computed from 500' to 50' altitude on each run for  $w_g$ ,  $v_g$ ,  $\theta$ ,  $\phi$ ,  $\psi$ ,  $a_x$ ,  $a_y$ ,  $a_z$ ,  $p$ ,  $q$ ,  $r$  and glide slope error. These same data were collected at discrete points along the trajectory including the touchdown point. Tables 2, 3, 4 and 5 present the mean and rms data for the time average statistics. As can be seen there is no statistical difference among these parameters.

The touchdown parameters, however, are statistically significantly different. Tables 6 and 7 show the raw and average data. Figure 4 shows scatter plots for  $a_y$  and  $\phi$ . Differences are clearly illustrated. The parameters  $a_y$ ,  $\phi$ ,  $a_z$ ,  $\theta$ ,  $p$ ,  $q$ , and  $r$  are statistically different between Drive A and Drive B. No significant difference exists between Drive A and no motion but Drive B differs from no motion in  $a_y$ ,  $a_z$ ,  $\phi$ , and  $r$ . The smaller dispersions of the data occur for Drive B. All testing was done for  $\alpha = .05$  level of significance.

## CONCLUSIONS AND RECOMMENDATIONS

Differing drive equations have been shown to cause a statistically significant change in touchdown parameters in the landing of an AMST similar aircraft utilizing a conventional approach. No significant difference was seen in the power approach phase.

Extreme caution should therefore be exercised in the choice of drive equations for use with a limited motion base simulator.

## BIBLIOGRAPHY

Pollard, J.J. and C. Jackson, "An Investigation of the Multicrew Motion System Capabilities and Drive Signal Effects," AFFDL TM 76-25-FGD, November 1975.

TABLE 2 - RAW MEAN APPROACH DATA

MEAN 500' - 50' Motion System Test

Run #	w	v	θ	φ	ψ	a <sub>x</sub>	a <sub>y</sub>	a <sub>z</sub>	p	q	r	GS Err
Drive B												
3	4.81	3.26	1.84	.17	90.93	-.28	-.13	-.04	.01	.10	.02	-25.6
4	7.30	3.02	1.51	-.04	90.72	-.26	-.08	.07	.01	.10	.04	-17.4
12	6.25	.50	1.52	.37	90.03	-.18	-.08	.20	-.02	-.06	.03	-13.3
15	7.19	1.95	1.63	.28	90.02	-.11	-.07	.29	-.02	.03	.02	-51.8
16	8.01	1.31	1.20	.53	89.53	-.07	-.04	-.04	.02	.04	.02	-17.2
19	4.34	1.65	1.94	.26	90.47	-.37	-.11	.16	-.02	.15	.01	-26.6
21	3.30	.69	1.55	.05	89.91	.10	.10	.41	-.02	-.08	.00	-14.6
23	3.32	.68	1.43	-.12	89.80	-.03	.04	-.31	-.04	.13	.02	-50.0
31	4.43	-.15	1.32	.39	90.54	-.30	-.14	.17	.00	.00	.06	-32.0
32	1.13	.51	3.63	-.20	90.52	-.28	.06	.22	-.04	.04	-.02	-117.9
Drive A												
1	2.13	.67	1.46	.63	90.11	.07	-.17	-.29	.04	-.01	.05	-39.4
2	7.33	2.14	1.57	.43	90.23	-.32	-.06	-.08	.02	.12	-.02	-18.2
7	5.64	1.28	1.50	.23	89.69	-.11	.10	-.04	-.01	.00	-.05	-21.3
8	6.96	2.65	2.17	-.08	90.67	-.27	-.08	.19	.02	-.03	.04	-29.4
10	4.17	1.14	1.80	.30	90.20	-.03	-.15	.09	.02	-.01	.03	-45.6
11	8.14	2.96	2.39	-.03	90.61	-.16	-.11	-.07	.03	.10	.03	-40.8
14	6.46	-.20	.72	.24	90.17	-.08	-.06	-.37	-.01	.05	.00	00.9
17	3.84	2.00	1.30	.33	90.01	-.16	.00	.12	-.03	.06	-.01	6.05
20	5.11	.61	1.67	.15	89.88	-.03	.01	.07	-.03	.00	.01	11.3
25	2.66	.61	.22	.38	90.10	-.18	-.01	.07	-.03	.05	-.06	-23.7
No Motion												
5	8.86	3.16	1.85	.05	90.51	-.13	-.05	-.24	.00	.09	.01	-12.1
9	5.00	2.36	1.81	.28	89.00	-.32	.16	.07	-.07	.04	.02	-22.0
13	5.92	1.36	1.43	.70	90.08	-.09	-.22	.32	.06	-.09	.05	-16.0
22	2.11	.82	2.31	1.24	90.32	-.21	-.62	-.01	-.14	.01	.00	-35.3
24	5.05	-.11	.93	.02	89.84	.01	.00	.30	.03	-.02	.01	-10.6
26	2.89	.33	1.39	.22	90.14	-.21	.02	.11	.01	.03	-.01	-29.6
27	.88	-.40	1.79	.18	89.61	-.09	.11	.21	.08	.02	.01	-45.9
28	2.63	+0.02	2.08	-.01	90.04	.03	.03	.02	.00	-.02	-.01	-43.1
29	1.65	.65	1.12	.10	90.48	.03	-.08	-.14	.01	.06	.02	-34.6
30	3.24	.42	2.32	.21	90.18	-.18	-.10	.20	.00	.06	.01	-72.1

TABLE 3 -- AVERAGE MEAN AND DISPERSION OF MEAN APPROACH DATA  
Mean 500' - 50' Motion System Test

	$w_g$	$v_g$	$\theta$	$\phi$	$\psi$	$a_x$	$a_y$	$a_z$	$p$	$q$	$r$	GS Err
Drive B												
Mean	5.01	1.34	1.75	.17	90.25	-.18	-.04	.11	-.01	.04	.02	-36.5
Std Dev	2.16	1.12	.69	.24	.45	.15	.08	.20	.02	.07	.02	31.4
Drive A												
Mean	5.24	1.34	1.48	.26	90.18	-.13	-.05	-.02	.00	.03	.00	-17.7
Std Dev	2.02	1.02	.64	.21	.29	.15	.08	.18	.03	.05	.04	16.5
No Drive												
Mean	4.02	.86	1.70	.30	90.02	-.12	-.08	.08	.00	.02	.01	-32.13
Std Dev	2.20	1.13	.48	.39	.45	.12	.22	.18	.06	.05	.02	18.7

TABLE 4 -RAW RMS APPROACH DATA

RMS 500' - 50' MOTION SYSTEM TEST

Run #	$w_g$	$v_g$	$\theta$	$\phi$	$\psi$	$a_x$	$a_y$	$a_z$	$p$	$q$	$r$	GS Err
Drive B												
3	6.02	4.62	.72	.67	.90	.46	.48	2.08	.79	.67	.24	8.8
4	6.40	4.29	.74	.65	.51	.46	.45	2.16	.83	.70	.36	8.5
12	4.52	4.82	.74	.89	.47	.52	.55	2.31	.74	.68	.27	13.3
15	5.52	4.20	.69	.84	.61	.47	.57	1.99	.62	.72	.22	14.4
16	4.64	4.25	.27	.99	.88	.41	.71	1.85	.90	.61	.32	15.7
19	4.42	4.96	.78	.85	.70	.57	.59	2.26	.79	.72	.30	13.5
21	5.55	4.79	.86	.99	1.16	.54	.67	2.56	.74	.67	.33	39.2
23	6.39	2.06	.42	.79	.90	.31	.62	1.28	.71	.71	.39	19.1
31	4.92	2.08	1.26	.87	.55	.44	.59	1.50	.81	.48	.31	15.0
32	4.98	2.08	1.10	.84	.84	.46	.63	1.24	.70	.50	.34	27.5
Drive A												
1	6.47	4.46	.93	1.10	1.22	.60	.76	2.22	1.09	.67	.41	21.0
2	4.88	4.65	.95	.98	1.18	.64	.77	2.56	.94	.72	.43	8.5
7	4.80	4.00	.57	.58	.58	.45	.41	1.93	.53	.57	.24	12.6
8	4.31	3.98	.74	.37	.96	.46	.36	2.19	.37	.67	.33	15.4
10	5.20	4.24	.59	1.02	.62	.47	.64	2.12	.90	.65	.34	29.3
11	6.85	3.98	.72	.68	.93	.46	.50	2.36	.51	.73	.27	10.4
14	6.25	5.31	.54	.75	.42	.51	.49	2.15	.61	.56	.24	12.2
17	5.52	4.59	.72	1.16	.90	.54	.78	2.62	1.02	.73	.40	15.9
20	5.17	5.15	.56	1.07	1.03	.55	.77	2.53	.94	.68	.42	25.2
25	6.10	2.04	.47	1.00	1.03	.42	.73	1.22	1.14	.44	.35	7.0
No Motion Dr												
5	7.12	3.78	.30	.43	.63	.39	.42	2.02	.40	.63	.29	6.6
9	4.50	4.31	.99	1.57	1.95	.56	1.17	2.06	1.27	.75	.52	23.1
13	4.83	4.42	.76	1.08	.85	.46	.65	2.02	1.00	.65	.35	20.0
22	4.28	4.31	1.13	2.00	2.53	.77	1.82	2.83	3.43	1.15	1.97	27.4
24	5.41	2.27	.33	.58	.60	.32	.43	1.32	.64	.36	.31	10.0
26	5.81	2.33	.64	.69	.46	.34	.44	1.46	.59	.45	.19	4.5
27	5.14	2.11	.51	.76	.77	.35	.56	1.19	.70	.45	.36	16.4
28	5.14	1.96	.30	.54	.56	.31	.37	1.14	.40	.29	.26	18.2
29	5.80	2.25	.20	.35	.32	.31	.32	1.13	.29	.38	.21	7.0
30	5.52	2.32	.58	.98	1.07	.35	.69	1.12	.89	.36	.36	21.2

TABLE 5 - AVERAGE MEAN AND DISPERSION OF RMS APPROACH DATA

RMS 500' - 50' Motion System Test													
	$w_g$	$v_g$	$\theta$	$\phi$	$\psi$	$a_x$	$a_y$	$a_z$	$p$	$q$	$r$	GS Err	
Drive B													
Mean RMS	5.24	3.81	.76	.87	.75	.46	.58	1.92	.76	.64	.31	17.5	
Std Dev RMS	.84	1.22	.29	.11	.22	.07	.08	.45	.08	.09	.05	9.3	
Drive A													
Mean RMS	5.55	4.24	.68	.87	.89	.51	.62	2.19	.81	.64	.34	15.8	
Std Dev	.82	.90	.16	.26	.26	.07	.16	.41	.27	.09	.07	7.3	
No Drive													
Mean RMS	5.50	3.00	.57	.89	.97	.42	.69	1.62	.96	.55	.48	15.4	
Std Dev RMS	.82	1.05	.31	.53	.71	.14	.46	.57	.92	.26	.53	7.9	



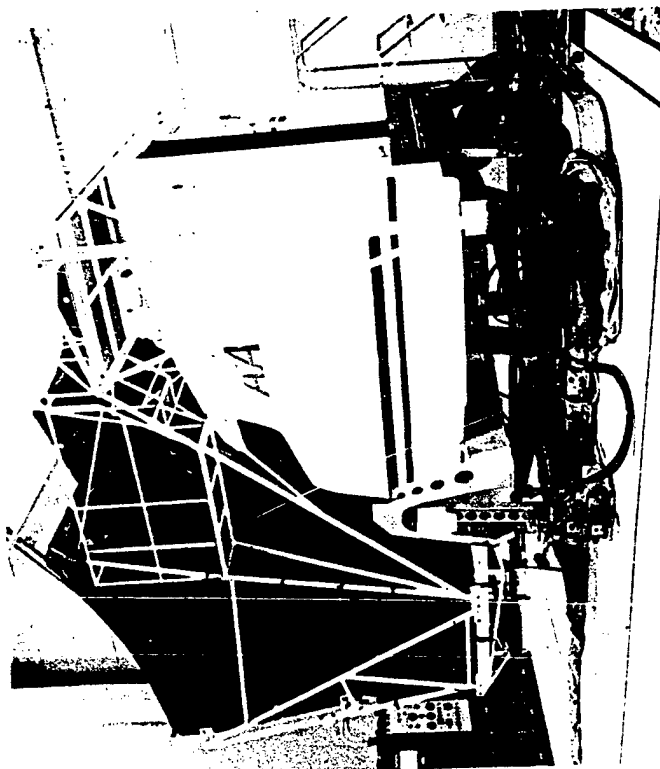
TABLE 6 - RAW TOUCHDOWN PARAMETERS

RUN #	Drive B	w <sub>g</sub>	v <sub>g</sub>	a <sub>x</sub>	a <sub>y</sub>	a <sub>z</sub>	θ	φ	ψ	p	q	r	y	h	ŷ
3	1.22	-1.22	-1.31	.53	.46	8.08	-1.05	89.14	.56	.06	.72	60.6	-7.69	-.36	
4	1.34	.85	-.46	.07	-.46	8.23	.17	89.63	.31	.84	.13	34.9	-3.54	-.37	
12	7.32	7.20	-1.90	.12	-3.73	8.08	.22	90.41	-.41	-.13	-.33	13.3	-5.00	-3.54	
15	.61	1.46	-1.63	-.36	1.34	9.54	.65	91.09	-.22	+1.52	.01	9.1	-5.24	-3.29	
16	9.76	5.49	-1.78	.02	-.07	8.81	.26	88.99	.17	1.20	.06	-15.1	-6.47	+1.83	
19	.85	3.78	-1.85	-.31	.61	10.52	.51	89.92	-.17	.01	-.03	4.4	-3.78	1.34	
21	-.12	3.66	-1.02	-.36	-.95	9.30	.70	91.00	.61	.94	.20	-50.3	-7.93	.12	
23	15.38	-2.07	-.41	.12	-1.00	7.25	-.02	90.41	-.56	.30	-.37	24.1	-1.34	-4.76	
31	-1.09	2.07	-1.46	-.07	1.00	7.78	.26	89.48	.46	1.23	.52	24.0	-4.51	-1.09	
32	-5.37	-1.34	-1.97	-.09	-2.12	9.59	.17	91.29	.61	.33	-.25	2.8	-3.78	-2.56	
Drive A															
1	11.1	-.12	-1.63	-.49	3.10	5.78	1.09	90.75	-.32	1.18	.13	-5.7	-3.29	-3.78	
2	-4.0	5.98	-2.22	.22	3.34	8.17	-.17	89.09	-.02	1.13	-.03	18.2	-7.20	1.09	
7	.48	2.80	-2.37	.39	3.58	8.91	-.56	91.00	-.46	.52	-.54	3.6	-3.05	-3.29	
8	10.62	4.02	-.85	-1.49	.56	7.30	1.78	91.34	+2.2	3.31	.94	4.2	-10.62	-.61	
10	4.51	2.84	-1.61	-.71	.12	7.44	1.88	90.17	1.29	1.72	.59	18.6	-7.20	-3.29	
11	7.56	-3.54	.24	.80	3.44	6.81	-.75	88.65	1.39	2.08	.67	30.1	-4.27	3.54	
14	4.76	9.76	-2.39	-.85	-4.71	6.76	1.68	89.92	.51	2.50	.52	-11.5	-9.39	.61	
17	1.95	5.61	-2.02	.02	-4.41	11.64	-.22	88.75	-.75	-.50	-.06	-21.5	-5.00	2.80	
20	1.83	7.56	-2.02	-.07	-2.66	10.32	.41	90.85	-.22	+1.16	.37	-30.0	-5.73	-1.58	
25	3.78	2.19	-1.85	-.95	-1.44	5.83	.26	91.00	.56	1.64	-.23	12.2	-7.69	1.83	
No Motion															
5	6.22	-2.56	-0.24	-.31	7.10	5.34	.41	90.32	.02	2.82	.11	26.38	-8.91	-1.09	
9	5.73	-3.17	-1.39	-1.07	-.61	8.81	1.19	92.22	.07	1.77	.28	21.89	-5.98	-.61	
13	3.78	-4.76	-.32	-.26	+2.80	7.83	.75	90.51	-.02	.52	-.01	50.9	-5.73	-3.78	
22	10.62	-3.66	-.61	1.05	.65	9.69	-1.68	89.09	.22	.20	.11	17.3	-2.31	4.02	
24	-1.95	3.66	-2.58	-.51	-.80	6.27	1.09	91.44	-.65	.64	-.11	-1.8	-1.58	-3.29	
26	10.62	.48	-1.24	.70	.41	7.69	-.36	90.02	.17	2.23	.79	23.04	-6.71	-.61	
27	-.85	.85	-1.39	-.56	-.80	7.64	.51	92.66	.17	.91	.11	-23.81	-4.27	-3.05	
28	.24	1.88	-.73	.22	1.78	6.71	-.41	89.97	-.51	1.54	-.09	15.74	-5.24	.12	
29	.12	-1.09	-1.22	.26	-.65	6.71	-.31	90.17	.80	1.45	-.11	45.31	-3.78	-1.58	
30	7.20	.85	-1.02	-.02	.26	7.49	-0.12	90.17	-1.34	.25	.11	40.39	-3.29	-3.05	

TABLE 7 - AVERAGE TOUCHDOWN PARAMETERS

	$w_g$	$v_g$	$a_x$	$a_y$	$a_z$	$\theta^*$	$\phi^*$	$\psi$	$p$	$q^*$	$r$	$y$	$h$	$z$
Drive B														
Mean	2.73	1.99	-1.38	-.03	-.49	8.72	.19	90.14	.14	.63	.07	10.8	-4.93	-1.27
S.D.	6.19	3.07	.58	.27	1.54	1.00	.49	.83	.44	.59	.35	29.6	2.02	2.19
Drive A														
Mean	4.68	3.71	-1.67	-.31	.09	7.89	.54	90.15	.22	1.47	.25	1.82	-6.34	-.27
S.D.	4.14	3.82	.81	.70	3.27	1.90	.99	1.01	.72	1.05	.45	19.02	2.52	2.65
No Drive														
Mean	4.17	-.75	-1.05	-.05	1.01	7.42	.11	90.66	-.11	1.27	.12	17.16	-4.78	-1.29
S.D.	4.64	2.72	.71	.62	2.44	1.25	.86	1.11	.59	.90	.27	26.15	2.19	2.30

MULTICREW SIMULATOR



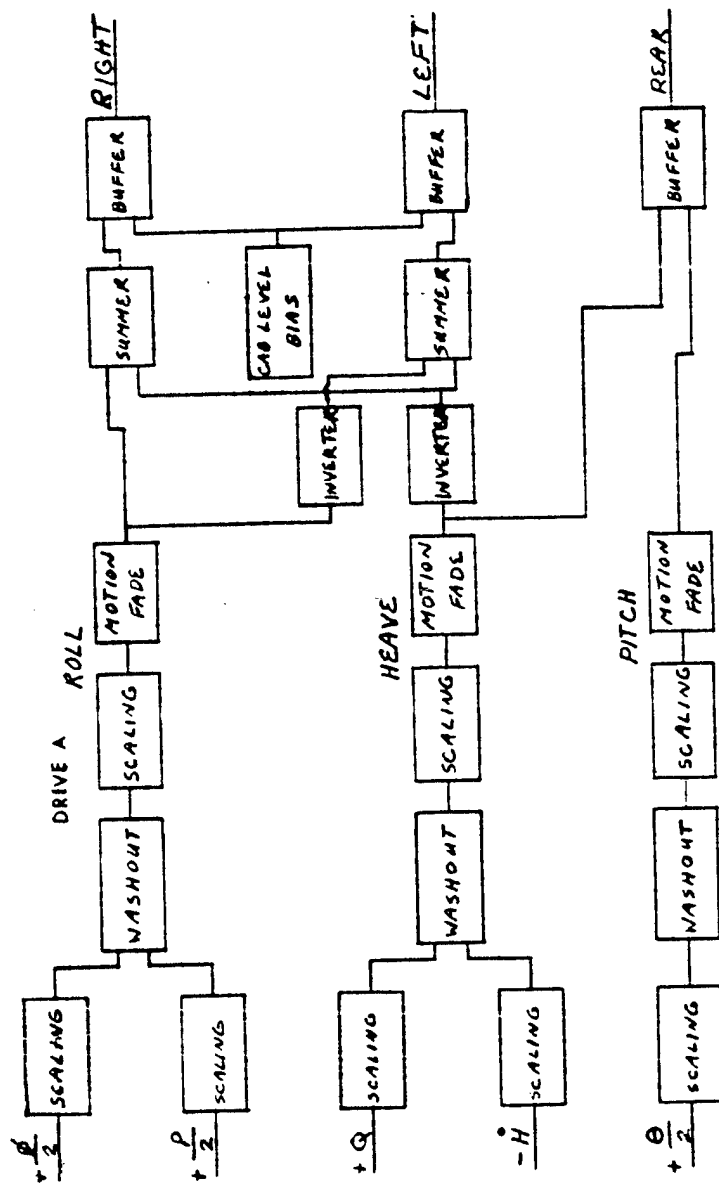


FIGURE 2--DRIVE A BLOCK DIAGRAM

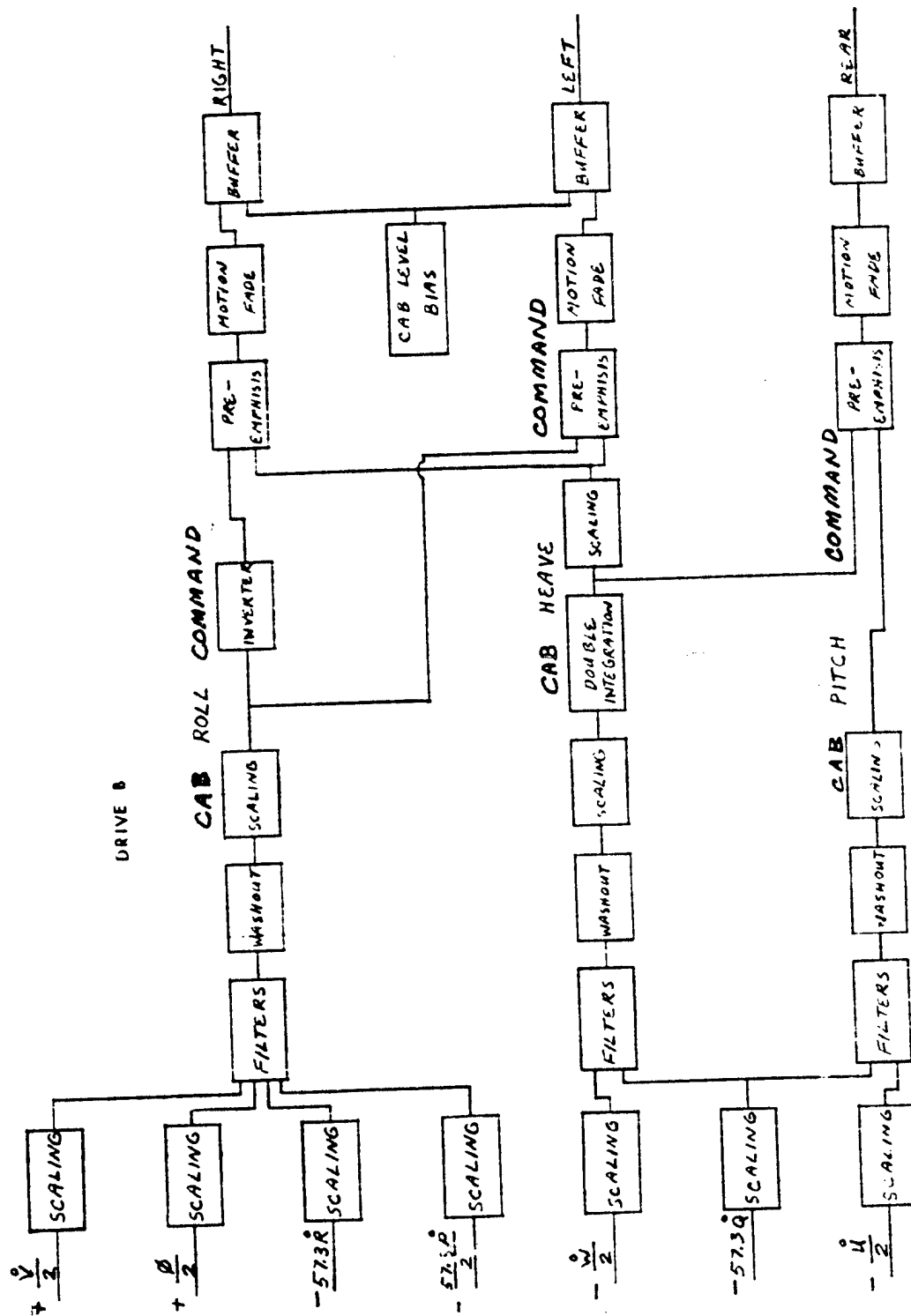


FIGURE 3 --DRIVE B BLOCK DIAGRAM

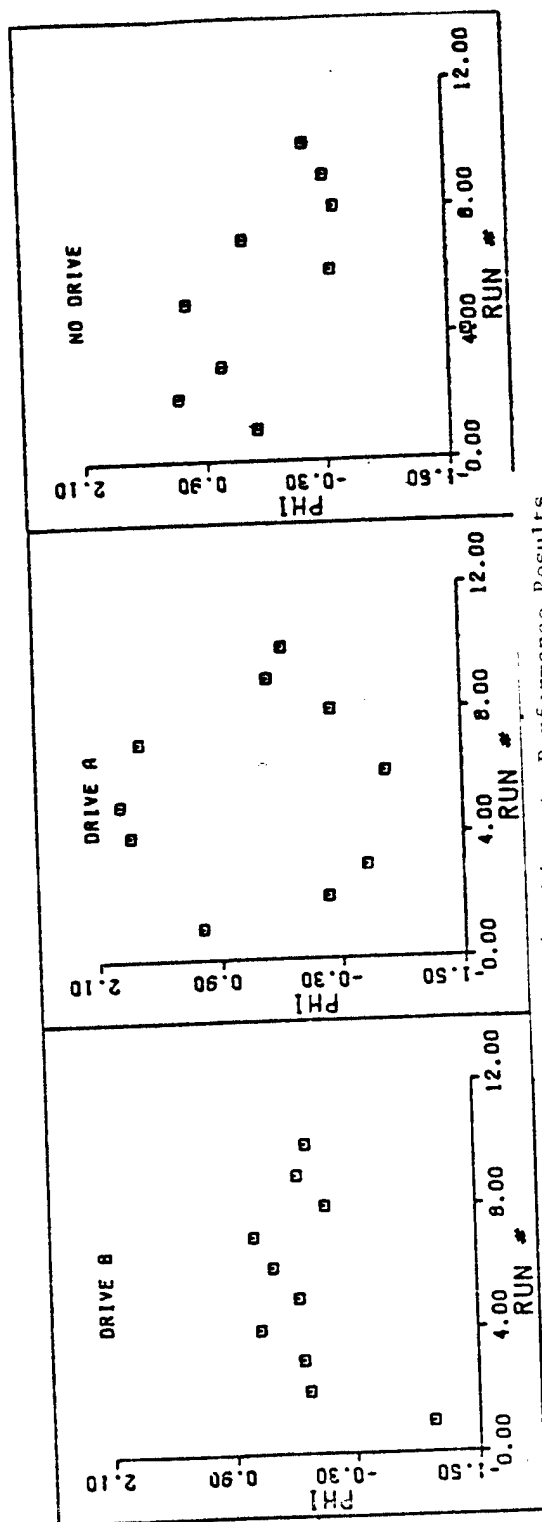
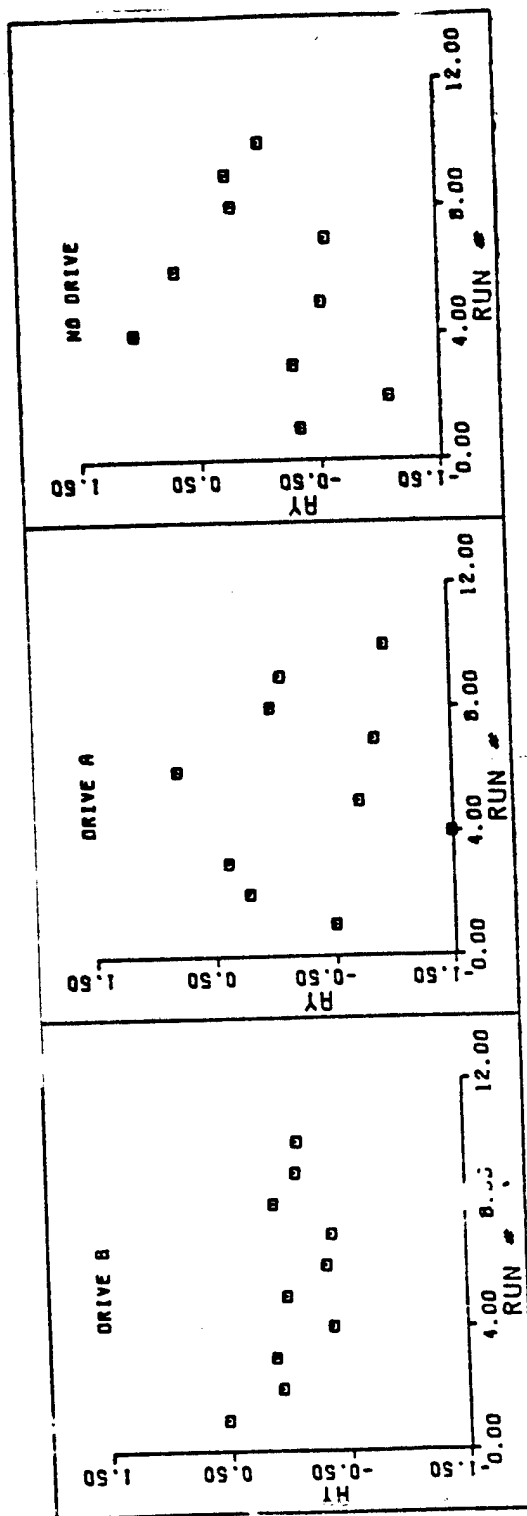


Figure 4 - Discrete Performance Results



# THRESHOLDS OF MOTION PERCEPTION

## MEASURED IN A FLIGHT SIMULATOR

R.J.A.W. Hosman and J.C. van der Vaart

Delft University of Technology  
Department of Aerospace Engineering

### SUMMARY

Thresholds for the perception of angular acceleration and specific forces were experimentally determined in a moving base flight simulator.

The thresholds were determined by using sinusoidally changing test signals at a number of frequencies. It was shown that the thresholds of the semicircular canals of the vestibular system are directly related to a minimum cupula displacement, if the latter is calculated in accordance with the well known overdamped torsion pendulum model.

When using the available otolith models, a similar direct relation for thresholds for specific forces and otolith displacement could not be established.

The experimentally determined thresholds for angular accelerations were significantly lower than those commonly found in the literature.

It was further shown that mentally "loading" subjects with additional tasks considerably increased the thresholds for motion perception.

### INTRODUCTION

For a number of years research has been performed at the Department of Aerospace Engineering of the Delft University of Technology in the field of manual control.

The investigations are primarily related to pilot behaviour, handling qualities of aircraft and flight simulation. See Refs. 1 and 2.

Theoretical work on pilot behaviour and handling qualities is aimed at the development of a self adaptive pilot model, experimental research is done to support this work on the pilot modelling and flight simulation, especially motion simulation.

The lack of detailed knowledge of motion perception necessary for its implementation in pilot models and the availability of a simulator with a three degree of freedom motion system with high fidelity characteristics, inspired the start of the experimental work on motion perception.

The motion system was developed at the Department of Mechanical Engineering under the responsibility of Viersma. The application of hydrostatic bearings in the hydraulic servo actuators results in almost rumble free simulator motions. In fact under normal conditions motion noise is below the thresholds of motion perception.

The simulator's three degrees of motion freedom allow five degrees

of freedom to be simulated: pitching and rolling rotations and heave translations in the normal frequency range of aircraft simulation and specific forces in the X- and Y-directions by tilting the simulator at very low frequencies. A general impression of the simulator is given in Fig. 1. Details of the motion system are summarized in the Appendix. In this paper the usual aircraft frame of reference OXYZ is used to define motions of the simulator as well as of the subjects.

It was decided to first determine the thresholds of motion perception using this particular simulator. Thereby the suitability of the simulator motion system for research on motion perception was to be evaluated. If the apparatus indeed showed to be an efficient tool for this purpose, a more extensive research program related to motion perception and the problems of pilot modelling and motion simulation, could be started.

Further, some answers might be found to questions concerning the applicability of the available vestibular models as well as of the related threshold values in the rather special case of pilot modelling and flight simulation. In particular effects due to the differences in laboratory environment and the working environment of the flightdeck, where a pilot controls the aircraft, are to be expected.

Finally it has to be considered that till now most research on the vestibular system was directed at passive motion perception in contrast to the pilot controlled situation where the motion perception plays part in the control of aircraft.

In the design of the experiments and in the interpretation of the results use has been made of a rather important and general concept of control by a human operator, namely that of the "internal model". This concept implies that for perception as well as for control a human operator uses an internal - or mental - model of the system to be controlled. At any moment this internal model is based on all the preceding information processed up to that moment. Thus the internal model can be seen as the result of a learning process.

When implementing motion perception in pilot models based on the internal model of the aircraft, the following should be borne in mind. The perception of motion does not originate from the vestibular system alone but is also based on the sensory information of pressure, touch and kinesthesia receptors on the one hand and visual cues on the other hand. It is of great importance to investigate the influence of these sensors on motion perception and to incorporate all relevant motion related information in pilot models and in flight simulation.

Based on the above considerations some experiments were performed to evaluate the simulator motion system and to investigate the influence of the information processing on motion perception.



## MOTION PERCEPTION, MODELS OF THE VESTIBULAR ORGANS AND PILOT BEHAVIOUR

### Motion and the flight environment

The effect of motion perception on the behaviour of a pilot controlling an aircraft is generally accepted as favourable. It has been experimentally demonstrated, see Ref. 3, that the presence of "motion" increases the control performance in the case of simulated systems with noted "difficult" control characteristics. The use of moving base simulators is therefore not only justified for improving simulation realism, motion provides the pilot with cues that appear to be as essential as visual inputs for the manual control of a given system.

Whereas this effect of motion cues on the control task is generally recognized, little appears to be exactly known about the motion a human pilot is able to feel (thresholds of perception), nor is it clear whether certain motion cues may be more essential than others, see Ref. 4. The work of many researchers is presently aimed at improving the knowledge in this particular field.

The research on motion perception has a long history. It has, from the beginning, been based on the function of the vestibular system, consisting of the semi-circular canals and the otoliths, man's sensors of angular acceleration and specific force respectively. Most investigations carried out have been related to laboratory situations where the experimental conditions were such that results are not readily extrapolated to the flight environment. In laboratory experiments subjects are usually strapped to maintain a fixed position of head and body. In contrast, a pilot in a flight environment is free to adjust his chair and the safety belts mostly do not restrict head and trunk movements. Apart from this difference in physical limitations an enormous difference may be observed in the psychological conditions of a laboratory subject and a pilot controlling an aircraft.

When studying the applicability of the models of the vestibular system, see Refs. 5 and 6, and the associated thresholds of motion perception in relation to pilot modelling and aircraft simulation, the above considerations should be taken into account.

A good starting point appears to consider the pilot as a multi-input multi-output system with certain (as yet unknown) information processing of all sensory input signals. Using this black box concept, one can try to evaluate the influence of the pilot's information processing of these signals. Of course the influence of the vestibular inputs should not be rejected or underestimated but should be considered as an integral part of the information processing of all sensory inputs.

### Mathematical models of motion perception

Presently only models for perception of motion by the vestibular system are available. These models, in which motion sensing by other organs such as

proprioceptors, etc. is not included, are briefly discussed below. For a complete description of the vestibular system and its characteristics, the reader is referred to a number of excellent reviews, Refs. 5, 7, 8, 9 and 10. A schematic drawing of a semi-circular canal is given in Fig. 2a.

According to the overdamped torsion pendulum analogy of the semi-circular canals of the vestibular organs as formulated by van Egmond, Jongkees and Groen, the transfer function, relating the Laplace transforms of input and output signals, is:

$$\frac{\xi(S)}{\alpha(S)} = \frac{1}{(S + a)(S + b)} \quad (1)$$

where:

$\xi$  = the cupula deflection  
 $\alpha$  = the input angular acceleration  
 $a \approx 0,1$  rad/sec  
 $b \approx 10$  rad/sec

In Fig. 3 the modulus and phase angle of the above transfer function are plotted.

In eq. (1) the constants  $a$  and  $b$  are dependent on the mechanical characteristics of the organ such as the moment of inertia of the endolymph, the spring stiffness of the cupula and the viscous damping of the endolymph in the canals. From experiments described in Refs. 6 and 8 it is clear that the coefficients  $a$  and  $b$  differ from subject to subject. As a consequence the above values have to be considered as averages.

Investigations into the perception of specific force have by far not been as successful as those into the perception of angular acceleration. The structure of the otoliths suggests the dynamics of an overdamped mass-spring-dashpot accelerometer, or, more exactly, a specific force sensor. A schematic drawing of an otolith is given in Fig. 2b. An attempt to measure and describe the dynamic properties has been made by Meiry, Ref. 10, resulting in the revised otolith model of Young and Meiry, Ref. 11, the transfer function of which is:

$$\frac{A_p(S)}{A_i(S)} = \frac{1.5}{(S + c)(S + e)} \cdot (S + 0.076) \quad (2)$$

where:

$A_p$  = perceived specific force  
 $A_i$  = input specific force  
 $c \approx 1.5$  rad/sec  
 $e \approx 0.19$  rad/sec

Eq. (2) may be divided into a part relating otolith displacement  $d$  and specific force  $A_i$ :

$$\frac{d(S)}{A_i(S)} = \frac{1.5}{(S + c)(S + e)} \quad (3)$$

and a neural processing term, relating perceived specific force  $A_p$  and otolith displacement  $d$ :

$$\frac{A_p(S)}{d(S)} = (S + 0.076)$$

The numerical values of the constants  $c$  and  $e$ , dependent on the mass of the otoconia, the viscous damping due to the endolymph and the supporting structure of the otolith and the restraining spring forces of the hair cells, are again to be taken as averages.

In Ref. 11 a reasonable fit of experimental data to the model according to eq. (2) is shown. Other researchers, however, give experimental results that are not in agreement with this model, see Refs. 6, 8, 12 and 13.

The ability of labyrinthine defective (L.D.) subjects to perceive tilt, though with decreased accuracy with respect to normal subjects, shows that touch, pressure and kinesthesia receptors also provide information on specific forces acting on the human body.

An indication that motion is possibly also perceived by the motion of internal organs is to be found when considering the transfer function of the human body for vibrations, see Ref. 14. There is a prominent resonance peak at about 2 c.p.s. for vertical vibration of the erect body, a resonance which is due to the mass, stiffness and damping of the internal organs within the trunk.

A slightly different otolith model is suggested by Mayne in Ref. 12. It is argued there that in the vestibular system the sensory cells can be divided into three groups, sensitive to otolith displacement, rate of displacement or both. The proposed transfer function becomes:

$$\frac{x_o(S)}{\ddot{u}(S)} = K_1 - \frac{K_2 \omega_1 \omega_2}{(S + \omega_1)(S + \omega_2)} \quad (4)$$

This expression can be visualized as describing both the characteristics of a conventional accelerometer (first right hand term of the equation) and of a differentiating accelerometer (second right hand term). Neglecting  $\omega_2$ , representing the upper break frequency, Mayne suggests the following transfer function:

$$\frac{x_o(S)}{\ddot{u}(S)} = K_1 - K_2 \cdot \frac{\omega_1}{S + \omega_1} \quad (5)$$

where:

$x_o$  = otolith displacement  
 $\ddot{u}$  = input specific force  
 $K_1 = 24.25 \text{ sec}^2$

$$K_2 = 15.26 \text{ sec}^2$$

$$\omega_1 = 0.232 \text{ rad/sec}$$

The difference between the above presented models, see Fig. 4, according to eqs. (2) and (5), is that the latter has a constant gain at high frequencies.

Whether the mechanical properties of the otoliths (mass, restraining force and damping) are also supposed to be accounted for in this model, is not quite clear.

#### Thresholds of motion perception, pilot models and the conception of an "internal model"

As already mentioned in the introduction the results of measuring the thresholds of motion perception in a three degree of freedom aircraft simulator will be discussed in this paper. As will be clear from the preceding discussion the semi-circular canals and the otolith organs behave as dynamic systems, usually described by relatively simple mathematical equations.

It stands to reason that neural signals from the cells in the cupula and the otolith are, in some way, proportional to cupula deflection and otolith displacement. These displacements are not only dependent of the input signals but also, of course, of the dynamics of the vestibular organs as described by eqs. (1) and (3). Therefore, the procedure used by van Egmond, Jongkees and Groen, Refs. 8 and 15, to correct the experimentally determined threshold values in the case of angular oscillatory accelerations by reducing the threshold values to a normalized frequency, is essentially correct. A similar procedure is followed in this paper by relating the threshold of motion perception to the cupula or otolith displacements.

The techniques described in Refs. 6, 8, and 10 to determine the constants in the models according to eqs. (1) and (3) are partly based on the determination of the threshold values. In this way there is a danger, however, that the importance of the thresholds is being over-emphasized and that numerical values of thresholds are considered as absolute.

It appears more appropriate to accept that all neural signals and in particular those resulting from cupula deflections or otolith displacements, are noisy signals, representing motion related measurements, see Fig. 7. Using the concept of an "internal model" as mentioned in the Introduction, these measurements can be thought as serving to update the estimate of the internal model of the state of the system to be controlled. Stated in terms of modern control theory, all sensory motion related signals (vestibular, visual, proprioceptive etc.) can thus be considered as being used by the human operator to improve the estimate of the state of the system to be controlled.

Returning now more specifically to the role of the vestibular organs, the above proposed concept firstly enables the thresholds of perception to be stated in terms of measurement noise: if the sensory signal is weak, it cannot be recognized from the background of measurement noise, see Fig. 5. This concept of thresholds in terms of unfavourable signal to noise ratio has already been stated elsewhere (Ref. 6).

Secondly, if the concept of the internal model is accepted it should be concluded that an influence of the internal model and the information processing on the thresholds measured is to be expected.

There is evidence that the state of the internal model indeed affects the thresholds of motion perception. It is well known that in vestibular sensing, as well as in hearing and vision, man is able to feel (or hear or see) a slowly increasing signal at a very low level, but is not able to definitely recognize it until it has exceeded a certain level (threshold). When next the signal is decreased, however, he can still recognize its characteristics far below this threshold: the internal model built during the preceding period helps to recognize the signal from a background of measurement noise.

Based on the foregoing, two experiments using the motion simulator, were designed. A first experiment was designed to measure thresholds in terms of cupula and otolith deflections. A second experiment was set up to demonstrate the influence of mental load of the pilot on the processing of the vestibular information.

The next Chapter described these experiments and the results obtained.

## EXPERIMENTS

### Experiment I. The effect of input signal frequency on thresholds of motion perception

Based on the models of the vestibular system as described in the preceding Chapter, a dependency of the threshold value on the frequency of sinusoidal input motions to be perceived should be expected and an experiment was designed to demonstrate this. Due to the limitations of the three degrees of freedom motion system, only pitch, roll and heave oscillations could be generated. The range of frequencies for these modes of motion were limited in a number of ways, as will become clear in the following.

Firstly the noise characteristics of the servo system set the minimum frequency of the heave motion at 1 rad/sec. The maximum frequency for heave was chosen equal to the maximum frequency for roll and pitch, i.e. 14 rad/sec.

Further the lower limit input signal frequency for roll and pitch was set by the fact that the pitch and roll angles necessary to produce pitch and roll accelerations at low frequencies become so large as to be recognized by the perception of change in specific force due to the change in gravity component. Given the simple relation, in the case of sinusoidal oscillations, between angular acceleration and angle of tilt and the threshold values for both angular acceleration and specific forces, the minimum frequency for pitch and roll was determined at 0.6 rad/sec.

Finally the maximum frequency for rotations was determined by the fact that the subject's head was not situated on the rotation axes of the simulator (see the Appendix). The specific forces acting at the position of the subject's head due to angular accelerations set the maximum frequency at 14 rad/sec.

For the heave mode 8 frequencies between 1 and 14 rad/sec and for the pitch and roll modes 10 frequencies between 0.6 and 14 rad/sec were chosen.

Two threshold values were obtained at each input frequency. The first

one when the amplitude was increasing and where the subject had to correctly identify both the mode (pitch, roll or heave) and the frequency of oscillation. This threshold value will be called the upper threshold in this paper. The second, lower threshold, was defined as the value measured when, with the amplitude of the test signal decreasing, the subject was no longer able to follow the oscillation. The subjects reported their observations verbally. An example of a time history of the test signal is given in Fig. 6. Two preliminary experiments were performed to establish the technique used in the final experiment. Especially the rates of increasing and decreasing the amplitude of the input signal showed to have a significant influence and consequently these rates had to be chosen as low as possible. In Fig. 6 an example of the time history of the input signal used to determine both the threshold values is shown.

Three subjects, general aviation pilots, participated in the experiment and three replications were taken. The 28 combinations of modes of motion and frequencies were presented to the subjects in random order in three sessions of approximately 30 minutes each for each replication. The preliminary experiments were also used to train the subjects. For the final experiment 504 threshold value measurements were made.

#### Experiment II. The effect of mental load on the thresholds of motion perception

One of the questions raised very often, see Refs. 6 and 16, is whether the thresholds for motion perception, as described in the previous Chapter, are applicable in the case of a pilot when performing a task in the aircraft. As this question is very important when designing washout filters for simulation and when developing pilot models, an experiment was designed to investigate the influence of mental load on threshold values. To mentally load the subjects two additional tasks were used. One was a control task, incorporating either the symmetric or asymmetric control characteristics of a simulated twinjet airliner, the other was an auditory binary choice task.

Five threshold values under different additional mental load conditions were determined using an oscillatory input signal for either pitch, roll or heave with increasing amplitude or a ramp function for specific force in X- or Y-directions by tilting the simulator.

During such a test the subject was asked to control the symmetric or the asymmetric motions of the simulated aircraft and to further observe and verbally report any disturbance caused by a test signal in the degrees of freedom not involved in the control task. The symmetric control task consisted of maintaining constant altitude by controlling the pitch attitude. In the asymmetric control task constant heading was to be maintained by controlling the roll angle. The simulated aircraft was disturbed by atmospheric turbulence in both cases.

The binary choice task was used at three levels, 0, 40 and 80% of the maximum the subjects could perform. This maximum was defined by the number of tones the subject could answer in one minute making not more than one error.

In Table 1 the experimental combinations used are summarized. In this experiment four subjects participated, three of them were general aviation pilots, two of whom also participated in Experiment I. The fourth was a student

pilot. As each experimental combination was repeated 4 times, the total number of threshold values determined was  $6 \times 5 \times 4 \times 4 = 480$ . These thresholds were determined during 288 runs of the additional tasks lasting 150 seconds each. As a rule two threshold values were obtained during one run, but in a limited number of runs no test signal was presented. This was done to avoid the subjects concentrating too much on the determination of the thresholds. The subjects were instructed and trained to do their best on the additional tasks and their performance in these tasks was monitored. In the case of poor performance test runs were rejected, thus improving the subject's motivation.

### Results of Experiment I

In Figs. 9 and 10 the input related threshold values for pitch and roll accelerations are plotted as a function of frequency. Both the values obtained with increasing and decreasing amplitudes, i.e. the upper and the lower thresholds respectively, are given with their standard deviations. The thresholds can be seen to increase with frequency while the slope of the upper threshold is nearly equal to one, thus approximating the slope of the inverse of the modulus of the transfer function of the cupula model (eq. (1)). The slope of the lower threshold is slightly smaller.

The pertaining results of the analysis of variance are summarized in Tabel 2. The difference in thresholds for pitch and roll appears to be negligible. This could be expected as both pairs of vertical semi-circular canals are activated by pitch as well as by roll accelerations, see Fig. 2c. The analysis of variance confirms this equality.

The difference between upper and lower thresholds is probably significant. The differences between subjects and the interactions of the subjects with the other main effects are significant. This is not amazing bearing in mind that, as stated in the preceding Chapter, each subject will have different vestibular characteristics.

The interaction between frequency and upper and lower threshold and hence the difference in slope of the upper and lower threshold is significant.

The threshold values for specific forces along the vertical axis are presented in Fig. 9. It will be clear that here a dependency of the input related threshold of frequency cannot be concluded, see also the results of the analysis of variance in Table 2.

The difference of the upper and lower thresholds, however, is probably significant. The threshold values again demonstrate significant differences for the subjects and the interaction between subjects and frequency. Just as for the angular accelerations a significant difference in slope of the upper and lower threshold was found.

### Results of Experiment II

In Table 3 the average input related threshold values of all experimental conditions are given. A review of the results of the analyses of variance is

presented in Table 4. The specific forces  $A_x$ ,  $A_y$  and  $A_z$  show a difference in input signal. For the specific forces  $A_x$  and  $A_y$  a ramp signal had to be used, whereas in the Z-direction a sinusoidal signal ( $\omega = 1.88$  rad/sec) was used. The input related threshold for specific force in the Z-direction is equal to the value found in Experiment I, see Fig. 9.

The higher values for the X- and Y-directions are in accordance with the otolith models (eqs. (2) and (4)) if it is assumed that the otolith displacement is a measure for the threshold value. The difference between the X- and Y-directions can, among others, have the following reasons.

Firstly the subjects were much more firmly fixed by the pilot's chair in the Y-direction than in the X-direction. The subjects often remarked that they observed changes in touch on their back due to roll angles of the simulator, thus influencing their perception.

Secondly the orientation of the macula relative to the X-axis for a normal seated subject could also be of importance.

The maximum increase of the threshold values due to the mental loading tasks is roughly 25, 50 and 100% for  $A_x$ ,  $A_y$  and  $A_z$  respectively. Analysis of variance, see Table 4, shows a possible significant increase for the thresholds in the Y- and Z-directions only. From the data it appears that the control task produced a larger increase in thresholds than the binary choice task. More research is necessary to elucidate the ways in which different sources of mental load influence the subjective threshold values.

The input related thresholds for angular acceleration show a significant increase due to the additional tasks. Differences for pitch and roll are small. The maximum increase of the threshold value is 40 and 80% for pitch and roll respectively.

It may be noticed that the threshold values presented here for the case of no additional task do not correspond with the values found in Experiment I. This is due to the fact that Experiment II was actually performed before Experiment I at a time when the strong dependency of thresholds on the rate of increase of amplitude was not yet fully appreciated, and the rates of increase had not yet been set at more appropriate lower values. With the original rate of increase, however, these threshold values can easily be reproduced.

Summarizing this paragraph it can be concluded that the threshold values for motion perception can indeed be influenced by the mental load of the pilot.

## DISCUSSION

Some conclusions to be drawn from the experiments described, hold for the perception of specific forces as well as for the angular accelerations. Therefore these more general conclusions will be discussed first, to be followed by a separate treatment of the findings that are more specifically related to either the perception of angular accelerations or to the perception of specific forces.



Differences among subjects, the internal model and the influence of additional tasks

From Experiment I, see Figs. 7, 8 and 9 it appears that the spread of the threshold values measured is rather large. The analyses of variance show that this is mainly a result of differences among subjects as well as interactions between subjects and the other main effects. After subtraction of these significant effects the remaining standard deviations, independent of subject, of the mean values for Experiment I as given in Figs. 7, 8 and 9 are  $0,103^{\circ}/\text{sec}^2$  and  $0,006 \text{ m}/\text{sec}^2$ .

These values cannot be ascribed to experiment related measurement noise alone but should also be interpreted as being caused by the noise present in the output signals of the vestibular systems themselves. Especially at threshold deflections of the cupula and at threshold deviations of the otolith the unfavourable signal to noise ratio seriously affects the motion perception as discussed earlier in this Report, see Fig. 5.

Apart from differences between subjects as far as physical characteristics of the vestibular systems are concerned, differences in judgment may also be present. Already during the evaluating experiment it appeared that some subjects were more inclined to guessing while others refrained from reporting on perceived motions until they were quite certain. This effect was diminished as much as possible by training but it nevertheless was still present in the final experiments.

Finally it should be remarked that the subjects usually reported that they were moving long before they were able to identify the mode (pitch, roll or heave) and the frequency of the test signal, which confirms the findings of Ref. 6.

The results of Experiment I demonstrate that the threshold value is considerably decreased if the motion is known and expected by the subject. This is in agreement with the idea that the human operator is able, by using an internal model of the system to be controlled, to predict the state of the system. In the case of a known sinusoidal motion cue the subject, using this internal model, only needs a relatively weak vestibular signal to observe the motion. Hence it is not amazing that the upper threshold values measured for angular accelerations are approximately two and a half times the lower threshold values and the upper thresholds for specific forces along the Z-axis are twice the lower threshold values.

The results of Experiment II show a significant influence of the additional tasks on the threshold values and this influence was strongest in the case of rotations, see Table 4. The conclusion from these findings is that threshold values for motion perception are determined partly by the physical characteristics of the semi-circular canals and the otoliths and partly by the processing of the vestibular information: the more attention the subject can share to motion perception, the lower the threshold values will be.

The above can be summarized by concluding that using an internal model gives the pilot a tool to improve the prediction of future motion cues and to improve the ability to perceive these cues. A mental loading of the pilot, however, oppresses the information processing of the vestibular signals. Hence threshold values will depend on the total workload and on the amount of necessary information the pilot can derive from the motion cues in order to

estimate the state of the aircraft with sufficient accuracy.

The thresholds for angular accelerations expressed  
in terms of minimum perceived cupula deflections

As already shown in the preceding Chapter the input related threshold value for angular accelerations increases with frequency in such a way that multiplying the input by the modulus of the transfer function according to eq. (1) should yield a nearly constant cupula deflection at the threshold. The modulus as a function of frequency, however, is only known if the parameters of the transfer function of each subject were known, which was not the case in the present experiments. Therefore an approximation suggested by Jongkees and Groen, see Ref. 15, was used. Between the break frequencies of the transfer function the modulus is approximated by:

$$M = \frac{1}{a \cdot \omega} \quad (6)$$

see Fig. 3.

For Experiment I the maximum input frequency was 14 rad/sec which is only slightly above the generally used break frequency of  $\frac{1}{b} = 10$  rad/sec (see Fig. 3), allowing the approximation according to eq. (6) still to be used to compute the cupula deflections for pitch and roll. The results are plotted in Fig. 10. It can be seen that the cupula deflection is not quite constant with frequency, which could be expected from Figs. 7 and 8. This may be caused by the experimental technique used to determine the threshold values. As stated before the rate of increase of the input signal has a strong influence on the thresholds determined.

Finally it is of course interesting to see how the threshold values determined experimentally compare with results of other experiments. For this purpose the threshold values have been corrected for the modulus of the transfer function (according to eq. (6)). The threshold values of angular acceleration thus derived are in fact those found at very low frequencies where the modulus is constant, see Fig. 3, and could be termed "cupula related thresholds". Theoretically these values should be equal to those found by experiments using step input accelerations. The following cupula related thresholds for pitch and roll accelerations are found.

Input acceleration	Upper threshold (°/sec <sup>2</sup> )	Lower threshold (°/sec <sup>2</sup> )
roll	0.023 - 0.035	0.0069 - 0.015
pitch	0.022 - 0.053	0.0082 - 0.026

These values are remarkably below those found by other researchers:

Input acceleration	Authors	Threshold ( $^{\circ}/\text{sec}^2$ )
yaw, sinusoidal, corrected	Jongkees, Groen, 1948, Ref. 13	0,18 - 2,0
yaw, step input	Meiry, 1965, Ref. 8	0,1 - 0,2
yaw, pitch, roll, step input	Clark, Stewart, 1968, Ref. 15	0,06 - 2,24

The thresholds for specific forces

As shown in the preceding paragraph a certain minimum cupula deflection can be considered to determine the lower bound of the thresholds for angular acceleration perception. However, nor from the literature nor from the results of the present experiments such a similar conclusion can be drawn with respect to otolith displacement. If, based on the input related thresholds in Experiment I and the revised otolith model of Meiry and Young (eq. (3)), the otolith displacement is computed, then the threshold appears to decrease with frequency. According to Mayne's model (eq. (5)) the otolith displacement would be independent of frequency. Mayne (Ref. 12), however, does not specify the upper break frequency  $\omega_2$  of his complete model (eq. (4)) and, as shown in Fig. 4, the modulus of the simplified model is constant at frequencies larger than 1 rad/sec. This can not actually be the case and the use of Mayne's model would only be justified if a reliable estimate of  $\omega_2$  were available.

At low frequencies both models have the same modulus, see Fig. 4, and are in correspondence with the higher threshold values found in Experiment II for the specific forces in the X- and Y-directions.

From Refs. 8 and 13 it can be concluded that the perception of specific forces is much more complicated than would be expected from the simple otolith models mentioned. As stated before, specific force perception by pressure, touch and kinesthesia receptors should not be excluded. As mentioned earlier labyrinthine defective subjects have thresholds for specific force perception that are only slightly higher than those of normal subjects (0,2 and 0,1  $\text{m}/\text{sec}^2$  respectively).

Another possible explanation of the fact that the threshold values determined do not fit the models could be that the subjects were seated in a normal pilot's chair without fixation of head and trunk. As already mentioned due to mass and stiffness of the internal organs of the body a resonance frequency is found at about 12 rad/sec (Ref. 14). Therefore the specific forces acting on the subject's head could in fact have been larger than the specific forces acting on the simulator.

At this moment only a provisional conclusion can be drawn. For oscillatory specific forces the threshold value is approximately 0.085  $\text{m}/\text{sec}^2$  fitting very well with the threshold values reviewed in Ref. 4.

Mach	1875	0.10 - 0.12 m/sec <sup>2</sup>
Jongkees and Groen	1946	0.06 - 0.13 m/sec <sup>2</sup>
Meiry	1965	0.10 m/sec <sup>2</sup>
Present experiment		
Upper threshold		0.07 - 0.03 m/sec <sup>2</sup>
Lower threshold		0.04 - 0.06 m/sec <sup>2</sup>

For very low frequencies as for instance a specific force due to sustained tilt, the threshold value is higher ranging from 0.35 - 0.50 m/sec<sup>2</sup> depending on the direction of the specific force.

### CONCLUSIONS

In this paper two experiments to investigate the motion perception of the pilot in the aircraft environment were described. The first experiment was carried out to measure threshold values for motion perception as a function of frequency. A second experiment was designed to demonstrate the effect of mental load on motion perception, especially on threshold values. Based on the results and the discussion in the preceding chapter, the following conclusions can be drawn.

1. Threshold levels for motion perception depend on the physical characteristics of the vestibular system as well as on the information processing of the motion related sensory signals.
2. As a consequence of the signal to noise ratio of the output signals of the vestibular system, physically determined thresholds are not to be considered as discrete values but rather as transition ranges from not perceivable to fully perceivable motions.
3. A considerable improvement of motion perception can be achieved and consequently lower thresholds are obtained if a human operator is able to identify an internal model of the motion to be perceived.
4. Threshold values for angular acceleration are directly related to a minimum perceivable cupula deflection.
5. Thresholds for specific forces cannot definitely be ascribed to otolith displacement alone. For oscillating specific forces a constant value independent of frequency is a good approximation for a pilot in an aircraft environment.

### REFERENCES

1. Hosman, R.J.A.W.: Pilot Vehicle analysis. AGARD Conference Proceedings,

No. 106, AGARD, 1971.

2. Hosman, R.J.A.W.: Pilot tracking behaviour under additional workload, Delft University of Technology, Department of Aerospace Engineering, Report VTH-199, 1975.
3. Bergeron, H.P., Adams, J.J., and Hurt, G.J.: The effects of motion cues and motion scaling on one- and two-axis compensatory control tasks. NASA-TN D 6110, 1971.
4. Davies, P.: Approval of flight simulator flying qualities. Aeronautical Journal, July 1975.
5. Young, L.R.: The current status of vestibular models. Automatica, Vol. 5, pp. 368-383, 1969.
6. Guedry, F.E.: Psychophysics of vestibular sensation. In: Kornhuber, H.H. (ed.): Handbook of Sensory Physiology. Volume VI/2, Springer Verlag, Berlin, Heidelberg, New York, 1974.
7. Kornhuber, H.H. (ed.): Handbook of Sensory Physiology. Volume VI/2. Vestibular system: Psychophysics, applied aspects and general interpretations. Springer Verlag, Berlin, Heidelberg, New York, 1974.
8. van Egmond, A.A.J., Groen, J.J. and Jongkees, L.B.W.: The function of the vestibular organ. Practica-Oto-Rhino-Laryngologica, Vol. XIV, Supplement 2, 1952.
9. Peters, R.A.: Dynamics of the vestibular system and their relation to motion perception, spatial disorientation and illusions, NASA CR-1303, 1969.
10. Meiry, J.L.: The vestibular system and human dynamic space orientation. NASA CR-628, 1966.
11. Young, L.R. and Meiry, J.L.: A revised dynamic otolith model. Proceedings of the third symposium on the role of the vestibular organs in space exploration. NASA SP-152, 1968.
12. Mayne, R.: A systems concept of the vestibular organs. In: Kornhuber, H.H. (ed.): Handbook of Sensory Psychology. Vol. VI/2, Springer Verlag, Berlin, Heidelberg, New York, 1974.
13. Graybiel, A.: Measurement of otolith function in man. In: Kornhuber, H.H. (ed.): Handbook of Sensory Psychology. Vol. VI/2, Springer Verlag, Berlin, Heidelberg, New York, 1974.
14. Garg, D.P. and Ross, M.A.: Vertical mode human body vibration transmissibility. I.E.E.E. Transactions on Systems, Man and Cybernetics. Vol. SMC-6, No. 2, February 1976.

15. Groen, J.J. and Jongkees, L.W.B.: The threshold of angular acceleration perception. J. Physiology, 107, 1-7, 1948.
16. Gundry, J.: Man and motion cues. Proceedings of the Royal Aeronautical Society Third Flight Simulation Symposium on "Theory and Practice in Flight Simulation", 1976.
17. Clark, B. and Stewart, J.D.: Thresholds for the perception of angular acceleration about the three major body axes. In: Fourth Symposium on The Role of the vestibular organs in Space Exploration, NASA SP-187, 1968.

#### APPENDIX

##### THE CHARACTERISTICS OF THE SIMULATOR MOTION SYSTEM

The three degree of freedom motion system of the simulator has three hydraulic servo actuators. These actuators, having hydrostatic bearings, produce a nearly rumble free motion of the simulator. The maximum attainable single degree of freedom performance is presented in Table 5.

The angular accelerations and the specific forces applied during the experiments are small in relation to the maximum performance of the motion system. As this puts high demands on the motion system with respect to the motion noise, a calibration program to determine the transfer functions between motion system input and output angular accelerations or specific forces and to evaluate the motion noise, was carried out.

For all input signals of Experiment I the modulus and phase shift of the transfer function was measured. In addition the power spectral density of the motion noise was computed. It turned out that due to small differences in the dynamic characteristics and due to slightly different loading of the servo actuators the input signals also excite the other two degrees of freedom.

As an example, the data for the heave motion are presented in Table 6. The amplitudes of the angular accelerations linearly related with the input heave signal are roughly one tenth of the thresholds for angular acceleration and increase with frequency.

The angular acceleration noise decreases with frequency hence increases with the amplitude of servo actuator speed.

Although the standard deviation may appear rather large, it should be borne in mind that the noise measured has a large bandwidth and moreover could not be perceived by the subjects. The noise of the vertical acceleration is small.

In Fig. 11 the position of the test subject relative to the rotational axes of the simulator is given.

Binary Choice Task	Control task	Symmetric			Asymmetric	
		Specific force $A_x$	Specific force $A_z$	Angular Acc $\dot{q}$	Specific force $A_y$	Angular Acc $\dot{p}$
0 %	-	1	1	1	1	1
40 %	-	2	2	2	2	2
80 %	-	3	3	3	3	3
0 %	asymmetric control task	4	4	4		
40 %		5	5	5		
80 %		6	6	6		
0 %	symmetric control task				4	4
40 %					5	5
80 %					6	6

Table 1a. Survey of the experimental conditions for which the thresholds are determined in Experiment II.  
Numbers are related to Table 4.

	Specific force $A_x$	Specific force $A_z$	Angular Acc $\dot{q}$	Specific force $A_y$	Angular Acc $\dot{p}$
motion test signal	ramp-function	sinusoidal $\omega = 1.88$ rad/sec	sinusoidal $\omega = 0.94$ rad/sec	ramp-function	sinusoidal $\omega = 0.94$ rad/sec

Table 1b. Survey of test signals used in Experiment II.

Main effects and interactions	Input related thresholds		
	Specific force $A_z$	Angular Acc.	
		$\dot{q}$	$\dot{p}$
Frequency		*****	*****
K Upper - Lower	**	**	***
Subjects	*****		*****
FS	*****	*****	*****
KS		*****	*
FK	*****	*****	*****
FKS			
Replicates			

$\alpha < 0.05$  \*  
 $\alpha < 0.025$  \*\*  
 $\alpha < 0.01$  \*\*\*  
 $\alpha < 0.005$  \*\*\*\*  
 $\alpha < 0.001$  \*\*\*\*\*

Table 2. Survey of the results of the analyses of variance on the results of Experiment I.

No	Input related threshold				
	Specific force			Angular Acc.	
	$A_x$ m/sec <sup>2</sup>	$A_y$ m/sec <sup>2</sup>	$A_z$ m/sec <sup>2</sup>	$\dot{q}$ o/sec <sup>2</sup>	$\dot{p}$ o/sec <sup>2</sup>
1	0.57	0.31	0.08	0.85	0.81
2	0.65	0.36	0.08	0.94	1.00
3	0.67	0.37	0.09	1.05	1.15
4	0.71	0.48	0.15	1.07	1.13
5	0.69	0.44	0.15	1.07	1.16
6	0.71	0.47	0.16	1.20	1.45

Table 3. The threshold values resulting from Experiment II.  
 Numbers are related to table 1a.



Main effects and interactions	Input related thresholds				
	Specific forces			Angular Acceleration	
	A <sub>x</sub>	A <sub>y</sub>	A <sub>z</sub>	$\dot{q}$	$\dot{p}$
Additional tasks	-	■	■■■■■■■	■■■■■■■	■■■■■
Subjects	■■■■■■■	■■■■■■■	■■■■■■■	■■■■■■■	■■■■■■■
AS	-	■■■■■	■	-	-
Replicates	-	-	-	-	-

$\alpha < 0.05$  ■  
 $\alpha < 0.025$  ■■  
 $\alpha < 0.01$  ■■■  
 $\alpha < 0.005$  ■■■■  
 $\alpha < 0.001$  ■■■■■■

Table 4. Survey of the results of the analyses of variance on the results of Experiment II.

	Travel	Speed	Acceleration
Heave	$\pm 0.3$ m	$\pm 1$ m/sec	+ 15 m/sec <sup>2</sup> - 28 m/sec <sup>2</sup>
Roll	$\pm 16^\circ$	$\pm 73^\circ/\text{sec}$	$\pm 1090^\circ/\text{sec}^2$
Pitch	$\pm 15.5^\circ$	$\pm 50^\circ/\text{sec}$	+ 315 <sup>o</sup> /sec <sup>2</sup> - 460 <sup>o</sup> /sec <sup>2</sup>

Table 5. Single degree of freedom performance of the three degree of freedom motion system of the flight simulator. September 1975.

Input frequency rad/sec	Modulus M	Phase angle (degrees)	Noise $\sigma_{Az}$ m/sec <sup>2</sup>	Pitch		Roll	
				Amplitude $\sigma_o$ /sec <sup>2</sup>	Noise $\sigma_d$ o/sec <sup>2</sup>	Amplitude $\sigma_o$ /sec <sup>2</sup>	Noise $\sigma_d$ o/sec <sup>2</sup>
14	0.675	-89	0.016	0.165	0.501	0.418	0.546
12	0.745	-77	0.017	0.114	0.615	0.343	0.675
10	0.834	-64	0.017	0.093	0.672	0.257	0.782
8	0.907	-50	0.018	0.129	0.734	0.133	0.803
6	0.968	-37	0.017	0.067	0.760	0.118	0.889
4	1.00	-24	0.018	0.031	0.817	0.086	0.953
2	1.01	-11	0.017	0.021	0.853	0.032	1.006
1	1.00	-5	0.018	0.031	0.894	0.021	1.071

Table 6. The transfer- and noise characteristics of the motion system for a sinusoidal input signal producing a heave acceleration amplitude of 0.085 m/sec<sup>2</sup>.

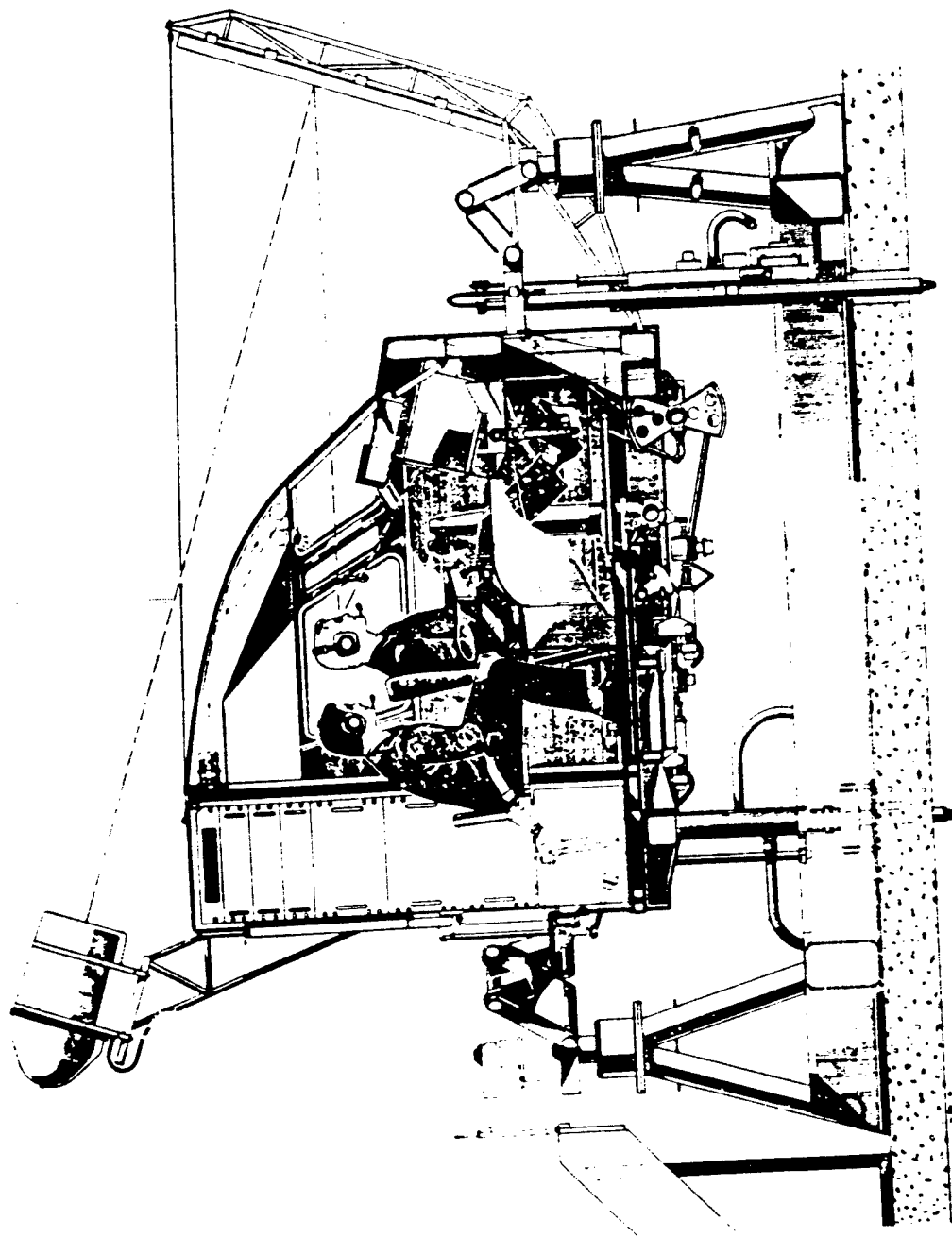


Fig. 1. Layout of the flight simulator.

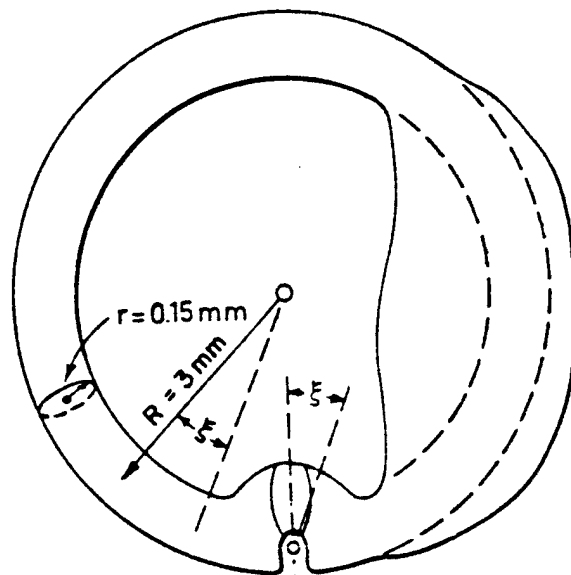


Fig. 2a. Schematic Diagram of the Semicircular Canal (Ref. 10).

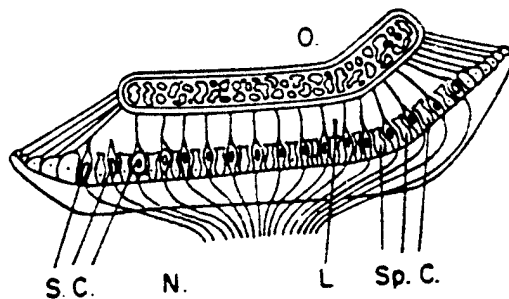


Fig. 2b. Schematic drawing of a cross section of an otolith and its macula. O is the otolith, suspended by strands which run from the margins to the macula, consisting of supporting cells (Sp.C.) and sensory cells (S.C.). Between the otolith and the macula there is a thin Layer (L) to allow the otolith to slide over the macula. N is the nerve (Ref. 10).

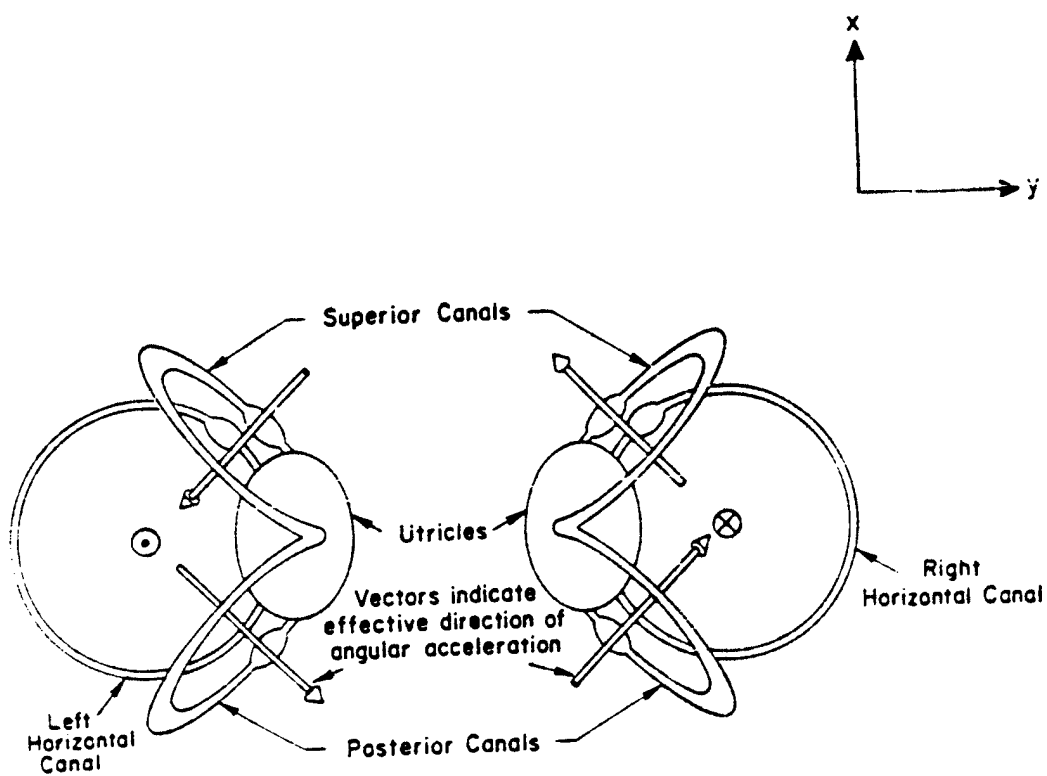


Fig. 2c. The approximate orientation of the sine-circular canals (Ref. 9).

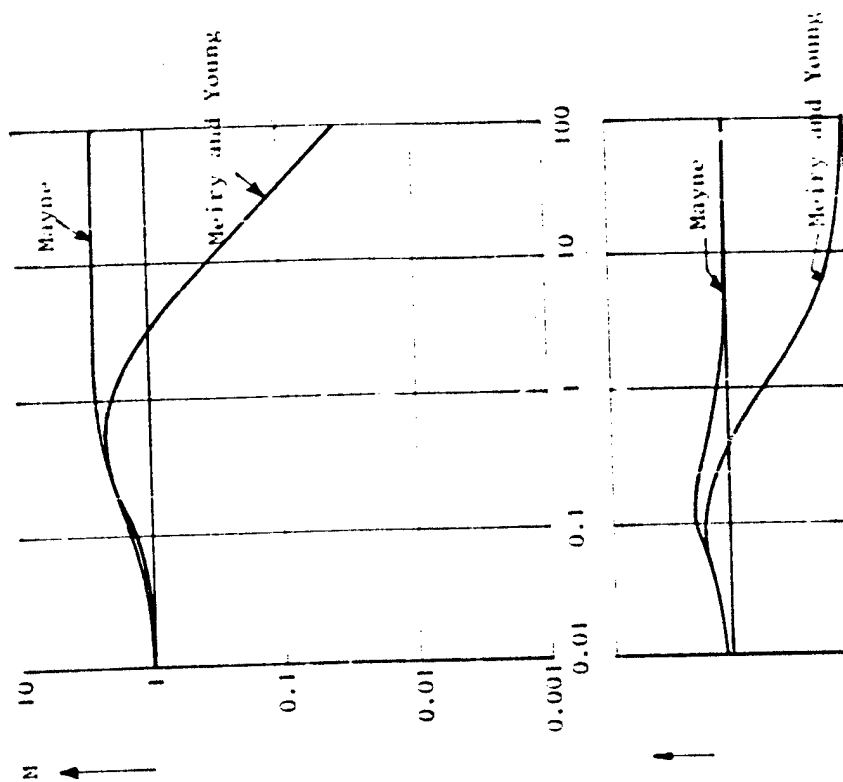


Fig. 4. Modulus and phase angle of the otolith according to eqs. (2) and (5).

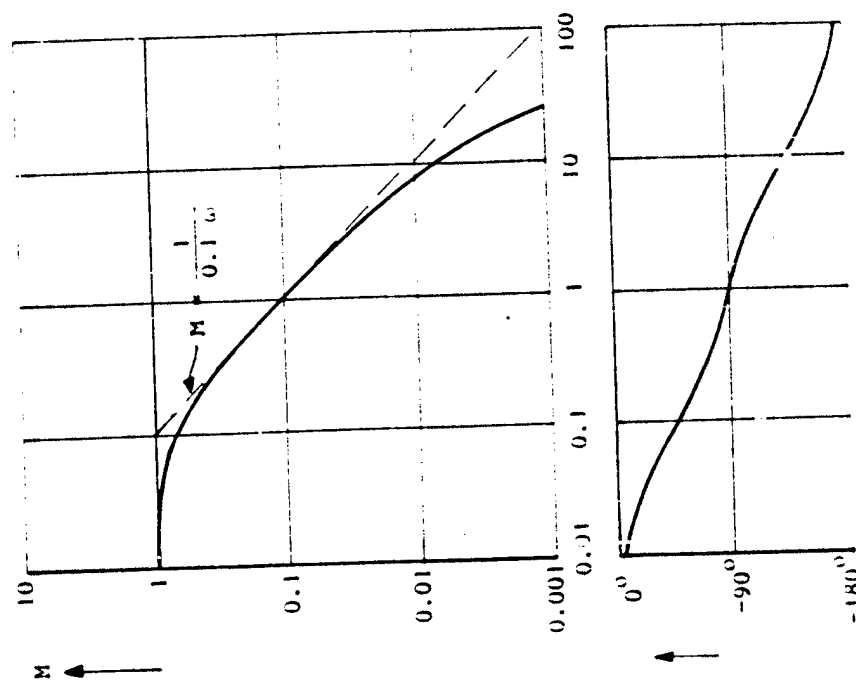


Fig. 3. Modulus and phase angle of the semi-circular canals according to eq. (1).

Amplitude

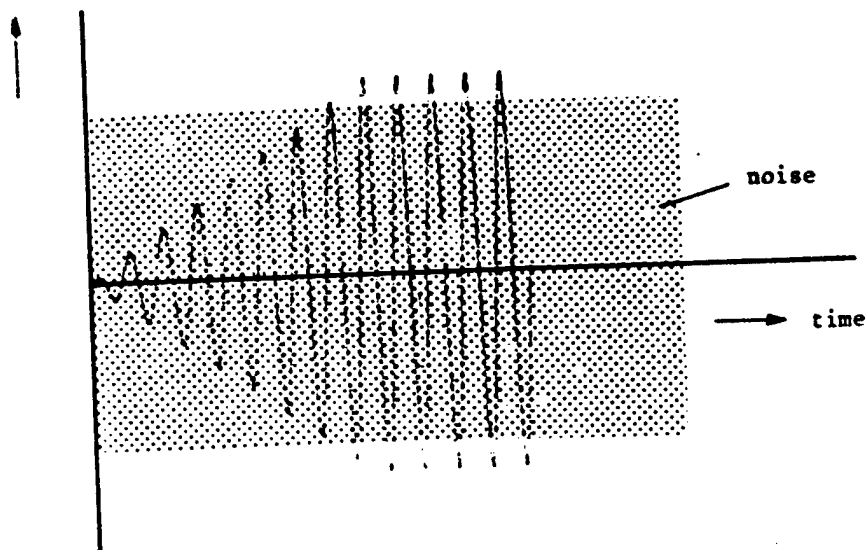


Fig. 5. Schematic diagram showing the change in signal to noise ratio of the vestibular output due to an increasing sinusoidal input motion cue.

Amplitude

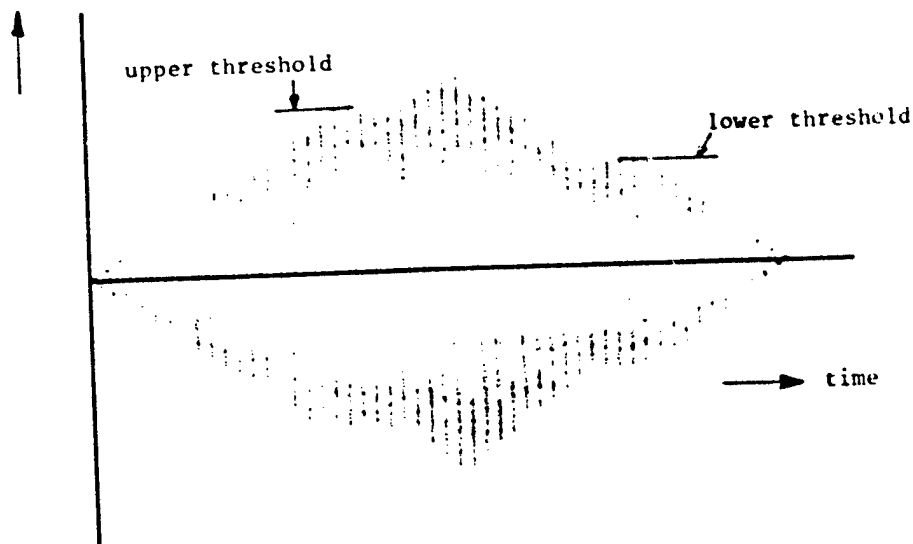


Fig. 6. Examples of the time history of the test signal to determine upper and lower thresholds.

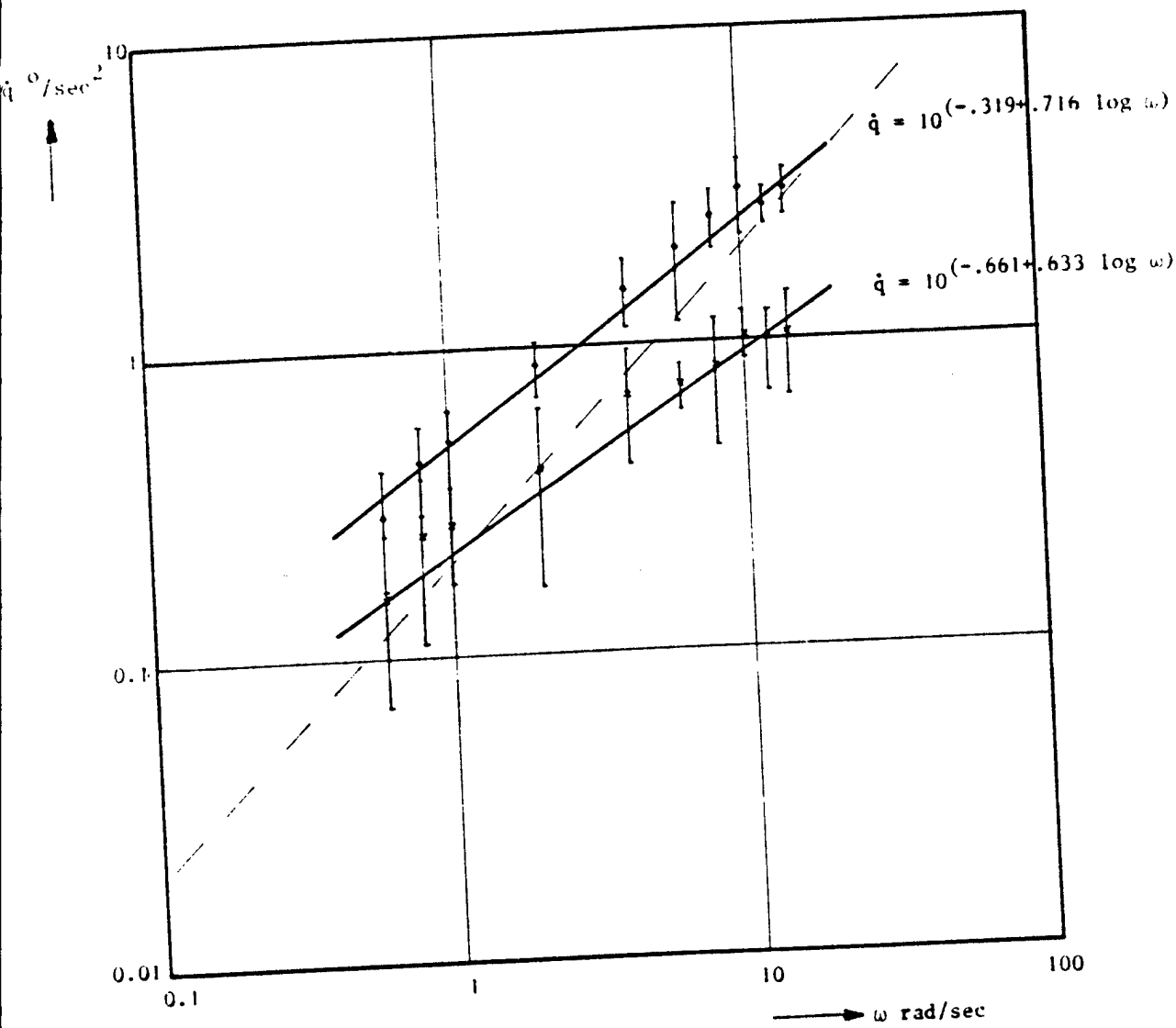


Fig. 7. Input related threshold values for pitch angular acceleration.



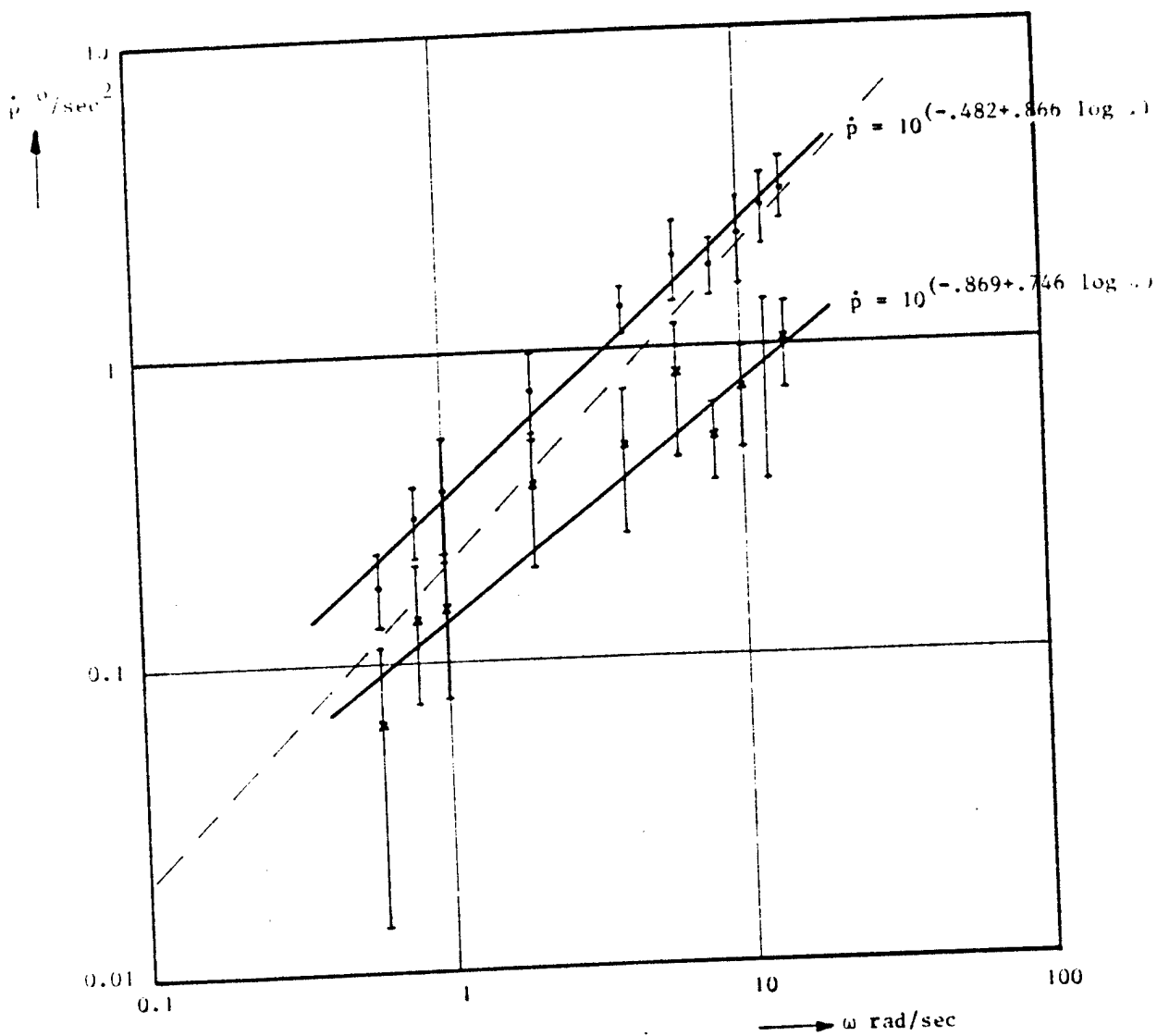


Fig. 8. Input related threshold values for roll angular acceleration.

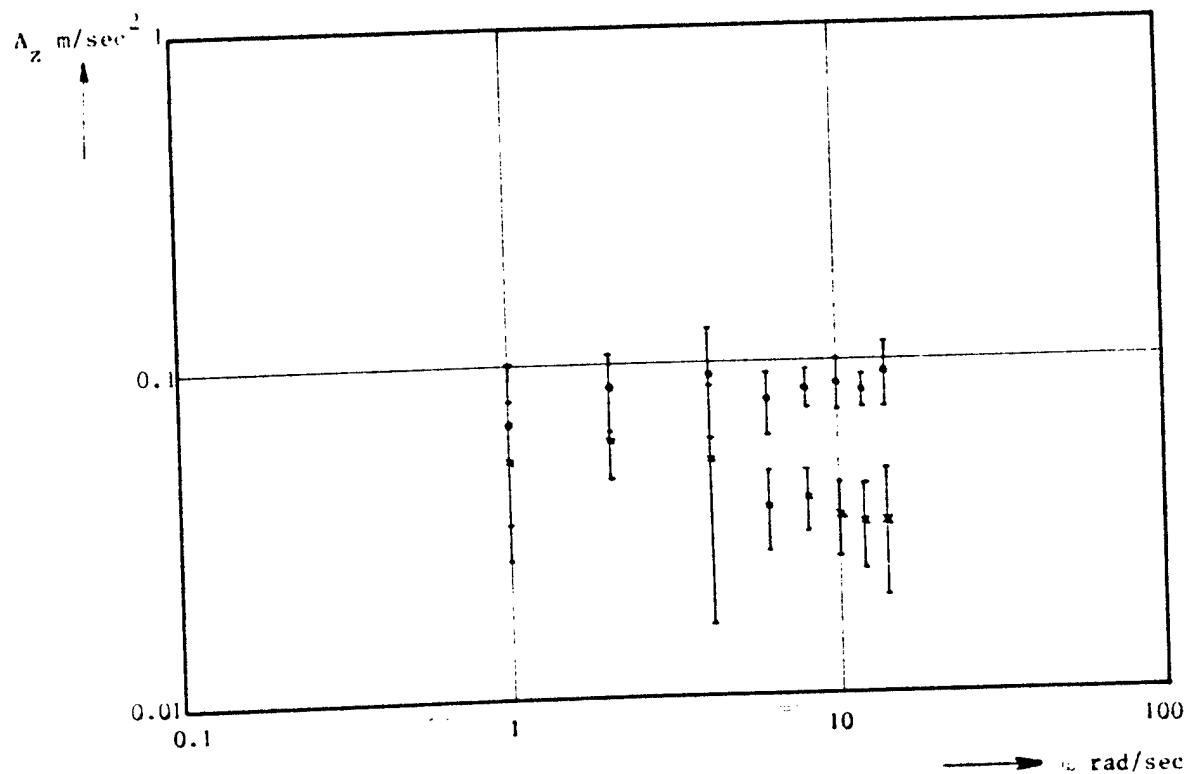


Fig. 9. Input related threshold values for specific force along the Z-axis.

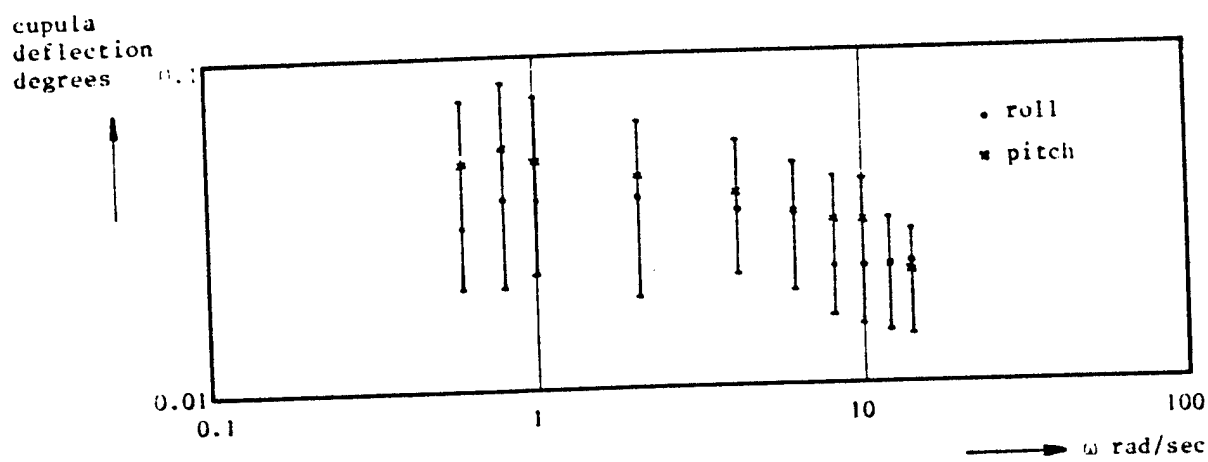


Fig. 10. Cupula deflection at threshold value for pitch and roll.

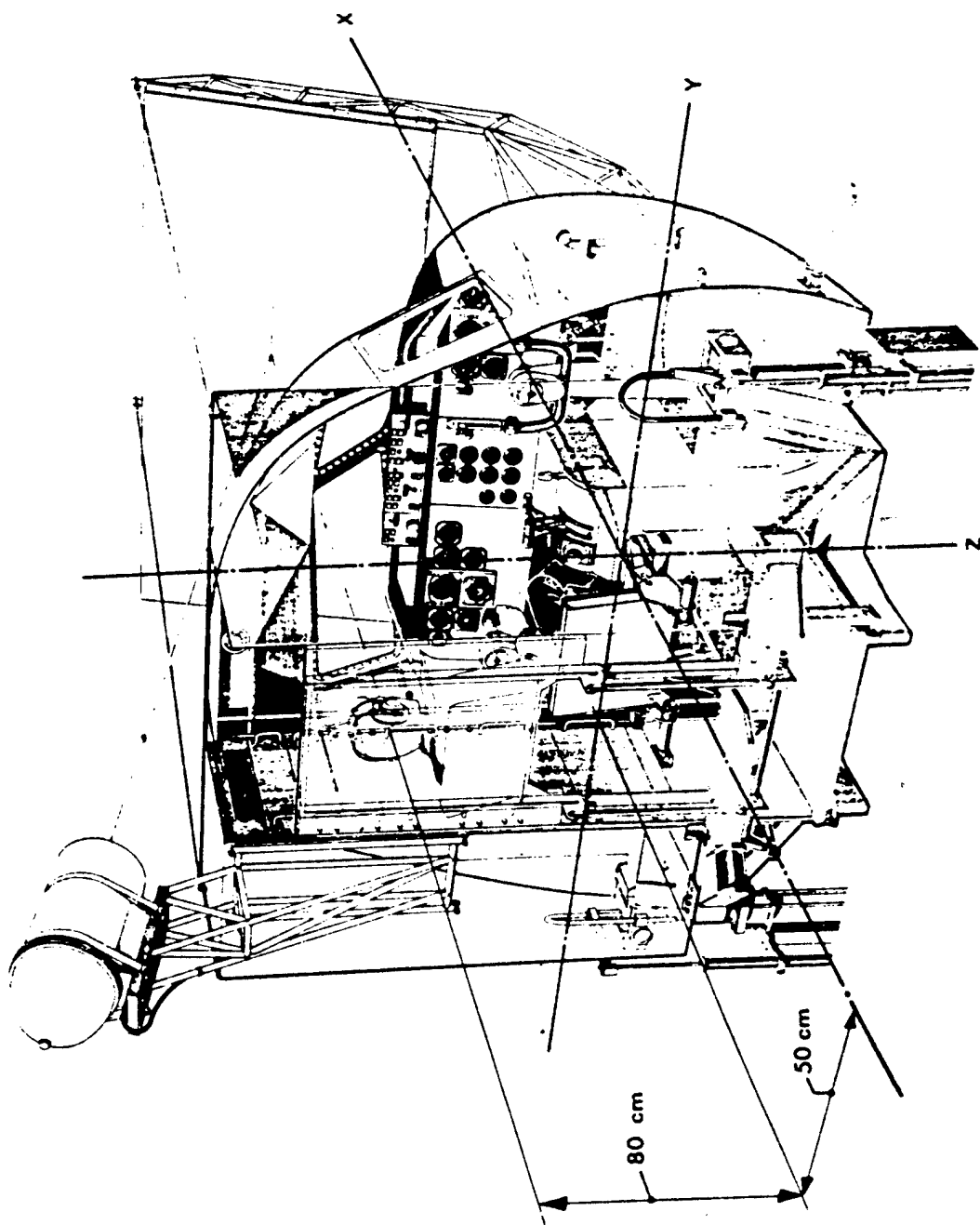


Fig. 11. Position of the subject relative to the axes of rotation.

BIOMECHANICAL RESPONSE AND MANUAL TRACKING PERFORMANCE  
IN SINUSOIDAL, SUM-OF-SINES, AND RANDOM  
VIBRATION ENVIRONMENTS\*

By William H. Levison

Bolt Beranek and Newman Inc.  
Cambridge, Massachusetts

ABSTRACT

A set of manual control experiments was conducted to explore biodynamic response and tracking performance in sinusoidal, sum-of-sines, and random z-axis vibration environments. Primary experimental variables were vibration spectrum, vibration amplitude, and stick spring gradient. Biomechanical response mechanisms were approximately linear for the vibration environments explored in this study and, with the exception of stick feedthrough, were independent of stick parameters. As seen in previous studies, stick feedthrough was considerably greater for the control stick with the higher spring gradient. Tracking performance was degraded by vibration primarily through an increase in effective pilot time delay and through increased motor-related pilot remnant. Good model results were obtained by assuming that motor noise/signal ratio and time delay varied linearly with rms shoulder acceleration. A model-based mapping procedure was defined and validated for extrapolating the results of single-sine vibration/tracking experiments to complex vibration environments. Mapping in the reverse direction was also validated.

INTRODUCTION

As technology continues to expand the performance envelope of military aircraft, pilots will have to function in increasingly severe physical environments. Vibration, either alone or in combination with other stressors, may be an important part of this environment. In order to better understand and predict the effects of vibration on pilot performance, the Aerospace

---

\*This work was sponsored by the Aerospace Medical Research Laboratory, Wright-Patterson Air Force Base, under Contract No. 33615-75-C-5043. Lt. Philip D. Houck was the Technical Monitor for this contract and Project Engineer for the AMRL experimental program.

Medical Research Laboratory has undertaken a long-term study of manual tracking in vibration environments. Recent programs have explored the nature of biomechanical response and the interactions between tracking, vibration and control-stick parameters [1-4].

This paper summarizes the results of a joint AMRL/BBN study that builds upon the results of these programs. This study had two major objectives: (1) to further define the interaction between vibration parameters and tracking performance, and (2) to develop a mapping procedure to extrapolate among single-sine, sum-of-sines, and random vibration environments. More details may be found in [5].

One of the difficulties of vibration research is that the vibration environments of ultimate interest are not the environments that are most amenable to laboratory exploration. A vibration environment encountered in flight may well consist of a component that is continuous in frequency over some band plus one or more sinusoidal (or near-sinusoidal) components. Laboratory shake tables, however, are often constrained to generating sinusoidal vibration inputs. Even when random vibration is possible, sum-of-sine (rather than continuous-frequency) inputs may be desired so as to maximize signal/noise ratios and thereby maximize the measurement bandwidth. Thus, an extrapolation (or "mapping") procedure is needed so that measurements obtained in one type of vibration environment can be used to predict the effects on performance of some other environment.

Because of the ways in which vibration influences tracking behavior, a simple weighting function will generally not be sufficient to extrapolate results from discrete sinusoid vibration environments to more complex environments. First of all, a number of biodynamic response mechanisms may be involved in determining the effects of vibration on tracking performance, with the various mechanisms having different response characteristics. Secondly, vibration-related performance degradation is largely not traceable to simple additive effects. Except for stick feedthrough (which typically accounts for a small fraction of the tracking error variance), the effects of vibration are manifested as increases in pilot remnant and in other adverse changes to basic information-processing capability. Finally, the pilot partially compensates for this unfavorable environment by re-adjusting the adaptable elements of his response behavior. Thus, in general, a rather comprehensive set of models will be required in order to allow the results of one set of experiments to be extrapolated to different experimental situations.

The "optimal-control" pilot/vehicle model appears to have a structure that allows one to predict adaptive changes in tracking response strategy that accompany whole-body vibration. This model has been applied successfully in previous studies of vibration/tracking [2-4] and forms the basis for the mapping procedure outlined in this paper.

The strategy adopted for this research study was basically as follows: (1) verify the linearity of biodynamic response mechanisms, (2) determine

the relation between biodynamic response and pilot-related model parameters, and (3) demonstrate a method for using the optimal-control model to predict tracking performance as a function of vibration parameters.

## DESCRIPTION OF EXPERIMENTS

Experimental apparatus and procedures were similar to those employed in the previous study. Therefore, only a brief description of experiments is given here. Readers desiring additional details on mechanization of the tracking task and vibration inputs are referred to [3].

The tracking task consisted of a single-axis compensatory task with K/s controlled-element dynamics. The tracking input was constructed by summing five sinusoids of random phase relations with amplitudes selected to approximate a first-order noise process having a break frequency at 2 rad/sec. This disturbance input was added to the pilot's control input to simulate a vehicle disturbance. Fore-aft motions of the control stick resulted in vertical motion of the tracking error, which was displayed on a CRT.

The test subject, control device, and display were located on the vibration table. Tracking response in the following vibration environments was explored: (1) single sinusoid vibration at 2, 3.3, 5, 7, and 10 Hz; (2) sum-of-sines vibration having equal acceleration components at 2, 3.3, 5, 7, and 10 Hz; (3) random continuous-frequency vibration, with the driving noise filtered in such a way as to approximate a flat acceleration spectrum over the range 2-10 Hz.

Nominal rms vibration amplitudes of 0.15 g and 0.3 g were explored for all environments; in addition, 0.2 g rms was explored for random vibration. All vibration was vertical (i.e., z-axis).

Two control sticks were used in this study, a "spring stick" having a spring constant of 7.5 lbs/inch and a "stiff stick" having a spring constant of 130 lbs/inch. The control stick was always located in the center position.

Seven subjects participated in all of the experimental conditions and provided the data base summarized in this report. An accelerometer mounted on the subject's shoulder permitted measurement of vibration transmitted to the body. Accelerometers mounted on a bitebar held between the teeth provided measurements from which head translational and rotational accelerations could be computed.

Each data-taking session consisted of a series of six trials lasting approximately 2 minutes each. Rest periods were provided between successive trials as desired by the subject. (A 30-second rest period was typical.) Each session consisted of one static trial and five trials under different vibration conditions. Presentation of experimental conditions was balanced across subjects to minimize bias in the results due to learning effects. By

the completion of the experimental program, each subject tracked in the static condition three times and under each vibration condition once for each of the two control stick configurations.

## EXPERIMENTAL RESULTS

### Biodynamic Response

Rms acceleration scores for shoulder and head response were averaged across the seven test subjects and analyzed to explore the effects of stick configuration (i.e., stiff or spring) on biodynamic response. No statistically significant differences with regard to stick configuration were found for these variables. Measures of vibration-induced control response, on the other hand, were strongly influenced by control stick parameters.

Figure 1 illustrates the basic linearity of the relevant biodynamic response mechanisms. Mean rms shoulder and head translation accelerations obtained in the complex-vibration experiments are shown versus rms platform acceleration. Data from the two control stick configurations are lumped in this presentation. The dashed lines (found through least-squares regression) indicate the best straight-line fits to the data that pass through the origin. In general, these fits lie within one standard deviation of the experimental measures. The linear fit is especially good for the rms shoulder acceleration, which seems to be the most critical biodynamic variable with regard to predicting tracking performance.

Describing functions relating control response to platform acceleration are shown in Figure 2 for the spring and stiff stick configurations. Measurements from the three types of vibration spectra (random, sum-of-sines and single-sine) are compared for the 0.3 g input. The single-sine describing function is a composite of the frequency-response measures obtained individually at each of the five vibration frequencies.

Except possibly for a greater phase lag associated with the random vibration input, there were no consistent differences in response behavior across the three vibration spectra. With regard to predicting input-correlated response power (which depends only on amplitude ratio), we can consider this response mechanism to be independent of the shape of the platform vibration spectrum. There were important differences between spring-stick and stiff-stick measurements, however, since feedthrough is determined by the interaction between the biomechanical configuration and control-stick characteristics such as mechanical impedance and electrical gain.

We conclude, therefore, that coupling between platform and control input can be treated as linear over the range of vibration amplitudes considered in this study. Accordingly, we can expect to predict response to complex vibration inputs on the basis of experiments made with single-sinusoid

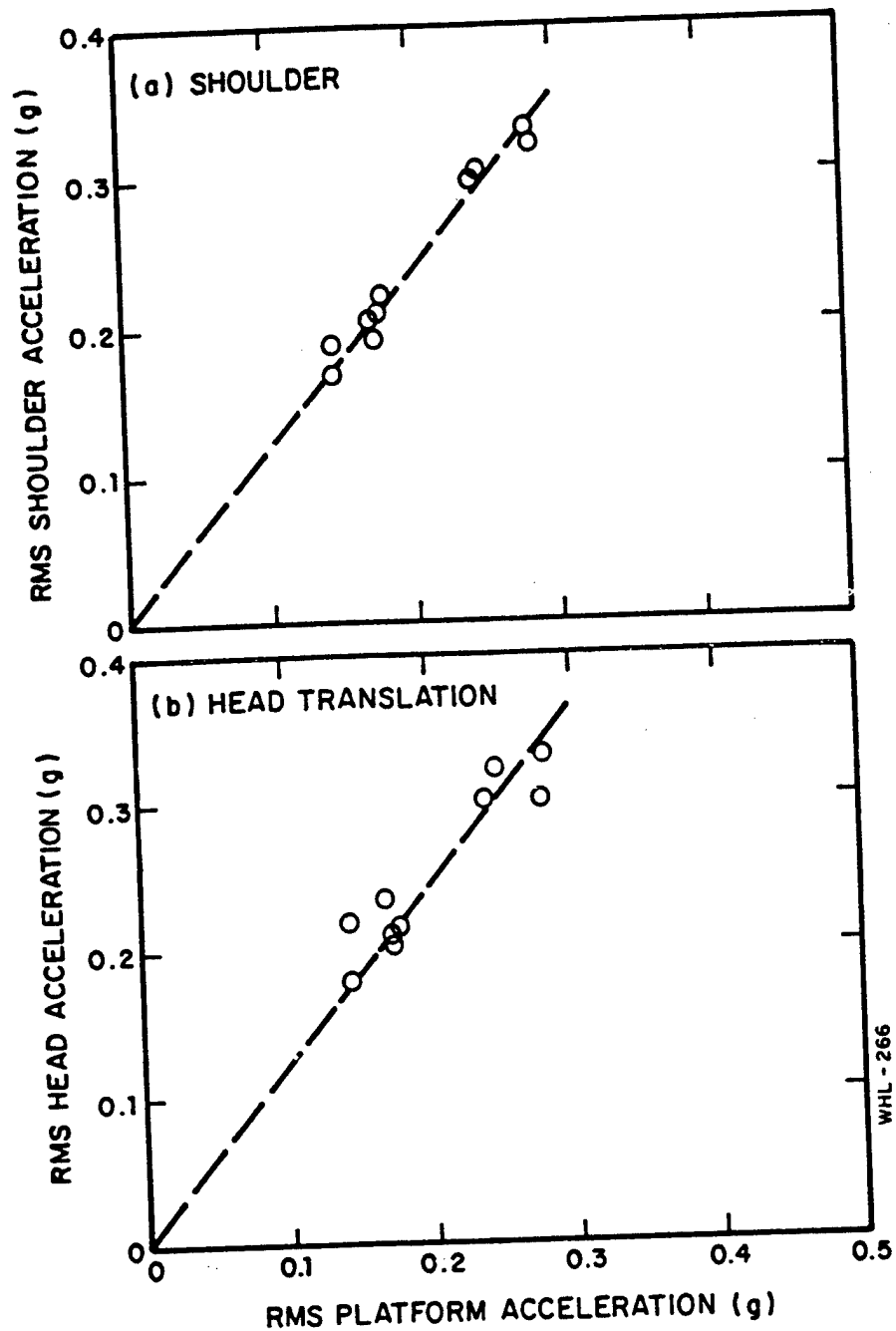


Figure 1. Relation Between Biodynamic Response Scores and Platform Acceleration  
Complex vibration spectra.



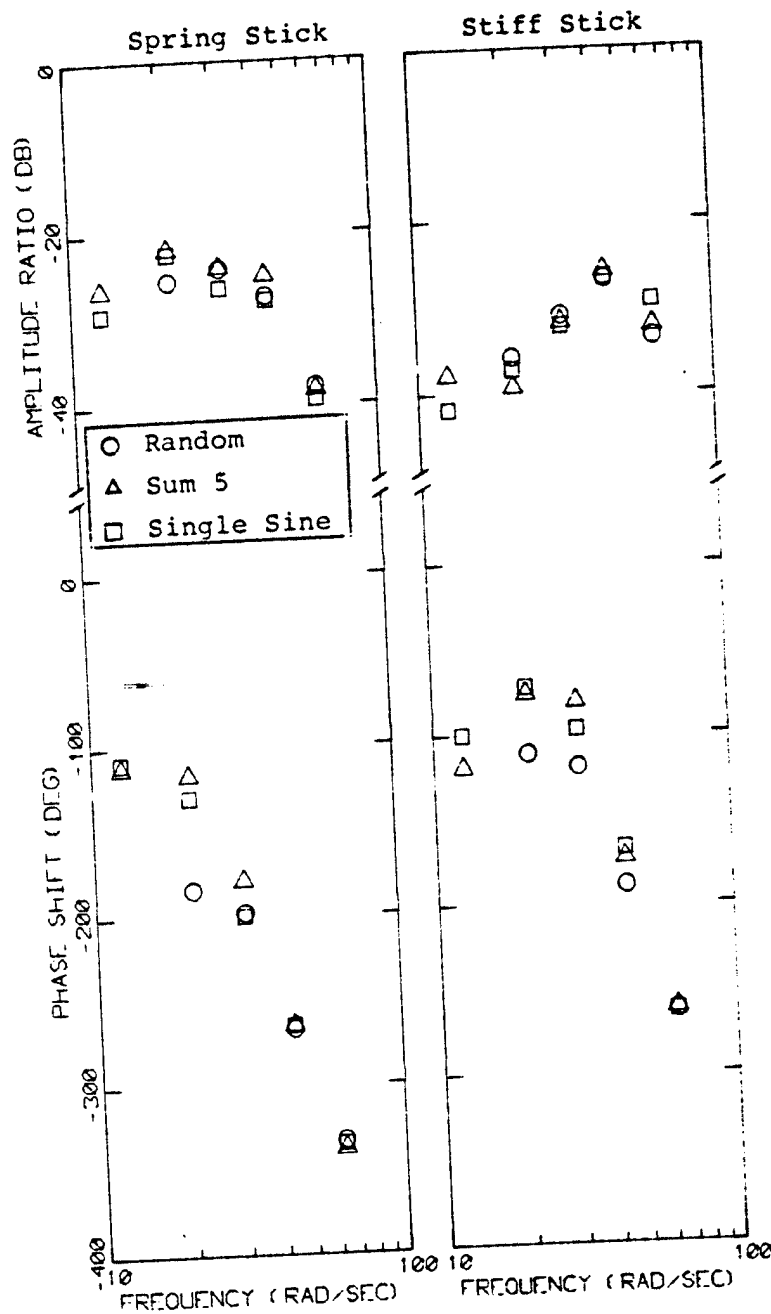


Figure 2. Effect of Vibration Spectrum on Control/Platform Describing Functions  
 0.3 g platform acceleration, average of 7 subjects.  
 0 dB = 1 inch/g.

WHL-267

vibration (and vice versa).\*

Figure 3 shows that the spectral content of the platform vibration had no consistent effect on the shoulder/platform describing function. Vibration amplitude also had negligible effect, indicating that this biodynamic response mechanisms is basically linear.

Describing functions relating head translational response to platform acceleration showed a similar degree of invariance across vibration parameters. The relationship between head rotation and platform was also largely invariant to vibration parameters, except for the amplitude ratio at the lowest vibration frequency (2 Hz). Figure 4 shows that the amplitude ratio increases as spectral complexity increases from single-sine to random. The total increase is relatively large (12 dB) and statistically significant. Analysis of variance shows that the differences between single-sine and sum-of-sine measures, and between sum-of-sine and random measures, are significant at the 0.05 level. (Differences in phase shift at 2 Hz were not significant.) Apparently, the subjects "predicted" the 2 Hz vibration input and thereby partially compensated for head motion response. As expected, predictive capability diminished with increasing spectral complexity.

If the biodynamic response mechanisms described above are linear, it should be possible to use the frequency-response curves obtained with any vibration spectrum and predict rms response motion for any other vibration spectrum (within the range of amplitudes and frequencies for which the data are valid). Of greatest practical interest is the ability to extrapolate from measurements obtained in single-sine vibration environments to predictions of response in complex vibration environments.

Rms biodynamic response scores were predicted for (a) vibration-correlated control input, (b) shoulder acceleration, and (c) head translation for each of the five (three random, two sum-of-sines) complex platform spectra explored in this study.

Extrapolation of single-sinusoid measurements was performed as follows. Biodynamic transfer functions obtained from single-sine experiments (averaged over vibration amplitude) were cascaded with the complex platform vibration spectra to yield predicted response spectra. For sum-of-sines vibration, estimates of response power predicted at each measurement frequency were summed to yield predicted mean-squared response power. For random platform vibration, the predicted response power spectral density was integrated over the frequency range 2-10 Hz to predict mean-squared

---

\*Until further data are obtained, predictions are restricted to steady-state vibration inputs. One is not justified in extrapolating these results to pulse-like acceleration inputs, for example.

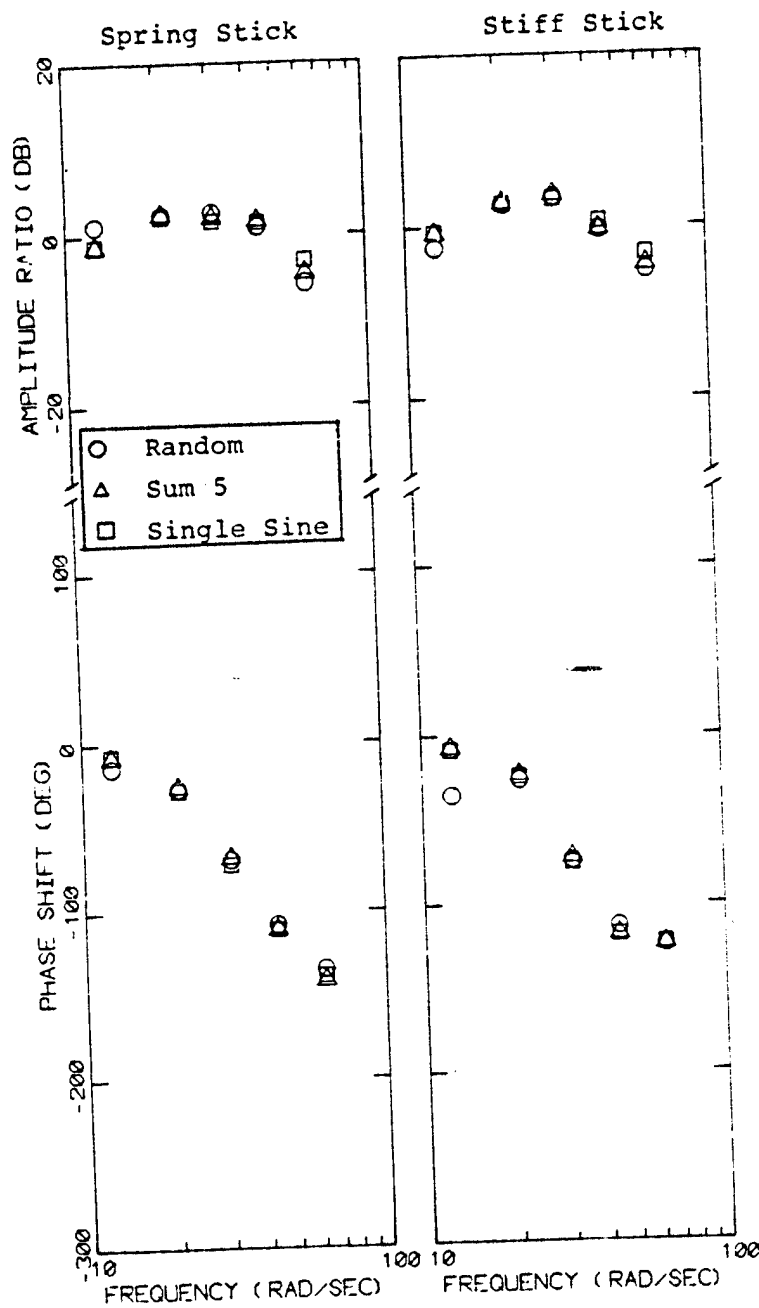


Figure 3. Effect of Vibration Spectrum on Shoulder/Platform Describing Function  
Average of 7 subjects. 0.3 g rms platform acceleration.  
0 dB = 1 g/g.

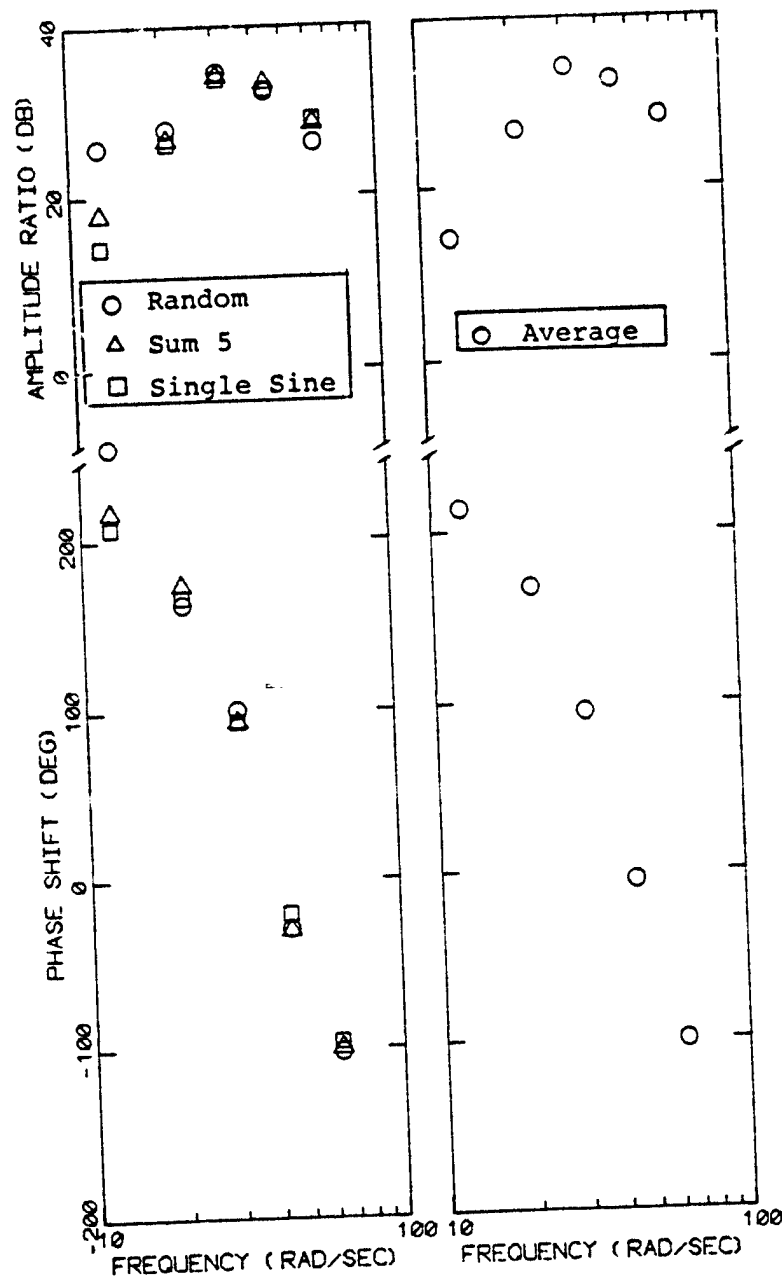


Figure 4. Effect of Vibration Spectrum on Describing Functions Relating Head Rotation to Platform Acceleration  
Average of 7 subjects. 0 dB - 1 (radian/sec<sup>2</sup>)/g.

response power.\* Square roots of these predictions were performed to obtain estimates of rms response.

Predicted and measured rms response scores are compared in Figure 5. Head and shoulder response scores have been averaged across the two stick configurations. On the whole, predictions agree reasonably well with measured quantities; average fractional difference is about 20%.

### Tracking Performance

Error and control scores for the complex vibration conditions are plotted versus vibration amplitude in Figure 6 and exhibit the following trends: (1) error and control scores increase monotonically with increasing vibration amplitude; (2) the increase in control score is more severe for the stiff stick; and (3) tracking error is less for the stiff stick than for the spring stick in the static case, but these differences become less as vibration amplitude is increased. These results are not surprising and generally reflect the findings of the earlier study of Levison and Houck [3].

The error scores associated with single-sine vibration were generally larger than scores associated with complex vibration. However, actual rms platform vibration levels were somewhat larger for single-sine experiments than for complex-vibration experiments for the same nominal vibration level [4]. Therefore, one cannot properly conclude from these results that single-sine vibration inputs are inherently more disruptive than complex vibration inputs.

Rms error and control scores were compared against various biodynamic response measures to determine the response variable (excluding stick feedthrough) most likely responsible for the degradation of tracking performance in vibration environments. Comparisons were made with (a) rms shoulder acceleration, (b) rms shoulder velocity, (c) rms rate-of-change of shoulder acceleration, and (d) estimated rms relative motion between eye point-of-regard and display. Data obtained from single-sine vibration trials were used in this test. Visual inspection of these comparisons revealed that the relation between error (or control) and biodynamic response variable was most nearly monotonic when shoulder acceleration was considered.

Relationships between tracking variables and rms shoulder acceleration are shown in Figure 7. The contribution of stick feedthrough has been removed from the control scores shown in this figure, since we are interested

---

\*Straight-line interpolation was performed between estimates of response power density at adjacent measurement frequencies on a log-log basis. Piecewise integration over the entire range of measurement frequencies was then performed.

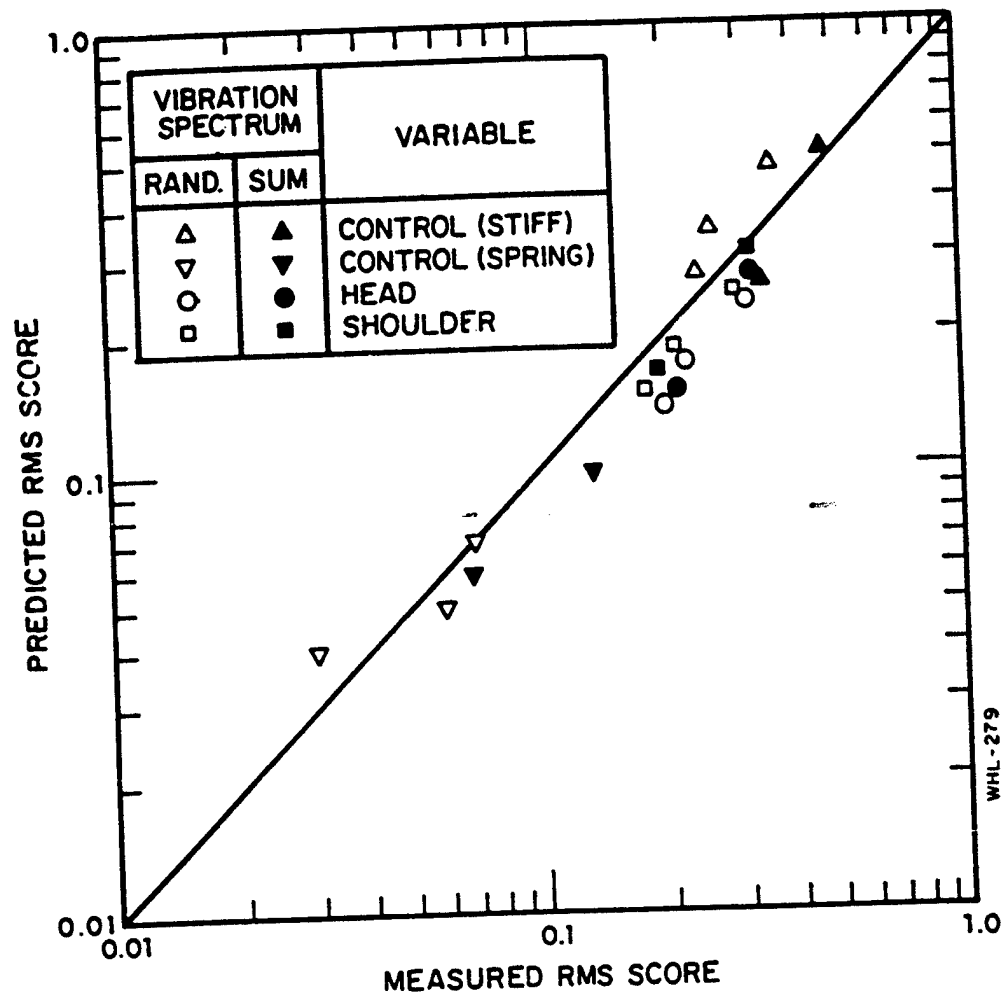


Figure 5. Comparison of Predicted and Measured Rms Scores

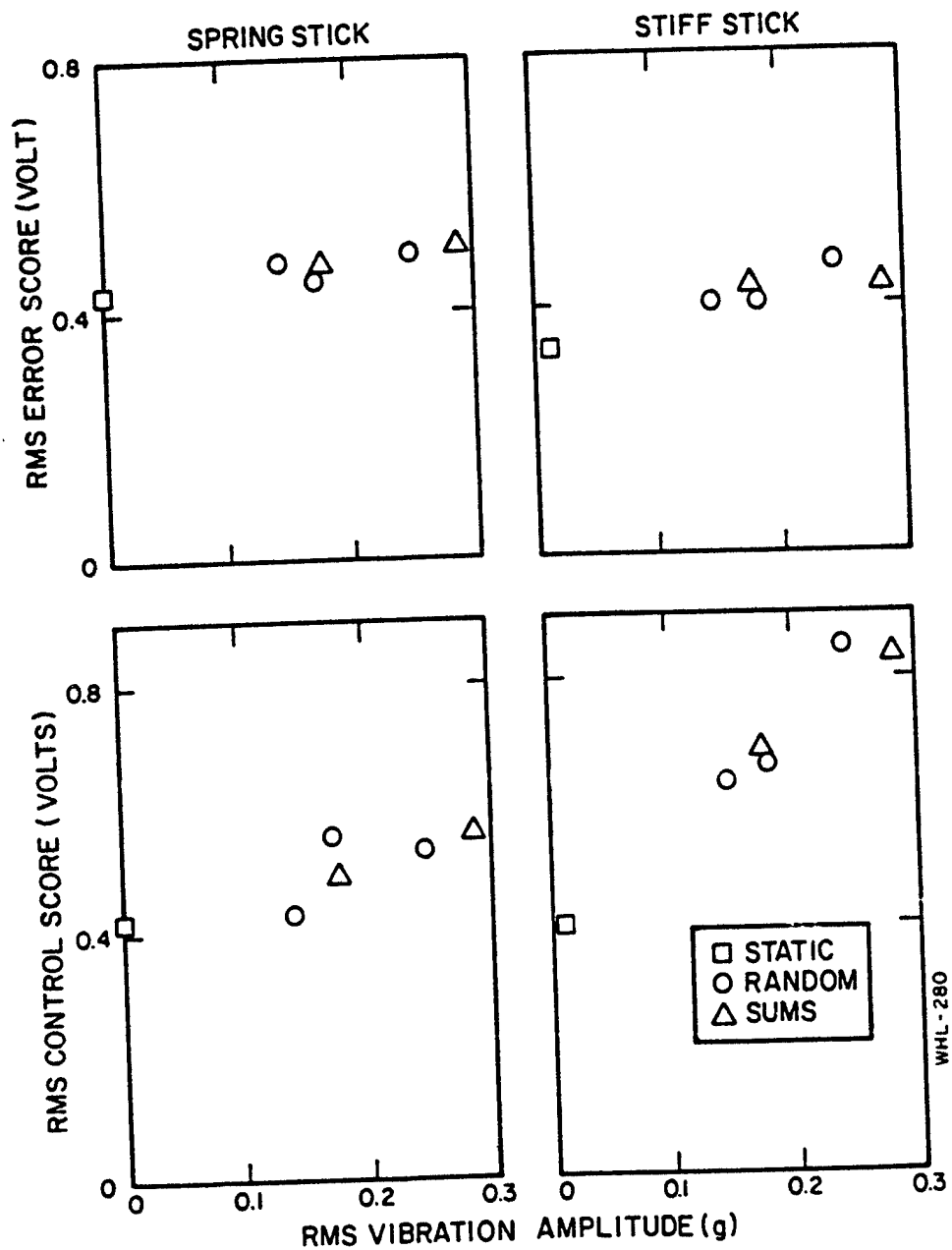


Figure 6. Effect of Vibration Amplitude on Rms Performance  
Average of 7 subjects.

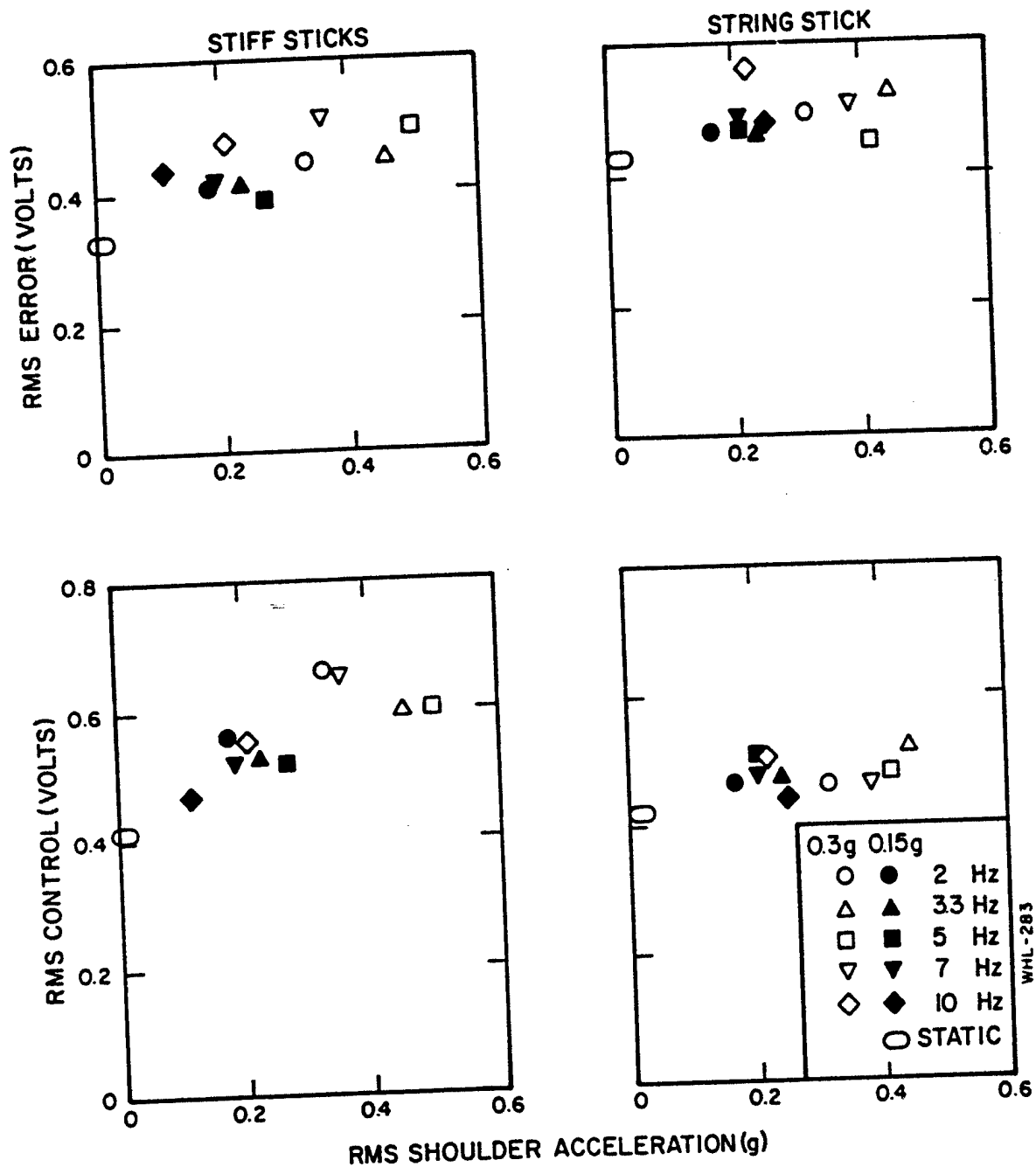


Figure 7. Tracking Variables Versus Shoulder Acceleration  
Single-sine vibration environments.  
Average of 7 subjects.



here primarily in the effect of vibration on tracking response behavior. Relationships between tracking variables and the other biodynamic variables considered (not shown here) tended to show less structure than the relationships shown in Figure 7. Therefore, we have tentatively concluded that motor-related interference with tracking performance is associated primarily with shoulder acceleration. There may, of course, be other response variables not explored in this study (say, elbow acceleration) that correlate equally well or better. Nevertheless, as we show later, reliable predictions of tracking performance can be made on the assumption that motor-related pilot model parameters vary linearly with rms shoulder acceleration.

The effects of vibration on frequency-response measures are typified by Figure 8, which compares static performance with performance in the 0.3 g, sum-of-sines vibration environment. Results are for the spring stick configuration. Amplitude ratio and phase shift refer to the pilot describing function and relate control activity (in volts) to tracking error (volts); "rem/cor" is the ratio of remnant-related stick power to input-correlated stick power at each input frequency.\*

Increasing the rms platform acceleration from 0 (static) to 0.3 g produced the following general trends: (1) amplitude ratio decreased at frequencies below 6.3 rad/sec, remained nearly constant at 6.3 rad/sec, and increased at 10.5 rad/sec;\*\* (2) phase lag increased at 6.3 and 10.5 rad/sec; (3) remnant ratio generally increased at all frequencies. On the whole, deviations from static measurements were greater for the 0.3 g platform acceleration than for the 0.15 g environment, and vibration effects were greater for stiff-stick tracking than for spring-stick tracking. The single-sine vibration environments showed similar influence on frequency-response measurements, with 7 Hz vibration having a somewhat greater effect than 2 Hz vibration. Overall, the frequency-response measures are similar to those found by Levison and Houck [3].

Model analysis using the optimal-control model [5-8] was performed so that vibration-induced performance changes could be interpreted in terms of changes in the pilot's basic information-processing capabilities. A second-order model of the pilot/stick interface was included in the description of system dynamics as described in [5].

Static tracking results were first matched to provide a baseline set

---

\*The ratio is based on what the input-correlated and remnant-related spectra would be if the tracking input spectrum were continuous rather than sum-of-sines. Details of this computation are given in [3].

\*\*Changes in frequency response are referred to input frequencies. Other than having been included in the set of input frequencies, the frequencies of 6.3 and 10.5 rad/sec have no special significance.

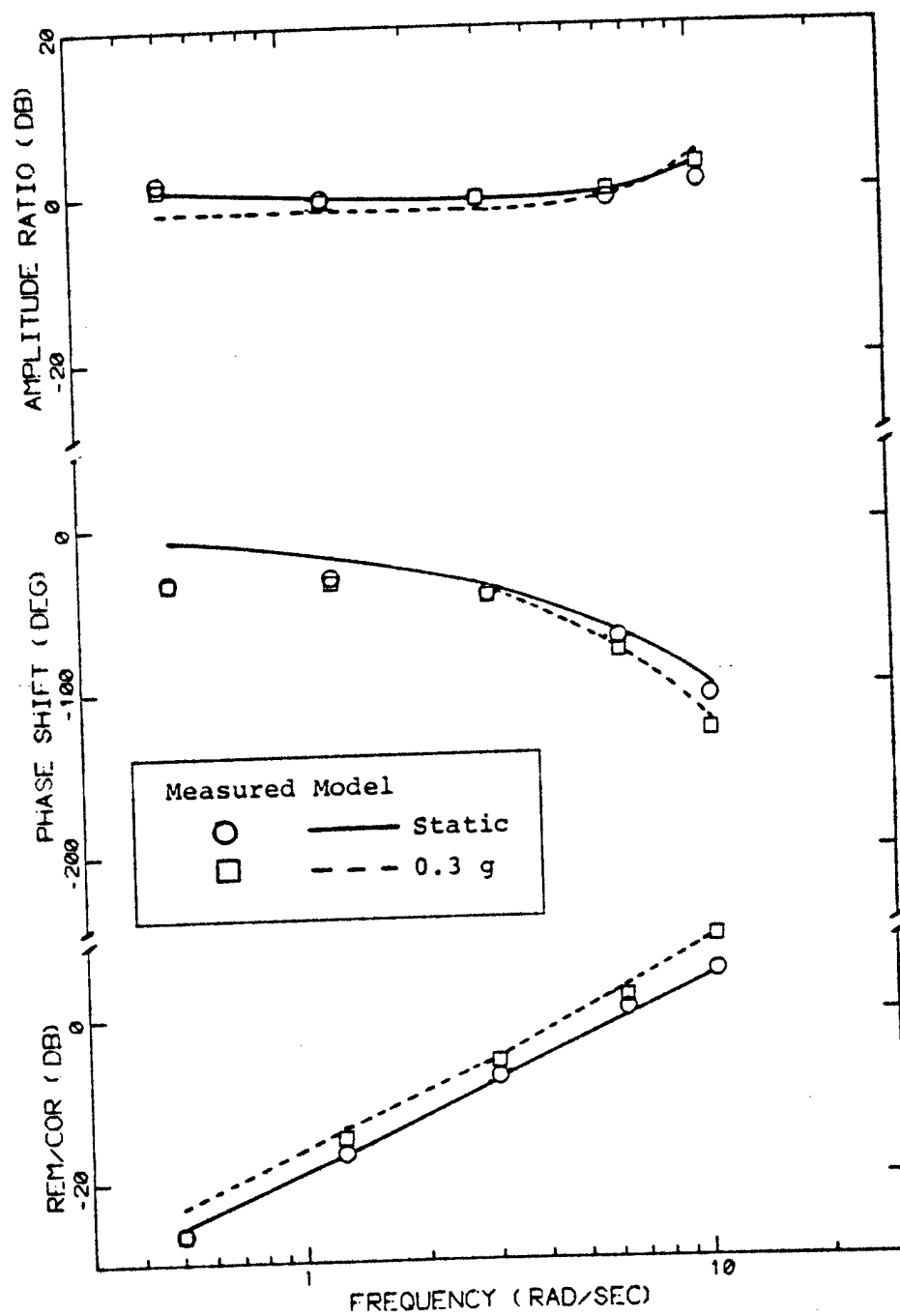


Figure 8. Comparison of Measured and Model Frequency-Response Measures, Spring Stick  
Sum-of-sines vibration.

of pilot-related model parameters. The following values--used also to match static results in the preceding study [3]--provided a good match to static results: 0.15 second time delay, a "motor time constant" of 0.1 seconds, an observation noise/signal ratio of -21 dB, and a motor noise/signal ratio of 0.004 (about -30 dB).

The sum-of-sines 0.3g vibration data were then matched to determine the effects of vibration on pilot-related model parameters. As in the preceding study, two vibration-dependent parameters were identified: time delay and motor noise/signal ratio. Time delay was increased to 0.2 seconds, and motor noise/signal ratio was increased to 0.02. As shown by the solid curves in Figure 7, these parameter changes allow the pilot/vehicle model to reproduce the trend of the frequency-domain results, and both error and control scores (shown further on) are reproduced to within an accuracy of about 5%.

Once the 0.3g data were matched, the 0.15g sum-of-sines results were analyzed to determine the appropriate relationships between pilot parameters and rms shoulder acceleration. A linear variation of both time delay and noise/signal ratio with rms shoulder acceleration provided a good match to the data and was adopted for the mapping procedure outlined in the following section of this paper.

The increment in time delay for 0.3 g vibration was the same as that found by Levison and Houck for a similar vibration environment [3]. However, the motor signal/noise ratio was only half that found in the earlier study, and no visual effects were found in this study. These differences may well reflect a higher level of subject familiarity with the vibration environment in this study. First of all, the experimental program was completed in a shorter period of time than in the Levison and Houck study; thus, there was greater opportunity for the subjects to optimize the tracking strategy for the vibration environments. Secondly, the subjects had participated in a tracking study exploring the same plant dynamics and similar vibration environment for the three months prior to this study, which allowed them to begin this experimental program in a high state of training.

#### MAPPING AMONG VIBRATION ENVIRONMENTS

A general model structure is described below which is intended for predicting tracking performance in a variety of control situations. In addition to predicting the effects of vibration amplitude and spectral shape (which are given primary emphasis in this report), the model can predict performance as a function of (a) vehicle dynamics, (b) tracking input characteristics, (c) control-stick characteristics, (d) display gain, (e) performance requirements, and (f) attention to the task. Numerical relationships between pilot-related tracking parameters and biodynamic response parameters are based on the experimental results documented in [5]; until further data are available, these relationships must be considered valid only for z-axis vibration and for the specific biodynamic configuration explored in this study.

This model is used as the basis of a "mapping" procedure for extrapolating results obtained in a given vibration environment to other vibration environments. A definition and demonstration of the mapping procedure follows the discussion of the basic model.

### Model Structure

An outline of the model structure is diagrammed in Figure 9. This model consists of the optimal-control pilot/vehicle model referred to above, plus an element (labeled "vibration feedthrough") to account for control inputs linearly related to platform vibration. For simplicity of exposition we consider a single-variable tracking task; extension of the model to multi-input, multi-control systems is straightforward.

Input variables shown in Figure 9 are the tracking input,  $i$ , assumed to be a zero-mean Gaussian random process; the platform vibration,  $\alpha_p$ ; the pilot's observation noise process,  $v_e$ ; and the pilot's motor noise process,  $v_u$ . Response variables include tracking error,  $e$ , the pilot's control force,  $u$ , the electrical control input provided by the control device,  $\delta_e$ , the control input due to vibration feedthrough,  $\delta_v$ , and the total control input,  $\delta$ , given as the sum of the tracking and feedthrough control components. (We assume that platform vibration is at frequencies beyond the bandpass of the man/machine system so that the pilot cannot effectively track out the feedthrough-related inputs.) Error and observation noise are shown as vector quantities, since the pilot will generally obtain and use both displacement and velocity information from a single error indicator [10, 11].

The reader is directed to the literature for detailed mathematical discussion of the basic optimal-control model [6, 7]. Pilot-related model parameters and relevant biodynamic response properties are reviewed below.

Time delay. The following empirical relationship was found in this study:  $T = 0.15 + 0.15\alpha_s$ , where  $T$  is the pilot's effective time delay in seconds, and  $\alpha_s$  is the rms shoulder acceleration in g's.

Observation Noise. In the ideal display situation, each component of the observation noise vector  $v_e$  scales with the corresponding rms variance of the corresponding display quantity. In non-ideal situations, threshold and residual noise components must also be considered, as described in [5, 8, 9]. There is some evidence -- albeit inconsistent -- that degradation of visual information due to vibration can be represented as an increment in the residual noise variance. Levison and Houck obtained a good match to experimental data by setting the residual noise variance (associated with perception of indicator displacement) equal to the estimated variance of the relative displacement between eye point-of-regard and display [3]. On the other hand, best results were obtained in this study by ignoring visual effects altogether. Clearly, additional study is needed to determine how head and/or eye movements interfere with acquisition of visually-presented information in a tracking task.

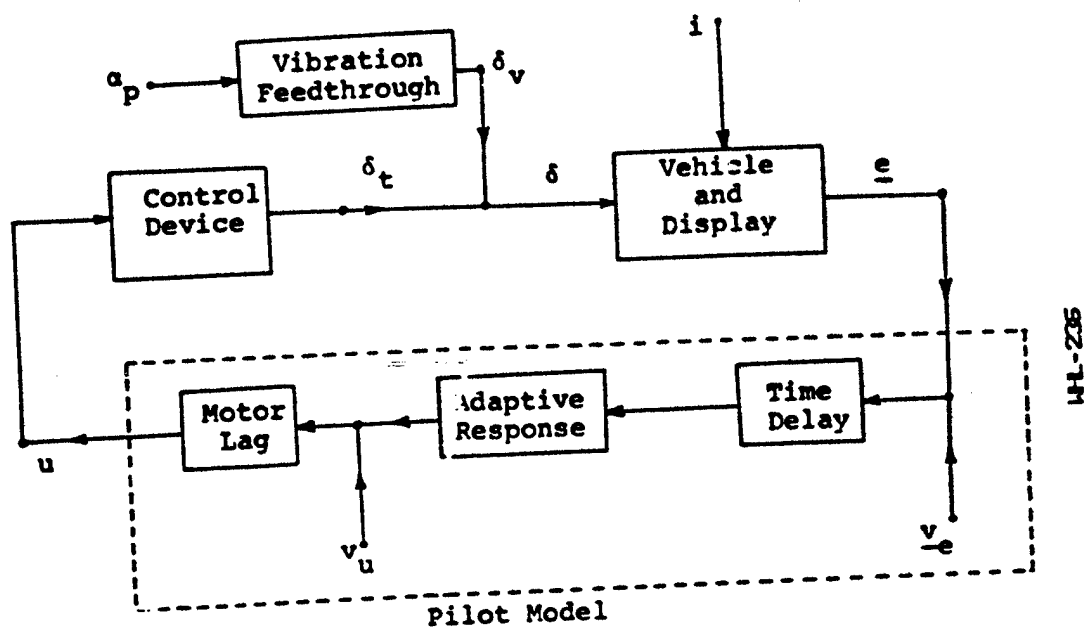


Figure 9. Outline of the Model Structure

Motor Noise. The following empirical relation was found in this study:  $V_u = (0.004 + 0.05\alpha_s) \sigma_u^2$ , where  $V_u$  is the variance of the motor noise and  $\sigma_u^2$  the variance of the pilot's control input.

Motor Time Constant. For most single-variable tracking tasks in which excessive control forces are not required, the pilot will adopt a control strategy appropriate to minimizing a weighted sum of error and control-rate variances. The relative weighting on control-rate variance is chosen to yield a motor time constant (i.e., first-order lag) of about 0.1 seconds. Results of this study, as well as of the study of Levison and Houck [3], indicate that motor time constant is not effected by Z-axis platform vibration.

Stick Feedthrough. "Stick feedthrough" is defined as the portion of control motion that is linearly related to the platform vibration due to biomechanical coupling. Once the relationship between platform vibration and control response has been determined, the contribution of feedthrough to error and control variances can be predicted for a given platform vibration spectrum as described in the literature [3-5].

#### The Mapping Procedure

Because of the limited data base available for validation, the generality of the mapping procedure is restricted to the following situations: (1) the tracking task is single-input, single output; (2) vibration occurs at frequencies beyond the effective man/machine response bandwidth; (3) vibration is applied in a single linear axis. All of these assumptions simplify the mapping procedure. In particular, if the second assumption holds, the pilot will not effectively track out the unwanted inputs produced by vibration feedthrough. Thus, we can compute variance scores due to feedthrough separately from variance scores related to the tracking input and combine the results.

For purposes of demonstration, assume that a series of single-sine vibration experiments have been performed and that we wish to extrapolate these results to a specific complex vibration environment. (The procedure for extrapolating from complex to single-sine environments is virtually identical.) The mapping procedure is outlined in Figure 10.

Tracking performance in sum-of-sines and random vibration environments was predicted on the basis of the single-sine vibration results obtained in the AMRL experimental program described above. The following procedure, which generally parallels the mapping scheme defined in Figure 10, was employed:

1. Static tracking results were first analyzed to determine pilot-related model parameters. Parameter values obtained in the Levison and Houck study [3] provided a good match to static performance in this study.

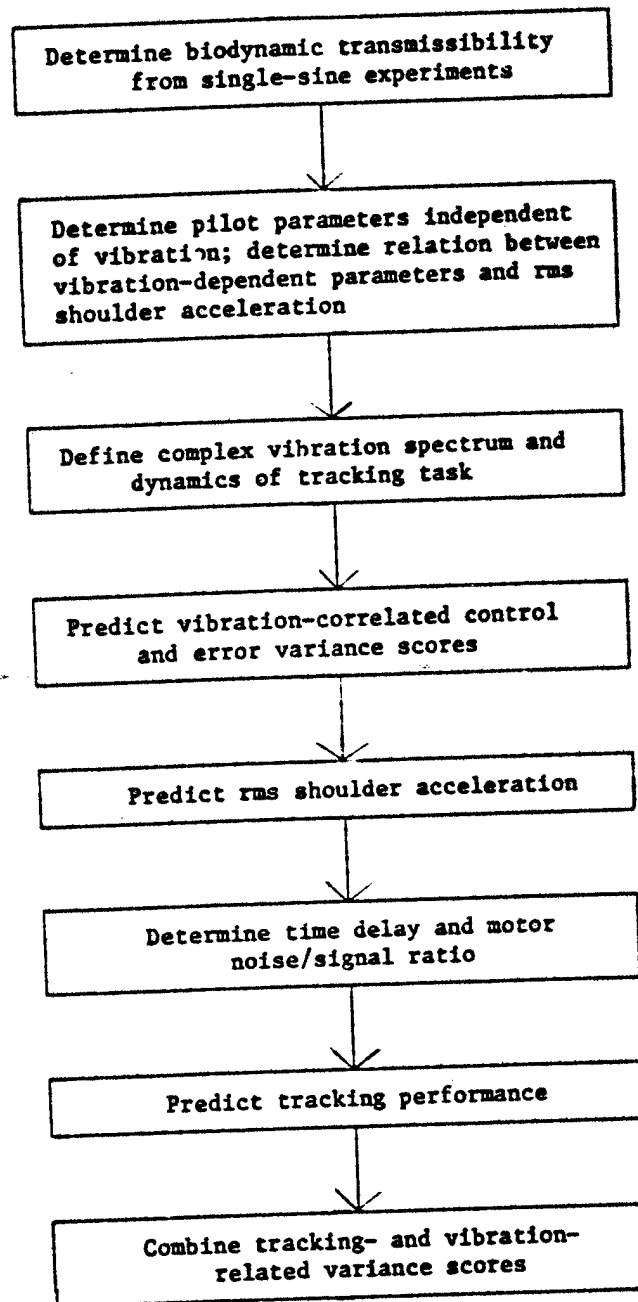


Figure 10. Mapping Single-Sine to Complex Vibration Environments

2. The sum-of-sines results were matched to determine the relation between vibration-dependent pilot parameters (time delay and motor noise) and biodynamic response parameters.\*
3. Biodynamic describing functions obtained with single-sine vibration (averaged across g levels as well as across subjects) were used to predict rms shoulder vibration and vibration-correlated control variance for the sum-of-sines and random vibration spectra. Variance scores for the sum-of-sines environments were predicted by simply adding the platform spectrum (in dB) to the appropriate transfer magnitude (in dB), transforming to absolute units, and summing across frequencies. A curve-fitting procedure was needed, however, to perform frequency-domain integrations required for random vibration inputs. The single-sine transfer magnitudes were cascaded with the power density levels of the platform acceleration at the five measurement frequencies; piecewise-linear approximations to the resulting power density spectrum were made on a log-output versus log-frequency basis; each straight-line segment was integrated analytically; and the results were combined to yield the variance (and rms) of the biodynamic response variable.
4. The remainder of the mapping procedure defined in Figure 10 was carried out, except that the computation of vibration-correlated error was omitted because of its small contribution (generally less than 2%) to total error variance.

Rms error and control scores predicted in this manner are compared with experimental results in Figures 11 and 12 for the spring and stiff stick configurations, respectively. Also shown in this figure are the standard errors for each of the experimental measures. Model predictions reproduced the trends of the data quite well, generally falling within one standard error of the mean.

The reverse mapping is also demonstrated in [5], in which results of the sum-of-sines vibration conditions are extrapolated to single-sine vibration inputs. Again, predicted rms error and control scores were within one standard deviation of the experimental means.

---

\*One of the objectives of this analysis was to determine as reliably as possible in the empirical relation between pilot parameters and biodynamic response in a complex vibration environment. Therefore, the sum-of-sines data were used, rather than the single-sine data that would have been used in a pure demonstration of the mapping procedure.



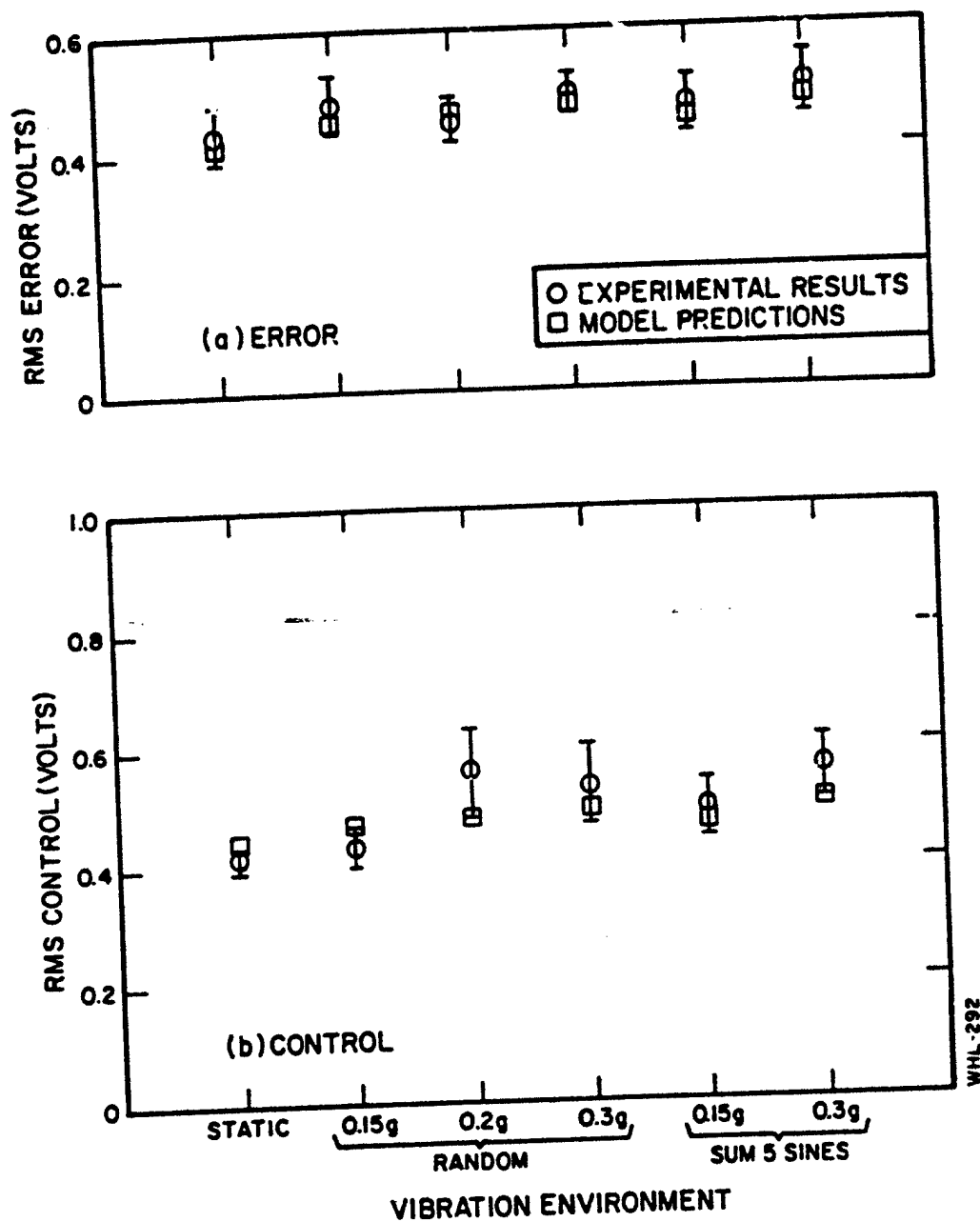


Figure 11. Measured and Predicted Performance Scores for Spring-Stick Configuration

Average of 7 subjects

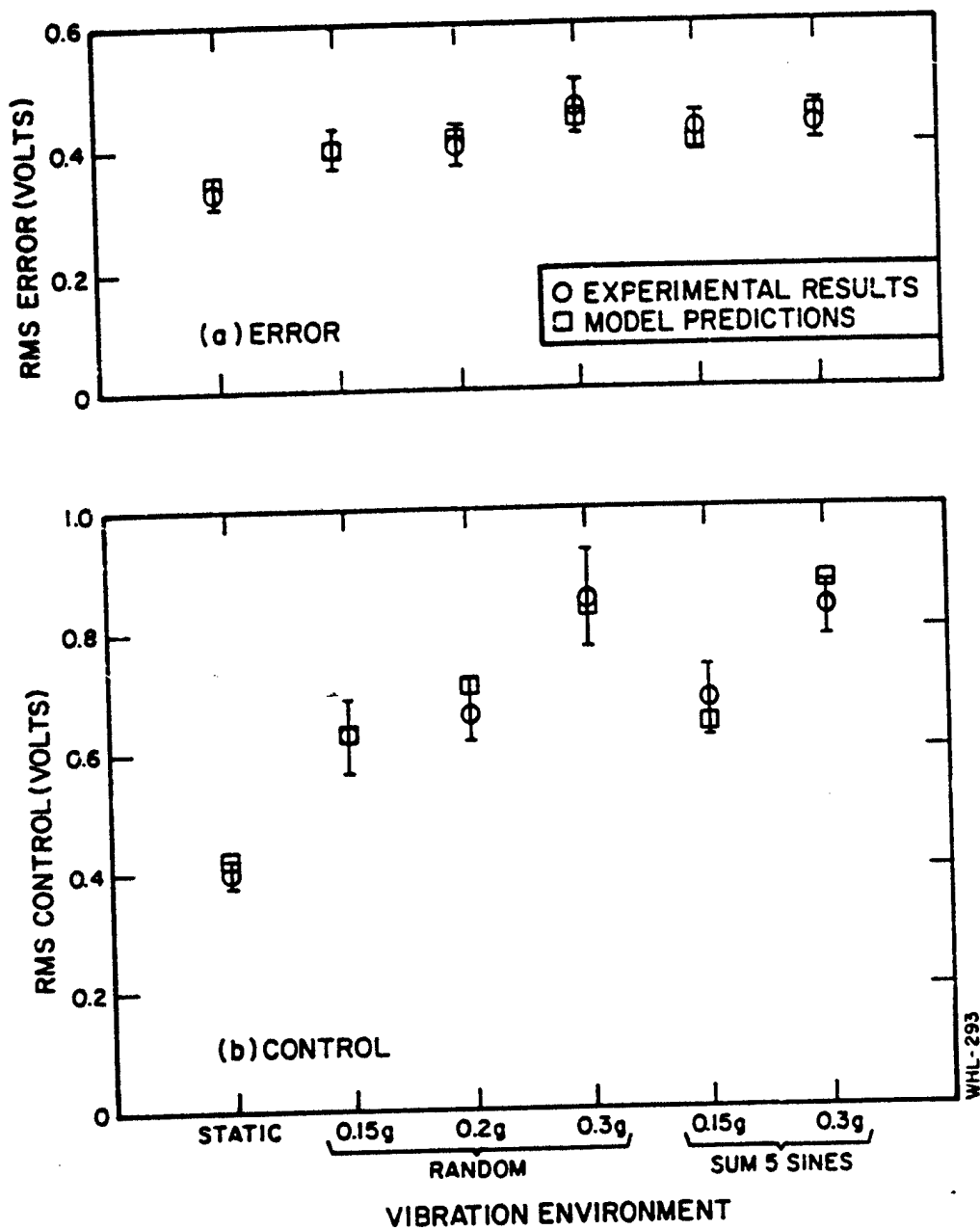


Figure 12. Measured and Predicted Performance Scores for Stiff-Stick Configuration

Average of 7 subjects.

## SUMMARY

The results of the study documented in [5] may be summarized as follows:

*Biomechanical Response.* Biomechanical response mechanisms were essentially linear for the range of vibration amplitudes and spectra explored in this study. Rms shoulder and head acceleration scores varied linearly with rms platform acceleration. In addition, describing functions relating control input, shoulder acceleration, and head translational and rotational accelerations to platform acceleration were largely independent of the parameters of the platform vibration.

*Effects of Stick Parameters.* Shoulder and head response to platform vibration was independent of stick parameters, whereas feedthrough was considerably more severe for the stiff stick than for the spring stick. Although static error scores were less for the stiff stick, vibration induced a relatively greater increase in error for the stiff-stick than for the spring-stick tracking tasks.

*Stick Feedthrough.* Stick feedthrough for the stiff stick was similar to that obtained in a similar experimental situation by Levison and Houck [3]; feedthrough for the spring stick; however, was considerably less than that in the prior study.

*Vibration Interference Effects.* Feedthrough accounted for a negligible fraction (2% or less) of the tracking error variance. In terms of the pilot/vehicle model employed in the analysis, the important effects appeared to be an increase in motor-related remnant and time delay. Both the motor noise/signal ratio and time delay appeared to vary linearly with rms shoulder acceleration. No interference with visual processes was identified.

*Mapping Procedure.* A model-based mapping procedure was defined and verified for extrapolating the results of single-sine vibration/tracking experiments to complex vibration environments. Mapping in the reverse direction was also verified.

Because we lack models for extrapolating existing results to other axes of vibration or other biomechanical configurations, the mapping procedure defined in this paper is intended to apply only to z-axis vibration and to the biomechanical configuration employed in recent AMRL studies. We can, however, extrapolate results to other steady-state z-axis vibration patterns, provided that rms platform vibration is on the order of 0.3 g or less. Furthermore, because of the demonstrated capability of the underlying pilot/vehicle model to predict tracking performance in a variety of

control situations, we expect the mapping procedure to be useful in exploring tracking tasks beyond those studied in the laboratory.

#### REFERENCES

1. Allen, R. W.; Jex, Henry R.; and Magdaleno, R. E.: Manual Control Performance and Dynamic Response During Sinusoidal Vibration. AMRL-TR-73-78, Aerospace Medical Research Laboratory, Wright-Patterson Air Force Base, Ohio, October 1973.
2. Levison, William H.: Analysis of Vibration-Induced Pilot Remnant. BBN Report No. 2608, Final Report, Bolt Beranek and Newman Inc., Cambridge, Mass., under Contract No. F33615-71-C-1207, August 1973.
3. Levison, William H.; and Houck, Philip D.: Guide for the Design of Control Sticks in Vibration Environments. AMRL-TR-74-127, Aerospace Medical Research Laboratory, Wright-Patterson Air Force Base, Ohio, February 1975.
4. Levison, William H.: Effects of Control-Stick Parameters on Tracking Performance in a Vibration Environment. Proc. of the Eleventh Annual Conference on Manual Control, Ames Research Center, Moffett Field, California, May 1975.
5. Levison, William H.: Biomechanical Response and Manual Tracking Performance in Sinusoidal, Sum-of-Sines, and Random Vibration Environments, AMRL-TR-75-94, Aerospace Medical Research Laboratory, Wright-Patterson Air Force Base, Ohio, April 1976.
6. Kleinman, D.L.; Baron, S.; and Levison, W. D.: An Optimal-Control Model of Human Response, Part 1: Theory and Validation. *Automatica*, Vol. 6, pp. 357-369, 1970.
7. Kleinman, D. L.; Baron, S.; and Levison, W. H.: A Control Theoretic Approach to Manned-Vehicle Systems Analysis. IEEE Trans. on Auto. Control, Vol. AC-16, No. 6, December 1971.
8. Kleinman, D. L.; and Baron, S.: Analytic Evaluation of Display Requirements for Approach to Landing. NASA CR-1952, November 1971.
9. Baron, S.; and Levison, W. H.: A Manual Control Theory Analysis of Vertical Situation Displays for STOL Aircraft. NASA CR-114620, April 1973.
10. Levison, W. H.; Baron, S.; and Kleinman, D. L.: A Model for Human Controller Remnant. IEEE Trans. Man-Machine Systems, Vol. MMS-10, No. 4, December 1969.

11. Levison, W. H.: The Effects of Display Gain and Signal Bandwidth on Human Controller Remnant. Wright-Patterson Air Force Base, Ohio, AMRL-TR-70-93, March 1971.